

D I S S E R T A T I O N

Modification of Ultra-High Vacuum Surfaces Using Free Radicals

ausgeführt zum Zwecke der Erlangung des akademischen Grades eines
Doktors der technischen Wissenschaften

unter der Leitung von

Prof. Dr. Herbert Störi
E134 – Institut für Allgemeine Physik

under the supervision of

Dr. Noël Hilleret
CERN–LHC–VAC

eingereicht an der Technischen Universität Wien
Fakultät für technische Naturwissenschaften und Informatik

von

Dipl. Ing. Georg Vorlaufer
Matrikelnr. 8626046
A-1180 Wien, Martinstraße 90

Wien, im Februar 2002

Kurzfassung

In den meisten Ultrahochvakuumanlagen bestimmen die Gasabgabe aus Festkörpern und die Desorption von Oberflächenadsorbaten Enddruck und Zusammensetzung des Restgases. Speziell im Strahlvakuum von Beschleunigern wie dem LHC, wo Oberflächen intensiver Synchrotronstrahlung und Beschuß durch energetische Ionen und Elektronen ausgesetzt sind, können Oberflächeneigenschaften wie Desorptionsrate oder Sekundärelektronenrate den Betrieb des Beschleunigers wesentlich beeinflussen.

Etablierte Behandlungsmethoden wie etwa Ausheizen unter Vakuum oder Oberflächenkonditionierung mit Hilfe einer Glimmentladung wurden in der Vergangenheit bereits erfolgreich eingesetzt, um Oberflächen für die Verwendung im Ultrahochvakuum zu konditionieren, aber diese Methoden sind oftmals schwierig anzuwenden, zum Beispiel wenn die Vakuumkammern nicht oder nur schwer zugänglich sind.

In dieser Arbeit wird eine alternative Behandlungsmethode untersucht, die sich die hohe chemische Aktivität von freien Radikalen, das sind elektrisch neutrale Molekülfragmente, zunutze macht. Freie Radikale (im Falle dieser Arbeit Stickstoff- bzw. Sauerstoffradikale) werden mit Hilfe eines Mikrowellenplasmas erzeugt und anschließend durch die Vakuumapparatur gepumpt, wo sie mit Oberflächen auf unterschiedliche Art und Weise reagieren und dabei Adsorbate entfernen und/oder die chemische Zusammensetzung der Oberfläche verändern können.

Um den Effekt einer solchen Behandlung mit Radikalen beurteilen zu können, wurden die Oberflächen behandelter und unbehandelter Proben mit unterschiedlichen Methoden untersucht und miteinander verglichen. Einen besonderen Schwerpunkt stellt in diesem Zusammenhang die Messung der Gasdesorptionsrate dar. Zu diesem Zweck wurde eine experimentelle Vakuumanlage aufgebaut, die die Messung der durch Elektronenbeschuß induzierten Gasdesorptionsrate *in situ* erlaubt, das heißt ohne die Probe zwischen Behandlung und Messung an Luft auszusetzen.

Im Hinblick auf eine mögliche Anwendung für die Behandlung von Strahlrohren eines Beschleunigers wurde eine detaillierte Studie der Radikalenverteilung in einem zylindrischen Rohr mit Hilfe einer Computersimulation durchgeführt. Das physikalische Modell für diese Computersimulation basiert auf Konzepten der Strömungsmechanik und Reaktionskinetik. Radikalenverteilungen wurden auch auf experimentellem Wege durch Messung der Rekombinationswärme bestimmt, und die Resultate dieser Messungen wurden mit jenen der Simulation verglichen.

Diese Arbeit wurde am CERN in der Vakuumgruppe der LHC Division durchgeführt und hatte zum Ziel, die Methode der freien Radikale im allgemeinen und ihre Anwendbarkeit für die Behandlung von Oberflächen im Strahlvakuum des LHC im speziellen zu untersuchen. Mit Hilfe der vorliegenden Daten aus Experiment und Simulationsrechnung können die Möglichkeiten und Grenzen dieser Methode aufgezeigt und für eine praktische Anwendung günstige Behandlungsparameter angegeben werden.

Abstract

In ultra-high vacuum systems outgassing from vacuum chamber walls and desorption of surface adsorbates are usually the factors which determine pressure and residual gas composition. In particular in beam vacuum systems of accelerators like the LHC, where surfaces are exposed to intense synchrotron radiation and bombardment by energetic ions and electrons, surface properties like the molecular desorption yield or secondary electron yield can strongly influence the performance of the accelerator.

Well-established treatment methods like vacuum bake-out or glow-discharge cleaning have been successfully applied in the past to condition ultra-high vacuum surfaces, but these methods are sometimes difficult to carry out, for example if the vacuum chambers are not accessible.

In this work, an alternative treatment method is investigated. This method is based on the strong chemical reactivity of free radicals, electrically neutral fragments of molecules. Free radicals (in the case of this work, nitrogen and oxygen radicals) are generated in a microwave plasma source and pumped through a vacuum chamber where they can react with the surface in various ways, thereby removing surface adsorbates and/or changing the chemical composition of the surface.

In order to assess the effect of radical treatment, surfaces of radical treated samples have been analysed using various techniques and compared with surfaces of non-treated samples of the same material. Special emphasis has been put on the measurement of the molecular desorption yield. For this purpose an experimental vacuum system has been set up which permits measurements of the molecular desorption yield induced by electron bombardment (ESD) *in situ*, i.e. without exposing the sample to atmosphere between radical treatment and measurement.

In view of a possible application to accelerator beam pipes, the distribution of radicals in cylindrical tubes has been studied in detail by means of a computer simulation whose underlying physical model incorporates concepts of fluid dynamics and chemical kinetics. Radical distributions have also been determined experimentally from measurements of the heat of recombination. Results of these measurements are compared with those from the computer simulation.

This work has been carried out in the vacuum group of the LHC division at CERN with the aim to investigate the radical treatment method in general and its application for the conditioning of surfaces in the LHC beam vacuum system in particular. With the experimental and simulation results presented in this work, it is possible to demonstrate capabilities and limitations of the radical treatment method and to specify favourable operating conditions for practical applications.

Contents

I	Introduction	1
1	Overview	2
2	CERN and the LHC	3
2.1	A short introduction of CERN	3
2.2	The LHC project	4
2.3	An introduction of the LHC beam vacuum system	8
2.4	Beam related dynamic vacuum effects and their impact on LHC	11
2.4.1	Desorption by synchrotron radiation	11
2.4.2	Ion induced pressure instability	13
2.4.3	Beam induced electron multipacting	14
3	Treatment of UHV surfaces by means of radicals	19
3.1	Cleaning for vacuum applications	19
3.2	Free radicals	20
3.3	Radicals for surface treatment	22
3.4	The radical generator	23
II	Characterisation of Radical Treated Surfaces	27

4	Electron stimulated desorption of molecules from radical treated surfaces	28
4.1	Description of the experiment	28
4.2	Experimental setup	29
4.3	Determination of the molecular desorption yield	35
4.3.1	Theoretical and experimental prerequisites	35
4.3.2	Measurement procedure	39
4.4	Results	42
4.4.1	Treatment efficiency of nitrogen and oxygen radicals . . .	42
4.4.2	Reduction of the molecular desorption yield by oxygen radical treatment	43
4.4.3	Development of the molecular desorption yield under continuous electron bombardment – simulation of the beam scrubbing effect	43
5	Surface analysis of radical treated samples	51
5.1	Introduction	51
5.2	Experimental setup	51
5.3	Results from surface analysis	54
5.3.1	Experimental runs no. 1 and 1a	54
5.3.2	Experimental runs no. 2 and 3	55
5.3.3	Experimental runs no. 4 and 5	56
5.3.4	Experimental run no. 6	58
5.4	Results from secondary electron yield measurements	59
III	Characterisation of the Radical Flow	71
6	Computer simulation of the radical flow	72
6.1	Introduction	72

6.2	The model	74
6.2.1	Description of the model	74
6.2.2	Equations of state	77
6.2.3	Transport equations	79
6.2.4	Boundary conditions for a cylindrical tube	89
6.2.5	Model parameters for the binary mixture of nitrogen radicals and molecules	94
6.3	Numerical solution	97
6.3.1	Integration of the transport equations over a finite volume cell	97
6.3.2	Discretization scheme	107
6.3.3	Solution algorithm	113
6.3.4	Implementation	116
6.4	Results	117
6.4.1	Verification of the simulation	117
6.4.2	Simulation results for a typical set of parameters	117
6.4.3	Characteristic decay length of radicals	118
6.4.4	Application of the simulation to an LHC dipole cold bore tube	119
6.4.5	Application of the simulation to a 4 mm inner diameter copper tube	121
7	Temperature probes	134
7.1	Description of the experiment	134
7.2	Experimental setup	137
7.3	Data evaluation	140
7.3.1	Voltage to temperature conversion	140
7.3.2	Calculation of the heat of recombination	141
7.3.3	Determination of the radical density	147

7.4	Results	150
7.4.1	Nitrogen radicals	150
7.4.2	Comparison of temperature probe measurements with simulation	150
7.4.3	Oxygen radicals	153
IV	Summary	165
8	Discussion	166
9	Conclusion	168
	Appendix	169
A	Fundamental physical constants	170
B	Some LHC design parameters	171
C	ESD experiment: settings and calibration data	173
D	Calculation of partial pressures from gauge and mass spectrometer data	176
E	The covariant formalism	180
F	Cylindrical co-ordinate system	184
	Bibliography	186
	Acknowledgements	199
	Curriculum Vitae	200

List of Tables

5.1	Layer thickness (in nm) from Auger depth profiles	57
6.1	Summary of the transport equations	74
6.2	Arrhenius parameters for the third order recombination of nitrogen radicals	85
6.3	Coefficients of the Shomate equation for atomic and molecular nitrogen for the range of $298 < T < 6000$	94
6.4	Specific thermodynamic quantities for atomic and molecular nitrogen	96
6.5	The faces of a finite volume cell	99
7.1	Polynomial coefficients for the characteristic curves of an E-type thermocouple	141
7.2	Some temperature probe properties	142
7.3	Recombination probability of nitrogen radicals on stainless steel	150
C.1	Effective pumping speed	173
C.2	Emission current of the Bayard Alpert gauges and the quadrupole mass spectrometer	173
C.3	Absolute sensibilities of the Bayard Alpert gauges	174
C.4	Sensibilities relative to H_2^+ of the quadrupole mass spectrometer	174
C.5	Cracking pattern of the quadrupole mass spectrometer	175

List of Figures

2.1	General Layout of the Large Hadron Collider	5
2.2	Schematic drawings of the four LHC detectors	6
2.3	Cross section of a LHC dipole cryomagnet assembly	8
2.4	Picture of a prototype beam screen, inserted into a sample beam pipe	10
2.5	Typical plots of the secondary electron yield of copper as a function of the primary electron energy	17
3.1	Light emission in the afterglow region of a nitrogen plasma . . .	23
3.2	Photograph of the radical generator	25
3.3	Sectional drawing (schematic) of the radical generator	26
4.1	Schematic drawing of the experimental setup for the ESD measurements	30
4.2	Cutaway drawing of the sample transfer system for the ESD experiment	31
4.3	Exploded view of the sample holder for the ESD experiment . .	32
4.4	A set of calibration curves for carbon monoxide	38
4.5	Typical desorption pulses	40
4.6	Molecular desorption yields of two copper samples treated with nitrogen and oxygen radicals	45
4.7	Comparison of the treatment efficiency of nitrogen and oxygen radicals	46

4.8	Reduction of the molecular desorption yield by oxygen radical treatment	47
4.9	The molecular desorption yield as a function of the electron dose – Comparison of an untreated and an oxygen radical treated sample	48
4.10	The number of desorbed molecules as a function of the electron dose – Comparison of an untreated and an oxygen radical treated sample	49
4.11	The molecular desorption yield as a function of the number of desorbed molecules – Comparison of an untreated and an oxygen radical treated sample	50
5.1	Schematic drawing of the sample preparation system	52
5.2	A sample at “position 0” during radical treatment	53
5.3	Auger electron spectra from experimental run no. 1	60
5.4	Relative concentrations of surface atoms, calculated from Auger electron spectra no. 1 and 1a	61
5.5	SEM images of samples “as received” and “position 0” from experimental run no. 1	62
5.6	Relative concentrations of surface atoms, calculated from Auger electron spectra no. 2 and 3	63
5.7	Auger electron spectra from experimental run no. 4	64
5.8	Relative concentrations of surface atoms, calculated from Auger electron spectra no. 4 and 5	65
5.9	X-ray photo-electron spectra (full scan) of samples “as received” and “position 1” from experimental run no. 4	66
5.10	X-ray photo-electron spectra (first detail) of samples “as received” and “position 1” from experimental run no. 4	67
5.11	X-ray photo-electron spectra (second detail) of samples “as received” and “position 1” from experimental run no. 4	68
5.12	Relative concentrations of surface atoms, calculated from Auger electron spectra no. 6	69

5.13	Secondary electron yield measurements of oxygen radical treated samples	70
6.1	Geometry used for the computer simulation	75
6.2	Subdivision of the simulation domain into finite volume cells . .	76
6.3	Mass flow through an infinitesimal surface element	81
6.4	Forces acting on an infinitesimal surface element	86
6.5	Scheme to derive the wall boundary condition for the radical mole fraction	92
6.6	Graph of the enthalpy as a function of the temperature	95
6.7	Outline drawing of a finite volume cell	98
6.8	The weighting factors $f^{(w)}$ and $f^{(e)}$ as a function of the Peclet number Pe according to the power-law scheme	111
6.9	Staggered grid arrangement for the solution of the Navier-Stokes equations	112
6.10	Outline of the simulation algorithm	115
6.11	Comparison of Poiseuille's law with simulation results	122
6.12	Simulation results: temperature and radical mole fraction	123
6.13	Simulation results: axial and radial velocity components	124
6.14	Simulation results: pressure and mass flow	125
6.15	Simulation results: cross section averaged radical mole fraction as a function of the axial co-ordinate for a fixed value of $X_{in} = 0.5$	126
6.16	Simulation results: cross section averaged radical mole fraction as a function of the axial co-ordinate for a fixed value of $\frac{\partial p}{\partial z} = 12.5 \text{ Pa} \cdot \text{m}^{-1}$	127
6.17	Simulation results: characteristic decay length ζ for a fixed value of $X_{in} = 0.5$	128
6.18	Simulation results: characteristic decay length ζ for a fixed value of $\frac{\partial p}{\partial z} = 12.5 \text{ Pa} \cdot \text{m}^{-1}$	129
6.19	Simulation results for a cold bore tube: velocity and temperature	130

6.20	Simulation results for a cold bore tube: molar density and radical mole fraction	131
6.21	Simulation results for a cold bore tube: total and partial pressure	132
6.22	Simulation results for a 4 mm inner diameter copper tube	133
7.1	Picture and cutaway drawing of a temperature probe	135
7.2	Experimental setup to measure the radical distribution along a test vacuum chamber	138
7.3	Pictures of the temperature probe experiment	139
7.4	Measurement data of an experimental run with nitrogen at 500 Pa and $10 \text{ Pa} \cdot \text{m}^3 \cdot \text{s}^{-1}$	144
7.5	Measurement data of an experimental run with nitrogen at 200 Pa and $4 \text{ Pa} \cdot \text{m}^3 \cdot \text{s}^{-1}$	145
7.6	Temperature probe results for N_2 : heat of recombination as a function of the temperature probe position	154
7.7	Temperature probe results for N_2 : heat of recombination as a function of pressure and flow rate	155
7.8	Temperature probe results for N_2 : heat of recombination of as a function of pressure and mean velocity	156
7.9	Temperature probe results for N_2 : radical concentration as a function of the temperature probe position	157
7.10	Temperature probe results for N_2 : radical mole fraction as a function of the temperature probe position	158
7.11	Temperature probe results for N_2 : radical partial pressure as a function of the temperature probe position	159
7.12	Measurement data from an experimental run with nitrogen at 500 Pa and $10 \text{ Pa} \cdot \text{m}^3 \cdot \text{s}^{-1}$ with the radical source being repeatedly switched on and off	160
7.13	Evaluation of temperature probe data (500 Pa, $10 \text{ Pa} \cdot \text{m}^3 \cdot \text{s}^{-1}$) using a second order model	161
7.14	Comparison of characteristic decay lengths ζ of nitrogen radicals obtained from temperature probe data and simulation	162

7.15	Temperature probe results for Ar – O ₂ : heat of recombination and concentration of oxygen radicals as a function of the temperature probe position	163
7.16	Temperature probe results for Ar – O ₂ : partial pressure and mole fraction of oxygen radicals as a function of the temperature probe position	164
F.1	Cylindrical co-ordinate system	184

List of Symbols

Symbol	Description	Unit
$\langle \phi \rangle_A$	Cross section averaged flow variable	varies
A	Cross sectional area of the tube	m^2
A	Surface area of the temperature probe	m^2
a	Speed of sound	$\text{m} \cdot \text{s}^{-1}$
C_p	Specific constant pressure heat capacity of the temperature probe	$\text{J} \cdot \text{kg}^{-1} \cdot \text{K}^{-1}$
$C_{p,k}$	Specific constant pressure heat capacity of the k th species	$\text{J} \cdot \text{kg}^{-1} \cdot \text{K}^{-1}$
$\overline{C_p}$	Specific constant pressure heat capacity of the gas mixture	$\text{J} \cdot \text{kg}^{-1} \cdot \text{K}^{-1}$
c	Speed of light	$\text{m} \cdot \text{s}^{-1}$
D_k	Mixture averaged diffusion coefficient of the k th species	$\text{m}^2 \cdot \text{s}^{-1}$
D	Radical diffusion coefficient in case of a binary mixture	$\text{m}^2 \cdot \text{s}^{-1}$
e	Specific total energy	$\text{J} \cdot \text{kg}^{-1}$
e	Elementary charge	C
\tilde{g}	Metric tensor	1
H	Molar Enthalpy	$\text{J} \cdot \text{mol}^{-1}$
h_k	Specific enthalpy of the k th species	$\text{J} \cdot \text{kg}^{-1}$
h_k^r	Specific enthalpy of the k th species at reference conditions	$\text{J} \cdot \text{kg}^{-1}$

continued on next page

continued from previous page

Symbol	Description	Unit
h_k^0	“Extrapolated” specific enthalpy of the k th species at $T = 0$ K, assuming an ideal gas	$\text{J} \cdot \text{kg}^{-1}$
h	Specific enthalpy of the gas mixture	$\text{J} \cdot \text{kg}^{-1}$
k	Boltzmann constant	$\text{J} \cdot \text{K}^{-1}$
k_i	Rate constant of the i th chemical reaction	varies
k_3	Rate constant of the third order volume recombination reaction of nitrogen radicals	$\text{m}^6 \cdot \text{mol}^{-2} \cdot \text{s}^{-1}$
k_1	Rate constant of the first order surface recombination reaction of nitrogen radicals	$\text{m} \cdot \text{s}^{-1}$
L	Tube length	m
\dot{M}	Total mass flow through an arbitrary cross section of the tube	$\text{kg} \cdot \text{s}^{-1}$
m	Mass of the temperature probe	kg
n	Molar density	$\text{mol} \cdot \text{m}^{-3}$
n_k	Molar density of the k th species – also: the concentration of the k th species	$\text{mol} \cdot \text{m}^{-3}$
Pe	Peclet number	1
p	Total pressure of the gas mixture	Pa
p_k	Partial pressure of the k th species	Pa
\dot{Q}	Volumetric flow rate	$\text{Pa} \cdot \text{m}^3 \cdot \text{s}^{-1}$
\dot{Q}_{recomb}	Rate of heat deposited on the temperature probe due to chemical reactions	W
\dot{q}_{recomb}	Rate of heat density deposited on the temperature probe due to chemical reactions	$\text{W} \cdot \text{m}^{-2}$

continued on next page

continued from previous page

Symbol	Description	Unit
$\dot{Q}_{cooling}$	Rate of heat extracted from the temperature probe due to cooling processes	W
R	Inner tube radius	m
Re	Reynolds number	1
r	Radial coordinate	m
r	Bending radius	m
S	Pumping speed	$\text{m}^3 \cdot \text{s}^{-1}$
\vec{s}	Unit length surface normal	1
T	Temperature	K
T_∞	Ambient Temperature	K
T_{cj}	Cold junction temperature	K
U_{tc}	Thermoelectric voltage produced by a thermocouple	V
\vec{u}	Bulk velocity of the gas mixture	$\text{m} \cdot \text{s}^{-1}$
u	Component of \vec{u} in axial direction	$\text{m} \cdot \text{s}^{-1}$
v	Component of \vec{u} in radial direction	$\text{m} \cdot \text{s}^{-1}$
\vec{V}_k	Diffusion velocity of the k th species	$\text{m} \cdot \text{s}^{-1}$
W_k	Molar mass of the k th species	$\text{kg} \cdot \text{mol}^{-1}$
\overline{W}	Molar mass of the gas mixture	$\text{kg} \cdot \text{mol}^{-1}$
X_k	Mole fraction of the k th species	1
X	Radical mole fraction in case of a binary mixture	1
Y_k	Mass fraction of the k th species	1
z	Axial coordinate	m
\mathcal{A}_ϕ	Coefficients of the discretized transport equation of flow variable ϕ	varies
\mathcal{C}_ϕ	Convective coefficient of flow variable ϕ	varies
\mathcal{D}_ϕ	Diffusive coefficient of flow variable ϕ	varies

continued on next page

continued from previous page

Symbol	Description	Unit
\mathcal{S}_ϕ	Source term of flow variable ϕ	varies
Φ	Dissipation function	$\text{W} \cdot \text{m}^{-3}$
γ	Recombination probability of nitrogen radicals on a surface	1
γ	Relativistic factor	1
η	Molecular desorption yield	1
κ	Index of isentropic expansion	1
λ	Thermal conductivity of the gas mixture	$\text{W} \cdot \text{m}^{-1} \cdot \text{K}^{-1}$
μ	Dynamic viscosity of the gas mixture	$\text{Pa} \cdot \text{s}$
$\hat{\mu}$	Second viscosity of the gas mixture	$\text{Pa} \cdot \text{s}$
ρ	Mass density of the gas mixture	$\text{kg} \cdot \text{m}^{-3}$
ρ_k	Mass density of the k th species	$\text{kg} \cdot \text{m}^{-3}$
$\dot{\sigma}_k$	Net production rate of the k th species due to surface reactions	$\text{mol} \cdot \text{m}^{-2} \cdot \text{s}^{-1}$
$\dot{\sigma}$	Radical net production rate due to surface reactions in case of a binary mixture	$\text{mol} \cdot \text{m}^{-2} \cdot \text{s}^{-1}$
$\tilde{\tau}$	Stress tensor	$\text{N} \cdot \text{m}^{-2}$
$\dot{\omega}_k$	Net production rate of the k th species due to volume reactions	$\text{mol} \cdot \text{m}^{-3} \cdot \text{s}^{-1}$
$\dot{\omega}$	Radical net production rate due to volume reactions in case of a binary mixture	$\text{mol} \cdot \text{m}^{-3} \cdot \text{s}^{-1}$
ζ	Characteristic decay length	m

Part I

Introduction

1 Overview

The subject of this thesis is a novel technique for the treatment and conditioning of surfaces exposed to ultra-high vacuum which utilises the strong chemical activity of free radicals. Carried out in the vacuum group of the LHC division at CERN its motivation originates from the special requirements on the beam vacuum of the LHC and surfaces exposed to this vacuum.

An introduction of CERN and the LHC is given in chapter 2. Special emphasis is put on the LHC vacuum system and beam related dynamic vacuum effects which are described in more detail.

In chapter 3, the method of free radicals is presented and compared to well established methods like glow-discharge cleaning and vacuum bake-out.

Experiments that investigate the effects of radicals on surfaces are described in chapters 4 and 5. These experiments are of phenomenological nature, i.e. their results describe the change of surface properties like molecular desorption yield, secondary electron yield, and chemical composition of a surface due to a particular treatment recipe, and not the fundamental physical processes that lead to these changes.

In part III, the flow of radical containing gas is investigated in detail. In chapter 6 the (macroscopic) physical laws which govern this flow are studied. These laws can be expressed as partial differential equations, which are solved numerically by means of a computer simulation. The radical flow has also been investigated experimentally. This experiment and its results, which agree very well with the results of the computer simulation, is described in chapter 7.

Finally, a summary and conclusion is presented.

This thesis does not have a distinct theory part. Instead, theoretical pre-requisites for a particular experiment are presented where they are needed. The same holds for the results, which for each experiment (or simulation) are given at the end of the corresponding chapter.

2 CERN and the LHC

2.1 A short introduction of CERN

CERN [1] – *Centre Européenne pour la Recherche Nucléaire*, the European Organisation for Nuclear Research – was founded in 1954 by 12 European states with the intention to re-establish fundamental physics research in the post world war II Europe. Since then the number of member states has been increasing up to the present number of 20: Austria, Belgium, Bulgaria, Czech Republic, Denmark, Finland, France, Germany, Greece, Hungary, Italy, Netherlands, Norway, Poland, Portugal, Slovak Republic, Spain, Sweden, Switzerland, and the United Kingdom. Currently CERN employs just under 3000 people of different skills and professions and additionally about 6500 scientists from all over the world come to CERN to do their research, thus making it one of the biggest research institutes for high energy physics in the world.

Since many years particle accelerators have been representing the most powerful tools for researchers in high energy physics. Hence, the development and construction of particle accelerators has been one of CERN's main tasks since its first days. CERN's accelerator complex, consisting of linear and circular machines, is now the most versatile in the world providing beams of a variety of particles in a large range of energies.

Thus, since its beginning, CERN has been providing the means for the high energy physics community to make new discoveries and to test existing theories with precision measurements. It has been helping to establish our present picture of the elementary particles and their interactions – the so called *standard model of particle physics*.¹

Despite the success of the standard model, whose predictions could be verified

¹For a history of particle physics cf. [2], for an introduction to the standard model of particle physics cf. [3]

at the level of 0.1% or better by experiments at LEP, SLC, and Tevatron, some aspects of the theory are still obscure and there are several reasons to believe that this is not the ultimate theory of particle physics [4]. Hence, there are strong physics arguments to continue fundamental research at even higher energies. Motivated and supported by these arguments, an even more powerful accelerator, the LHC, is currently under construction at CERN, and is due to become operational in 2005.

2.2 The LHC project

The LHC, the *Large Hadron Collider*, has been designed to collide protons at a centre-of-mass energy of 14 TeV with a luminosity of $10^{34} \text{ cm}^{-2} \cdot \text{s}^{-1}$ [5, 6]. In addition it will provide collisions between lead nuclei up to a centre-of-mass energy of 1150 TeV.² A list of LHC design parameters is given in appendix B.

The LHC will be placed into the existing tunnel of the LEP collider, the *Large Electron Positron Collider*, whose operation had been stopped at the end of 2000 and which has been dismantled. Following this tunnel, the LHC will have a circumference of about 26.7 km. As shown in figure 2.1 the general layout of the LHC has an eightfold structure, thereby following the layout of its predecessor LEP. Each of these octants consists of an *arc*, which basically contains the main bending magnets (the *main dipoles*), focussing (quadrupole) magnets, and higher order correction magnets, followed by a so called *long straight section*³ with a length of about 500 m.

The two proton beams, each made up of 2835 tightly packed *bunches* of protons (1.05×10^{11} protons per bunch), resulting in a current of 0.536 A per beam, will be circulating in clockwise and anti-clockwise direction in two separate beam pipes which are inserted into a common bending magnet. These beams are brought into collision at four points called *interaction points*.

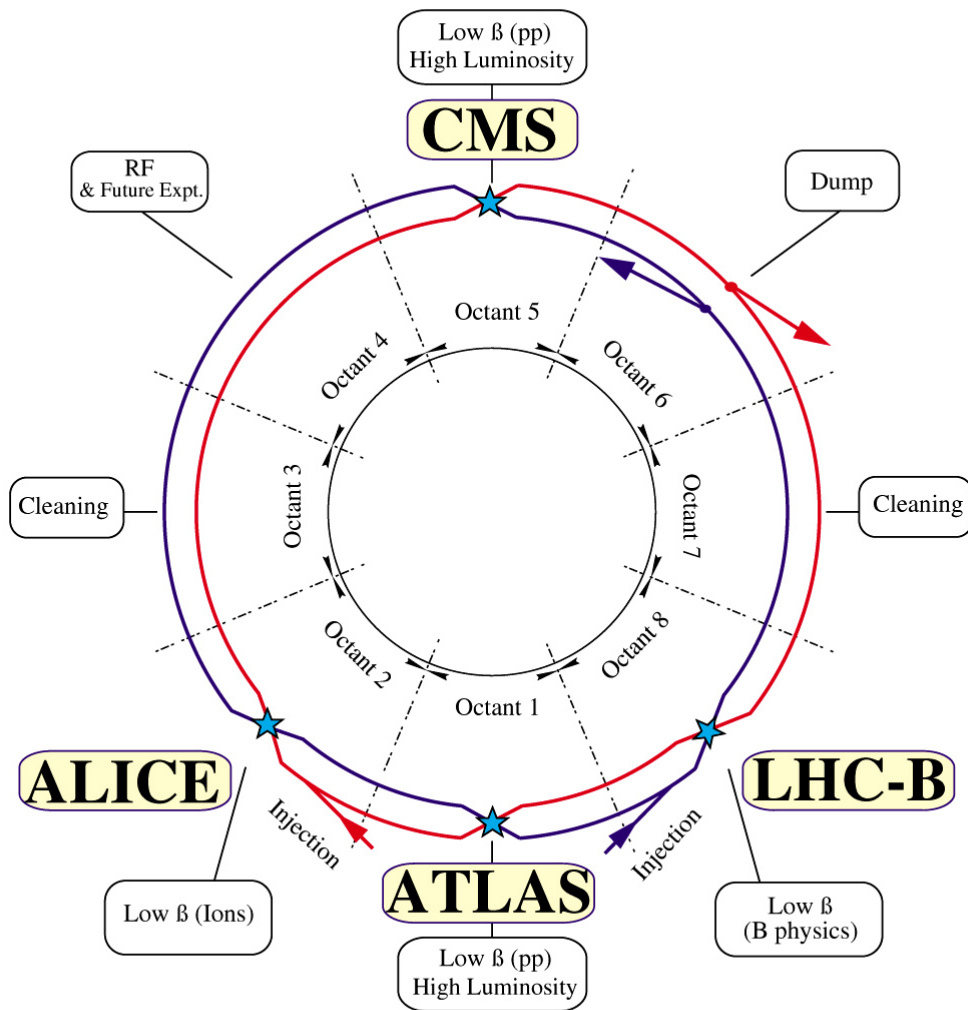
At these four interaction points huge particle detectors will be installed to measure properties like energy and momentum of the particles emerging from the interaction point after the collision of high energetic particles. These detectors, depicted in figure 2.2, are:

- ATLAS (*A Toroidal Lhc ApparatuS*), a general purpose detector for $p-p$ collisions, designed to exploit the full discovery potential of the LHC [7]

²This corresponds to 82×7 TeV, since a lead nucleus contains 82 protons.

³there are also so called *short straight sections* which are considered as part of the arcs

LHC LAYOUT



CERN AC _ E12-4A_ V18/9/1997

Figure 2.1: General Layout of the Large Hadron Collider

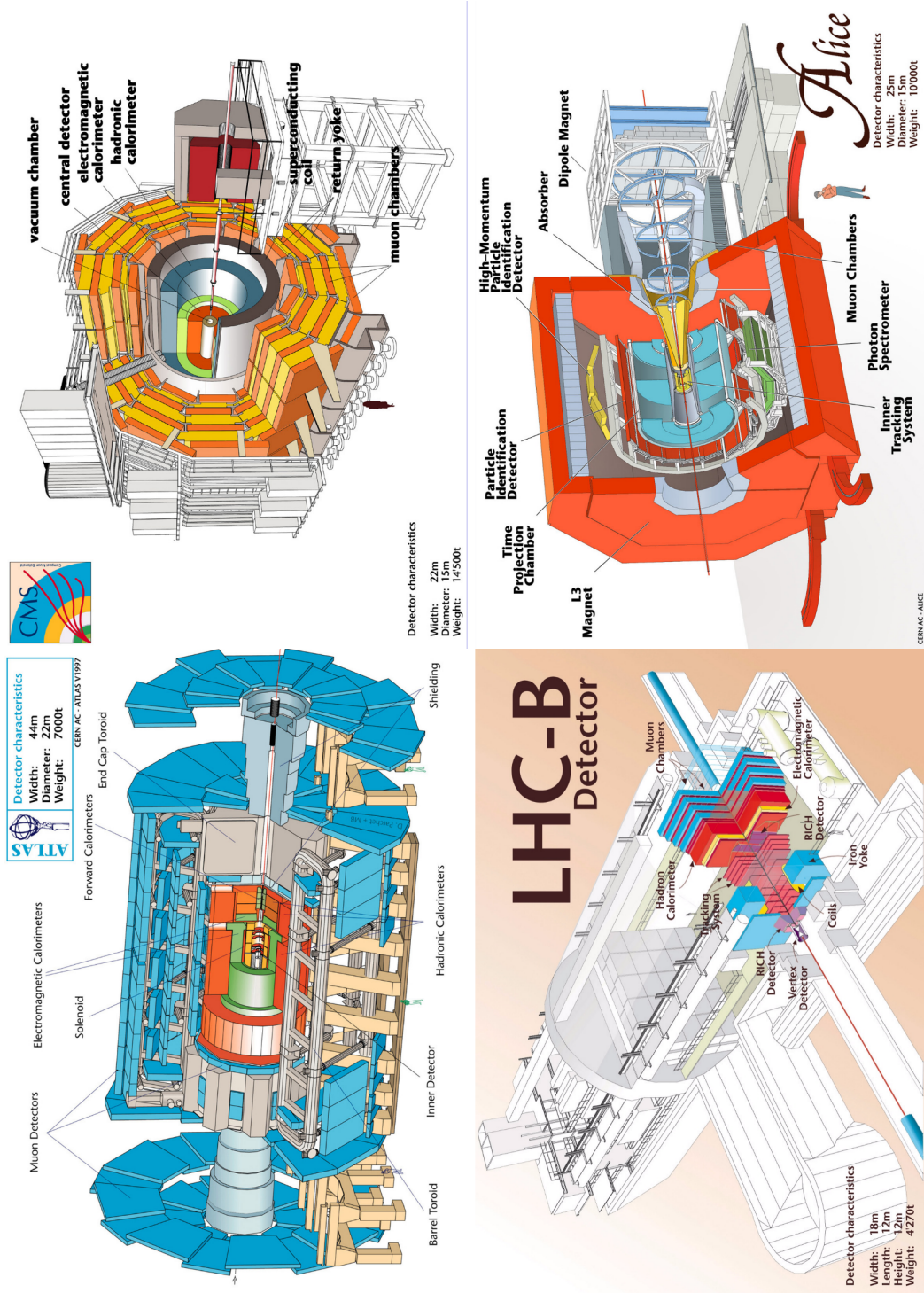


Figure 2.2: Schematic drawings of the four LHC detectors

- CMS (*Compact Muon Solenoid*), another general purpose detector, designed to detect cleanly the various signatures for new physics by identifying and precisely measuring muons, electrons, and photons over a large energy range and at high luminosity [8]
- LHCb, designed to exploit the large number of b-hadrons produced at the LHC in order to make precision studies of CP asymmetries and of rare decays in the B-meson systems [9]
- ALICE (*A Large Ion Collider Experiment*), the only detector of the LHC accelerator fully dedicated to the physics of heavy ion collisions, to establish and to study the phase transition from hadronic matter to deconfined partonic matter, the so called *quark gluon plasma* [10]

The Large Hadron Collider is designed to accelerate protons to an unprecedented energy of 7 TeV. To reach this energy, LHC's main bending magnets, the *main dipoles*, have to provide a nominal magnetic field of about 8.4 T. The current required to create this field is about 11.8 kA and constraints on geometry and heat budget require that the magnet coils are made of superconducting cables (cf. [11, 12]). These cables consist of fine strands (7 μm diameter) of a Nb-Ti alloy woven into a mesh of copper strands. Hence, the whole magnet has to be cooled below the critical temperature of the superconductor (the Nb-Ti alloy), which is achieved by means of superfluid helium at 1.9 K. About 80% of the total length of the accelerator will be held at these temperatures, thus making the LHC one of the biggest cryogenic facilities in the world [13].

As shown in figure 2.3, the beam pipes for the two counter-rotating beams, together with a pair of superconducting coils each, are incorporated into a common iron yoke, thereby saving space and cooling power. This assembly, called the *cold mass*, is then cooled to 1.9 K by superfluid helium. The cold mass is insulated from ambient temperature by a surrounding vacuum vessel, the so called *cryostat*.⁴ The total length of an assembled main dipole is about 16 m and a total number of 1232 of these magnets will be built into the LHC. The smooth operation of the main dipoles is one of the crucial points in the operation of the LHC, since a *quench*, i.e. the transition from superconducting to resistive state, of a single magnet can interrupt machine operation for several hours.

⁴For a more detailed description cf. [15, 16, 17, 18]

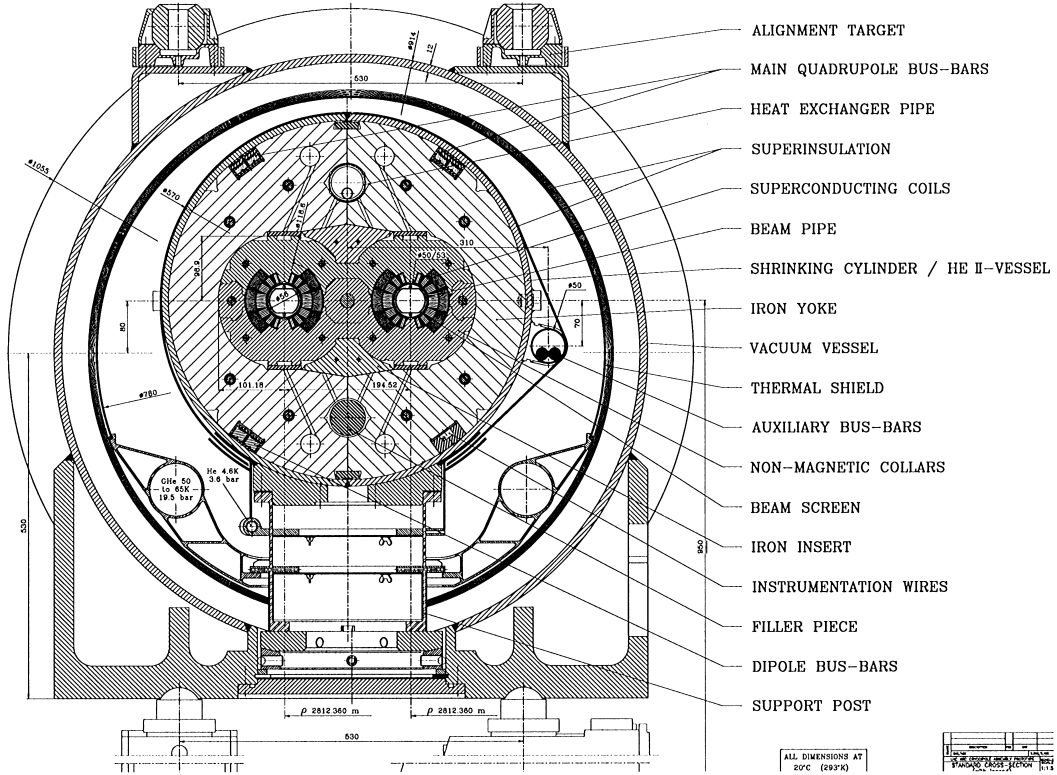


Figure 2.3: Cross section of a LHC dipole cryomagnet assembly (graphic taken from [14])

2.3 An introduction of the LHC beam vacuum system

As illustrated in figure 2.3, the beam pipes for the two counter-rotating beams (inner diameter 50 mm) are directly built into the inner openings the magnet (inner diameter 56 mm), thus being in direct contact with the cold mass and acting at the same time as the inner wall of the magnet cryostat (the so called *cold bore*) [19, 20, 21, 22, 14]. This construction implies, that the walls of the beam vacuum system will have the same temperature as the cold mass itself, namely 1.9 K during operation. At this temperature, gases except helium have a negligible vapour pressure, hence the beam pipe will effectively act as a *cryopump* with basically unlimited capacity, making external pumping superfluous during operation [21, 22]. External pumps are required only for the initial pump-down of the vacuum system.

The LHC will be the first superconducting accelerator which is exposed to intense synchrotron radiation. According to [23], the instantaneous power radiated by a charged particle, in this case a proton, travelling on a circular orbit is given by

$$P_{s.r.} = \frac{1}{4\pi\epsilon_0} \frac{2}{3} \frac{e^2}{c^3} \frac{v^4}{r^2} \gamma^4 \quad (2.1)$$

where e is charge of the proton (i.e. the elementary charge), c the speed of light in vacuum, v the velocity ($v \approx c$), r the bending radius ($r = 2784.32$ m for the main dipoles), and γ the relativistic factor ($\gamma = 7461$ for 7 TeV protons). Substituting the numerical values into equation (2.1) results in a value for the instantaneous power radiated by one proton of $P_{s.r.} = 1.84 \times 10^{-11}$ W. Having 2835 bunches with 1.05×10^{11} protons per bunch distributed over the circumference of LHC (26658.883 m) results in an average linear proton density of about $1.12 \times 10^{10} \text{ m}^{-1}$, hence the linear heat load caused by synchrotron radiation in the main dipoles is about $0.2 \text{ W} \cdot \text{m}^{-1}$.

This heat load, if transferred to the cold mass, would increase excessively the heat dissipated in the superconducting magnets, hence the cold mass has to be shielded against synchrotron radiation. This is achieved by means of the so called *beam screen*, a racetrack shaped tube with two *cooling capillaries* attached to its two flat parts, which actively cool the beam screen to a temperature between 5 K and 20 K by means of pressurised helium gas (cf. [21]). The beam screen has a diameter of 44 mm and the flat parts are separated by 36 mm. A picture of a prototype beam screen, inserted into a sample beam pipe is shown in figure 2.4.

Another feature of the beam screen is a thin layer of oxygen free high conductivity copper (thickness about $50 \text{ }\mu\text{m}$), which is co-laminated with the base material of the beam screen, a low permeability stainless steel. This layer is intended to carry the beam-induced image currents, thus reducing the machine impedance to an acceptable value. The chosen value for the thickness of the copper layer is in fact a compromise between low impedance and mechanical stability. Eddy currents, induced during a magnet quench are inversely proportional to the impedance. These eddy currents, in conjunction with the magnetic field of the dipole can result in very high Lorentz forces acting on and leading to deformation of the beam screen [24, 25, 26]. Without beam screen these image currents would flow through the beam pipe and produce an unacceptably high resistive heat load on the cold mass, which in turn would lead to a quench of the magnet. In the present configuration

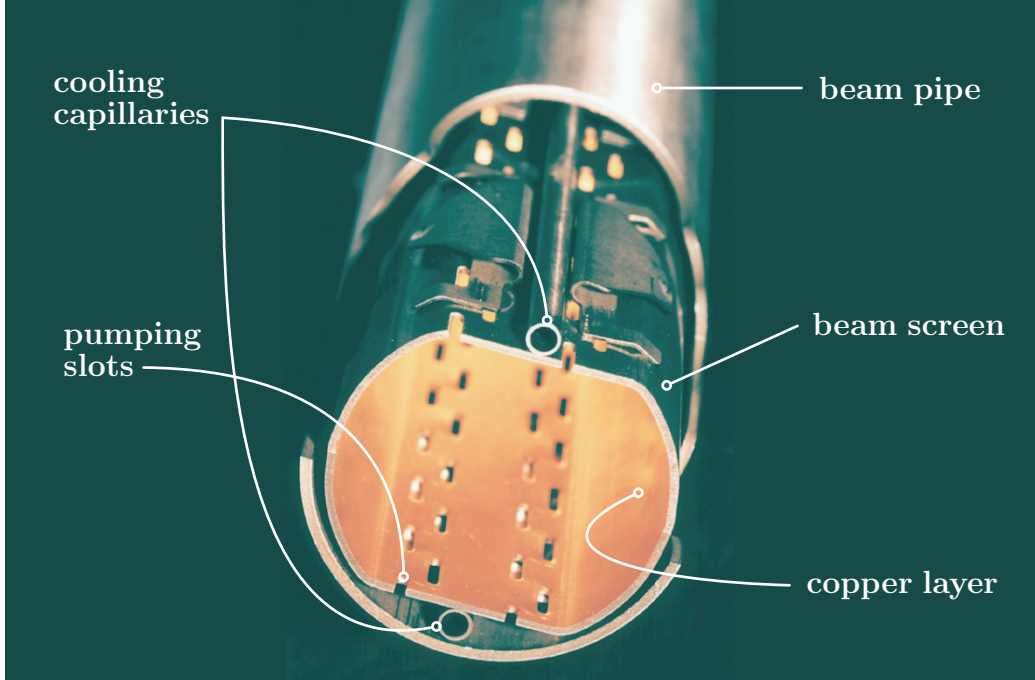


Figure 2.4: Picture of a prototype beam screen, inserted into a sample beam pipe

the heat load due to image currents, about $0.1 \text{ W} \cdot \text{m}^{-1}$ [27, 28], is intercepted by the beam screen.

A third important feature of the beam screen are the pumping slots incorporated into the flat parts of the beam screen, amounting to about 4% of the its total surface. Residual gas molecules can travel through these pumping slots and reach the cold bore wall where they will be permanently adsorbed [14]. The purpose of the pumping slots will be discussed in more detail in conjunction with the dynamic vacuum effects in the next section.

As a last, nevertheless important point, the beam loss due to nuclear scattering should be mentioned in the context of this introduction. A small fraction of scattered protons escapes from the aperture of the beam pipe and penetrates the surrounding material, thereby producing a shower of secondary particles which is finally absorbed by the cold mass. There is no way that these scattered particles can be absorbed by the beam screen, and therefore the machine design includes an allowance of about $0.1 \text{ W} \cdot \text{m}^{-1}$ for the linear heat load due to nuclear scattering for the two beams [22]. The linear heat load $P_{n.s.}$ (for one beam) can be expressed as

$$P_{n.s.} = \frac{I_{beam}}{e} N_G \sigma_{n.s.;G} E \quad (2.2)$$

where $I_{beam} \approx 0.536$ A is the (nominal) current of the proton beam, e the elementary charge,⁵ N_G the number density of gas G , $\sigma_{n.s.;G}$ the cross section for nuclear scattering of a proton on a molecule of gas G (for hydrogen molecules and 7 TeV protons, it is $\sigma_{n.s.;H_2} \approx 5 \times 10^{-30}$ m² [22]), and $E = 7$ TeV the proton energy. With the above mentioned numerical values and with $P_{n.s.} < 0.05$ W · m⁻¹, it follows from equation (2.2) that $N_{H_2} \lesssim 2.66 \times 10^{15}$ m⁻³ and in consistency with this requirement an upper limit for the residual number density of hydrogen molecules of $N_{H_2} = 1 \times 10^{15}$ m⁻³ has been chosen for the design of the beam vacuum system [22]. Assuming a gas temperature of 10 K, the resulting upper limit for the partial pressure of hydrogen is given as $p_{H_2} = 1.38 \times 10^{-7}$ Pa $\approx 1 \times 10^{-9}$ torr. Corresponding values for other gases can be found in [21] or [22].

2.4 Beam related dynamic vacuum effects and their impact on LHC

2.4.1 Desorption by synchrotron radiation

Synchrotron radiation photons hit the inner surface of the beam screen where they are either absorbed or scattered, thereby releasing all or part of their energy. In consequence, residual gas molecules adsorbed on this surface can be released into the gas phase, i.e. they are *desorbed*, if the available energy exceeds the energy of the bond between gas molecule and surface.

In general, the energy spectrum of the synchrotron radiation, emitted by a charged particle moving on a circular orbit with almost speed of light can be characterised by the so called *critical energy*, given by [23]

$$E_c = \frac{3}{2} \frac{\hbar c}{r} \gamma^3 \quad (2.3)$$

and the number of photons emitted by each beam particle per unit time can be calculated from [23]

⁵In fact, it is $I_{beam}/e = \nu_p$, i.e. the number of protons passing through an arbitrary cross section of the beam pipe per unit time

$$\nu_\gamma = \frac{15\sqrt{3}}{8} \frac{P_{s.r.}}{E_c} = \frac{5\sqrt{3}}{6} \frac{\alpha c}{r} \gamma \quad (2.4)$$

where \hbar is the reduced Planck constant, c the speed of light in vacuum, α the fine-structure constant, r the bending radius, and γ the relativistic factor. In the case of LHC, it is $E_c \approx 44.1$ eV and $\nu_\gamma \approx 8.46 \times 10^6$ s⁻¹. With an average linear proton density of $\mathcal{N}_p \approx 1.12 \times 10^{10}$ m⁻¹ an average *linear photon flux* can be calculated as

$$\dot{\mathcal{N}}_\gamma = \nu_\gamma \mathcal{N}_p \approx 9.45 \times 10^{16} \text{ s}^{-1} \cdot \text{m}^{-1}. \quad (2.5)$$

The number of desorbed molecules is proportional to this photon flux, hence

$$\dot{\mathcal{N}}_G = \eta \dot{\mathcal{N}}_\gamma. \quad (2.6)$$

The constant of proportionality η is called the *molecular desorption yield* and is usually given in units of molecule · photon⁻¹.⁶ η is in fact not a constant but depends on several factors, among others the nature of the desorbed gas, the surface material, temperature, and pre-treatment and the “history” of the surface, i.e. the number of photons the surface has been exposed to.

The phenomenon of desorption by synchrotron radiation, also called *photon stimulated desorption* or *photon induced desorption*, has been subject to extensive studies in the past (cf. [29, 30] in the context of LEP, [31, 32, 33, 34, 35, 36, 37] in the context of LHC and/or the SSC, the *Superconducting Super Collider*). Values for η at conditions relevant for LHC, given in above cited literature, range from some 10⁻³ molecule · photon⁻¹ for H₂ to some 10⁻⁵ molecule · photon⁻¹ for CO₂ and CH₄. After a long exposure of the surface to synchrotron radiation these values are reduced by 1 ... 2 orders of magnitude, an effect which is also called *beam scrubbing*.

In the case of cryogenic vacuum systems, molecules in the gas phase are readily pumped by the cold walls. These molecules are only lightly bound to the surface, i.e. *physisorbed*, and they can be re-desorbed by synchrotron radiation with a much higher yield. This process is called the *recycling* of previously physisorbed molecules and the corresponding desorption yield, usually denoted by η' , can exceed η by several orders of magnitude (cf. [32, 36]). Recently, the cracking of adsorbed molecules by synchrotron radiation has been identified as

⁶Nevertheless the physical dimension of η is 1

an additional mechanism which can contribute significantly to the gas load in the beam vacuum system [37].

At this point the importance of the pumping slots of the beam screen can be well explained. A fraction of the desorbed and recycled gas molecules can travel through these slots and reach the surface of the cold bore. Since this surface is shielded from synchrotron radiation, these molecules are not recycled and hence can be permanently cryosorbed on the beam pipe. Thus, unlike the inner surface of the beam screen where molecules are continuously recycled, the pumping slots provide the means to remove gas effectively and permanently from the beam vacuum system.

2.4.2 Ion induced pressure instability

Positive ions can be produced in the beam vacuum system through the ionisation of residual gas molecules by the beam particles with typical ionisation cross sections for 7 TeV protons in the range of 10^{-22} m^2 [38]. These positive ions are then repelled by the positive space charge of the beam and accelerated towards the beam screen where they transfer their kinetic energy onto the surface. In the arcs of the LHC ion energies at impact are typically in the range of several 100 eV [22, 39]. Like with photon stimulated desorption, the number of molecules, desorbed due to the impact of energetic ions, is proportional to the number of incident ions, hence

$$\dot{\mathcal{N}}_G = \eta_i \dot{\mathcal{N}}_+ \quad (2.7)$$

with $\dot{\mathcal{N}}_G$ being the linear flux of molecules of species G , desorbed from the beam screen, and $\dot{\mathcal{N}}_+$ the linear flux of ions hitting the beam screen. η_i is like before called the *molecular desorption yield*, but this time expressed in units of molecule \cdot ion $^{-1}$. Again, η_i is not a constant. It depends not only on the nature of ions and desorbed molecules, the ion energy, nature and temperature of the surface [40, 41], but also on the surface preparation and condition [42]. In the case of cryogenic vacuum systems, we can again distinguish between tightly bound, chemisorbed molecules and physisorbed molecules. Whereas it is $\eta_i \approx (1 \dots 10) \text{ molecule} \cdot \text{ion}^{-1}$ in the case of chemisorbed molecules it can be several thousand molecules per ion for physisorbed molecules [43, 44].

If one gas species G is dominant, $\dot{\mathcal{N}}_+$ can be expressed as

$$\dot{\mathcal{N}}_+ = \sigma_{i.;G} N_G \frac{I_{beam}}{e} \quad (2.8)$$

where $\sigma_{i.;G}$ is the ionisation cross section of this species, N_G its number density, I_{beam} the proton beam current, and e the elementary charge.

It can be seen from the preceding paragraphs (n.b. equations (2.7) and (2.8)) that the process of ion stimulated desorption in a beam vacuum system is “self-amplifying”⁷ and could result in a pressure run-away (or *pressure instability*) if the gas is not pumped away with a sufficient pumping speed, an effect which has been observed at the ISR, the *Intersecting Storage Rings*, at CERN (cf. [38]). However, in the cold parts of the LHC the ion induced desorption should not pose any serious problems to the beam vacuum due to the distributed cryo-pumping of the cold walls [22].

2.4.3 Beam induced electron multipacting

Electron multipacting is a phenomenon known from high power radio frequency and microwave cavities where it manifests itself in RF power consumption and break down. It is caused by the synchronuous motion of free electrons in an alternating electric field. First free electrons are produced by field emission, photo-electric effect, or ionisation of residual gas molecules by cosmic rays. These electrons are accelerated towards the surface of the cavity by the electric field where they, when hitting the surface with sufficient energy, can produce secondary electrons. If the electric field changes its direction at the same time, these secondary electrons are accelerated towards the opposite surface where they in turn produce additional electrons. If the *secondary electron yield*, i.e. the number of secondary electrons produced per incident electron, exceeds unity, the number of electrons which are “bouncing” back and forth is increasing exponentially (also known as the “build-up of the *electron cloud*”), finally leading to the break-down of the cavity (cf. [45, 46, 47]). In general, for electron multipacting to develop, the following two conditions must be fulfilled [48]:

- the electrons must be able to traverse the vacuum chamber in synchronism with the electric field and

⁷hence an increase of gas density results in an increase of the ion flux which in turn results in an increase of the molecular desorption rate which results in an even faster increase of the gas density ...

- the electron energy at impact must result in a secondary electron yield greater than unity.

Since several years a similar effect has been observed in the beam pipes of high current proton accelerators (cf. [48, 49, 50, 51]). This phenomenon is called *beam induced multipacting* because the alternating electric field is generated by the bunched proton beam. In the case of LHC with its cryogenic vacuum system, the build-up of an electron cloud can have the following implications:

- excessive heat load on the vacuum chamber surfaces (computer simulations give values up to $15 \text{ W} \cdot \text{m}^{-1}$ [52, 53]),
- strong pressure rise due to the desorption of adsorbed molecules from the beam screen surface by impact of electrons (*electron stimulated desorption*), and
- coherent oscillations of the proton beam with the electron cloud, leading to emittance growth and luminosity decrease or even beam loss [14].

In the arcs of the LHC, primary electrons are massively created through the photo-electric effect due to the high flux of synchrotron radiation photons. The production rate of photo-electrons per proton (ν_{e-}) is proportional to the production rate of synchrotron radiation photons (ν_γ):

$$\nu_{e-} = 0.45 \nu_\gamma Y. \quad (2.9)$$

Y is the *effective quantum yield*, i.e. the number of photo-electrons produced per incident photon. A value of $Y \approx 0.1$ is commonly assumed for LHC relevant conditions [54]. Only about 45% of the incident photons have enough energy⁸ to produce photo-electrons [53], hence the factor of 0.45 in equation (2.9).

Synchrotron radiation photons emitted by a travelling proton bunch hit the circumference of an arbitrary cross section (normal to the beam axis) of the beam screen at about the same moment as the proton bunch travels through this cross section, hence the instantaneous production rate of photo-electrons varies in synchronism with the bunch structure of the beam [54]. Furthermore, since photons are preferably emitted in the forward tangential direction of the

⁸i.e. an energy greater than the work function of copper, about 4 eV [52]

beam orbit, the instantaneous production rate of photo-electrons has also an azimuthal dependency. For a surface material with high reflectivity, photons are likely to be reflected many times before producing a photo-electron, hence the photo-electrons are distributed uniformly over the beam screen surface. On the other hand, if the reflectivity of the surface is low, synchrotron radiation photons are likely to produce photo-electrons at already at their first impact on the surface, hence the photo-electron distribution follows that of the photons. The initial electron distribution has an influence on the development of beam induced multipacting especially in the parts of the accelerator where a strong magnetic field is present, e.g. in the main dipoles.⁹

Photo-electrons receive approximately a “kick-like” acceleration towards the beam axis by the passing proton bunch, which is proportional to the number of protons in the bunch and hence proportional to the beam current. From the condition for the onset of multipacting – electrons must be able to traverse the beam vacuum from wall to wall before the arrival of the next bunch – a critical beam current can be calculated. For nominal LHC parameters the energy gain during kick acceleration is about 200 eV and the critical beam current for the onset of multipacting is $I_{crit} \approx 0.19$ A [48].

As with the RF related multipacting, the secondary electron yield δ must exceed unity to develop beam induced multipacting. In fact, since some of the secondary electrons can get out of phase with the electron cloud movement and are lost without further multiplication, the critical value of the secondary electron yield $\delta_{crit.}$ is greater than 1. For nominal LHC operating conditions it is $\delta_{crit.} \approx 1.3$ [14].

Because of the critical influence of the secondary electron yield for the development of multipacting and hence for the operation of LHC, this parameter has been the topic of extensive research work carried out in the LHC vacuum group over the last years (cf. [55, 56, 57, 58, 47, 59]). A summary of the main experimental results concerning the secondary electron yield of copper is given in [55], and the curves shown in figure 2.5 show typical examples for these results. The curve denoted as “as received” refers to a surface prepared for installation in the vacuum system, whereas the “fully conditioned” curve refers to a surface with all contaminants stripped off. It can be seen that the maximum secondary electron yield can be reduced significantly by means of proper conditioning of the surface, i.e. during beam operation (*beam scrubbing*) or by surface conditioning (bake-out, argon glow discharge

⁹Due to Lorentz forces, electrons are bound to move in spirals around the magnetic field lines.

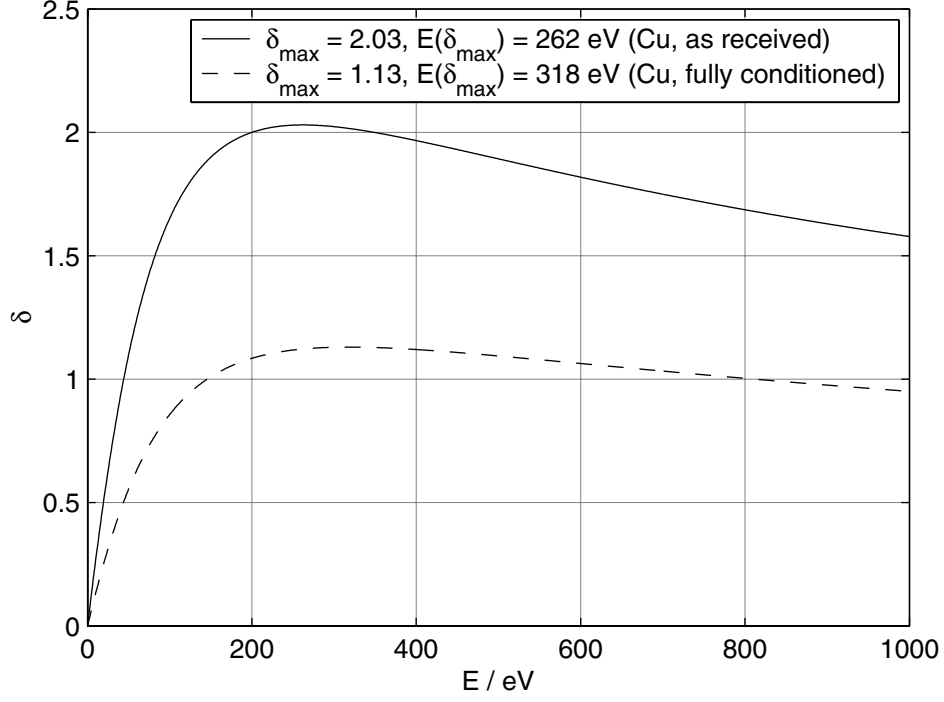


Figure 2.5: Typical plots of the secondary electron yield of copper as a function of the primary electron energy (data taken from [55])

treatment, ...).

As a last point in this section the desorption of gas molecules by electrons, called *electron stimulated desorption*, should be mentioned. The desorption rate is proportional to the rate of impinging electrons and characterised by the *molecular desorption yield* η_e (given in units of molecule \cdot electron $^{-1}$, cf. sections 2.4.1 and 2.4.2)

$$\dot{\mathcal{N}}_G = \eta_e \dot{\mathcal{N}}_{e-}. \quad (2.10)$$

Again, η_e is not a constant but depends on the energy of impinging electrons, the nature of the desorbed gas, the material, temperature, treatment, and history of the surface [41, 42, 60, 61, 62].

Due to the electron stimulated desorption, the build-up of an electron cloud manifests itself also by a strong increase in the residual gas pressure. In

fact, pressure rises up to a factor of 60 could be observed in the SPS¹⁰ during runs with LHC-type beams [50]. Thus, an electron cloud in the beam vacuum system of the LHC would most probably raise the pressure during the conditioning period to an unacceptably high level for the cryogenic system of the LHC.

¹⁰ *Super Proton Synchrotron*, one of CERN's accelerators which will be used to pre-accelerate and inject beam particles into the LHC

3 Treatment of UHV surfaces by means of radicals

3.1 Cleaning for vacuum applications

As we have shown in the previous chapter, the condition of surfaces exposed to the beam vacuum is an essential parameter for the operation of an accelerator like the LHC. But the surface condition is not only important for the vacuum system of an accelerator, it determines the quality and performance of almost all ultra-high vacuum systems and applications. The outgassing from surfaces determines for example not only the base pressure which can be reached in a particular vacuum system, but also the composition of the residual gas, which in turn can limit e.g. the quality of surface treatment processes or the sensibility of surface analysis instruments and other (ultra-high) vacuum applications that are nowadays widely used in research and industry.

Hence, conditioning, or *cleaning* of surfaces is in almost all cases a necessary step during the construction and operation of vacuum systems. The conditioning process has to be chosen according to the requirements of a particular application [63]. Typical conditioning processes involve one or more chemical cleaning steps¹ (cf. [63, 64, 65]) of parts prior to installation in a vacuum system and final treatment under vacuum before the first operation and if re-conditioning is needed (e.g. after the vacuum system has been vented with air). Two main conditioning procedures have been well established at CERN and elsewhere since many years: *vacuum bake-out* and *glow-discharge cleaning* (cf. [66, 67, 68]).

The idea behind these two procedures is quite the same: energy has to be transferred to the surface in order to release gas, adsorbed on the surface and/or dissolved in the bulk material, into the volume where it can be pumped

¹by means of degreasers, solvents, detergents, acids, or demineralised water

away. For vacuum bake-out the whole vacuum chamber is heated from outside (typical: 300 °C for 24 h for an all-stainless-steel chamber), hence, thermal energy is transferred to the surface. In the case of glow-discharge cleaning – as the name implies – a glow-discharge is maintained inside the vacuum chamber, typically using argon as process gas. To drive the discharge, an electrode² must be installed in the vacuum chamber. Positive ions, created in the discharge region, are accelerated towards the surface of the vacuum chamber³ by the electric field in the cathode sheath of the discharge. Hence, in the case of glow-discharge cleaning, energy is transferred to the surface in form of kinetic energy of the ions.

Both of these procedures have their advantages and draw-backs. Vacuum bake-out has the great advantage that it can be performed *in situ*, i.e. the system can remain under vacuum and re-contamination is greatly avoided. On the other hand, treatment time is very long and access to the vacuum chambers is necessary in order to install the bake-out equipment. In case of glow-discharge cleaning, the treatment can be very short and effective. The disadvantage is, that for most applications the anode has to be removed after treatment, hence the vacuum chamber has to be vented to atmosphere. In addition ions could be implanted into the surface, which is in general an unwanted effect.

At this point the method of *surface treatment by free radicals* shall be introduced as a possible alternative and/or complement to the aforementioned procedures. This method, originally proposed by Jean-Luc Dorier and Noël Hilleret in the context of cleaning for vacuum service, is in principle based on dry chemical etching, i.e. etching by a chemically reactive gas, in our case *free radicals*. Cleaning of vacuum chambers by reactive gas has already been investigated in the past (e.g. [69, 70, 71]). On the other hand, free radical methods are already quite commonly applied in semiconductor industry, e.g. for photoresist stripping or isotropic etching (cf. [72, 73, 74]).

3.2 Free radicals

In the context of this work, the term *free radical* means a neutral (in terms of electrical charge) fragment of a molecule that has been detached from its

²which is biased to a positive potential with respect to the vacuum chamber, hence the anode

³which, for the glow-discharge, acts as the cathode

“natural” environment, the molecular compound. Free Radicals can be either atoms of species, whose natural form is a diatomic molecule, like for example N, O, H, or F, or chemical compounds like for example the CH₃ radical. In our work, we will deal with the radicals N and O.

Due to their unbalanced electron configuration, radicals are highly reactive. Hence, their chemical potential is very high, and reactions involving radicals are usually very fast and highly exothermic. In fact, many chemical reactions proceed through intermediate formation of radicals, even if the reactants and final products are stable molecules.

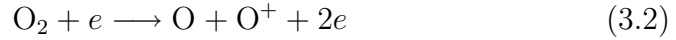
In general free radicals are produced in regions with high energy density, like in plasmas or laser beams. In case of this work, radicals are produced by means of a microwave plasma.

In a plasma, radicals can be produced through several reaction channels, e.g. for oxygen radicals (cf. [73, 75])

- impact dissociation:



- dissociative ionisation:



- dissociative attachment:



- dissociative recombination:

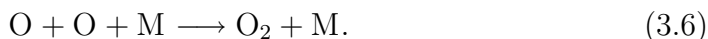


- excitation transfer (e.g. if argon is present):



Since radicals are electrically neutral, they can easily leave the plasma zone and enter plasma free regions, the so-called *afterglow*, where they will react with other species and/or recombine with each other. This recombination proceeds

mainly through one channel, the so called *three-body recombination*,⁴ e.g. for oxygen



This third body can be another gas molecule – let us call this kind of reaction *volume recombination* – or it can be any solid surface. In this case we talk about *surface recombination*. Since the probability of ternary collisions is very low at usual pressure ranges of plasmas, surface recombination will almost always be the dominant recombination process.

Volume recombination is frequently accompanied by light emission⁵. A well known example is the so-called *Lewis-Rayleigh afterglow*, emitted during the volume recombination of nitrogen atoms [76, 77], which is often used for diagnostic purposes and could also be observed during our experiments (see figure 3.1).

3.3 Radicals for surface treatment

There are several mechanisms, how radicals can interact with surfaces. One mechanism has already been mentioned and we suppose that this is also the main mechanism under normal circumstances. It is the surface recombination of radicals. The surface acts as the third body for the recombination reaction and absorbs (all or part of) the excess energy, produced by this reaction.⁶ Hence, like with bake-out or glow-discharge treatment, cleaning of surfaces is achieved by transferring energy to the surface, in this case chemical energy.

Since radicals are chemically very active, we can imagine two additional mechanisms of radical–surface interaction:

- chemical reaction with surface adsorbates resulting in the formation of volatile reaction products, which then can be readily pumped away,
- direct chemical reaction with the surface material, creating surface layers with properties that are more favorable for a particular application, e.g.

⁴since a two-body reaction is not possible due to energy and momentum conservation

⁵if reaction products are not in the energetical ground state

⁶e.g. about $500 \text{ kJ} \cdot \text{mol}^{-1}$ for the recombination of O_2 or $940 \text{ kJ} \cdot \text{mol}^{-1}$ for the recombination of N_2

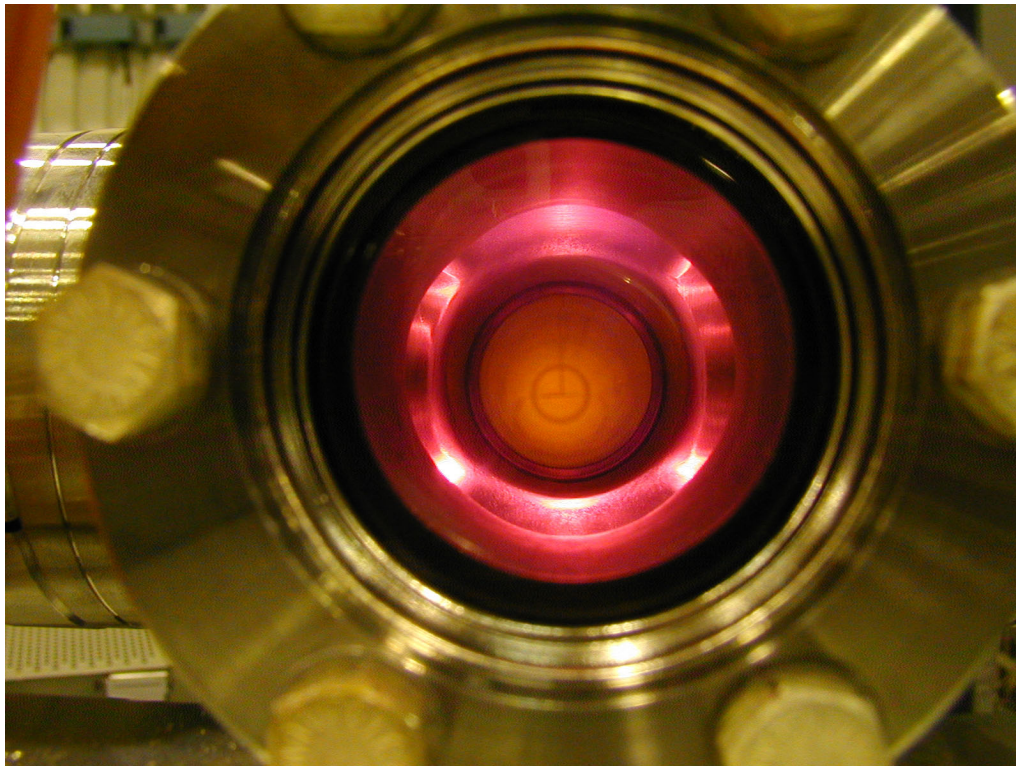


Figure 3.1: Light emission in the afterglow region of a nitrogen plasma

lower secondary electron yield or lower sticking probability or which form a diffusion barrier for gases dissolved in the bulk material.

These effects could also be achieved by glow-discharge treatment, if the corresponding gases are mixed into the process gas during the discharge. However, the main difference of radical treatment as compared to glow-discharge treatment is the complete absence of energetic ions.

3.4 The radical generator

Radicals are produced by means of a microwave plasma. This plasma is provided by an industrial type so-called *radical generator* (XRG-801 microwave radical generator by Secon Semiconductor Equipment [79]). A picture of the radical generator is shown in figure 3.2, a schematic drawing in figure 3.3. The energy required to ignite and maintain the plasma is provided by a

2.45 GHz magnetron with a nominal power of 1 kW,⁷ which emits microwaves into a resonant cavity. The cavity can be tuned by a movable end plate. The process gas is flowing through a reaction tube made of alumina (Al_2O_3), which is passing through the wave guide at the point where the amplitude of the microwave is at maximum. The nominal operating range of the radical generator is between 0.5 mbar and 5 mbar and can be extended down to 1 μbar by means of a adjustable solenoid field, which is bending the trajectories of free electrons, hence effectively increasing the probability of the electrons for collision with and ionisation of gas molecules at low pressures. The radical generator is designed in such a way, that only electrically neutral particles can leave the plasma zone. The average power density in the plasma is specified by the manufacturer as greater than $40 \text{ W} \cdot \text{cm}^{-2}$. Ignition of the plasma can be assisted by means of a halogen light bulb,⁸ mounted in front of the window at the gas inlet of the radical generator. The radical generator can be connected to any vacuum chamber by means of a standard KF 40 flange adaptor.

⁷like it can be found in many microwave ovens

⁸a standard 12 V spot light

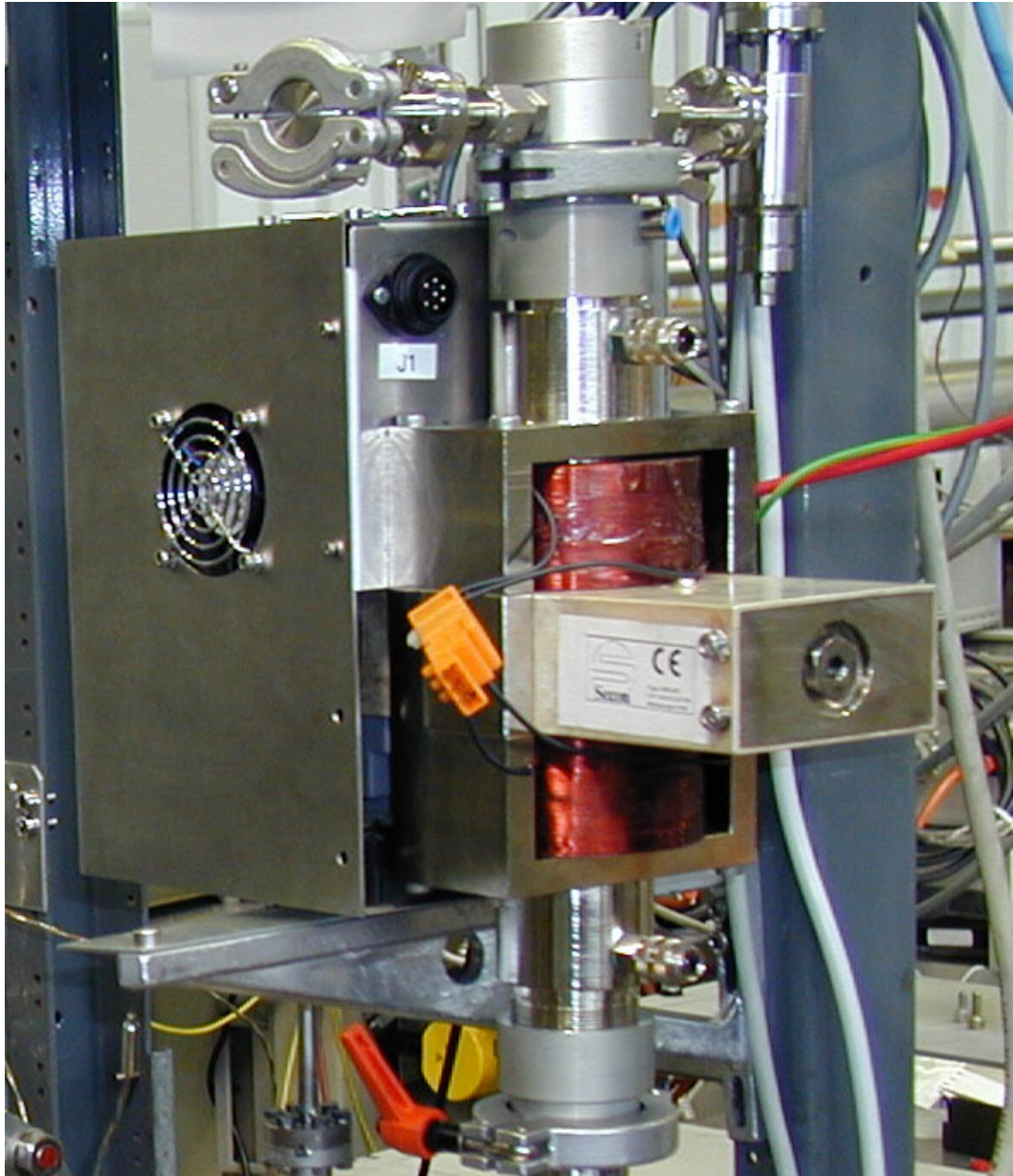


Figure 3.2: Photograph of the radical generator

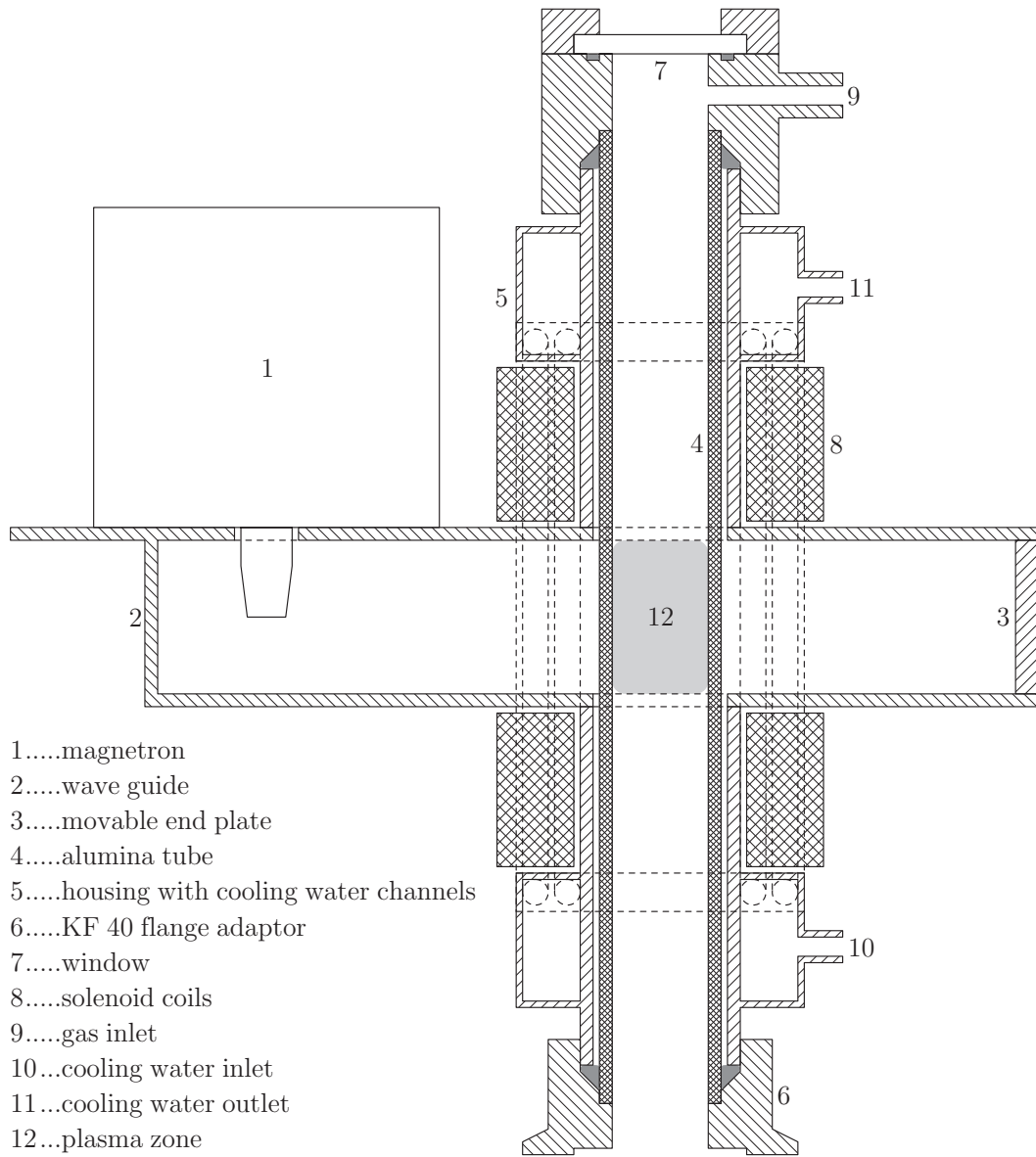


Figure 3.3: Sectional drawing (schematic) of the radical generator

Part II

Characterisation of Radical Treated Surfaces

4 Electron stimulated desorption of molecules from radical treated surfaces

4.1 Description of the experiment

The purpose of this experiment is to investigate the efficiency of the radical treatment procedure for the removal of surface contaminants. It has been shown already in chapter 2, that the desorption of gas molecules adsorbed on the surfaces of the beam vacuum system, induced by photons, ions, and/or electrons has a major influence on the performance of the accelerator. Thus, the molecular desorption yield (η , the number of molecules desorbed per incident photon, ion, or electron) has been chosen in this work as a measure of the “cleanliness” of a surface.

The idea is to measure the molecular desorption yield of a sample before and after a treatment with radicals *in situ*, i.e. without exposing the sample to atmosphere between treatment and measurement. The *reduction* of the molecular desorption yield, achieved by a particular treatment recipe can then be compared with the reduction achieved by other treatment recipes. Furthermore, similar experiments have been carried out since many years in order to investigate other cleaning procedures (e.g. [42, 65, 66, 78]), hence the radical treatment can be compared with those cleaning procedures. At last, the reduction of η can be compared with the reduction due to *beam scrubbing*, i.e. the conditioning of a surface during the operation of the accelerator.

In our experiment, the sample material is OFHC (*Oxygen Free High Conductivity*) copper, because this corresponds to the inner surface of the LHC beam screen (see chapter 2). The samples are bombarded by electrons, i.e. we measure the electron stimulated molecular desorption (*ESD*) yield.

The reason for this choice is the simplicity of the experimental setup. As it will be shown in the next section electrons can be easily produced using a hot filament and can be accelerated towards the sample simply by applying a (electrostatic) potential difference between sample and filament. Hence an electron stimulated experiment is much easier to implement than comparable experiments for ion induced desorption (requires an ion gun) or photon induced desorption (requires a synchrotron or another high intensity light source).

4.2 Experimental setup

As shown in figure 4.1 on page 30, the experimental setup consists of two vacuum chambers separated by a butterfly valve. The upper vacuum chamber is used to load samples into the vacuum system and to perform radical treatment on these samples. This chamber shall be called the *treatment chamber*. The pressure in the treatment chamber is typically in the range of a few mbar. The lower vacuum chamber is used to perform the ESD measurement. It shall be called the *measurement chamber*. The pressure during measurement is typically in the range of 1×10^{-8} mbar. Samples are transferred from one chamber to the other through the (opened) butterfly valve by means of a specially designed transfer system (see figure 4.2 on page 31).

Prior to installation into the vacuum system the actual sample, an eye shaped plate with a thickness of 2 mm, is mounted onto a sample holder, as shown in figure 4.3 on page 32. This sample holder is equipped with a bayonet. The corresponding bayonet socket is incorporated into the vacuum side end of the transport rod, an electro-polished cylindrical stainless steel bar which is fed through the vacuum chamber using a differentially pumped O-ring sealed feed-through (not shown in the figures). This feed-through allows for translational and rotational movement of the transport rod. Once the sample (together with the sample holder) is suspended on the transport rod, it can be either positioned in the upper vacuum chamber for treatment purposes or transferred to the measurement chamber where it can be placed on the sample support ring. The sample holder is equipped with small hooks which fit into the corresponding slits incorporated into the sample support. The design is made in such a way that the hooks lock the sample holder onto the support ring when the bayonet fixing is unlocked and vice versa. Hence, the transport rod can be withdrawn from the lower to the upper vacuum chamber, thereby leaving the sample holder safely locked on the support ring.

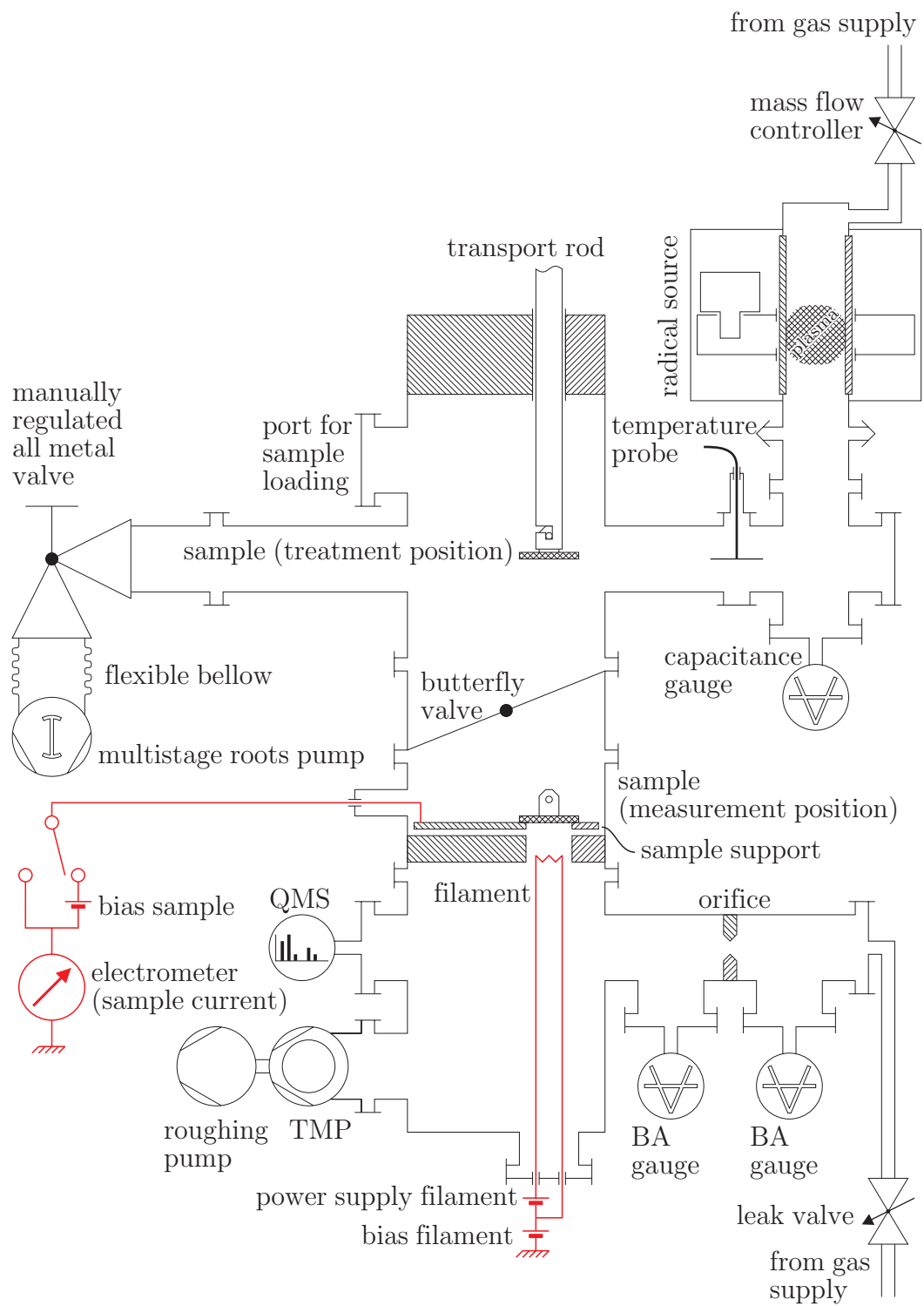


Figure 4.1: Schematic drawing of the experimental setup for the ESD measurements

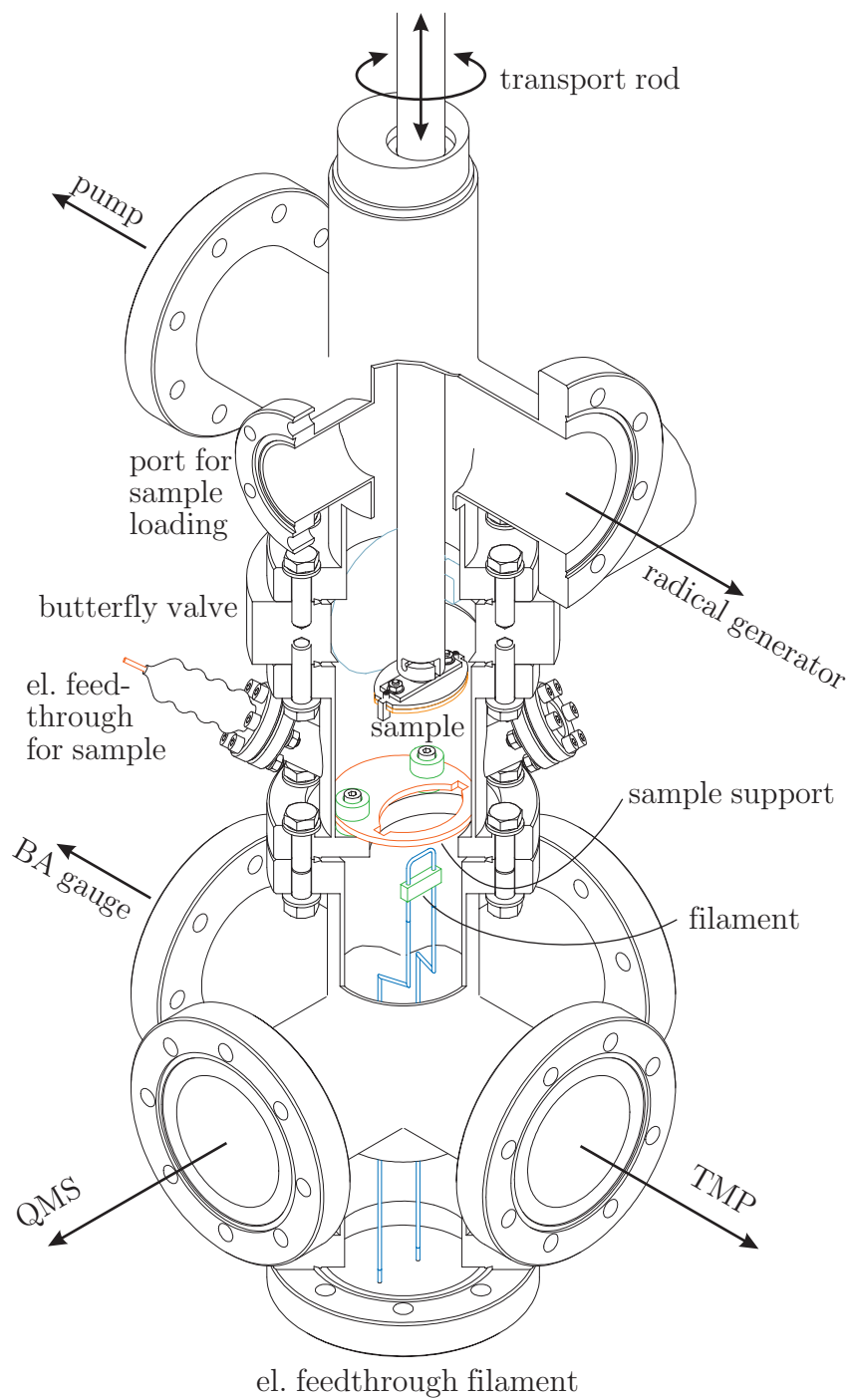


Figure 4.2: Cutaway drawing of the sample transfer system

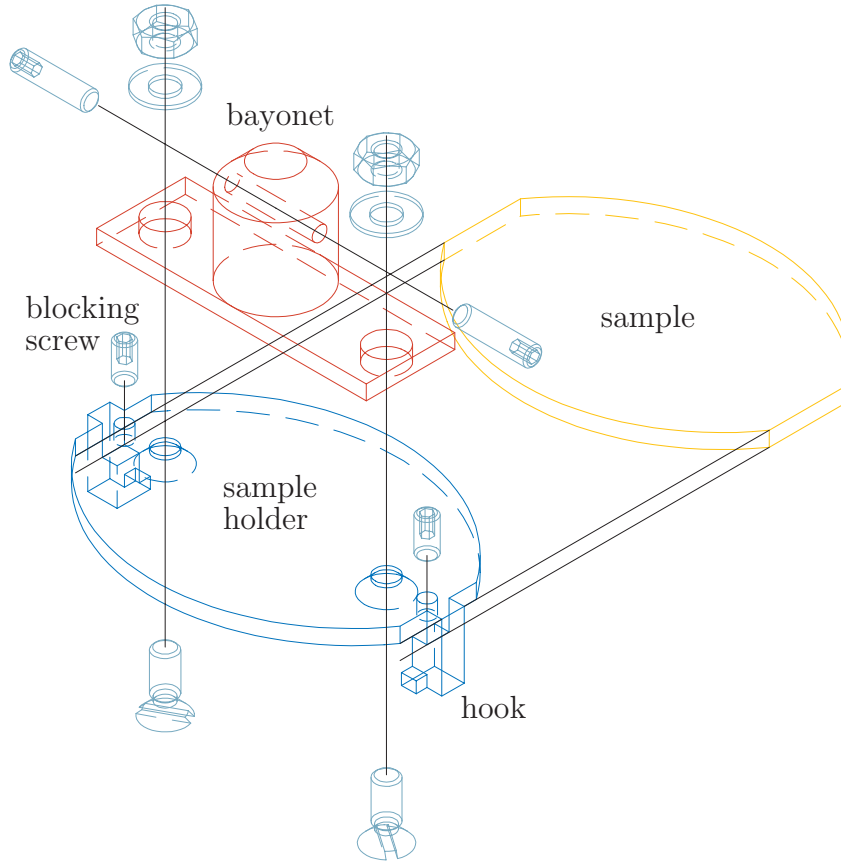


Figure 4.3: Exploded view of the sample holder

As said already, samples can be treated with radicals in the treatment chamber. Radicals are produced by an industrial type radical source – an XRG-801 microwave radical generator by Secon Semiconductor Equipment [79] (see chapter 3) – and pumped through the vacuum chamber by means of a multistage roots-type dry pump – an ADP 81 by Alcatel [80]. This pump has a nominal pumping speed of $120 \text{ m}^3 \cdot \text{h}^{-1}$ and the effective pumping speed can be regulated by means of a manually regulated valve. The flow rate of the process gas is regulated by a type 1179A mass flow controller by MKS instruments [81] (full range 10000 standard cubic centimetre per minute). The total pressure in the vacuum chamber is monitored by a Balzers CMR263 compact capacitance gauge [82] (full range 11 mbar). The experiment is also equipped with a so-called *temperature probe* whose purpose is described in detail in chapter 7. The distance between sample and radical source is about

50 cm and the tube which connects the radical source to the experimental vacuum chamber has an inner diameter of 35 mm.

The lower vacuum chamber is equipped with the following instrumentation, required for the measurement of the electron stimulated desorption yield:

- a pumping group, consisting of a turbomolecular pump (*TMP*) with a nominal pumping speed of $50 \text{ l} \cdot \text{s}^{-1}$ and a roughing pump
- a quadrupole mass spectrometer (*QMS*) – QMG 112 by Balzers instruments – with a secondary electron multiplier for partial pressure measurement
- a Bayard Alpert gauge – SVT (Société de Verrerie et Thermométrie) type 305 [83] – for total pressure measurement
- a heated tungsten filament, placed at a distance of about 2 cm below the sample for the electron production

For calibration purposes a gas injection line, equipped with an all metal fine dosing variable leak valve (by VAT), is connected to the vacuum chamber. In addition, this injection line is equipped with an orifice and a second Bayard Alpert gauge, a model by CSF (this company does not exist anymore [83]) developed for the ISR (*Intersecting Storage Rings*) at CERN. As we will see later on, this setup permits the calibration of the mass spectrometer and the measurement of the effective pumping speed of the turbomolecular pump.

The tungsten filament is powered by a direct current power supply (typical operating conditions: $2 \dots 3 \text{ A}$, $4 \dots 9 \text{ W}$) and is biased to +15 V with respect to ground¹ in order to prevent electrons from hitting the surrounding vacuum chamber. Electrons are extracted from the filament and accelerated towards the sample by applying a positive potential (with respect to the filament) to the sample. For this purpose, the sample support ring is electrically isolated from the vacuum chamber.² A bias voltage supply, switchable between 0 V and +315 V is connected to the sample support by means of a vacuum power feed-through. In addition this electrical connection is equipped with an electrometer in order to measure the electron current received by the sample. Electron bombardment is initiated by switching the bias voltage from 0 V to

¹hence, as well with respect to the surrounding vacuum chamber, which is grounded

²by means of ceramic spacers

+315 V, thereby generating a potential difference between sample and filament of +300 V, hence the electrons hit the sample with an kinetic energy of 300 eV.

Radical treatment as well as measurement processes are controlled by and measurement data are recorded by a central computerised data acquisition system, implemented in LabView.³ The software is written in such a way that measurement data are automatically stored in a database together with the relevant operating parameters, hence erroneous recording of measurement data is largely avoided. Furthermore, stored data can be retrieved easily later on for analysis and visualisation.

A complete experimental run for one sample involves the following steps:

1. chemical cleaning of the sample at the CERN surface treatment workshop
2. insertion of the sample (mounted on the sample holder) into the vacuum system
3. transfer to the measurement chamber
4. after about 24 hours,⁴ measurement of the molecular desorption yield of the sample “as received”
5. transfer to the treatment chamber
6. radical treatment of the sample
7. transfer back to the measurement chamber
8. after about 24 hours, measurement of the molecular desorption yield of the radical treated sample
9. repeat steps 5 – 8

³the hardware consists of a PC operating under Windows NT 4, equipped with a National Instruments [84] PCI 1200 multifunction I/O card. Incoming and outgoing signals are conditioned and (de)multiplexed using the modular SCXI signal conditioning hardware, also by National Instruments.

⁴time required for the pumpdown of the measurement chamber until a pressure of about $5 \times 10^{-9} \dots 1 \times 10^{-8}$ torr is reached

4.3 Determination of the molecular desorption yield

4.3.1 Theoretical and experimental prerequisites

Basic equations

In a vacuum chamber which is in thermal equilibrium, i.e. where temperature and pressure is constant over the whole volume, the partial pressure of each species is related to the its molar density according to *Dalton's law*

$$p_j = n_j R T \quad (4.1)$$

and the total pressure is related to the total molar gas density by the *ideal gas law*

$$p = n R T. \quad (4.2)$$

In the equations (4.1) and (4.2) p_j and n_j are the partial pressure and molar density of species j , p and n the total pressure and molar density, R the molar gas constant, and T the absolute temperature. If the transformation of species (e.g. due to chemical reactions) can be neglected then it holds for the partial pressure of each species

$$V \frac{\partial p_j}{\partial t} = \dot{Q}_j - p_j S_j \quad (4.3)$$

and in the steady state

$$\dot{Q}_j = p_j S_j. \quad (4.4)$$

In equations (4.3) and (4.4) V is the volume of the vacuum chamber and \dot{Q}_j and S_j are the overall gas load⁵ (due to outgassing, leaks, etc.) and the effective pumping speed of species j , respectively. Let us assume that without electron stimulated desorption, the vacuum chamber has reached a steady state which is characterised by the “background” pressure $p_j^{(0)}$. The desorption of gas

⁵measured in units of $\text{Pa} \cdot \text{m}^3 \cdot \text{s}^{-1}$

molecules adsorbed on the surface of the vacuum chamber represents just an additional gas load for the vacuum system, hence, with the presence of electron stimulated desorption the pressure will rise to a new steady state value⁶, say $p_j^{(1)}$. This pressure rise can be characterised by the following equation

$$(p_j^{(1)} - p_j^{(0)}) S_j = \eta_j \frac{I_S}{e} k T \quad (4.5)$$

where η_j is the molecular desorption yield, I_S the current of impinging electrons, e the elementary charge, and k the Boltzmann constant. The fraction I_S/e gives the number of electrons hitting the surface per unit time. Since η_j is per definition the number of gas molecules (of species j) desorbed per incident electron (cf. section 2.4), the expression $\eta_j I_S/e$ gives the number of molecules desorbed due to electron bombardment per unit time.

Pumping speed

In order to calculate the molecular desorption yield η_j from equation (4.5), we have to measure the partial pressure of species j (with and without desorption) and the electron current I_S . In addition, we have to know the temperature and the effective pumping speed of the vacuum system for species j . Fortunately the measurement of the pumping speed is a relatively straight forward process and has to be done only once. It shall be explained briefly in the following paragraphs.

For the measurement of the effective pumping speed, we make use of the orifice, the second Bayard Alpert gauge and the gas injection system, as illustrated in figure 4.1. Prior to gas injection the vacuum system is in steady state, hence the signals from the two gauges do not change with time. During injection of a pure gas, the signals of the two gauges increase until a new steady state value is reached. This new balance is characterised by the equation

$$\Delta p_j S_j = (\Delta \hat{p}_j - \Delta p_j) C_j. \quad (4.6)$$

Δp_j and $\Delta \hat{p}_j$ are the pressure rises measured by gauge 1 and 2, respectively,⁷

⁶the characteristic rise time is actually given by the quotient V/S_j

⁷In fact, a total pressure gauge cannot measure partial pressure, but since we are injecting gas of a single species, the increase in total pressure corresponds to the increase in partial pressure of this species.

and C_j is the conductance of the orifice for species j , which is for molecular flow simply given by

$$C_j = A \frac{\bar{v}_j}{4} \quad (4.7)$$

where A is the opening area of the orifice and \bar{v}_j the mean thermal velocity of species j . Calculation of the effective pumping speed follows directly from equation (4.6). Table C.1 in appendix C summarises the values of the effective pumping speed for the most common residual gases.

Functional principles of ionisation gauges

Bayard Alpert type gauges do not measure pressure directly, i.e. by measuring the force per unit area. Instead, they measure a current of positive ions generated by the ionisation of residual gas molecules (cf. [85]). The ionising particles are electrons emitted by a hot filament, the so-called *hot cathode*. Thus, the raw signal coming from those gauges is an electrical current which is proportional to the number of emitted electrons (also called the *emission current*) and the residual gas density, i.e. (for a fixed temperature)

$$I^* = I_e^* \sum_j s_j^* p_j \quad (4.8)$$

where I^* is the raw gauge signal, also called the *gauge collector current*, and I_e^* the emission current. s_j^* is called the *absolute sensibility* of the gauge for species j . Values for the absolute sensibilities of the two gauges used in this experiment are given in table C.3 in appendix C.

The quadrupole mass spectrometer works in principle like an ionisation gauge. First, residual gas molecules are ionised and/or cracked into smaller fragments using electrons as ionising particles. The resulting (positive) ions are sent through a quadrupole mass filter (cf. [86]) where they are selected according to their mass-to-charge ratio. Those ions which pass the filter are then counted. In the case of our experiment the quadrupole mass spectrometer counts ions by means of a so-called *secondary electron multiplier*. Hence, the raw output signal of the mass spectrometer is an electron current, proportional to the ion count rate, which is in turn proportional to the emission current and the density of residual gas molecules, i.e. (again for a fixed temperature)

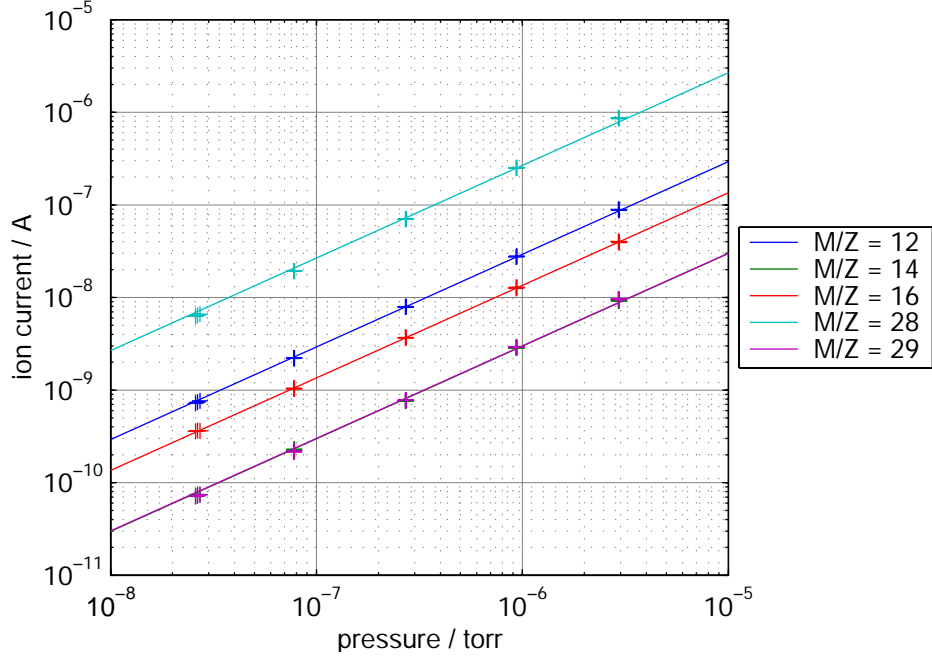


Figure 4.4: A set of calibration curves for carbon monoxide

$$I_m^+ = I_e \sum_j s_{m,j} p_j. \quad (4.9)$$

The subscript m indicates the setting of the mass filter, i.e. the mass-to-charge ratio of the ions that can pass the filter. In fact, m is the approximate numerical value of the ion mass, measured in atomic mass units, divided by the ionisation degree. From here on, the mass-to-charge ratio will be denoted as M/Z . I_m^+ is the raw output signal of the mass spectrometer at $M/Z = m$, also called the *ion current*, and $s_{m,j}$ is the *absolute sensibility* of the mass spectrometer at $M/Z = m$ for species j . I_e is again the emission current.

Before the mass spectrometer can be used as a measuring device, values for the sensibilities $s_{m,j}$ have to be determined by means of a calibration procedure. For the purpose of the calibration pure gases are injected into the vacuum system and the change in the mass spectrometer signal is recorded together with the change in the total pressure. A typical set of such calibration curves is shown in figure 4.4.

The absolute sensibilities can change significantly with time with a typical

timescale of days, but they change proportional to each other.⁸ hence, absolute sensibilities are usually given as a multiple of a *reference sensibility* s_{ref} ,⁹ i.e.

$$s_{m,j} = s_{ref} s'_j x_{m,j}. \quad (4.10)$$

s'_j is called the *relative sensibility* for species j and $x_{m,j}$ the *cracking pattern* for species j at $M/Z = m$. Relative sensibilities and cracking patterns do not change significantly with time. Tables C.4 and C.5 in appendix C summarise numerical values for s'_j and $x_{m,j}$, respectively, obtained from calibration process.

In order to determine partial pressures from the mass spectrometer signal, the reference sensibility has to be calculated each time, thereby making use of the signal of the total pressure gauge. A detailed description of a procedure for the determination of partial pressures and the estimation of their uncertainties is given in appendix D.

4.3.2 Measurement procedure

The molecular desorption yield shall be determined for the gases hydrogen (H_2), methane (CH_4), ethane (C_2H_6), carbon monoxide (CO), carbon dioxide (CO_2), and water vapor (H_2O). For this purpose data are recorded with the mass spectrometer set at $M/Z = 2, 12, 14, 15, 16, 18, 27, 28$, and 44. For each setting of the mass spectrometer a *desorption pulse* is recorded, i.e. the bias voltage of the sample is switched from 0 V to +315 V, kept there for about 10 seconds, and then switched back to 0 V, while at the same time the signals of the total pressure gauge and the mass spectrometer and the sample current are recorded.

In figure 4.5, signals of two desorption pulse, recorded with as setting of the QMS of $M/Z = 44$ are shown. The upper graph shows the signal from an untreated sample (“as received”), whereas the lower graph shows the signal from the same sample after a treatment with nitrogen radicals. These two graphs give a good example of how the current of bombarding electrons (i.e.

⁸i.e. the mass spectrometer can count more or less ions per emitted electron, but it does so in the same manner for all kinds of ions

⁹the reference sensibility is by convention equal to the absolute sensibility of the mass spectrometer for H_2^+

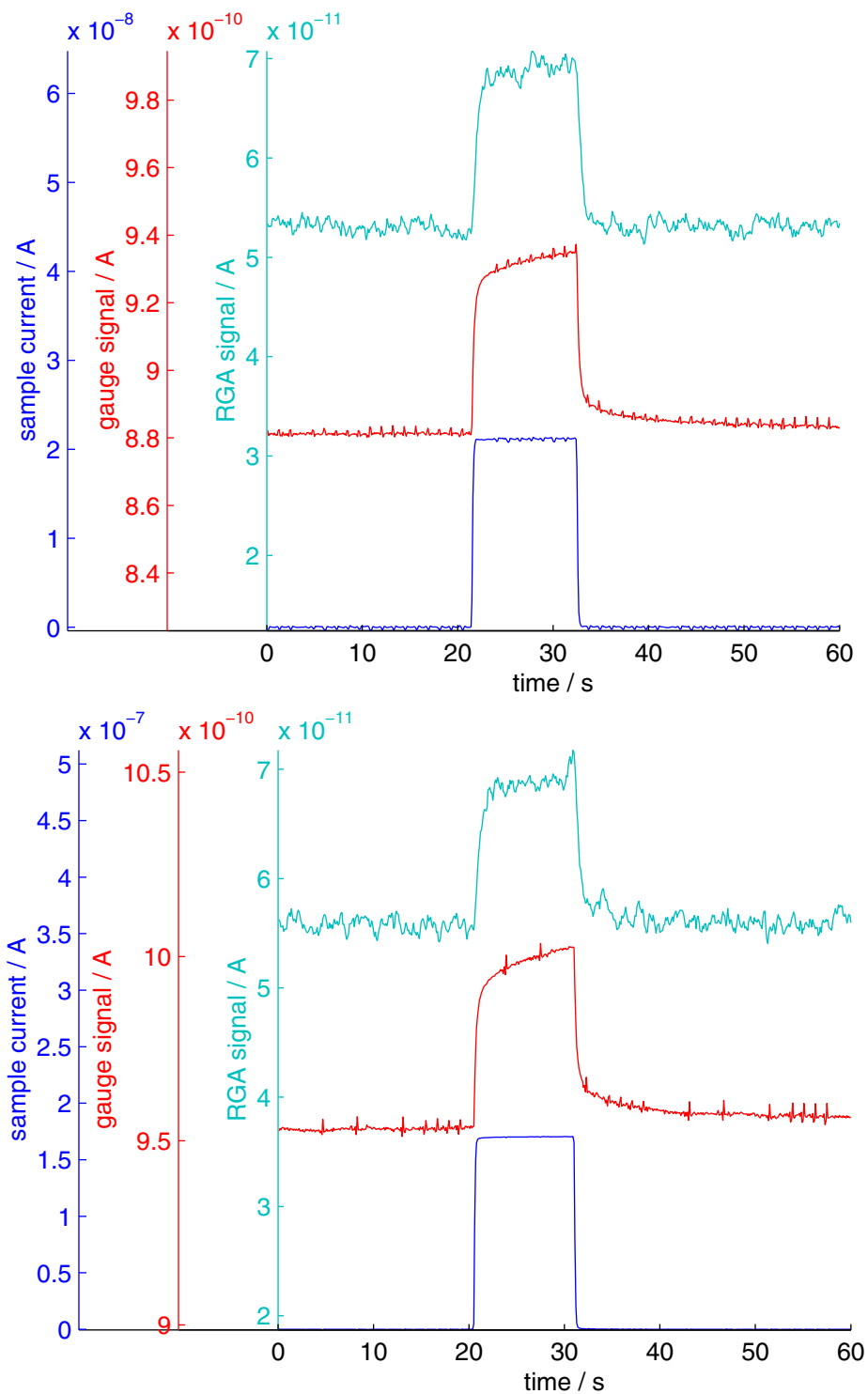


Figure 4.5: Desorption pulses, recorded at $M/Z = 44$. Upper graph: sample as received, lower graph: same sample after treatment

the sample current) has to be chosen sufficiently high¹⁰ in order to get an acceptable signal-to-noise ratio in the gauge and QMS signals. Of course, a higher sample current would produce a better signal (i.e. a higher Δp), but this also means that molecules would be desorbed at a much higher rate, which in turn means that the sample would already be cleaned by the measurement process itself. Hence, the correct choice of the sample current represents a compromise between a good signal and a sufficiently low desorption rate. Since the rate of electrons emitted by the filament is a strong function of its temperature (*Richardson's law*, cf. [87], p. 42), the sample current can be adjusted by limiting the current which is heating the filament.

The desorption pulses as shown in figure 4.5 contain all the information required to calculate η (except for calibration data). As mentioned already in the previous section, the formula for the calculation of the molecular desorption yield is given by

$$(p_j^{(1)} - p_j^{(0)}) S_j = \eta_j \frac{I_S}{e} k T \quad (4.11)$$

or

$$\eta_j = \frac{(p_j^{(1)} - p_j^{(0)}) S_j e}{I_S k T}. \quad (4.12)$$

The partial pressures $p_j^{(0)}$ are determined from the gauge and mass spectrometer signals before and after the desorption pulse. Likewise, the partial pressures $p_j^{(1)}$ are determined from the gauge and mass spectrometer signals during the desorption pulse. Values for the effective pumping speed S_j are taken from table C.1 on page 173. Since the experiment has been operated at room temperature, T is assumed to be 300 K.¹¹

The estimated variance of η_j is given through the law of propagation of uncertainties as

$$\frac{\sigma^2(\eta_j)}{\eta_j^2} = \frac{\sigma^2(p_j^{(0)}) + \sigma^2(p_j^{(1)})}{(p_j^{(1)} - p_j^{(0)})^2} + \frac{\sigma^2(I_S)}{I_S^2} \quad (4.13)$$

¹⁰n. b. that the sample current in the lower graph is about ten times higher than in the upper graph whereas the gauge and QMS signals are basically unchanged

¹¹A deviation of the temperature of a few degrees does not change the result significantly.

where the variances $\sigma^2(p_j^{(0)})$ and $\sigma^2(p_j^{(1)})$ are estimated from the total pressure gauge and mass spectrometer data as indicated in appendix D and the variance of the sample current, $\sigma^2(I_S)$, is taken from measurement.

4.4 Results

4.4.1 Treatment efficiency of nitrogen and oxygen radicals

Measurements of the molecular desorption yield have been carried out for samples treated by N and O radicals. In the case of nitrogen radicals, industrial type nitrogen 45 has been used as process gas, i.e. the gas fed into the radical source. In the case of oxygen radicals the process gas has been a mixture of 90 % argon 46 and 10 % oxygen 48.

In order to compare the treatment efficiency of these two process gases, the molecular desorption yield has been measured after 30 min, 1 h, 2 h, and 4 h of treatment time, respectively. The flow rate of the process gas has been set to $5 \text{ Pa} \cdot \text{m}^3 \cdot \text{s}^{-1}$ and the effective pumping speed to $0.02 \text{ m}^3 \cdot \text{s}^{-1}$, hence the average pressure in the treatment chamber has been about 250 Pa.

In figure 4.6 on page 45 the molecular desorption yield as a function of the treatment time is shown for two samples treated with nitrogen (upper graph) and oxygen (lower graph) radicals, respectively. The samples have initial desorption yields η which are in the same order of magnitude, but nevertheless not equal. Hence, in order to compare the two samples, η has to be normalised in some way.

Figure 4.7 on page 46 shows the *normalised desorption yield*, i.e. η divided by η of the non-treated sample, for the main desorbed gases (upper graph) and the normalised total molecular desorption yield¹² (lower graph) of the two samples, thus enabling direct comparison of the efficiency of the nitrogen and oxygen radical treatment.

Figure 4.7 shows clearly that the treatment with oxygen radicals reduces the molecular desorption yield much faster than a comparable treatment with nitrogen radicals, but after a long enough treatment time both treatments result in a similar reduction of η .

¹²i.e. the total number of molecules desorbed per incident electron

4.4.2 Reduction of the molecular desorption yield by oxygen radical treatment

In the previous section, a comparison between nitrogen and oxygen radical treated samples has been presented, showing that oxygen radicals are more efficient in the beginning. To investigate this efficiency in more detail, a series of measurements with oxygen radicals have been carried out. For each of these measurements, a “fresh” sample has been measured and treated for 30 min using the argon–oxygen mixture as described in the previous section. The flow rate of the process gas has been varied between $1 \text{ Pa} \cdot \text{m}^3 \cdot \text{s}^{-1}$ and $10 \text{ Pa} \cdot \text{m}^3 \cdot \text{s}^{-1}$ whereas the effective pumping speed has been kept at $0.02 \text{ m}^3 \cdot \text{s}^{-1}$.

Figure 4.8 on page 47 summarises the results of these measurements. It can be seen, that the molecular desorption yields for the species H_2 , CH_4 , and C_2H_6 are reduced more efficiently than for the other species, where η is reduced significantly only at higher flow rates of the process gas.

4.4.3 Development of the molecular desorption yield under continuous electron bombardment – simulation of the beam scrubbing effect

In order to simulate the conditioning of the beam screen in the LHC during operation (cf. chapter 2), samples have been exposed to continuous electron bombardment while measuring at the same time the molecular desorption yield. For this purpose a special data acquisition software has been developed, which allows a fully automated measurement process. As opposed to the previously described measurement η by means of desorption pulses, data for this experiment are taken under continuous electron bombardment by “rotating” through the settings M/Z of the quadrupole mass spectrometer. From time to time (about each 30 min) electron bombardment is switched off in order to measure the background pressure.

The results of two such conditioning experiments are shown in figures 4.9, 4.10, and 4.11 on pages 48–50. The first set of curves is recorded during the conditioning of a non-treated sample whereas the second set of curves stems from a sample treated with oxygen radicals. After measuring the initial molecular desorption yield, marked as “as received” in figure 4.9 – which is in good agreement with the initial desorption yield of the non-treated sample –

the sample has been treated for 12 min using the argon–oxygen gas mixture at a flow rate of $10 \text{ Pa} \cdot \text{m}^3 \cdot \text{s}^{-1}$, followed by a intermediate measurement of η (marked as “treatment 1”) and a second treatment, this time for 18 min. After the second treatment the conditioning experiment has been carried out for this sample (marked as “treatment 2”). It can be seen from the graphs that in order to reach the same reduction of η as with the radical treatment, the non-treated sample has to accumulate about $10^{16} \text{ electron} \cdot \text{cm}^{-2}$. At the end of the conditioning process, i.e. at an accumulated electron dose of about $10^{19} \text{ electron} \cdot \text{cm}^{-2}$, the two samples exhibit the same molecular desorption yield.

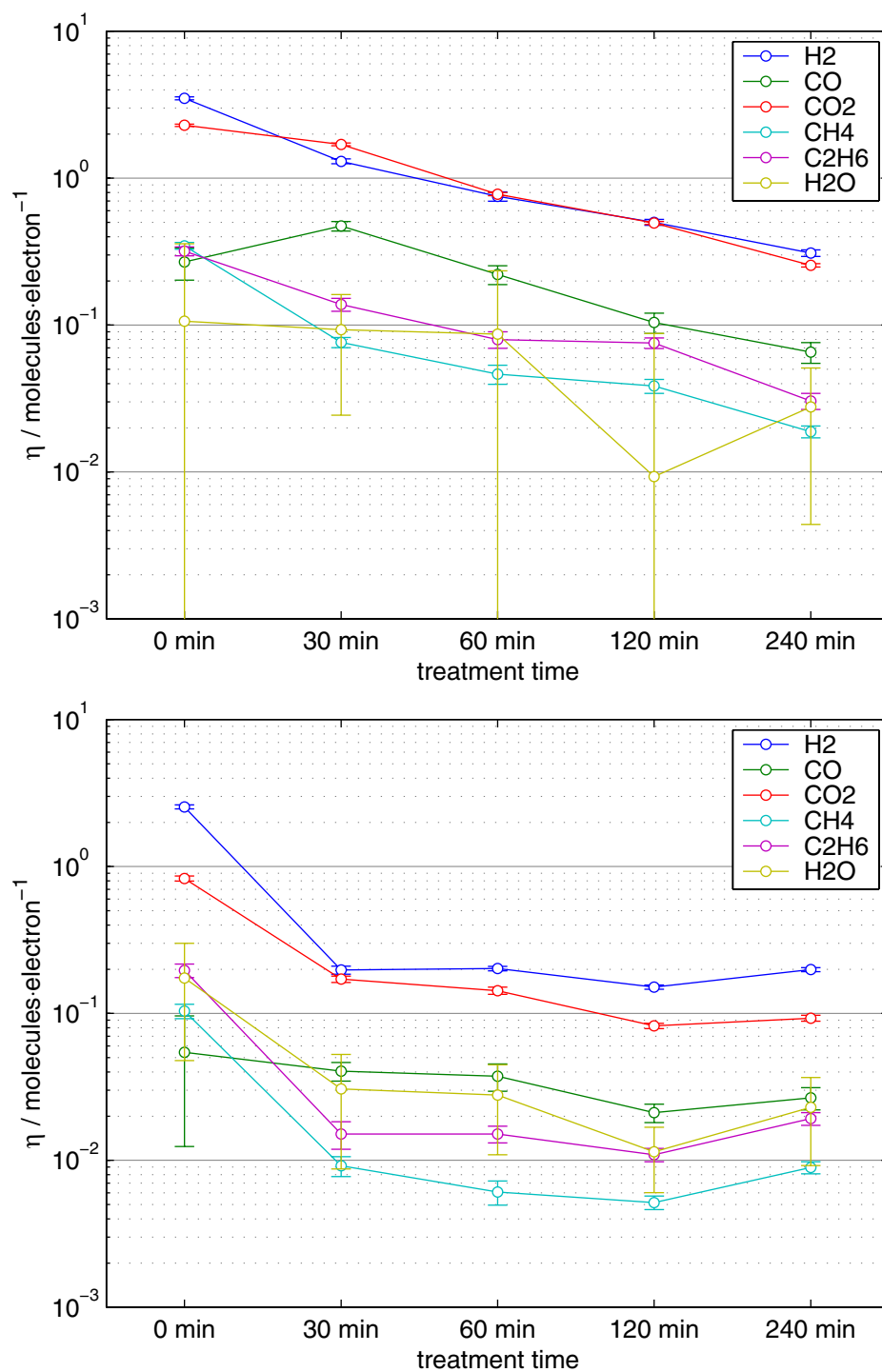


Figure 4.6: Molecular desorption yields of two copper samples treated with nitrogen radicals (upper graph) and oxygen radicals (lower graph)

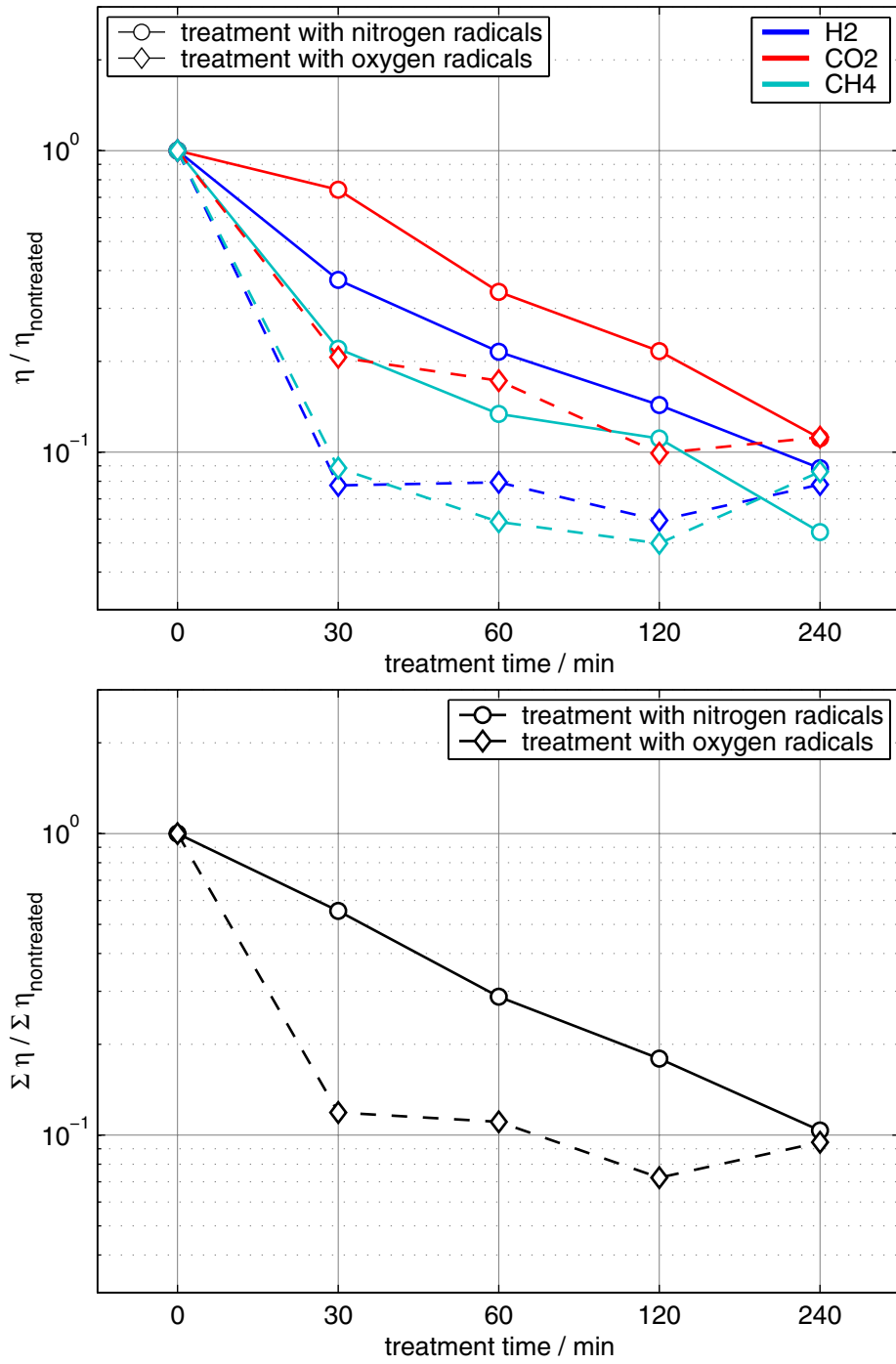


Figure 4.7: Comparison of the treatment efficiency of nitrogen and oxygen radicals (a detailed description is given in the text)

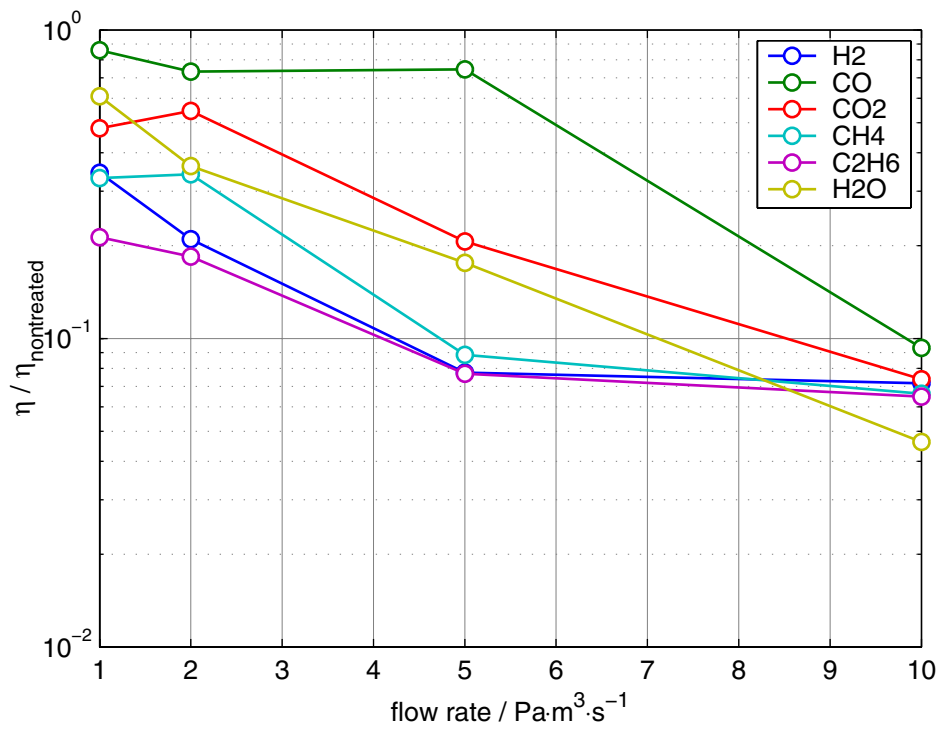


Figure 4.8: Reduction of the molecular desorption yield by oxygen radical treatment. The flow rate, shown on the abscissa of the graph, is that of the process gas (90% Ar + 10% O₂) as set by the mass flow controller. The pumping speed has been set to 0.02 m³ · s⁻¹. Each sample (= data point in the graph) has been treated for 30 min.

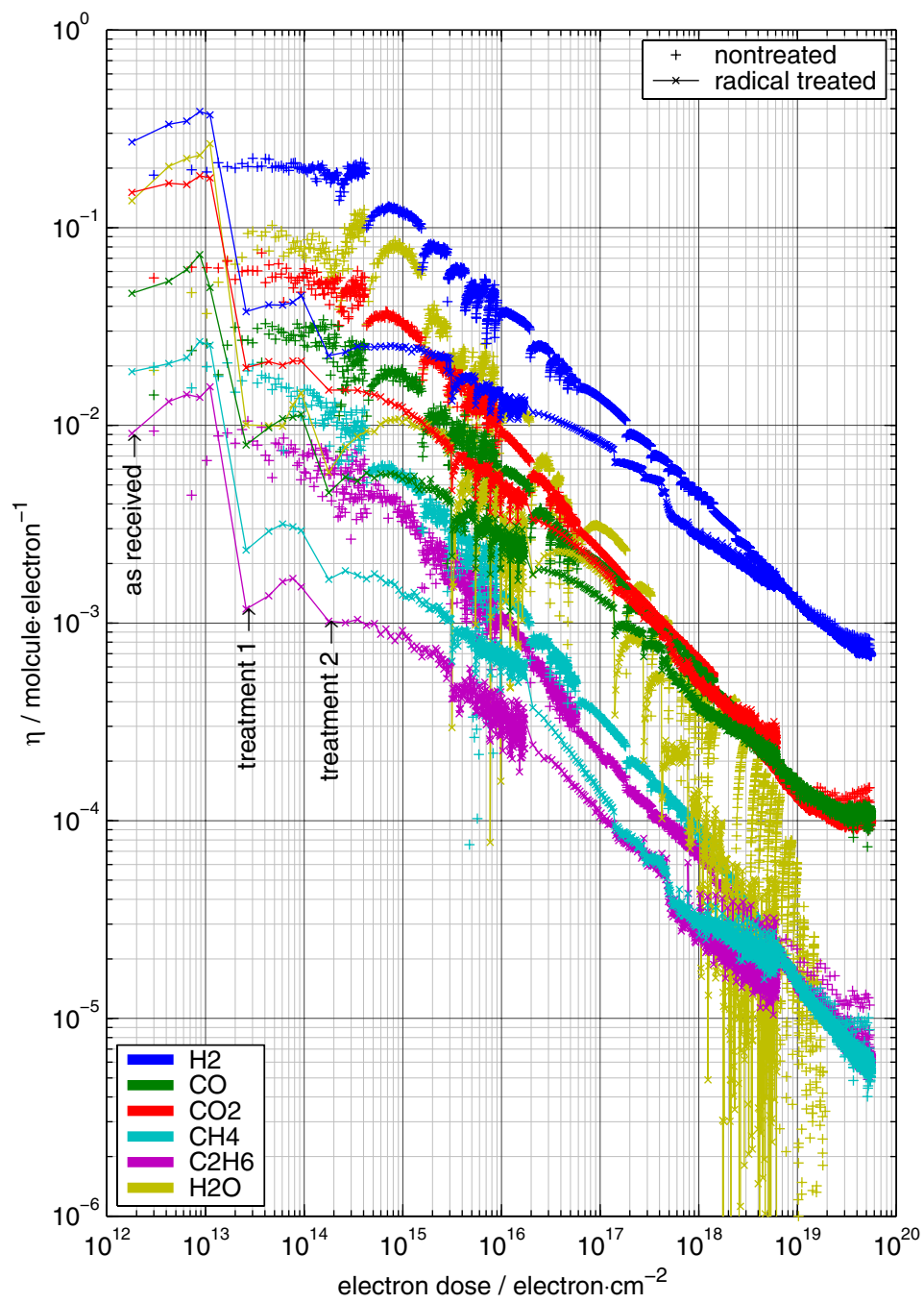


Figure 4.9: The molecular desorption yield as a function of the electron dose – Comparison of an untreated and an oxygen radical treated sample (for further description, see the text)

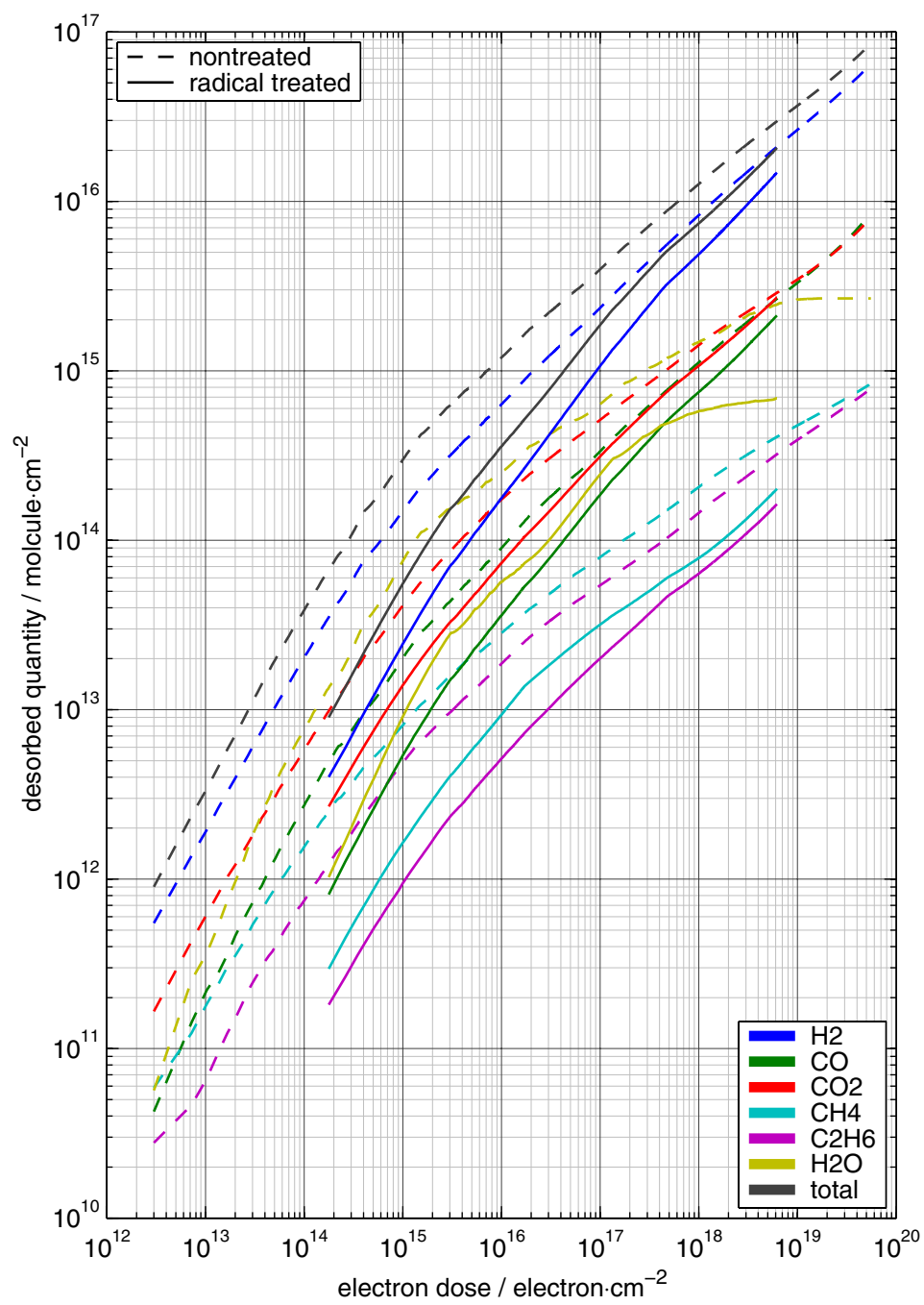


Figure 4.10: The number of desorbed molecules as a function of the electron dose – Comparison of an untreated and an oxygen radical treated sample (for further description, see the text)

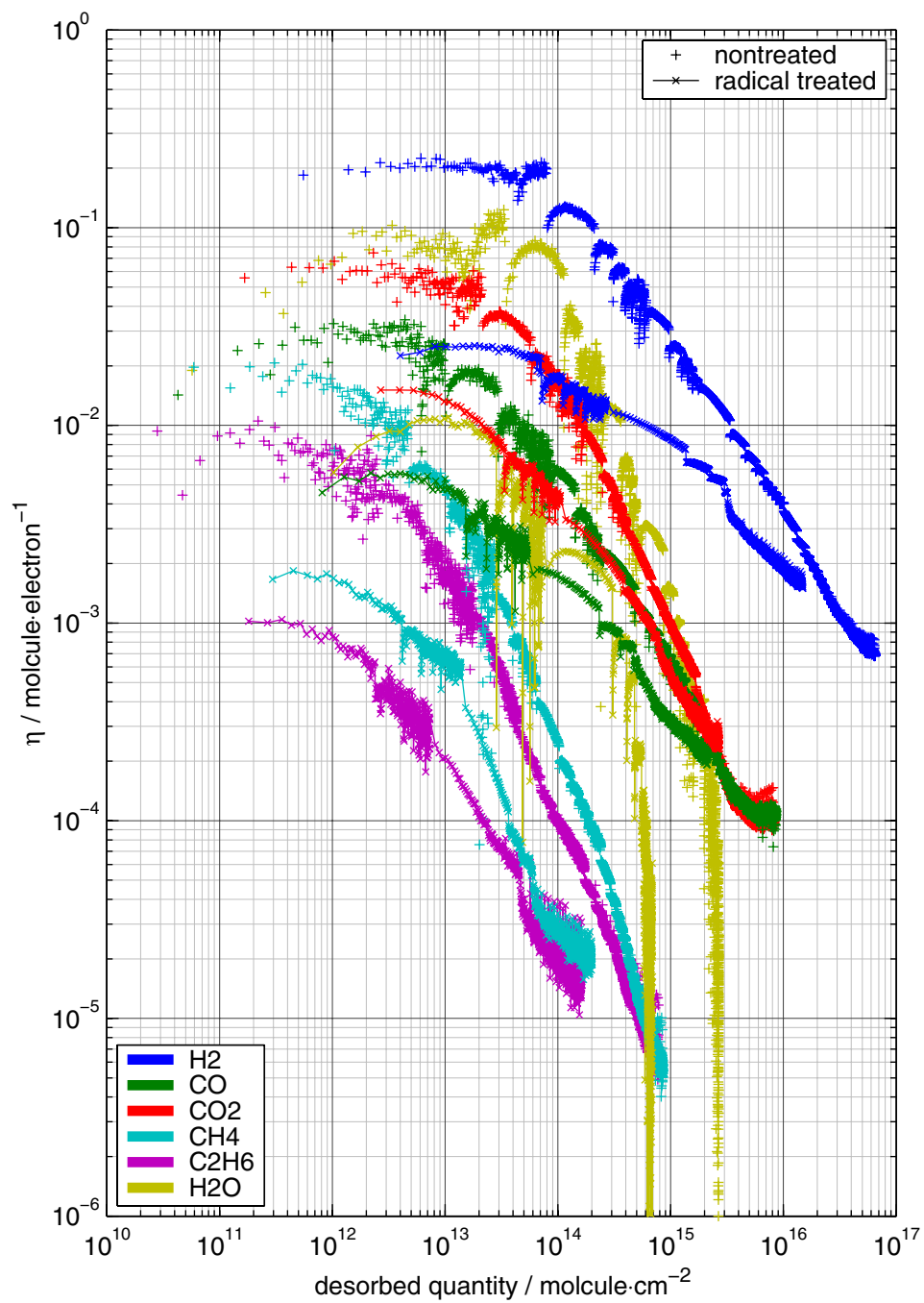


Figure 4.11: The molecular desorption yield as a function of the number of desorbed molecules – Comparison of an untreated and an oxygen radical treated sample (for further description, see the text)

5 Surface analysis of radical treated samples

5.1 Introduction

In the course of this work, the surfaces of several OFHC copper samples, after treatment with radicals, have been analysed using a variety of surface analysis techniques. Auger electron spectroscopy (*AES*) represented the main analysis tool that was in some cases complemented by X-ray photo-electron spectroscopy (*XPS*) and scanning electron microscopy (*SEM*), thereby utilising industrial type instruments available at CERN (EST division, Surface and Material Technologies Group). Finally, the secondary electron yield of radical treated samples has been measured utilising an experimental system, developed and built at the LHC vacuum group (cf. [56, 88, 58]).

All of these surface analyses had to be performed *ex situ*, i.e. the samples had to be taken out of the treatment chamber and inserted into the vacuum system of the analysis instrument, thereby exposing them to atmosphere. The time these samples spent in atmosphere between treatment and analysis was in general not longer than 30 min and most of the times less than 10 min. Nevertheless a certain amount of re-contamination could not be avoided. Hence, the results of these analyses, which shall be reported in this chapter, should be seen under these aspects.

5.2 Experimental setup

As it is shown in figure 5.1, the sample preparation system or *treatment chamber* is simply a long stainless steel tube (inner diameter 35 mm) with the radical source attached to one end and the pump attached to the other

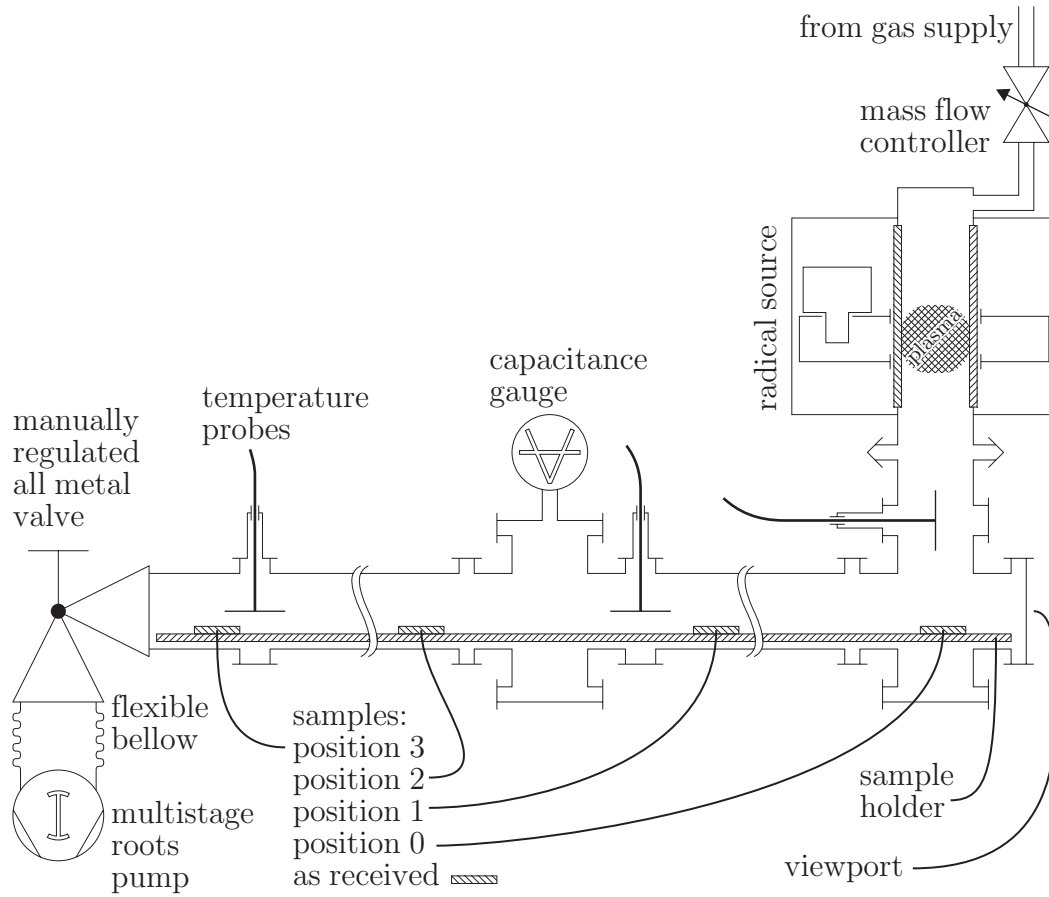


Figure 5.1: Schematic drawing of the sample preparation system

end. The flow rate of process gas is controlled by a mass flow controller and the pressure in the chamber monitored by a capacitance manometer (cf. chapters 4 and 7). Furthermore, temperature probes are installed whose purpose is explained in chapter 7.

Four samples – small OFHC copper plates, dimensions about $1\text{ mm} \times 10\text{ mm} \times 40\text{ mm}$ – can be mounted on the sample holder¹ 35 cm apart from each other – denoted by “position 0” ... “position 3” – and the whole assembly can be inserted into the treatment chamber via a demountable viewport (see also figure 5.2). A fifth sample, denoted by “as received”, which is not treated but nevertheless analysed for reference, complements the set of samples that form one experimental run.

¹a stainless steel rail, dimensions $2\text{ mm} \times 20\text{ mm} \times 1200\text{ mm}$

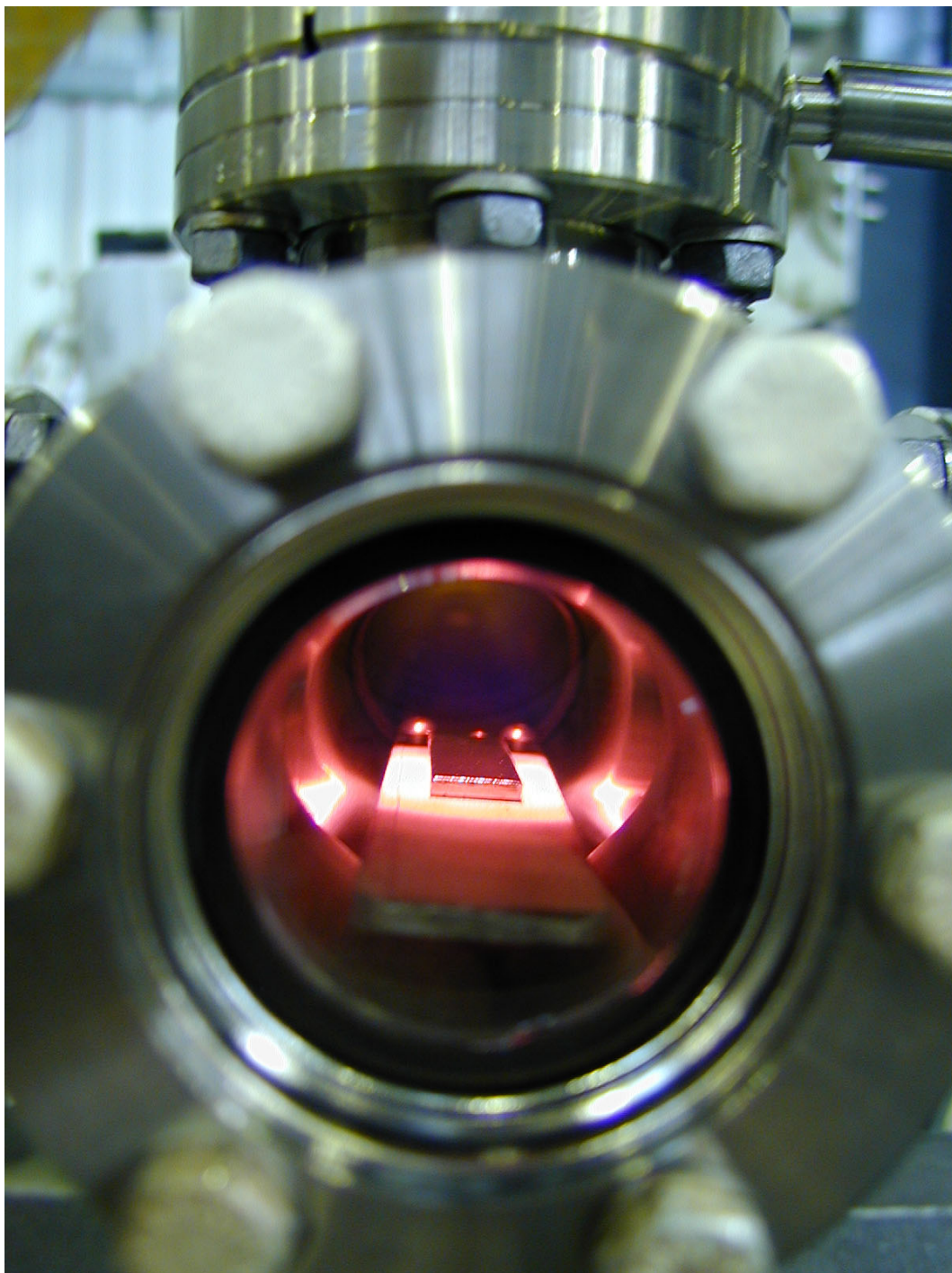


Figure 5.2: A sample at “position 0” during radical treatment

5.3 Results from surface analysis

The AES and XPS analyses have been carried out by Mauro Taborelli and Daniel Latorre (CERN-ESR-SM), whose results shall be presented and conclusions quoted here.

5.3.1 Experimental runs no. 1 and 1a

Treatment parameters:

- process gas: nitrogen
- flow rate: $10 \text{ Pa} \cdot \text{m}^3 \cdot \text{s}^{-1}$
- pressure: 500 Pa
- treatment time: 120 min

Auger electron spectra obtained from these samples are shown in figure 5.3 on page 60. Atomic concentrations, calculated from these spectra are shown in figure 5.4 on page 61. Furthermore these samples have been exposed to laboratory air for 24 h after the first AES measurement and re-measured afterwards (denoted as “1a”).

Quoting from the notes of M. Taborelli and D. Latorre [89]:

...The amount of C found on the sample at position 0 is much lower than on other air exposed copper samples investigated so far in the laboratory. This means that ...the effect at position 0 can be considered as a cleaning from the adsorbed C overlayer. ...

The cleaning reveals other impurities whose signal was masked by the C adsorbates present on the “as received” surface, like K, Na, Cr, Cl, S. ...K is present at an unusually high concentration and no clear explanation for its origin can be given. The intensity in the “position 0” sample seems to be too high to explain by masking through C the fact that no K signal appears on the spectrum of the “as received” sample. A different cleaning procedure would be the best way to distinguish whether it is present on the surface before the nitrogen treatment or is produced by the latter.

As we already remarked the relative amount of Cu is higher in the “position 0” sample than in the “as received” indicating a general cleaning of the surface. In other words the signal of Cu is stronger in the latter case because the coverage by impurities and adsorbates is lower than on the as received surface. ...

The Auger line-shape of the N line is similar to that of nitrides, especially for the samples in position 1, 2, 3. ...

and for the samples re-measured after 24 h of air exposure:

The only changes observed with respect to the analyses before air exposure are given by the slight increase of C intensity for all samples ... The increase is also observed in the calculated concentrations. However, almost no increase of O was observed and the slight increase can easily be ascribed to O in the adsorbed hydrocarbons. The concentrations and intensities for N and Cu decrease due to the thicker coverage by C.

SEM images from these samples are shown in figure 5.5 on page 62. Grain boundaries appear much sharper on the sample at “position 0” than on the “as received” sample, indicating again that the overlayer of adsorbates has been reduced quite significantly.

5.3.2 Experimental runs no. 2 and 3

For these experiments the samples have been pre-treated by SUBU (chemical polishing: solution of sulfamic acid, hydrogen peroxide, butanol and ammonium citrate at 72 °C). Otherwise treatment parameters for experimental run no. 2 have been identical to those of no. 1. For experimental run no. 3, no radicals have been produced. Instead, the samples have been exposed to a flux of nitrogen for 3 h while at the same time the treatment chamber was baked at 150 °C.

The results from Auger electron spectroscopy are summarised in figure 5.6 on page 63. The atomic concentrations of the two “as received” samples are in quite good agreement, providing that the SUBU treatment is rather reproducible.

The samples in position 0 ...3 of experimental run no. 2 show surface compositions which are quite similar to that of experimental run no. 1. Quoting again from [89] for experimental run no. 3:

...The sample at “position 0” is practically identical to the as received sample. It is therefore quite different from the sample of position 0 when the plasma is turned on, since no decrease of O and C is observed this time with respect to the “as received” surface.

...

From position 0 to 1 we observe an increase of C and a decrease of Cu concentration. This behaviour of C is similar to that found for the radicals-treated samples, but the a clear difference consists in the lower amount of N and in the higher amount of C which covers all the other signals, including O. So there is no trace of cleaning effect.

5.3.3 Experimental runs no. 4 and 5

These two experimental runs deal with oxygen radical treated samples. In both cases samples have been pre-treated by SUBU. Radical treatment parameters for run no. 4 were:

- process gas: argon + oxygen (molar fractions 90% and 10%, respectively)
- flow rate: $8 \text{ Pa} \cdot \text{m}^3 \cdot \text{s}^{-1}$
- pressure: 400 Pa
- treatment time: 30 min

and for experimental run no. 5:

- process gas: helium + oxygen (molar fractions 90% and 10%, respectively)
- flow rate: $6 \text{ Pa} \cdot \text{m}^3 \cdot \text{s}^{-1}$
- pressure: 260 Pa
- treatment time: 30 min

	exp. no. 4		exp. no. 5	
	C	O	C	O
as received	1.2	1	1.2	0.7
position 0	1.7	14.8	0.9	5.1
position 1	1.4	3.8	0.7	4.1
position 2	1.2	3.2	0.7	3.7
position 3	1.7	2.8	0.8	3.1

Table 5.1: Layer thickness (in nm) from Auger depth profiles

Auger spectra of run no. 4 are shown in figure 5.7 on page 64. Figure 5.8 on page 65 shows the surface composition (from both runs) derived from Auger analysis.

For each sample, Auger depth profiles have also been recorded and the results of these measurements are summarised in table 5.1.

In addition, X-ray photo-electron spectra, recorded from the samples “as received” and “position 1” of experimental run no. 4, are displayed in figures 5.9, 5.10, and 5.11 on pages 66–68.

Quoting from [89] for experimental run no. 4:

The as received sample is similar to the previous “as received”. The sample at position 0 exhibits a low amount of impurities and a large thickness of oxide. The oxide is probably produced by O₂ plasma, which can reach this surface in line-of-sight to the source.
...

No particular impurities appear by going from sample in position 1 to 3, and in particular no C increase is observed. The samples are supposed to be exposed only to O radicals and are all equally oxidised, however with a thinner oxide layer than for position 0, but a thicker layer than for the “as received” sample. Indeed, XPS analysis performed on the surface of position 1 reveals that the oxide consists essentially of CuO and is different from the native oxide on the “as received sample”, which is close to Cu₂O. This can be concluded both from the occurrence in the spectrum of the sample at position 1 of two satellite-peaks in the Cu2p spectrum and from a pronounced O1s component at a binding energy of 529.7 eV, which is typical of CuO (530.5 eV for Cu₂O and 529.6 eV for CuO from literature).

Experimental run no. 5 gives essentially the same results but the reduction of C and the thickness of O are less marked than in the case of the argon–oxygen treatment.

5.3.4 Experimental run no. 6

For this experiment the samples (as before, pre-treated by SUBU) have been heavily contaminated with hydrocarbons (by immersing them into pump oil followed by superficial cleaning with an alcohol soaked handkerchief). Afterwards these samples have been treated with oxygen radicals using the following treatment parameters:

- process gas: argon + oxygen (molar fractions 90% and 10%, respectively)
- flow rate: $8 \text{ Pa} \cdot \text{m}^3 \cdot \text{s}^{-1}$
- pressure: 400 Pa
- treatment time: 90 min

Results from Auger analysis are summarised in figure 5.12 on page 69. The thickness of the carbon layer has been determined as 13.6 nm for the “as received” sample and 1.3 nm, 12.4 nm, and 28.4 nm for the samples at position 0 ... 2.

Quoting from [89]

The untreated surface exhibits only C, demonstrating the high level of contamination. In contrast, the sample in position 0 is much cleaner and O and Cu signals can be detected. The contamination level is still higher than for the usual “as received” samples and higher than for all samples just cleaned with Ar+O₂ without previous contamination. So the contamination is not completely removed. ...

A continuous C increase is observed by moving from position 0 to 2, and in fact also to position 3, since the contamination was here so thick that the analysis could not be performed. This fact is also confirmed by the thickness of the contamination. ...

5.4 Results from secondary electron yield measurements

Like before, the samples have been pre-treated by SUBU and then treated by oxygen radicals with the following treatment parameters:

- process gas: argon + oxygen (molar fractions 90% and 10%, respectively)
- flow rate: $8 \text{ Pa} \cdot \text{m}^3 \cdot \text{s}^{-1}$
- pressure: 400 Pa
- treatment time: 30 min

The measurement and analysis of the secondary electron yield has been carried out by Bernard Henrist from the LHC vacuum group. The results are summarised in figure 5.13 on page 70. It can be seen that the radical treated samples all have a maximum secondary electron yield that is lower than that of the “as received” sample². This behaviour is in agreement with an earlier work, carried out at the vacuum group [57].

²which has already a lower maximum secondary electron yield than “normal” technical copper surfaces due to the SUBU treatment – cf. figure 2.5 on page 17

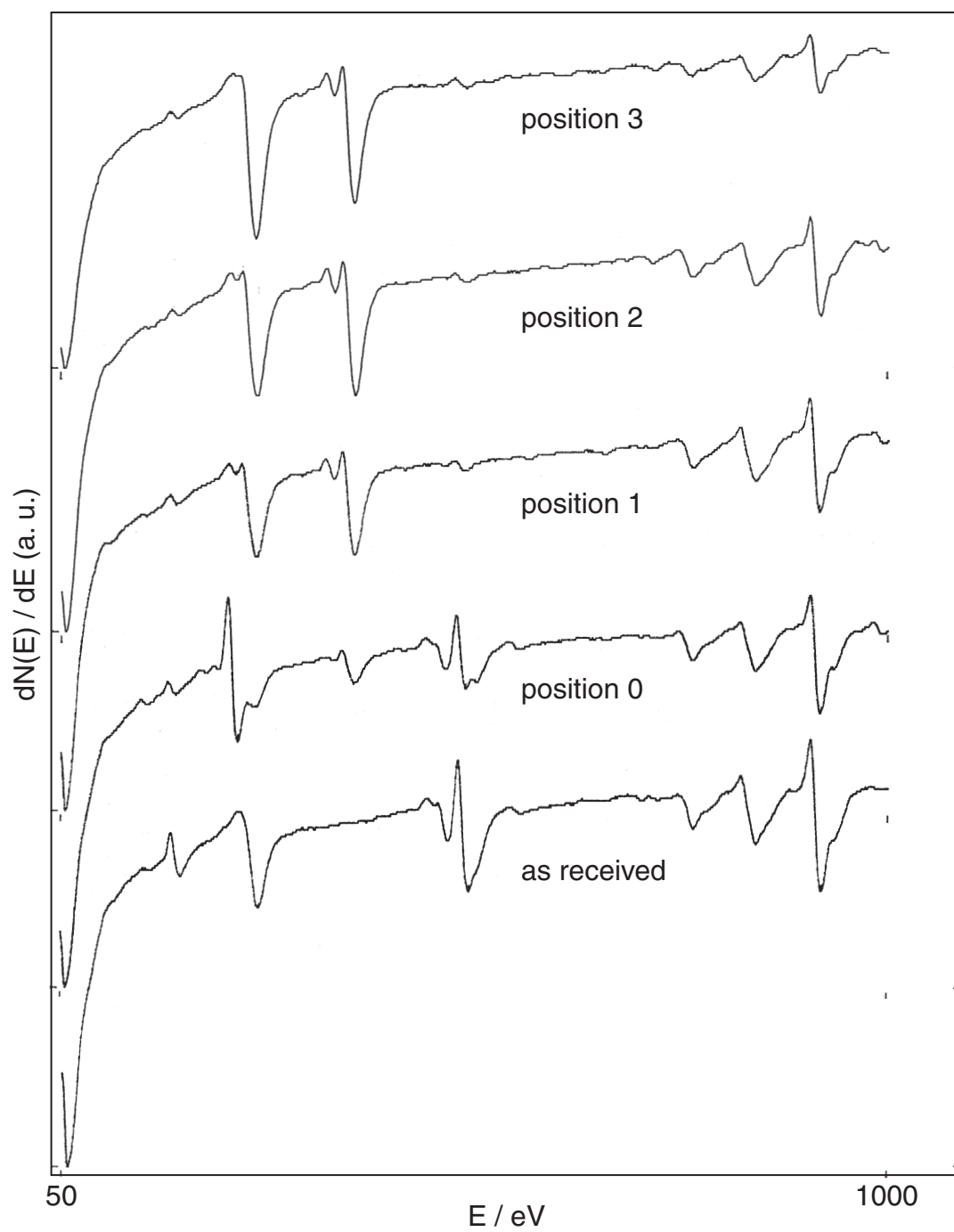


Figure 5.3: Auger electron spectra from experimental run no. 1

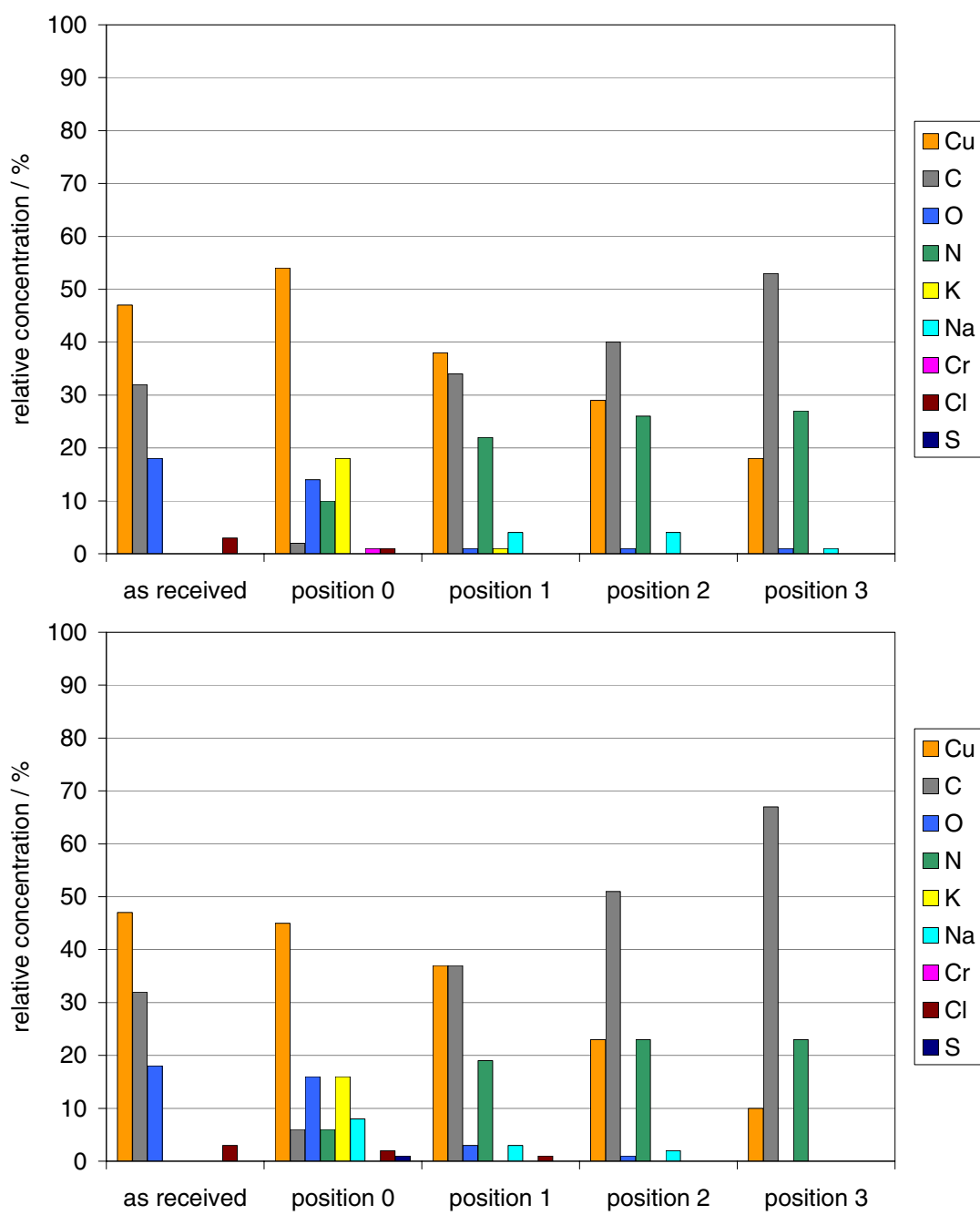


Figure 5.4: Relative concentrations of surface atoms, calculated from Auger electron spectra no. 1 (upper graph) and 1a (lower graph)

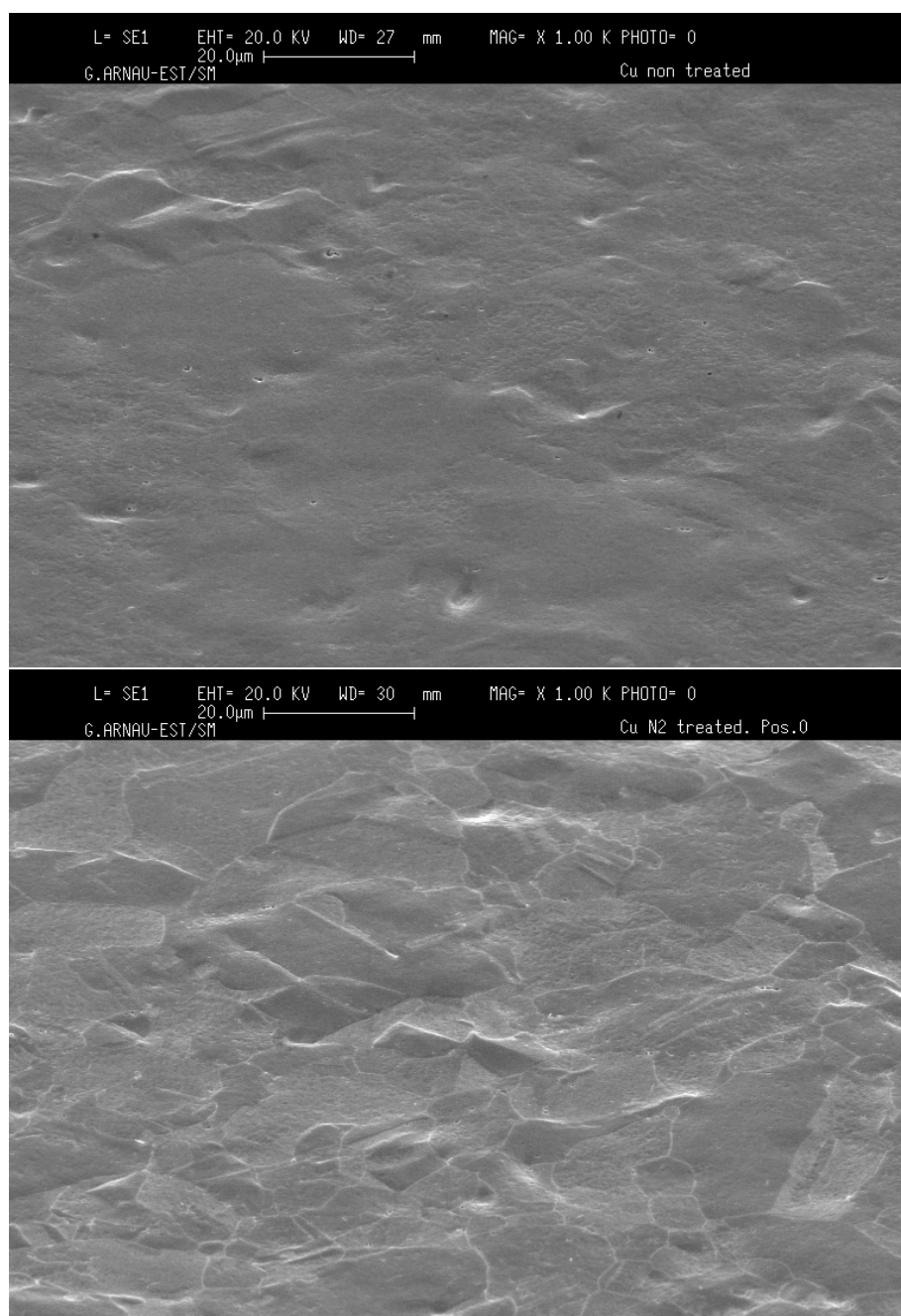


Figure 5.5: SEM images of samples “as received” (upper image) and “position 0” (lower image) from experimental run no. 1

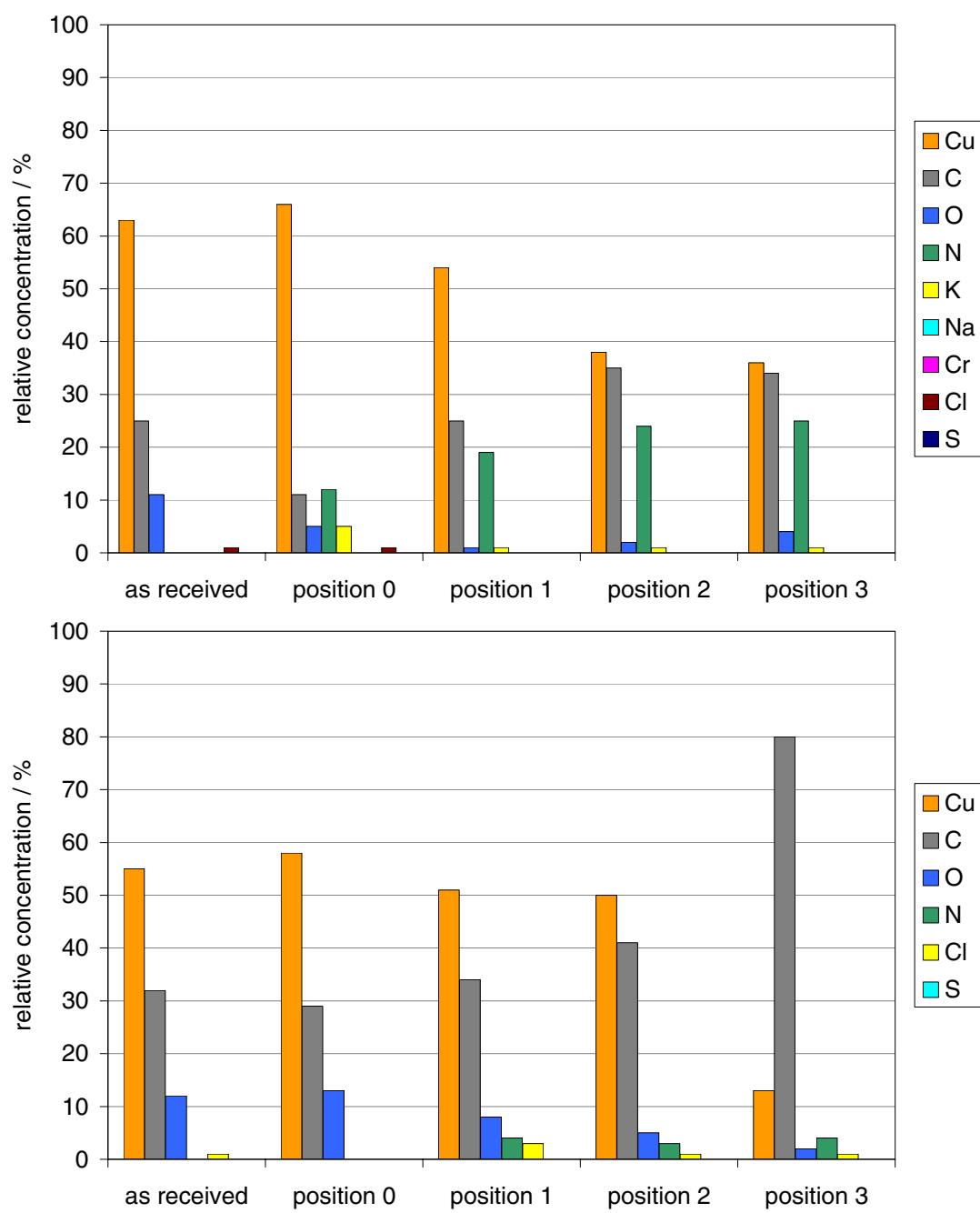


Figure 5.6: Relative concentrations of surface atoms, calculated from Auger electron spectra no. 2 (upper graph) and 3 (lower graph)

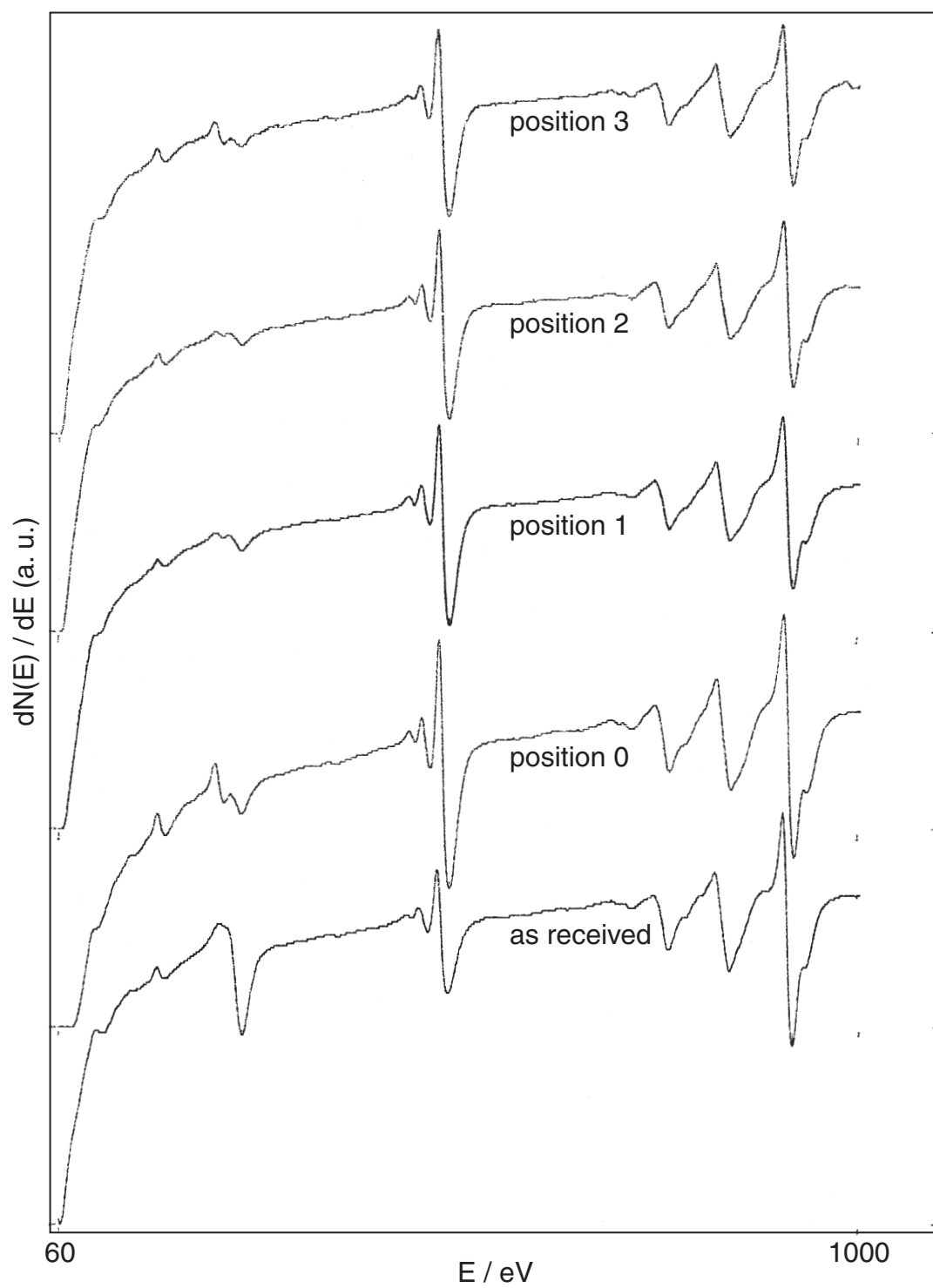


Figure 5.7: Auger electron spectra from experimental run no. 4

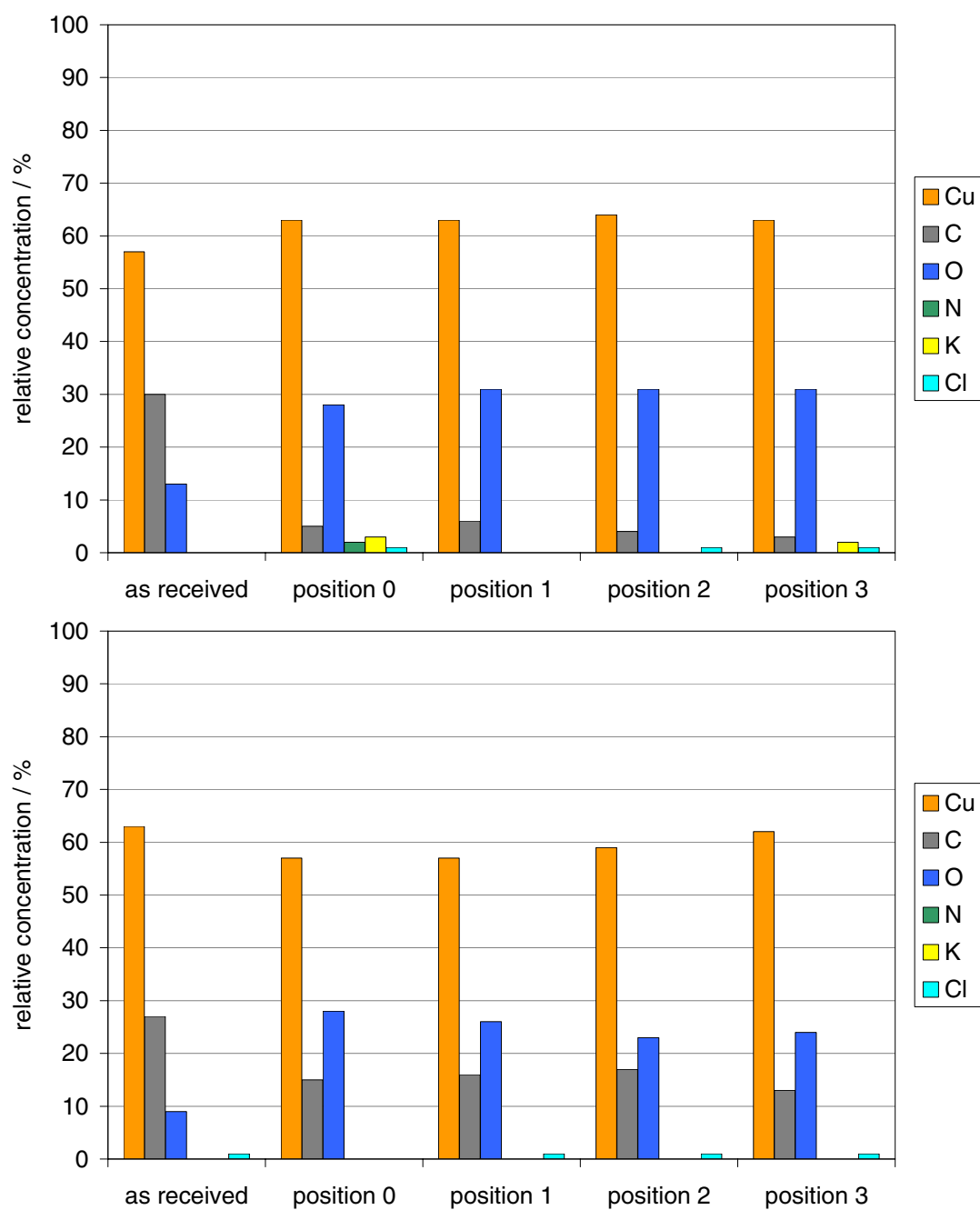


Figure 5.8: Relative concentrations of surface atoms, calculated from Auger electron spectra no. 4 (upper graph) and 5 (lower graph)

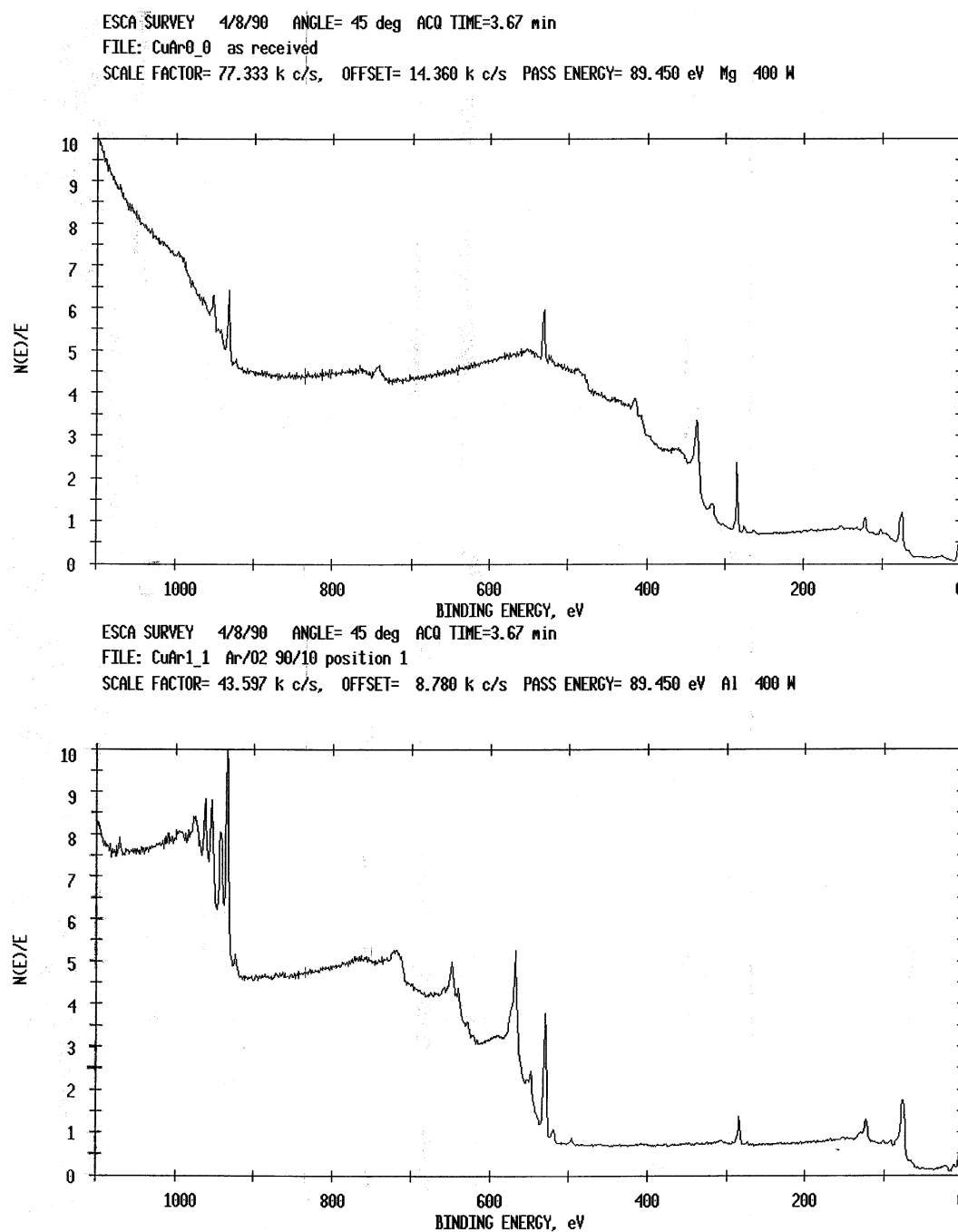


Figure 5.9: X-ray photo-electron spectra (survey scan) of samples “as received” (upper graph) and “position 1” (lower graph) from experimental run no. 4

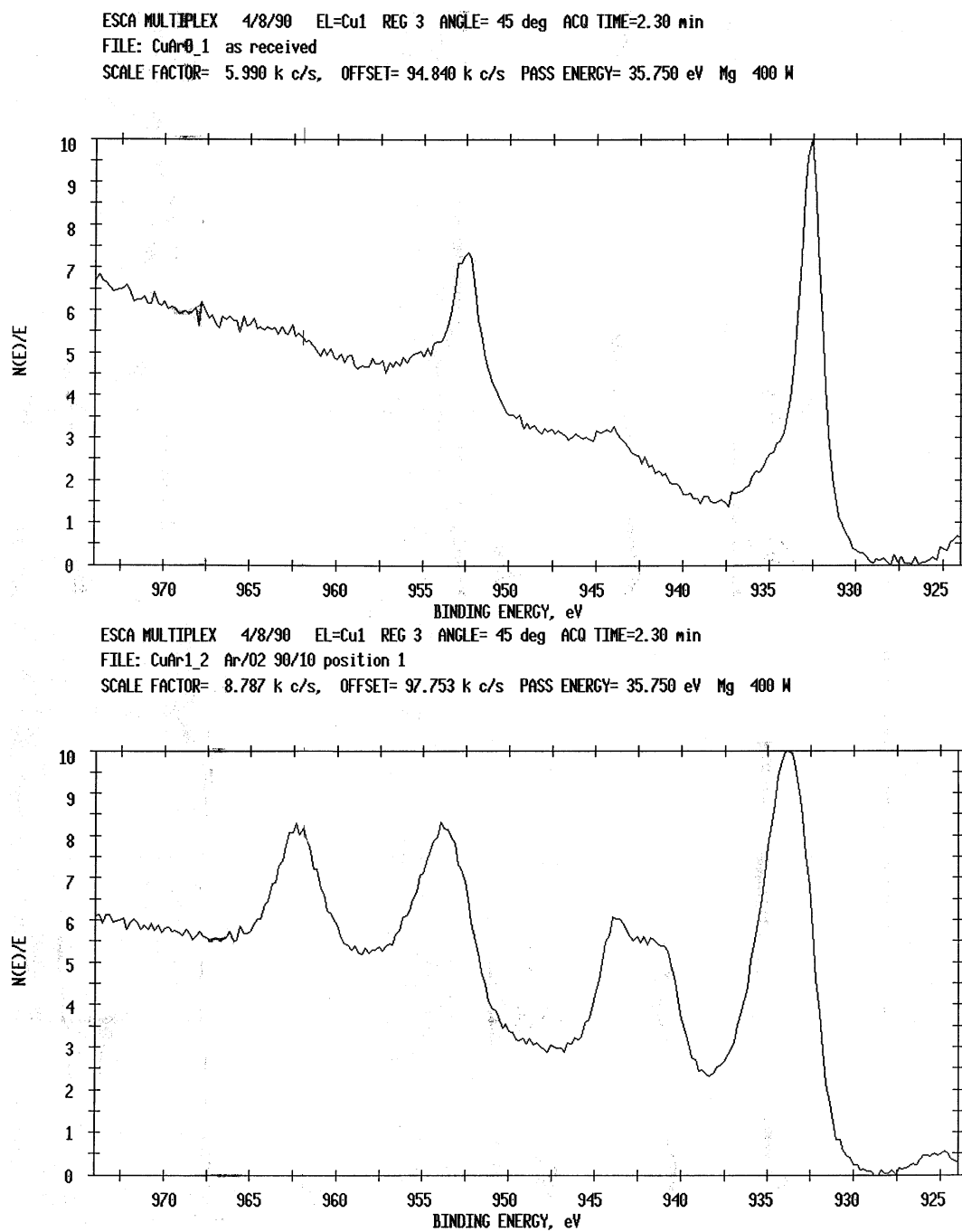


Figure 5.10: X-ray photo-electron spectra of samples (first detail) “as received” (upper graph) and “position 1” (lower graph) from experimental run no. 4

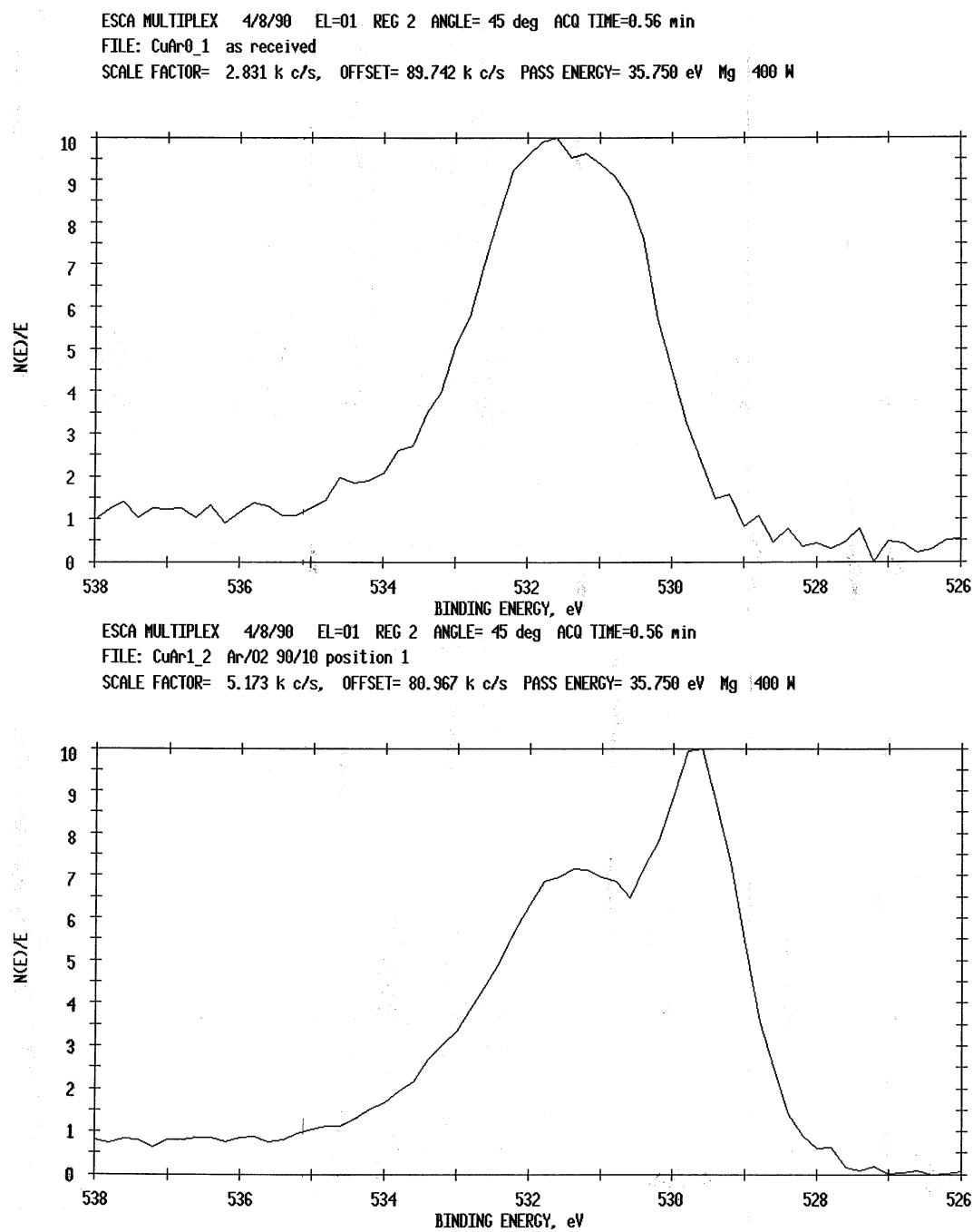


Figure 5.11: X-ray photo-electron spectra of samples (second detail) “as received” (upper graph) and “position 1” (lower graph) from experimental run no. 4

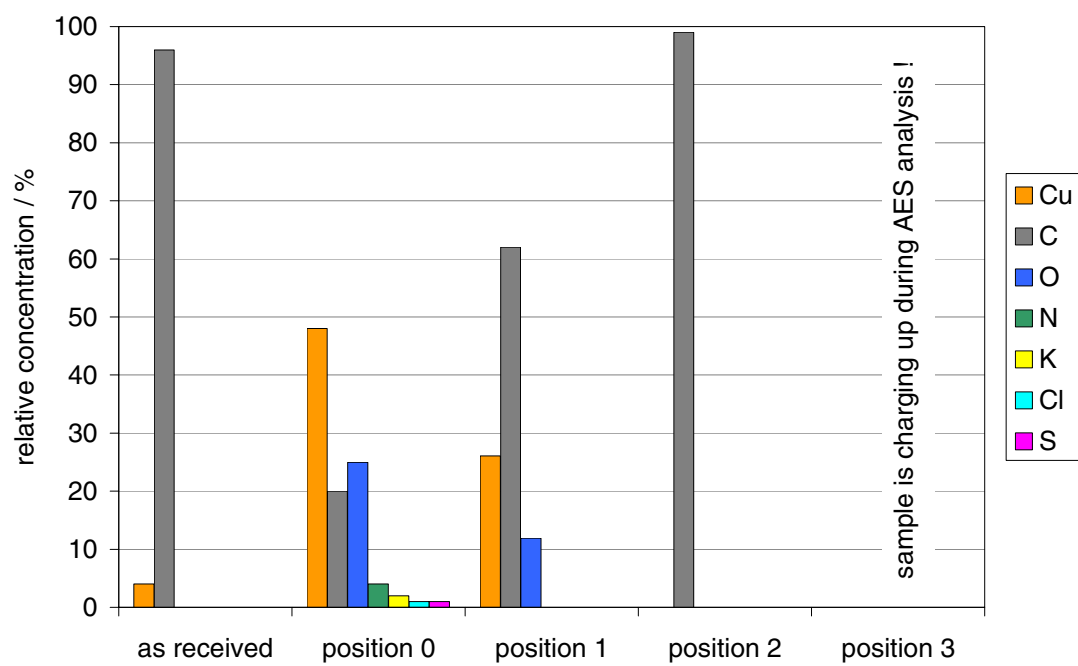


Figure 5.12: Relative concentrations of surface atoms, calculated from Auger electron spectra no. 6

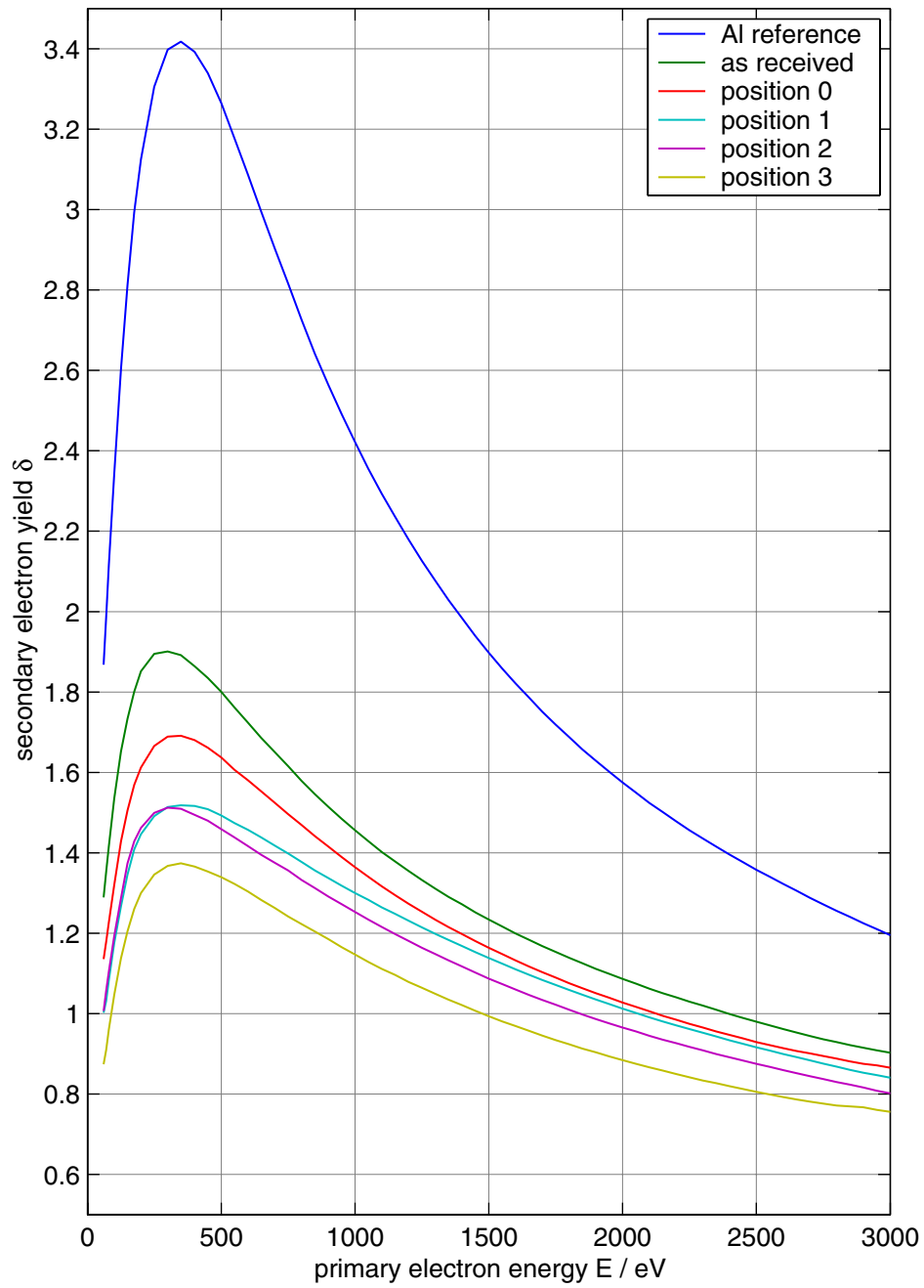


Figure 5.13: Secondary electron yield measurements of oxygen radical treated samples

Part III

Characterisation of the Radical Flow

6 Computer simulation of the radical flow

6.1 Introduction

The purpose of the simulation is to calculate the distribution of radicals in the gas flow downstream of the plasma zone (the *flowing afterglow*). The transport of radicals due to the gas flow itself and due to diffusion is simulated as well as the most important chemical reactions leading to a loss of radicals, in particular the recombination of radicals on solid surfaces.

The underlying physical model consists of a system of partial differential equations describing the transport of mass, energy, momentum and species concentrations in a flowing continuous medium. Furthermore, chemical reactions are included in the model in the form of chemical reaction kinetics. For the purpose of this simulation, it is sufficient to look only at the time independent (the *steady state*) versions of these equations. As it will be shown further down, the equations are non-linear and are linked to each other in a quite complex way, hence, analytical solutions can be found only under very special conditions and by making rigorous simplifications. Usually only approximate solutions can be found by means of numerical solution methods.

It has to be stated at this point, that the numerical calculations of chemical reactions and of flowing media (*computational fluid dynamics*) are gaining more and more interest in research and industry, at least since computing power has become extremely cheap and readily available. Main fields of application are combustion chemistry (fuel combustion, reactor design, optimisation of combustion engines, etc.) and plasma chemistry (plasma-assisted chemical vapour deposition, hard coatings, semiconductor industry, etc.). Several software packages are commercially available which

cover fluid dynamics and/or chemical reaction kinetics.¹ Despite the existence of commercial software products, there are still many reasons to use “hand-made” software, one of which is certainly the usually very high price of a license for such a product.

Methods of numerical chemistry and/or computational fluid dynamics have been applied successfully to study complex plasma chemistry (e.g. [99, 100, 101, 102, 103]) or to study the transport of reactive species in the (flowing) afterglow of a plasma (e.g. [104, 105, 106, 107, 77]).

¹In the domain of chemical reaction design there is, for example, CHEMKIN, originally developed by Sandia National Laboratories (cf. [90]), now distributed by [91], which provides besides a vast chemical kinetics database also code libraries to compute gas-phase, multicomponent transport properties [92], as well as solvers for time dependent and steady state zero and one dimensional problems [93, 94, 95].

In the domain of computational fluid dynamics, there are for example the software packages PHOENIX [96] or StarCD [97], which also support computation of chemical reacting flows. Finally, the general purpose finite element software package ANSYS [98] provides also functionality for computational fluid dynamics.

equation	transported quantity	# of equations
continuity equation	ρ	1
momentum balance	$\rho \vec{u}$	3 components
energy balance	h	1
species transport	$n_k, X_k, \text{ or } Y_k$	K (one for each species)

Table 6.1: Summary of the transport equations

6.2 The model

6.2.1 Description of the model

As already menthioned above, the model is governed by partial differential equations describing the transport of physical quantities in a flowing continuous medium. These equations are summarised in table 6.1.

The variables (which are henceforth called the *flow variables*) that occur in these equations are the temperature T , the pressure p , the mass density ρ , the bulk velocity \vec{u} , the species concentrations n_k , and the enthalpy h , or any combination thereof. There are two flow variables more than there are transport equations, hence two more equations are needed to complete the model. Through the assumption of *thermodynamic equilibrium* these equations are provided by the *equations of state*.

As shown in figure 6.1, a rather simple geometry has been chosen for the model. It represents a long straight tube with circular cross section of constant radius. The plasma zone ends just at the inlet of the tube and a pump is attached at the outlet of the tube. The simulation domain is the cylindrical volume defined by the inlet and the outlet plane and the inner surface of the tube. The co-ordinate system is chosen in such a way, that its origin is located at the centre of the inlet cross section and the z-axis is parallel to the axis of the tube. Boundary conditions are met at the tube wall ($r = R$), at the tube inlet ($z = 0$), and at the tube outlet ($z = L$).

In order to make the equations suitable for a numerical solution algorithm, a discretization scheme has to be developed. This is achieved by means of the *finite volume method* [108]. As indicated in figure 6.2, the whole simulation domain is partitioned into small, but finite-sized volume cells. These cells do not overlap each other and there are no gaps between adjacent cells.

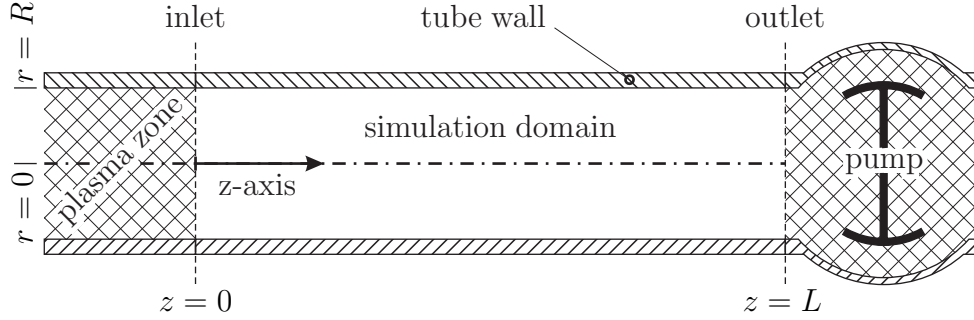


Figure 6.1: Outline of the geometry used for the computer simulation of the flowing afterglow.

Flow variables are taken to have constant values within each cell volume (excluding cell faces) and their values are related to the values in neighbouring cells by describing their flux through the cell boundaries. The result of this discretization is a system of difference equations which, in combination with the equations of state, can be solved numerically by a computer using the appropriate algorithm. The solution is a set of spatial distributions for the flow variables.

The following simplifications and assumptions have been made to derive the model's equations:

- The gaseous mixture of radicals and stable molecules acts like a perfect gas in local thermodynamic equilibrium, i.e. the equations of state for an ideal gas can be applied throughout the whole simulation domain.
- The flow is *laminar*. This implies that
 - the mean free path of the gas particles is much smaller than the tube diameter, hence the gas can be treated as a *continuous medium*, and
 - the flow is free of turbulence (*eddy currents*), hence flow variables change their value smoothly over any chosen distance.
- There is no diffusion of gas particles into or out of the tube wall.
- Chemical reactions take place instantaneously. The movement of gas particles during the duration of a chemical reaction can be ignored.
- The gas flow consists only of those species (radicals and stable molecules) that are present at the tube inlet and their (direct) reaction products.

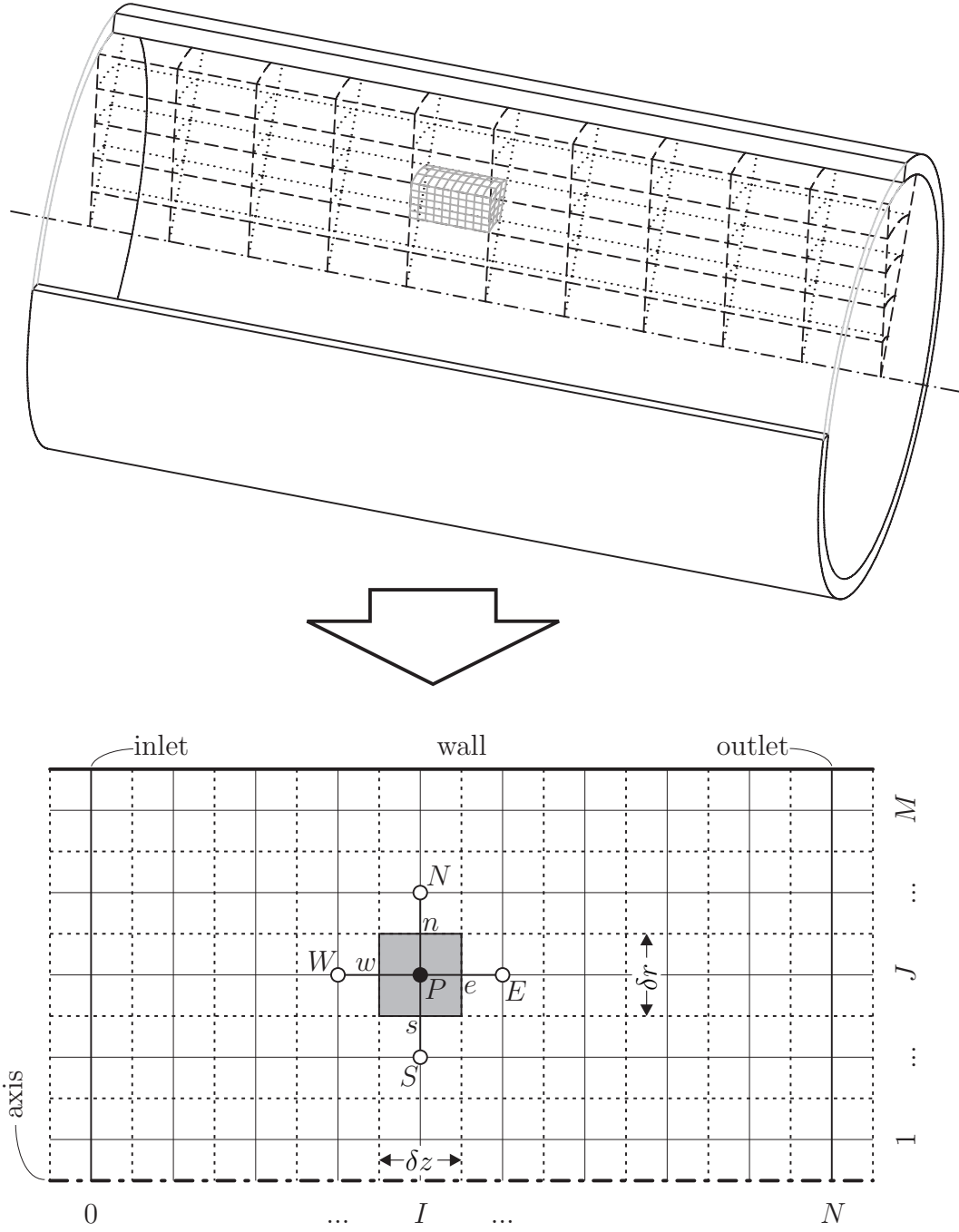


Figure 6.2: Subdivision of the simulation domain into finite volume cells and the grid arrangement derived from this subdivision by connecting the centre point of each cell with the centre point of its nearest neighbours

Desorption of surface contaminants and chemical reaction of radicals with surface contaminants can be neglected.

- The gas flow contains no electrically charged particles.
- Acceleration due to gravity can be ignored.

In the present work, the simulation has been carried out for a binary gas mixture consisting of atomic and molecular nitrogen, using the simple axisymmetrical geometry described above, but the model, which is presented in detail in section 6.2.3, is applicable to any kind of gas mixture (with the limitations of the assumptions made above) and any kind of (Cartesian and non-Cartesian) co-ordinate system.

6.2.2 Equations of state

Ideal gas law

The most common equation of state for ideal gases is the *ideal gas law*, given by

$$p = n R T \quad (6.1)$$

where p is the total pressure, n the molar density, and T the absolute temperature of the gas mixture. R is the universal gas constant.

Having a gas mixture of K species with the molar densities n_k ($k = 1 \dots K$), the partial pressure p_k of each species is given by *Dalton's law*

$$p_k = n_k R T. \quad (6.2)$$

Equations (6.1) and (6.2) hold only if all constituent species have the same temperature. The molar density of the gas mixture is then given by

$$n = \sum_{k=1}^K n_k, \quad (6.3)$$

and the total pressure by

$$p = \sum_{k=1}^K p_k. \quad (6.4)$$

The mole fraction X_k of the k th species is defined by

$$X_k = \frac{n_k}{n} \quad (6.5)$$

and it follows from equation (6.3), that

$$\sum_{k=1}^K X_k = 1. \quad (6.6)$$

The mass density of the gas mixture ρ is given by

$$\rho = \overline{W} n \quad (6.7)$$

where \overline{W} , the molar mass of the gas mixture, is defined by the molar masses W_k of all the species through

$$\overline{W} = \sum_{k=1}^K W_k X_k. \quad (6.8)$$

We can also define the partial mass density of the k th species as

$$\rho_k = W_k n_k \quad (6.9)$$

and the mass fraction of the k th species as

$$Y_k = \frac{\rho_k}{\rho}. \quad (6.10)$$

Since

$$\rho = \sum_{k=1}^K \rho_k \quad (6.11)$$

it follows

$$\sum_{k=1}^K Y_k = 1 \quad (6.12)$$

and

$$Y_k = \frac{W_k}{\overline{W}} X_k. \quad (6.13)$$

Enthalpy

Another equation of state relates the specific enthalpy h to the temperature. For the specific enthalpy of the k th species, h_k it is

$$h_k = h_k^r + \int_{T_r}^T C_{p,k}(\theta) d\theta \quad (6.14)$$

where h_k^r is the specific enthalpy of the k th species at reference conditions ($T = T_r$) and $C_{p,k}$ is the specific constant pressure heat capacity of the k th species. In the temperature range which is of interest in this model, $C_{p,k}$ can be assumed to be constant, hence equation (6.14) simplifies to

$$h_k = h_k^r + C_{p,k}(T - T_r) \quad (6.15)$$

or, with the definition²

$$h_k^0 := h_k^r - C_{p,k} T_r, \quad (6.16)$$

$$h_k = h_k^0 + C_{p,k} T. \quad (6.17)$$

The specific enthalpy of the gas mixture is then given by

$$h = \sum_{k=1}^K Y_k h_k = \sum_{k=1}^K Y_k h_k^0 + \overline{C_p} T \quad (6.18)$$

where

$$\overline{C_p} = \sum_{k=1}^K Y_k C_{p,k} \quad (6.19)$$

is the constant pressure heat capacity of the gas mixture.

6.2.3 Transport equations

Throughout this section, all flow variables like temperature, pressure, or velocity are taken to be functions of the spatial co-ordinates \vec{r} and time t . This dependency will however not be written explicitly for the sake of readability. For example, it is implicitly assumed for the temperature, that $T := T(\vec{r}, t)$.

On the other hand, parameters like heat capacity, thermal conductivity, or viscosity do not depend explicitly on the spatial co-ordinates. However, they

²We could call h_k^0 the “extrapolated” specific enthalpy of the k th species at absolute zero temperature, assuming that the k th species is an ideal gas.

are functions of the flow variables themselves, hence depend indirectly on the spatial co-ordinates and time, a fact which has to be accounted for when performing differentiation or integration.

Since the model has axial symmetry, it is advantageous to use a cylindrical co-ordinate system where each point in space is identified by a radial co-ordinate r , an angular co-ordinate φ ,³ and an axial co-ordinate z . Since the base vectors of such a co-ordinate system are functions of the co-ordinates themselves, special care must be taken when stating physical quantities that are vectors (like the velocity) or tensors (like the stress tensor) and when performing spatial differentiation or integration. The *covariant* formalism (cf. [109], [110], or [111]) provides the mathematical means to deal with these circumstances in a correct way and will be used throughout this section.

As long as only scalar and vector quantities are involved, the “classical” notation, where vector quantities are written as entities (in this work, a symbol with an overset right arrow, e.g. \vec{u}), is preferred over the component notation (the same symbol with a subscript index, e.g. u_i or a superscript index, e.g. u^i), because it is easier to read. However, this notation is unclear when tensor quantities are involved, and component notation is used in this case.

A general overview of the covariant formalism will be given in appendix E, whereas the application of the covariant formalism to cylindrical co-ordinates will be given in appendix F.

Continuity equation

Since mass can neither be generated nor destroyed, the conservation law for mass is simply:

Lemma 1 *The rate of increase of mass inside an arbitrary volume is equal to the net rate of flow of mass into this volume.*

The corresponding equation is

$$\int_V \frac{\partial \rho}{\partial t} dV = - \oint_{\mathcal{R}(V)} \rho \vec{u} \cdot \vec{s} dA \quad (6.20)$$

where $\mathcal{R}(V)$ denotes the boundary surface of the volume V and \vec{s} is the unit length vector normal to the surface and pointing out of V . ρ is the mass

³Though due to the axial symmetry, the flow variables do not depend on φ

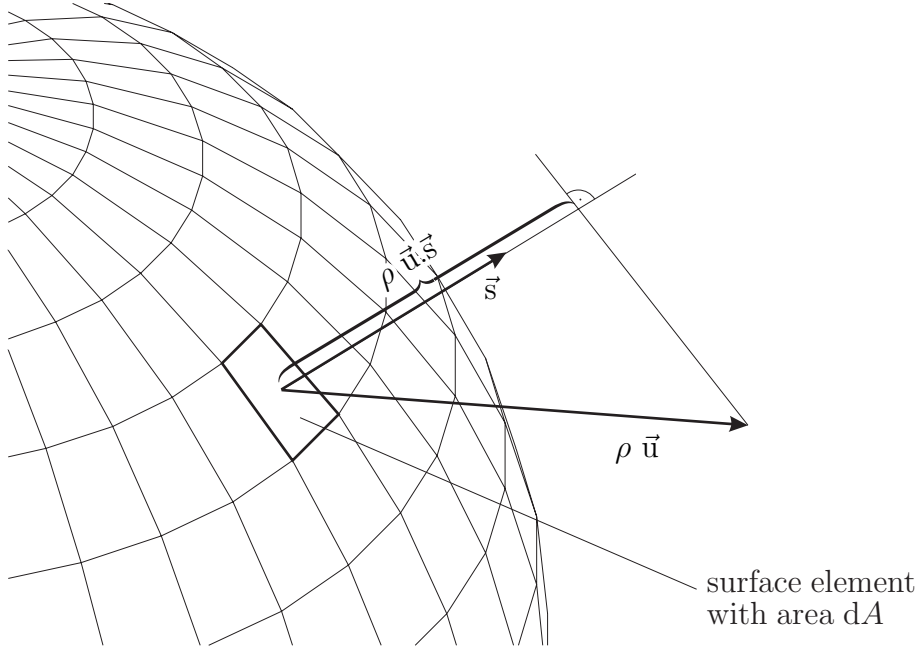


Figure 6.3: Mass flow through an infinitesimal surface element

density and \vec{u} is the bulk velocity⁴ of the gas flow. Figure 6.3 illustrates the right hand side of equation (6.20).

Equation (6.20) is the *integral* form of the (time dependent) mass continuity equation, which can be transformed by virtue of *Gauss' law* into its *differential* form:

$$\int_V \frac{\partial \rho}{\partial t} dV + \int_V \text{div}(\rho \vec{u}) dV = 0 \quad (6.21)$$

or, since the integration volume is arbitrary, simply

$$\frac{\partial \rho}{\partial t} + \text{div}(\rho \vec{u}) = 0. \quad (6.22)$$

The fact that the statements made by equations (6.20) and (6.22) are physically equivalent is most useful to find convenient formulations for the discretization of the continuity equation later on.

⁴The bulk velocity is not to be mixed up with the random thermal velocity which is supposed to cancel out at each point due to the local thermal equilibrium

Species equation

As it was already stated in the previous section, mass can neither be generated nor destroyed. Nevertheless, the gas composition can change. Mass fractions of one or more species can be transformed into mass fractions of other species by means of chemical reactions. In addition, diffusion processes take place due to gradients in the species concentration, resulting in additional fluxes. The balance of any species can be expressed in words as follows:

Lemma 2 *The rate of increase of the number of particles of one species inside an arbitrary volume is equal to the net rate of flow of particles of this species into that volume plus the net rate of production of particles of this species inside that volume due to chemical reactions.*

The equation corresponding to this statement is given (for the k th species) in its integral form by

$$\int_V \frac{\partial n_k}{\partial t} dV = - \oint_{\mathcal{R}(V)} n_k (\vec{u} + \vec{V}_k) \cdot \vec{s} dA + \int_V \dot{\omega}_k dV, \quad (6.23)$$

or in its differential form by

$$\frac{\partial n_k}{\partial t} + \text{div}(n_k \vec{u}) + \text{div}(n_k \vec{V}_k) - \dot{\omega}_k = 0. \quad (6.24)$$

Here, \vec{V}_k is the diffusion velocity and $\dot{\omega}_k$ the net production rate of the k th species due to chemical reactions in the volume. Surface reactions are not accounted for at this point. They enter the model in the form of special boundary conditions (see section 6.2.4).

Equation (6.24) can be transformed into an equation for the mass fraction Y_k by multiplying it with W_k and a bit of rearrangement:

$$\frac{\partial(\rho Y_k)}{\partial t} + \text{div}(\rho Y_k \vec{u}) + \text{div}(\rho Y_k \vec{V}_k) - W_k \dot{\omega}_k = 0. \quad (6.25)$$

Summing up equation (6.25) over all species, we get

$$\frac{\partial \rho}{\partial t} + \text{div}(\rho \vec{u}) + \text{div}\left(\rho \sum_{k=1}^K Y_k \vec{V}_k\right) - \sum_{k=1}^K W_k \dot{\omega}_k = 0. \quad (6.26)$$

Since mass is conserved by chemical reactions

$$\sum_{k=1}^K W_k \dot{\omega}_k = 0 \quad (6.27)$$

and the first two terms of equation (6.26) correspond to the left hand side of the continuity equation (6.22), equation (6.26) reduces to

$$\text{div}(\rho \sum_{k=1}^K Y_k \vec{V}_k) = 0. \quad (6.28)$$

A more stringent requirement for the diffusion velocities as that represented by equation (6.28) is given in literature (cf. [112], [92], [95]) as

$$\sum_{k=1}^K Y_k \vec{V}_k = 0. \quad (6.29)$$

The preceding paragraphs show, that from the $K + 1$ equations defined by (6.22) and (6.25), only K are linear independent. This fact can be accounted for by solving the species equations only for $K - 1$ species, preferably those with the smallest mass fractions, and calculating the mass fraction of the last species by means of equation (6.12).

According to [95], the diffusion velocity is given by

$$\vec{V}_k = -D_k \text{grad} \ln X_k + \vec{\mathcal{W}}_k + \vec{\mathcal{V}} \quad (6.30)$$

where D_k is the mixture averaged diffusion coefficient of the k th species and $\vec{\mathcal{V}}$ is a correction velocity (which is the same for all species, but can vary from one point to the next) that is introduced to satisfy equation (6.29). $\vec{\mathcal{W}}_k$ is the thermal diffusion velocity, which is significant only for very light species (specifically, species having a molar mass of less than 5 kg/kmol, [92]) and will not be considered here. The mixture averaged diffusion coefficient is computed as ([92], [95])

$$D_k = \frac{\sum_{\substack{j=1 \\ j \neq k}}^K W_j X_j}{\bar{W} \sum_{\substack{j=1 \\ j \neq k}}^K X_j / D_{jk}}. \quad (6.31)$$

where the D_{jk} are the binary diffusion coefficients.

In the case of a binary mixture, equation (6.31) gives simply

$$D_1 = \frac{W_2}{W} D_{12} \quad \text{and} \quad D_2 = \frac{W_1}{W} D_{12} \quad (6.32)$$

and the correction velocity $\vec{\mathcal{V}}$ is equal to zero:

$$\begin{aligned} \vec{\mathcal{V}} &= \sum_{k=1}^K Y_k D_k \text{grad} \ln X_k = \\ &= \frac{W_1}{W} X_1 \frac{W_2}{W} D_{12} \frac{\text{grad} X_1}{X_1} + \frac{W_2}{W} X_2 \frac{W_1}{W} D_{12} \frac{\text{grad} X_2}{X_2} = \\ &= \frac{W_1 W_2}{W^2} D_{12} \text{grad}(X_1 + X_2) = 0. \end{aligned} \quad (6.33)$$

Equation (6.24) can be written in the case of a binary mixture in the more familiar form

$$\frac{\partial(n X_1)}{\partial t} + \text{div}(n X_1 \vec{u}) - \text{div}(n D_1 \text{grad} X_1) - \dot{\omega}_1 = 0 \quad (6.34)$$

which is a second order partial differential equation for the mole fraction of species 1 (usually the radical). X_2 is then calculated by means of equation (6.6). Equation (6.34) corresponds to the *diffusion equation* according to *Fick's law*. Since in the case of a binary mixture, there is only one species equation to be solved, we might as well omit the subscript index and write

$$\frac{\partial(n X)}{\partial t} + \text{div}(n X \vec{u}) - \text{div}(n D \text{grad} X) - \dot{\omega} = 0. \quad (6.35)$$

In the case of the binary mixture of nitrogen radicals and nitrogen molecules, the most significant chemical reaction is a third order recombination reaction of the form



The production rate of nitrogen molecules in this reaction is given by

$$\dot{\omega}_{\text{N}_2} = k_3 (n X)^2 n \quad (6.37)$$

and since there are 2 nitrogen radicals destroyed for each produced nitrogen molecule, the production rate for radicals follows as

$$\dot{\omega} = -2 \dot{\omega}_{\text{N}_2} = -2 k_3 (n X)^2 n. \quad (6.38)$$

Parameter	Value	Unit
A	1.38×10^{-33}	$\text{cm}^6 \cdot \text{molecule}^{-2} \cdot \text{s}^{-1}$
A	500	$\text{m}^6 \cdot \text{mol}^{-2} \cdot \text{s}^{-1}$
E_a	4182 ± 1255	$\text{J} \cdot \text{mol}^{-1}$

Table 6.2: Arrhenius parameters for the third order recombination of nitrogen radicals

The rate constant k_3 is can be written in the usual Arrhenius form as

$$k_3 = A e^{E_a/RT}. \quad (6.39)$$

The values for the parameters A and E_a have been found in [113] and are listed in table 6.2.

Momentum equation

The balance of momentum in an arbitrary volume can be expressed in words like follows

Lemma 3 *The rate of increase of momentum inside an arbitrary volume is equal to the net rate of flow of momentum into this volume plus the sum of all forces acting on this volume.*

Two types of forces can be distinguished:

- surface forces
 - pressure force
 - viscous force
- body forces
 - gravity force
 - electromagnetic force
 - centrifugal force
 - Coriolis force

None of the body forces are of relevance for this model (acceleration due to gravity is neglected, there are no electromagnetic fields and no rotating parts) but surface forces have to be taken into account.

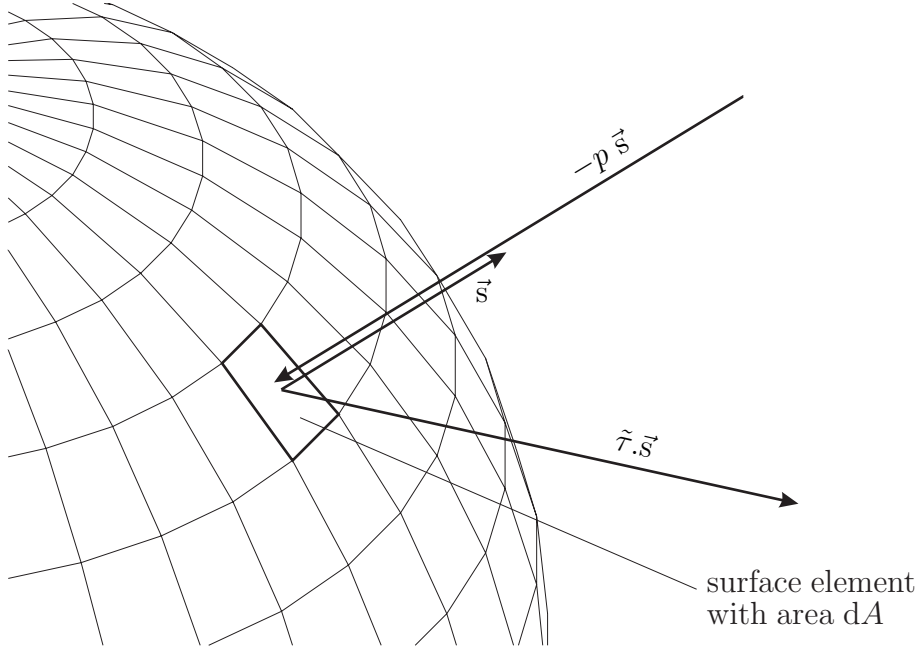


Figure 6.4: Forces acting on an infinitesimal surface element.

The pressure force is characterised by the (scalar) gas pressure p . It is always parallel to the surface normal and directed into the volume. On the other hand, the viscous force is characterised by the stress tensor $\tilde{\tau}$ and can have a component perpendicular to the surface as well as parallel to the surface (cf. *elongation* and *shear*). The two types of surface forces, pressure and viscous force are depicted in figure 6.4.

With the absence of body forces, the momentum balance is governed by

$$\int_V \frac{\partial(\rho u^i)}{\partial t} dV = - \oint_{\mathcal{R}(V)} \rho u^i u^j s_j dA - \oint_{\mathcal{R}(V)} p s^i dA + \oint_{\mathcal{R}(V)} \tau^{ij} s_j dA \quad (6.40)$$

or

$$\frac{\partial(\rho u^i)}{\partial t} + (\rho u^i u^j)|_j = -p|_i + \tau^{ij}|_j. \quad (6.41)$$

Again, equations (6.40) and (6.41) are the integral and differential representation of the same physical fact. Only this time, as opposed to the previous sections, the equations are written down using component notation.⁵

⁵In fact, equation (6.41) could also be written using classical vector notation: $\frac{\partial(\rho \vec{u})}{\partial t} + \text{div}(\rho \vec{u} \circ \vec{u}) = -\text{grad } p + \text{div } \tilde{\tau}$, where $\vec{a} \circ \vec{b}$ denotes the dyadic product of two vectors \vec{a} and \vec{b} and $\text{div } \tilde{c} = c^{ij}|_j \vec{g}_i$ is the “divergence” of a tensor \tilde{c}

Applying *Newton's law of viscosity*, which relates rates of deformation and viscous stresses in a linear way, it can be written for the components of the stress tensor (cf. [108], p. 22 or [110], ch. 6)

$$\tau_{ij} = \tau_{ji} = \mu (u_i|_j + u_j|_i) + \hat{\mu} g_{ij} u^k|_k \quad (6.42)$$

where μ is the *dynamic viscosity* and $\hat{\mu}$ the *second viscosity*. Not much data are available on the second viscosity, but according to [108], for gases it is usually assumed that

$$\hat{\mu} = -\frac{2}{3} \mu \quad (6.43)$$

Substituting equation (6.42) into equation (6.41) results in a set of three second order partial differential equations for the velocity components

$$\frac{\partial(\rho u^i)}{\partial t} + (\rho u^i u^j)|_j = -p|_i + (\mu (u^i|_j + u^j|_i) + \hat{\mu} g^{ij} u^k|_k)|_j. \quad (6.44)$$

Equations (6.44) are also known as the *Navier-Stokes equations*.

Energy equation

The balance of energy in an arbitrary volume can be expressed in words as follows

Lemma 4 *The rate of increase of the energy inside an arbitrary volume is equal to the net rate of flow of energy into this volume plus the net rate of work done by all the forces acting on the volume.*

The corresponding mathematical formulation is given by

$$\begin{aligned} \int_V \frac{\partial \rho e}{\partial t} dV = & - \oint_{\mathcal{R}(V)} \rho e u^j s_j dA - \oint_{\mathcal{R}(V)} q^i s_i dA - \\ & - \oint_{\mathcal{R}(V)} p u^i s_i dA + \oint_{\mathcal{R}(V)} \tau^{ij} u_i s_j dA \end{aligned} \quad (6.45)$$

or by

$$\frac{\partial \rho e}{\partial t} + (\rho e u^i)|_i = -q^i|_i - (p u^i)|_i + (\tau^{ij} u_i)|_j \quad (6.46)$$

where e is the *specific total energy* and \vec{q} is the *density of the heat flux*, caused by heat conduction and particle diffusion. The flow of energy caused by the

motion of the gas mixture itself is described in the first term on the right hand side of equation (6.45) and by the second term on the left hand side of equation (6.46), respectively. The last two terms on the right hand sides of equations (6.45) and (6.46) describe the rate of work done by the pressure and viscous force.

The specific total energy is the sum of the specific internal energy and the specific kinetic energy

$$e = e_{int} + e_{kin} = e_{int} + \frac{1}{2} u^i u_i \quad (6.47)$$

and the kinetic energy term can be eliminated from equation (6.46) by means of the momentum equations (6.41),⁶ resulting in

$$\frac{\partial \rho e_{int}}{\partial t} + (\rho e_{int} u^i)|_i = -q^i|_i - p(u^i|_i) + \tau^{ij}(u_i|_j). \quad (6.48)$$

The last term on the right hand side of equation (6.48) represents a source of internal energy due to viscous friction and is usually called the *dissipation function* and denoted by Φ

$$\Phi = \tau^{ij}(u_i|_j) = \mu(u^i|_j + u^j|_i)u_i|_j + \hat{\mu}(u^i|_i)^2. \quad (6.49)$$

As already mentioned above, two effects contribute to the heat flux density \vec{q} : the heat conduction due to temperature gradients (cf. *Fourier's law*) and the transport of heat due to particle diffusion.

$$\vec{q} = -\lambda \text{grad } T + \rho \sum_{k=1}^K Y_k \vec{V}_k h_k. \quad (6.50)$$

Here, λ is the thermal conductivity of the gas mixture and h_k is the specific enthalpy of the k th species. The \vec{V}_k are the diffusion velocities already mentioned above.

The specific internal energy can be eliminated by introduction of the specific enthalpy due to the relation $h = e_{int} + p/\rho$. Together with equations (6.49) and (6.50), equation (6.48) becomes (now using classical notation, since there

⁶By summing up equations (6.41) multiplied by u_i and subtracting the result from equation (6.46)

are no more tensor expressions)

$$\begin{aligned} \frac{\partial(\rho h)}{\partial t} + \text{div}(\rho h \vec{u}) &= \frac{\partial p}{\partial t} + \vec{u} \cdot \text{grad } p + \text{div}(\lambda \text{ grad } T) - \\ &\quad - \text{div}\left(\rho \sum_{k=1}^K Y_k \vec{V}_k h_k\right) + \Phi. \end{aligned} \quad (6.51)$$

Finally, by means of equations (6.17) and (6.18), and after considerable algebra,⁷ equation (6.51) becomes a second order partial differential equation for the absolute temperature T

$$\begin{aligned} \frac{\partial(\rho \overline{C_p} T)}{\partial t} + \text{div}(\rho \overline{C_p} T \vec{u}) + \text{div}\left(\rho \sum_{k=1}^K Y_k \vec{V}_k C_{p,k} T\right) &= \\ = \text{div}(\lambda \text{ grad } T) + \frac{\partial p}{\partial t} + \vec{u} \cdot \text{grad } p - \sum_{k=1}^K h_k^0 W_k \dot{\omega}_k + \Phi. \end{aligned} \quad (6.52)$$

Equation (6.52) is henceforth called the (time dependent) *temperature equation*.

6.2.4 Boundary conditions for a cylindrical tube

The solution of the differential equations described in the previous section is not possible without the appropriate boundary conditions. In this section, boundary conditions for the flow variables will be specified and/or derived for a cylindrical pipe, i.e. the geometry described in section 6.2.1. A special notation will be used for the velocity components: the radial component of \vec{u} is denoted by v and the axial component by u (see also section 6.3.1).

Temperature

The appropriate boundary conditions for the temperature are

$$\frac{\partial T}{\partial r}|_{r=0} = 0 \quad (\text{axis}), \quad (6.53)$$

$$T(R, z) = T_{\text{wall}}(z) \quad (\text{wall}), \quad (6.54)$$

$$T(r, 0) = T_{\text{in}}(r) \quad (\text{inlet}), \quad (6.55)$$

⁷By summing up equations (6.25), multiplied by h_k^0 , and subtracting the result from equation (6.51)

or alternatively

$$\frac{\partial T}{\partial z}\bigg|_{z=0} = 0 \quad (\text{inlet}), \quad (6.56)$$

and

$$\frac{\partial T}{\partial z}\bigg|_{z=L} = 0 \quad (\text{outlet}). \quad (6.57)$$

The axis boundary condition (6.53) is necessary to ensure axial symmetry and continuous behaviour of the temperature across the tube axis.

Velocity and pressure

With the arguments of symmetry and continuity, boundary conditions for pressure and velocity can be specified at the tube axis as

$$\frac{\partial p}{\partial r}\bigg|_{r=0} = 0, \quad (6.58)$$

$$v(0, z) = 0, \quad (6.59)$$

and

$$\frac{\partial u}{\partial r}\bigg|_{r=0} = 0. \quad (6.60)$$

At the tube wall, the appropriate boundary conditions are

$$v(R, z) = 0 \quad (\text{no-penetration condition}), \quad (6.61)$$

$$u(R, z) = 0 \quad (\text{no-slip condition}), \quad (6.62)$$

and

$$\frac{\partial p}{\partial r}\bigg|_{r=R} = 0. \quad (6.63)$$

The pressure is fixed at the inlet and the outlet of the tube

$$p(r, 0) = p_{in} \quad (6.64)$$

and

$$p(r, L) = p_{out} \quad (6.65)$$

with $p_{in} > p_{out}$. Due to the pressure – velocity coupling caused by the Navier-Stokes equations, the velocity field will adjust itself to the pressure gradient introduced by the boundary conditions (6.64) and (6.65). In addition, the continuity equation has to be respected at the inlet and outlet of the tube, hence boundary conditions for the velocity have to be chosen accordingly. If we set the radial velocity components to zero at the inlet and the outlet

$$v(r, 0) = 0 \quad (6.66)$$

and

$$v(r, L) = 0, \quad (6.67)$$

then the continuity equation reduces at the inlet and outlet to

$$\frac{\partial \rho u}{\partial z}|_{z=0} = 0 \quad \text{and} \quad \frac{\partial \rho u}{\partial z}|_{z=L} = 0 \quad (6.68)$$

and boundary conditions for the axial velocity component can be derived from equations (6.68) as

$$\frac{\partial u}{\partial z}|_{z=0} = -\frac{\partial \ln \rho}{\partial z}|_{z=0} u(r, 0) \quad (6.69)$$

and

$$\frac{\partial u}{\partial z}|_{z=L} = -\frac{\partial \ln \rho}{\partial z}|_{z=L} u(r, L). \quad (6.70)$$

Boundary conditions of the form of equations (6.69) and (6.70) are called *boundary conditions of the third kind*.

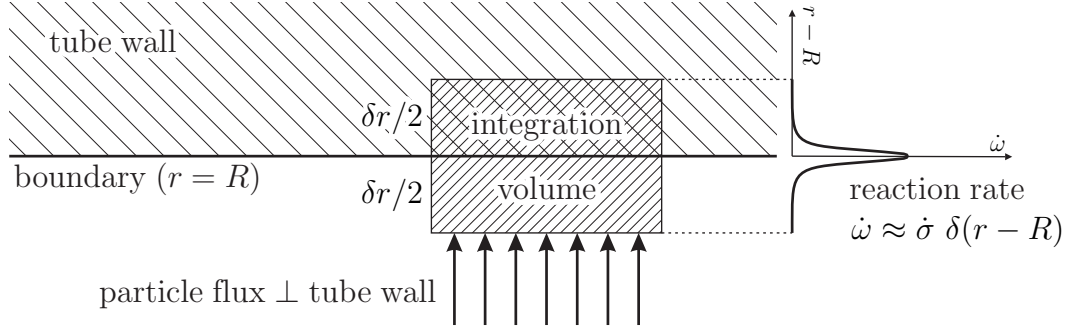


Figure 6.5: Scheme to derive the wall boundary condition for the radical mole fraction

Radical mole fraction

Boundary conditions for the radical mole fraction can be specified as

$$\frac{\partial X}{\partial r}|_{r=0} = 0 \quad (\text{axis}), \quad (6.71)$$

$$X(r, 0) = X_{in}(r) \quad (\text{inlet}), \quad (6.72)$$

and

$$\frac{\partial X}{\partial z}|_{z=L} = 0 \quad (\text{outlet}). \quad (6.73)$$

A wall boundary condition for the radical mole fraction can be obtained using the following procedure which is visualised in figure 6.5:

- In equation (6.95), replace the source term $\dot{\omega}$ by $\dot{\sigma} \delta(r - R)$, with $\delta(x)$ being the Dirac-delta function.
- Integrate this equation over a volume cell that crosses the wall boundary.
- Let $\delta r \rightarrow 0$.

This procedure may be summarised by the following equation⁸

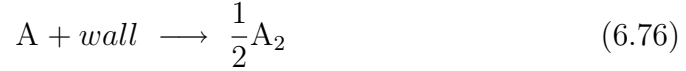
$$\lim_{\delta r \rightarrow 0} (n D \frac{\partial X}{\partial r} r \delta \varphi \delta z|_{R-\delta r/2}) = \lim_{\delta r \rightarrow 0} \int_{\delta V} \dot{\sigma} \delta(r - R) r dr d\varphi dz. \quad (6.74)$$

⁸The convective fluxes amount to zero because of the boundary conditions for u and v , equations (6.62) and (6.61), respectively, and because of the limit $\delta r \rightarrow 0$. The diffusive fluxes parallel to the tube wall also amount to zero because of $\delta r \rightarrow 0$.

After evaluation of the integral⁹ and calculation of the limit, we get

$$(n D \frac{\partial X}{\partial r})|_{r=R} = \dot{\sigma}. \quad (6.75)$$

In the case of a binary mixture of radicals and molecules, the predominant surface reaction is a first order recombination (cf. [106, 114, 105, 115, 77]) of the form



where A stands for the radical and A₂ for the molecule. The surface production rate of such a reaction is proportional to the concentration of radicals at the wall

$$\dot{\sigma} = -k_1 n X. \quad (6.77)$$

where k_1 , the *rate constant*, is usually given in terms of the mean thermal velocity $\bar{v} = \sqrt{8kT/\pi m}$ (k is the Boltzmann constant, T the absolute temperature, and m the mass of the radical) and a *recombination probability* γ [107, 115] as

$$k_1 = \frac{\bar{v}}{4} \frac{\gamma}{1 - \frac{\gamma}{2}}. \quad (6.78)$$

Using equations (6.77) and (6.78), equation (6.75) can be written as

$$D \frac{\partial X}{\partial r}|_{r=R} = \frac{\bar{v}}{4} \frac{\gamma}{1 - \frac{\gamma}{2}} X(R, z). \quad (6.79)$$

Equation (6.79) represents a boundary condition of the third kind for the radical mole fraction (cf. [116, 117, 118]). An alternative way to derive a relationship between diffusion and surface reaction and a more detailed discussion on surface recombination processes is given in chapter 7.

⁹The integral in the radial direction is given by $\int_{R-\delta r/2}^{R+\delta r/2} r \delta(r-R) dr = R$

Coefficient	nitrogen atom (N)	nitrogen molecule (N ₂)
<i>A</i>	21.13581	26.092
<i>B</i>	-0.388842	8.218801
<i>C</i>	0.043545	-1.976141
<i>D</i>	0.024685	0.159274
<i>E</i>	-0.025678	0.044434
<i>F</i>	466.311	-7.98923
$\Delta_f H_{298.15}^0$	4.726832×10^5	0

Table 6.3: Coefficients of the Shomate equation for atomic and molecular nitrogen for the range of $298 < T < 6000$

6.2.5 Model parameters for the binary mixture of nitrogen radicals and molecules

Enthalpy and heat capacity

The molar enthalpies of atomic and molecular nitrogen are given in [119] in the form of the so called *Shomate equation*

$$\frac{H^0 - H_{298.15}^0}{\text{kJ} \cdot \text{mol}^{-1}} = A t + B \frac{t^2}{2} + C \frac{t^3}{3} + D \frac{t^4}{4} - E \frac{1}{t} + F - \frac{\Delta_f H_{298.15}^0}{\text{kJ} \cdot \text{mol}^{-1}} \quad (6.80)$$

where H^0 and $H_{298.15}^0$ are the molar enthalpies at the desired temperature and at 298.15 K, respectively, and $\Delta_f H_{298.15}^0$ the *enthalpy of formation* at 298.15 K. t is given by

$$t = \frac{T}{1000K} \quad (6.81)$$

with T being the absolute temperature. The values of the coefficients are given in table 6.3.

In order to get a linear expression for the enthalpy as described in equation (6.17), equation (6.80) is fitted¹⁰ by the expression

$$H^0 - H_{298.15}^0 = C_{p,mol} (T - 298.15) \quad (6.82)$$

for $300 < T < 600$, which is the temperature range of interest in this work. $C_{p,mol}$ is the molar constant pressure heat capacity in $\text{J} \cdot \text{mol}^{-1} \cdot \text{K}^{-1}$. The data and fit functions are illustrated in figure 6.6.

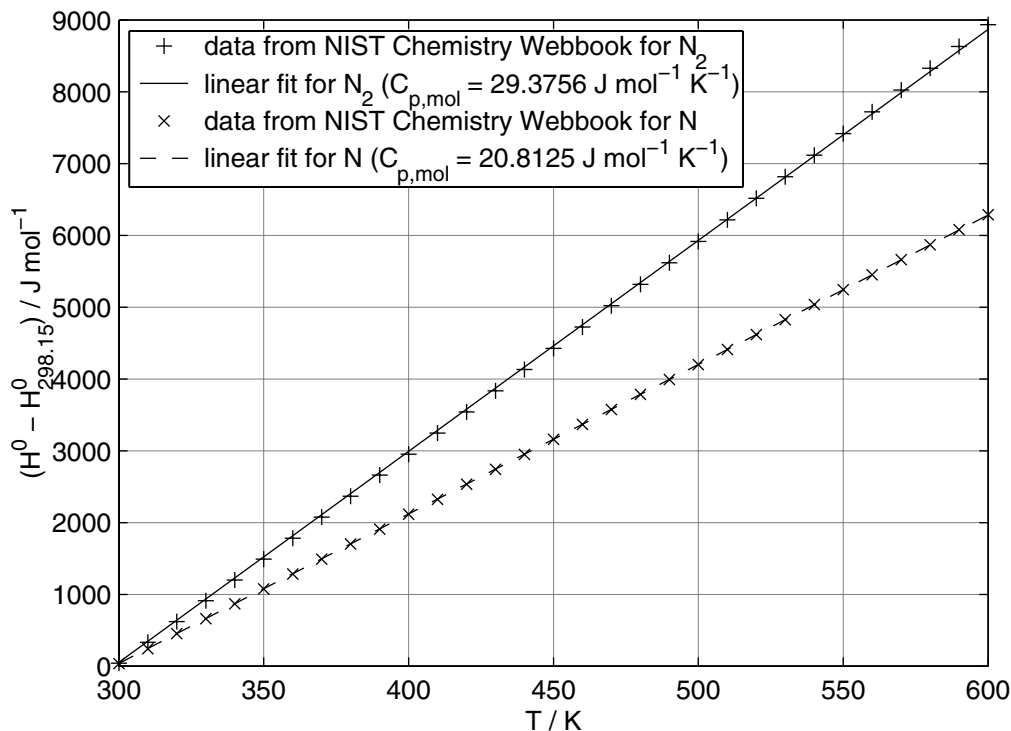


Figure 6.6: Graph of the enthalpy as a function of the temperature

It remains to specify the reference value $H_{298.15}^0$ for the enthalpies of atomic and molecular nitrogen. If we set the reference value for molecular nitrogen to zero, it follows for the reference value for atomic nitrogen

$$H_{298.15,N}^0 = \Delta_f H_{298.15,N}^0 = 4.726832 \times 10^5 \text{ J} \cdot \text{mol}^{-1}. \quad (6.83)$$

The corresponding specific quantities (quantities per kilogram) are calculated by dividing the molar quantities by the molar mass and are summarised in table 6.4.

Transport properties

The diffusion coefficient of nitrogen radicals in nitrogen molecules is derived from an expression given in [76]

$$\frac{D p_0}{\text{cm}^2 \cdot \text{torr} \cdot \text{s}^{-1}} = 2.29 \left(\frac{T}{\text{K}} \right)^{0.8} \quad (6.84)$$

¹⁰in the sense of a linear least squares fit

quantity	N	N ₂	unit
molar mass W	0.01401	0.02801	kg · mol ⁻¹
specific heat capacity C_p	1.4855×10^3	1.0488×10^3	J · kg ⁻¹ · K ⁻¹
reference specific enthalpy h^r	3.3739×10^7	0	J · kg ⁻¹
zero-point specific enthalpy h^0	3.3296×10^7	-3.1269×10^5	J · kg ⁻¹

Table 6.4: Specific thermodynamic quantities for atomic and molecular nitrogen

where p_0 is the *reduced pressure* ($p_0 = p \cdot 273 \text{ K}/T$) and T the absolute temperature.

Conversion of equation (6.84) to SI units gives

$$\frac{D p_0}{\text{m}^2 \cdot \text{Pa} \cdot \text{s}^{-1}} = 2.29 \cdot 10^{-4} \cdot 133 \left(\frac{T}{\text{K}} \right)^{0.8}, \quad (6.85)$$

hence, we can write for the value of the diffusion coefficient in SI units

$$\frac{D}{\text{m}^2 \cdot \text{s}^{-1}} = 1.12 \times 10^{-4} \left(\frac{T}{\text{K}} \right)^{1.8} \left(\frac{p}{\text{Pa}} \right)^{-1}. \quad (6.86)$$

Expressions for the thermal conductivity λ and the viscosity μ of molecular nitrogen are taken from [114]. They are given in SI units as

$$\frac{\lambda}{\text{W} \cdot \text{m}^{-1} \cdot \text{K}^{-1}} = 5.82 \times 10^{-5} \frac{T}{\text{K}} + 8.96 \times 10^{-3} \quad (6.87)$$

and

$$\frac{\mu}{\text{Pa} \cdot \text{s}} = 3.92 \times 10^{-8} \frac{T}{\text{K}} + 9.32 \times 10^{-6} \quad (6.88)$$

The thermal conductivity and viscosity of the gas mixture of nitrogen atoms and molecules are taken to be that of pure molecular nitrogen.

6.3 Numerical solution

6.3.1 Integration of the transport equations over a finite volume cell

After having described the model in a very general way in the preceding sections, the next step is to integrate the model's equations over a finite volume cell. Because of the geometry of the model, it is convenient to use a cylindrical co-ordinate system as described in section 6.2.1. The metric of the cylindrical co-ordinate system is described in appendix F. Furthermore, since the model is symmetrical with respect to the tube axis, all quantities are independent of the angular co-ordinate φ . Finally, we are interested only in the steady state solutions of the equations, hence all time derivatives can be set to zero.

A special notation will be used for convenience for the velocity \vec{u} . The contravariant components of \vec{u} are written as

$$u^i = \begin{pmatrix} v(r, z) \\ 0 \\ u(r, z) \end{pmatrix} \quad (6.89)$$

and, because of the metric of the cylindrical co-ordinate system, the covariant components follow as

$$u_i = \begin{pmatrix} v(r, z) \\ 0 \\ u(r, z) \end{pmatrix}. \quad (6.90)$$

The angular component of \vec{u} is set to zero, because we can assume that the flow field is free of rotation at the tube inlet and there is no net force acting in angular direction.

From here on, the dependency of the flow variables on the co-ordinates will not be written explicitly anymore.

As it is shown in figure 6.7, the shape of a volume cell is chosen in such a way that it reflects the symmetry of the model. It is located around a centre point with the co-ordinates (r_P, z_P) and has a radial spread of δr , an axial spread of δz , and an angular spread of $\delta\varphi$. The subscript letters of the cell face normals indicate the names of the corresponding cell face: north, south, east, west, front, and back.

The cell volume is given by

$$\delta V = r_P \delta r \delta\varphi \delta z \quad (6.91)$$

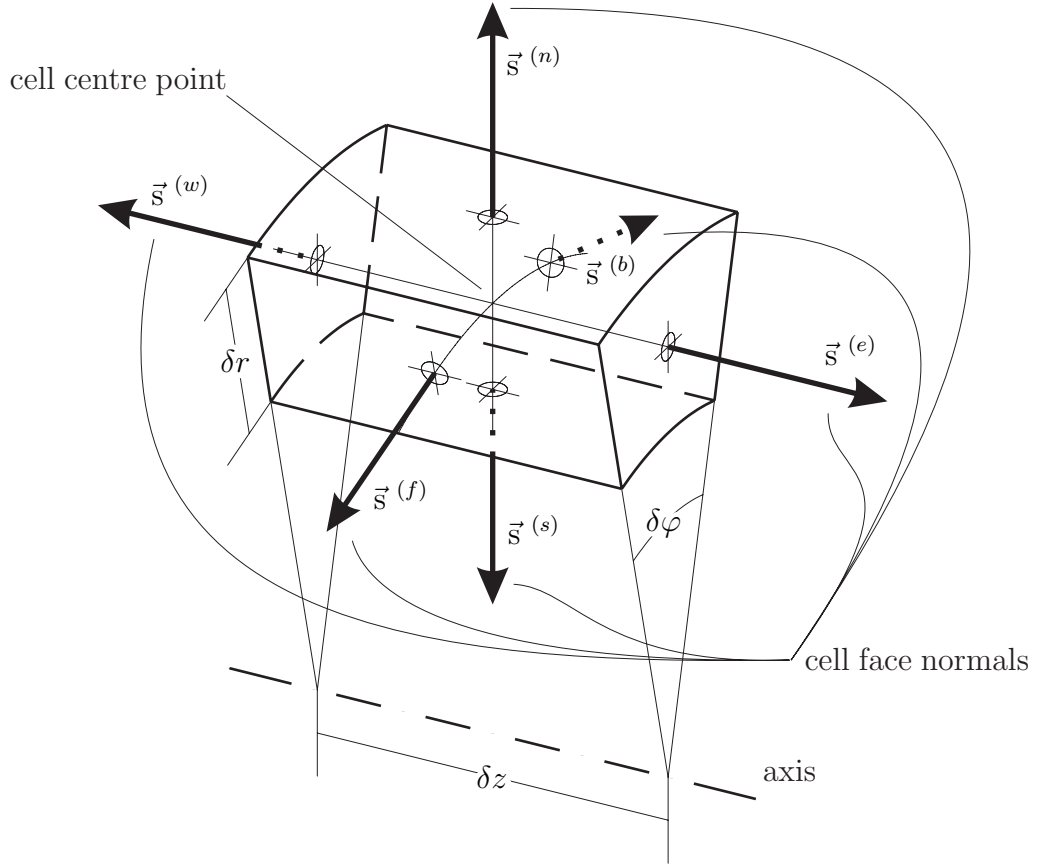


Figure 6.7: Outline drawing of a finite volume cell (a description is given in the text)

and the values of the area of each cell face are given in the third column of table 6.5. The second column of table 6.5 shows the covariant components of the outward directed unit length surface normals as indicated in figure 6.7.

Continuity equation

The continuity equation (6.20) is reduced in the steady state to

$$\oint_{\mathcal{R}(V)} \rho u^i s_i dA = 0. \quad (6.92)$$

Applying equation (6.92) to the finite volume cell and using the special notation

cell face	normal vector	face area
north face	$\vec{s}_i^{(n)} = (1, 0, 0)$	$\delta A^{(n)} = (r_P + \frac{\delta r}{2}) \delta \varphi \delta z$
south face	$\vec{s}_i^{(s)} = (-1, 0, 0)$	$\delta A^{(s)} = (r_P - \frac{\delta r}{2}) \delta \varphi \delta z$
east face	$\vec{s}_i^{(e)} = (0, 0, 1)$	$\delta A^{(e)} = r_P \delta r \delta \varphi$
west face	$\vec{s}_i^{(w)} = (0, 0, -1)$	$\delta A^{(w)} = r_P \delta r \delta \varphi$
front face	$\vec{s}_i^{(f)} = (-\sin \frac{\delta \varphi}{2}, r_P \cos \frac{\delta \varphi}{2}, 0)$	$\delta A^{(f)} = \delta z \delta r$
back face	$\vec{s}_i^{(b)} = (-\sin \frac{\delta \varphi}{2}, -r_P \cos \frac{\delta \varphi}{2}, 0)$	$\delta A^{(b)} = \delta z \delta r$

Table 6.5: The faces of a finite volume cell (a description is given in the text)

for \vec{u} (equation (6.89)) results in

$$\begin{aligned} \int_{(n)} \rho^{(n)} v^{(n)} dA^{(n)} - \int_{(s)} \rho^{(s)} v^{(s)} dA^{(s)} + \\ + \int_{(e)} \rho^{(e)} u^{(e)} dA^{(e)} - \int_{(w)} \rho^{(w)} u^{(w)} dA^{(w)} = 0 \end{aligned} \quad (6.93)$$

where the sub- or superscript letters in parentheses mean “evaluation at the corresponding cell face”. Front and back faces don’t contribute to the integral in equation (6.92) because their surface normals are perpendicular to the velocity vector. Since finite volume cells are assumed to be small enough so that flow variables can be considered constant over each cell face and inside the cell volume (though having different values in each of these domains), integration in equation (6.93) can be performed, resulting in

$$(\rho v \delta A)^{(n)} - (\rho v \delta A)^{(s)} + (\rho u \delta A)^{(e)} - (\rho u \delta A)^{(w)} = 0. \quad (6.94)$$

Species equation

The steady state, integral version of the diffusion equation for radicals (6.35) is given by

$$\oint_{\mathcal{R}(V)} n X u^i s_i dA = \oint_{\mathcal{R}(V)} n D X|^i s_i dA + \int_V \dot{\omega} dV \quad (6.95)$$

Equation (6.95) can be integrated by making the same assumptions as for equation (6.94), leading to

$$\begin{aligned}
& (n v X \delta A)^{(n)} - (n v X \delta A)^{(s)} + (n u X \delta A)^{(e)} - (n u X \delta A)^{(w)} = \\
& = (n D \frac{\partial X}{\partial r} \delta A)^{(n)} - (n D \frac{\partial X}{\partial r} \delta A)^{(s)} + \\
& \quad + (n D \frac{\partial X}{\partial z} \delta A)^{(e)} - (n D \frac{\partial X}{\partial z} \delta A)^{(w)} + \dot{\omega} \delta V. \quad (6.96)
\end{aligned}$$

Approximative expressions can be derived for the gradients of X on the cell faces by developing *Taylor series* for the cell centre point values of X . This procedure is demonstrated for the north face:

$$X^{(N)} = X^{(n)} + \frac{\partial X}{\partial r} \frac{\delta r}{2} + \frac{1}{2} \frac{\partial^2 X}{\partial r^2} \frac{\delta r^2}{4} + \mathcal{O}(\delta r^3) \quad (6.97a)$$

$$X^{(P)} = X^{(n)} - \frac{\partial X}{\partial r} \frac{\delta r}{2} + \frac{1}{2} \frac{\partial^2 X}{\partial r^2} \frac{\delta r^2}{4} + \mathcal{O}(\delta r^3) \quad (6.97b)$$

The capital superscript letters in parentheses indicate values of X at the cell centre point (P) and at the centre point of the neighbouring cell (N) as illustrated in figure 6.2 on page 76. Subtracting the second from the first equation (6.97) and dividing by δr yields the expression

$$\frac{\partial X^{(n)}}{\partial r} = \frac{X^{(N)} - X^{(P)}}{\delta r} + \mathcal{O}(\delta r^2) \quad (6.98)$$

which is approximating the differential quotient up to terms of the order of δr^2 . Equation (6.98) is also called the *central difference approximation* of the differential quotient $\frac{\partial X^{(n)}}{\partial r}$.

Approximations for the other cell faces are derived accordingly and can be summarised as

$$\frac{\partial X^{(n)}}{\partial r} = \frac{X^{(N)} - X^{(P)}}{\delta r} \quad \frac{\partial X^{(s)}}{\partial r} = \frac{X^{(P)} - X^{(S)}}{\delta r} \quad (6.99a)$$

$$\frac{\partial X^{(e)}}{\partial z} = \frac{X^{(E)} - X^{(P)}}{\delta z} \quad \frac{\partial X^{(w)}}{\partial z} = \frac{X^{(P)} - X^{(W)}}{\delta z} \quad (6.99b)$$

With the definitions

$$\mathcal{C}_X^{(n,s)} := (n v \delta A)^{(n,s)}, \quad (6.100a)$$

$$\mathcal{C}_X^{(e,w)} := (n u \delta A)^{(e,w)}, \quad (6.100b)$$

$$\mathcal{D}_X^{(n,s)} := \left(\frac{n D}{\delta r} \delta A \right)^{(n,s)}, \quad (6.100c)$$

$$\mathcal{D}_X^{(e,w)} := \left(\frac{n D}{\delta z} \delta A \right)^{(e,w)}, \quad (6.100d)$$

and

$$\mathcal{S}_X := \dot{\omega} \delta V, \quad (6.100e)$$

and the central difference approximations (6.99), equation (6.96) can be rewritten as

$$\begin{aligned} & \mathcal{C}_X^{(n)} X^{(n)} - \mathcal{C}_X^{(s)} X^{(s)} + \mathcal{C}_X^{(e)} X^{(e)} - \mathcal{C}_X^{(w)} X^{(w)} = \\ & = \mathcal{D}_X^{(n)} (X^{(N)} - X^{(P)}) - \mathcal{D}_X^{(s)} (X^{(P)} - X^{(S)}) + \\ & \quad + \mathcal{D}_X^{(e)} (X^{(E)} - X^{(P)}) - \mathcal{D}_X^{(w)} (X^{(P)} - X^{(W)}) + \mathcal{S}_X. \end{aligned} \quad (6.101)$$

The coefficients \mathcal{C}_ϕ and \mathcal{D}_ϕ are called the *convective* and *diffusive coefficients*, respectively, of the flow variable ϕ and \mathcal{S}_ϕ is called the *source term* of ϕ .

Temperature equation

In order to integrate the time independent temperature equation (6.52), it has first to be rewritten in an integral form (omitting time derivatives)

$$\begin{aligned} & \oint_{\mathcal{R}(V)} \rho (\overline{C_p} u^i + \sum_{k=1}^K Y_k C_{p,k} V_k^i) T s_i dA = \\ & \oint_{\mathcal{R}(V)} \lambda T |^i s_i dA + \int_V (\vec{u} \cdot \text{grad } p - \sum_{k=1}^K h_k^0 W_k \dot{\omega}_k + \Phi) dV. \end{aligned} \quad (6.102)$$

Performing the integration over the finite volume cell and applying central difference approximations for the temperature gradients on the cell faces yields

in analogy to equation (6.101)

$$\begin{aligned} \mathcal{C}_T^{(n)} T^{(n)} - \mathcal{C}_T^{(s)} T^{(s)} + \mathcal{C}_T^{(e)} T^{(e)} - \mathcal{C}_T^{(w)} T^{(w)} = \\ = \mathcal{D}_T^{(n)} (T^{(N)} - T^{(P)}) - \mathcal{D}_T^{(s)} (T^{(P)} - T^{(S)}) + \\ + \mathcal{D}_T^{(e)} (T^{(E)} - T^{(P)}) - \mathcal{D}_T^{(w)} (T^{(P)} - T^{(W)}) + \mathcal{S}_T. \end{aligned} \quad (6.103)$$

with the convective and diffusive coefficients given by

$$\mathcal{C}_T^{(n,s)} := (\rho (\overline{C_p} v + \sum_{k=1}^K Y_k C_{p,k} V_k^1) \delta A)^{(n,s)}, \quad (6.104a)$$

$$\mathcal{C}_T^{(e,w)} := (\rho (\overline{C_p} u + \sum_{k=1}^K Y_k C_{p,k} V_k^3) \delta A)^{(e,w)}, \quad (6.104b)$$

$$\mathcal{D}_T^{(n,s)} := \left(\frac{\lambda}{\delta r} \delta A \right)^{(n,s)}, \quad (6.104c)$$

and

$$\mathcal{D}_T^{(e,w)} := \left(\frac{\lambda}{\delta z} \delta A \right)^{(e,w)}, \quad (6.104d)$$

and the source term by

$$\mathcal{S}_T := \left(v \frac{\partial p}{\partial r} + u \frac{\partial p}{\partial z} - \sum_{k=1}^K h_k^0 W_k \dot{\omega}_k + \Phi \right) \delta V. \quad (6.105)$$

With the velocity components given by equations (6.89) and (6.90), the divergence of \vec{u} is given by

$$u^k|_k = \text{div } \vec{u} = \frac{v}{r} + \frac{\partial v}{\partial r} + \frac{\partial u}{\partial z}. \quad (6.106)$$

and the dissipation function Φ follows according to equation (6.49) as

$$\Phi = 2\mu \left[\left(\frac{v}{r} \right)^2 + \left(\frac{\partial v}{\partial r} \right)^2 + \left(\frac{\partial u}{\partial z} \right)^2 \right] + \mu \left(\frac{\partial v}{\partial z} + \frac{\partial u}{\partial r} \right)^2 + \hat{\mu} \left(\frac{v}{r} + \frac{\partial v}{\partial r} + \frac{\partial u}{\partial z} \right)^2 \quad (6.107)$$

Navier-Stokes equations

The time independent Navier-Stokes equations can be written as¹¹

$$\oint_{\mathcal{R}(V)} \rho u^i u^j s_j dA = - \int_V p|_i dV + \int_V \tau^{i,j}|_j dV. \quad (6.108)$$

The contravariant components of the stress tensor are given according to equation (6.42) by

$$\tau^{1,1} = 2\mu \frac{\partial v}{\partial r} + \hat{\mu} u^k|_k, \quad (6.109a)$$

$$\tau^{2,2} = \frac{1}{r^2} (2\mu \frac{v}{r} + \hat{\mu} u^k|_k), \quad (6.109b)$$

$$\tau^{3,3} = 2\mu \frac{\partial u}{\partial z} + \hat{\mu} u^k|_k, \quad (6.109c)$$

$$\tau^{1,3} = \tau^{3,1} = \mu \left(\frac{\partial v}{\partial z} + \frac{\partial u}{\partial r} \right), \quad (6.109d)$$

and

$$\tau^{1,2} = \tau^{2,1} = \tau^{2,3} = \tau^{3,2} = 0. \quad (6.109e)$$

The dyadic product $\rho u^i u^j$ (the *momentum flux density*) is given by

$$\rho u^i u^j = \rho \begin{pmatrix} v v & 0 & v u \\ 0 & 0 & 0 \\ v u & 0 & u u \end{pmatrix}. \quad (6.110)$$

Again, with the assumptions of constant values in the cell volume and on the cell faces, the integrals in equation (6.108) can be evaluated. This yields for the integral of the momentum flux density

$$\begin{aligned} \oint_{\mathcal{R}(V)} \rho u^1 u^j s_j dA &= \\ &= (\rho v v \delta A)^{(n)} - (\rho v v \delta A)^{(s)} + (\rho u v \delta A)^{(e)} - (\rho u v \delta A)^{(w)}, \end{aligned} \quad (6.111a)$$

¹¹The differential forms for the terms on the right hand side of equation (6.108) have been chosen because of the following reason: Due to the finite angular spread of the volume cell, the front and back faces are slightly “tilted” (cf. table 6.5), hence the integrals of pressure and stress over these faces would yield non-vanishing radial components. It turned out that the integration of equation (6.108) using the appropriate integral forms would involve more complicated expressions and lengthy algebra.

$$\oint_{\mathcal{R}(V)} \rho u^3 u^j s_j dA = (\rho v u \delta A)^{(n)} - (\rho v u \delta A)^{(s)} + (\rho u u \delta A)^{(e)} - (\rho u u \delta A)^{(w)}, \quad (6.111b)$$

and for the integral of the pressure force

$$\int_V p|{}^1 dV = \frac{\partial p}{\partial r} \delta V = \frac{p^{(n)} - p^{(s)}}{\delta r} \delta V, \quad (6.112a)$$

$$\int_V p|{}^3 dV = \frac{\partial p}{\partial z} \delta V = \frac{p^{(e)} - p^{(w)}}{\delta z} \delta V. \quad (6.112b)$$

In equation (6.112), the central difference approximation has been applied for the pressure gradients.

The integral of the viscous force yields the somewhat more complicated expressions

$$\begin{aligned} \int_V \tau^{1,j}|_j dV = & \left[-\frac{2\mu v}{r^2} + \frac{\partial}{\partial z} \mu \left(\frac{\partial v}{\partial z} + \frac{\partial u}{\partial r} \right) + \right. \\ & \left. + 2 \frac{1}{r} \frac{\partial}{\partial r} \mu r \frac{\partial v}{\partial r} + \frac{\partial}{\partial r} \hat{\mu} \left(\frac{v}{r} + \frac{\partial v}{\partial r} + \frac{\partial u}{\partial z} \right) \right] \delta V \end{aligned} \quad (6.113a)$$

and

$$\begin{aligned} \int_V \tau^{3,j}|_j dV = & \left[\frac{1}{r} \frac{\partial}{\partial r} r \mu \left(\frac{\partial v}{\partial z} + \frac{\partial u}{\partial r} \right) + \right. \\ & \left. + 2 \frac{\partial}{\partial z} \mu \frac{\partial u}{\partial z} + \frac{\partial}{\partial z} \hat{\mu} \left(\frac{v}{r} + \frac{\partial v}{\partial r} + \frac{\partial u}{\partial z} \right) \right] \delta V. \end{aligned} \quad (6.113b)$$

Axial component of the Navier-Stokes equations

Equation (6.113b) can be rearranged into

$$\begin{aligned} \int_V \tau^{3,j}|_j dV = & \left[\frac{\partial}{\partial z} (2\mu + \hat{\mu}) \frac{\partial u}{\partial z} + \frac{1}{r} \frac{\partial}{\partial r} r \mu \frac{\partial u}{\partial r} + \right. \\ & \left. + \frac{1}{r} \frac{\partial}{\partial r} r \mu \frac{\partial v}{\partial z} + \frac{\partial}{\partial z} \hat{\mu} \left(\frac{v}{r} + \frac{\partial v}{\partial r} \right) \right] \delta V. \end{aligned} \quad (6.114)$$

With the approximations

$$\frac{\partial}{\partial z} \psi \delta V = (\psi \delta A)^{(e)} - (\psi \delta A)^{(w)} + \mathcal{O}(\delta z^2) \quad (6.115a)$$

and

$$\frac{1}{r} \frac{\partial}{\partial r} (r \psi) \delta V = (\psi \delta A)^{(n)} - (\psi \delta A)^{(s)} + \mathcal{O}(\delta r^2), \quad (6.115b)$$

and the central difference approximation for the derivatives of the axial velocity component

$$\frac{\partial u^{(e)}}{\partial z} = \frac{u^{(E)} - u^{(P)}}{\delta z} \quad \frac{\partial u^{(w)}}{\partial z} = \frac{u^{(P)} - u^{(W)}}{\delta z} \quad (6.116a)$$

$$\frac{\partial u^{(n)}}{\partial r} = \frac{u^{(N)} - u^{(P)}}{\delta r} \quad \frac{\partial u^{(s)}}{\partial r} = \frac{u^{(P)} - u^{(S)}}{\delta r} \quad (6.116b)$$

the axial component of equation (6.108) can be brought into a form corresponding to equations (6.101) and (6.103), thereby making use of the expressions obtained in equations (6.111), (6.112), and (6.114):

$$\begin{aligned} & \mathcal{C}_u^{(n)} u^{(n)} - \mathcal{C}_u^{(s)} u^{(s)} + \mathcal{C}_u^{(e)} u^{(e)} - \mathcal{C}_u^{(w)} u^{(w)} = \\ & = \mathcal{D}_u^{(n)} (u^{(N)} - u^{(P)}) - \mathcal{D}_u^{(s)} (u^{(P)} - u^{(S)}) + \\ & + \mathcal{D}_u^{(e)} (u^{(E)} - u^{(P)}) - \mathcal{D}_u^{(w)} (u^{(P)} - u^{(W)}) - \frac{p^{(e)} - p^{(w)}}{\delta z} + \mathcal{S}_u. \end{aligned} \quad (6.117)$$

The convective and diffusive coefficients are given by

$$\mathcal{C}_u^{(n,s)} := (\rho v \delta A)^{(n,s)}, \quad (6.118a)$$

$$\mathcal{C}_u^{(e,w)} := (\rho u \delta A)^{(e,w)}, \quad (6.118b)$$

$$\mathcal{D}_u^{(n,s)} := \left(\frac{\mu}{\delta r} \delta A \right)^{(n,s)}, \quad (6.118c)$$

and

$$\mathcal{D}_u^{(e,w)} := \left(\frac{2\mu + \hat{\mu}}{\delta z} \delta A \right)^{(e,w)}, \quad (6.118d)$$

and the source term by

$$\begin{aligned} \mathcal{S}_u := & \left(\left(\mu \frac{\partial v}{\partial z} \delta A \right)^{(n)} - \left(\mu \frac{\partial v}{\partial z} \delta A \right)^{(s)} \right) + \\ & + \left(\left(\hat{\mu} \left(\frac{v}{r} + \frac{\partial v}{\partial r} \right) \right)^{(e)} - \left(\hat{\mu} \left(\frac{v}{r} + \frac{\partial v}{\partial r} \right) \right)^{(w)} \right) \frac{\delta V}{\delta z}. \end{aligned} \quad (6.119)$$

Radial component of the Navier-Stokes equations

By making use of the identity

$$\begin{aligned}\frac{\partial}{\partial r} \hat{\mu} \left(\frac{v}{r} + \frac{\partial v}{\partial r} \right) &= -\frac{\hat{\mu} v}{r^2} + \frac{\partial \hat{\mu}}{\partial r} \frac{v}{r} + \frac{\hat{\mu}}{r} \frac{\partial v}{\partial r} + \frac{\partial}{\partial r} \hat{\mu} \frac{\partial v}{\partial r} = \\ &= -\frac{\hat{\mu} v}{r^2} + \frac{\partial \hat{\mu}}{\partial r} \frac{v}{r} + \frac{1}{r} \frac{\partial}{\partial r} r \hat{\mu} \frac{\partial v}{\partial r},\end{aligned}\quad (6.120)$$

equation (6.113a) can be rearranged as

$$\begin{aligned}\int_V \tau^{1,j}|_j dV &= \left[\frac{1}{r} \frac{\partial}{\partial r} r (2\mu + \hat{\mu}) \frac{\partial v}{\partial r} + \frac{\partial}{\partial z} \mu \frac{\partial v}{\partial z} - \right. \\ &\quad \left. - (2\mu + \hat{\mu}) \frac{v}{r^2} + \frac{\partial \hat{\mu}}{\partial r} \frac{v}{r} + \frac{\partial}{\partial z} \mu \frac{\partial u}{\partial r} + \frac{\partial}{\partial r} \hat{\mu} \frac{\partial u}{\partial z} \right] \delta V\end{aligned}\quad (6.121)$$

By using the approximations (6.115) and the central difference approximations for the derivatives of the radial velocity component

$$\frac{\partial v^{(e)}}{\partial z} = \frac{v^{(E)} - v^{(P)}}{\delta z} \quad \frac{\partial v^{(w)}}{\partial z} = \frac{v^{(P)} - v^{(W)}}{\delta z} \quad (6.122a)$$

$$\frac{\partial v^{(n)}}{\partial r} = \frac{v^{(N)} - v^{(P)}}{\delta r} \quad \frac{\partial v^{(s)}}{\partial r} = \frac{v^{(P)} - v^{(S)}}{\delta r} \quad (6.122b)$$

the radial component of equation (6.108) can be written as

$$\begin{aligned}\mathcal{C}_v^{(n)} v^{(n)} - \mathcal{C}_v^{(s)} v^{(s)} + \mathcal{C}_v^{(e)} v^{(e)} - \mathcal{C}_v^{(w)} v^{(w)} &= \\ = \mathcal{D}_v^{(n)} (v^{(N)} - v^{(P)}) - \mathcal{D}_v^{(s)} (v^{(P)} - v^{(S)}) + \\ + \mathcal{D}_v^{(e)} (v^{(E)} - v^{(P)}) - \mathcal{D}_v^{(w)} (v^{(P)} - v^{(W)}) - \frac{p^{(n)} - p^{(s)}}{\delta r} \delta V + \mathcal{S}_v.\end{aligned}\quad (6.123)$$

The convective and diffusive coefficients are given by

$$\mathcal{C}_v^{(n,s)} := (\rho v \delta A)^{(n,s)}, \quad (6.124a)$$

$$\mathcal{C}_v^{(e,w)} := (\rho u \delta A)^{(e,w)}, \quad (6.124b)$$

$$\mathcal{D}_v^{(n,s)} := \left(\frac{2\mu + \hat{\mu}}{\delta r} \delta A \right)^{(n,s)}, \quad (6.124c)$$

and

$$\mathcal{D}_v^{(e,w)} := \left(\frac{\mu}{\delta z} \delta A \right)^{(e,w)}, \quad (6.124d)$$

and the source term by

$$\begin{aligned} \mathcal{S}_v := & \left(-\frac{2\mu + \hat{\mu}}{r} + \frac{\partial \hat{\mu}}{\partial r} \right) \frac{v}{r} \delta V + \\ & + \left(\left(\mu \frac{\partial u}{\partial r} \delta A \right)^{(e)} - \left(\mu \frac{\partial u}{\partial r} \delta A \right)^{(w)} \right) + \left(\left(\hat{\mu} \frac{\partial u}{\partial z} \right)^{(n)} - \left(\hat{\mu} \frac{\partial u}{\partial z} \right)^{(s)} \right) \frac{\delta V}{\delta r}. \end{aligned} \quad (6.125)$$

In equations (6.117) and (6.123), the terms involving pressure are written separately to emphasise their role as the “driving force” of the flow.

6.3.2 Discretization scheme

Scalar transport equations

As it has been shown already in figure 6.2 on page 76, the partitioning of the simulation domain into finite volume cells yields a grid-like structure, where each cell can be identified by a pair of indices (I, J) . The co-ordinates of the (I, J) -cell centre point are given by

$$(r_P, z_P)_{I,J} = ((J - 1/2) \delta r, I \delta z). \quad (6.126)$$

The first step of the discretization procedure is made by stating that a flow variable ϕ is only defined at these co-ordinates, henceforth called the *grid points*, such that

$$\phi((J - 1/2) \delta r, I \delta z) := \phi_{I,J}. \quad (6.127)$$

At all other co-ordinates, values for ϕ are obtained by interpolation between the grid points. The general form of the cell-integrated transport equations for scalar flow variables (6.101) and (6.103) can then be written for the (I, J) -cell as

$$\begin{aligned} \mathcal{C}_\phi^{(n)} \phi_{I,J}^{(n)} - \mathcal{C}_\phi^{(s)} \phi_{I,J}^{(s)} + \mathcal{C}_\phi^{(e)} \phi_{I,J}^{(e)} - \mathcal{C}_\phi^{(w)} \phi_{I,J}^{(w)} = \\ = \mathcal{D}_\phi^{(n)} (\phi_{I,J+1} - \phi_{I,J}) - \mathcal{D}_\phi^{(s)} (\phi_{I,J} - \phi_{I,J-1}) + \\ + \mathcal{D}_\phi^{(e)} (\phi_{I+1,J} - \phi_{I,J}) - \mathcal{D}_\phi^{(w)} (\phi_{I,J} - \phi_{I-1,J}) + \mathcal{S}_\phi. \end{aligned} \quad (6.128)$$

The coefficients \mathcal{C}_ϕ and \mathcal{D}_ϕ and the source term \mathcal{S}_ϕ can be calculated by making use of linear interpolation between gridpoints and central difference approximations for all derivatives. Of course \mathcal{C}_ϕ , \mathcal{D}_ϕ , and \mathcal{S}_ϕ can vary from one

cell to the next, but this dependency will be written explicitly only in these cases where its omission would lead to ambiguities. Hence, it is implicitly understood that for example $\mathcal{C}_\phi^{(n)} := \mathcal{C}_{\phi;I,J}^{(n)}$ or $\mathcal{S}_\phi := \mathcal{S}_{\phi;I,J}$.

The last step to obtain a complete discretization scheme for equation (6.128) is to find correct interpolation expressions for the cell face values of ϕ , $\phi_{I,J}^{(n,s,e,w)}$ on the left hand side of the equation. A general form of such an expression involving only the nearest neighbouring grid points can be written as

$$\phi_{I,J}^{(n)} = f^{(n)} \phi_{I,J} + (1 - f^{(n)}) \phi_{I,J+1}, \quad (6.129a)$$

$$\phi_{I,J}^{(s)} = f^{(s)} \phi_{I,J-1} + (1 - f^{(s)}) \phi_{I,J}, \quad (6.129b)$$

$$\phi_{I,J}^{(e)} = f^{(e)} \phi_{I,J} + (1 - f^{(e)}) \phi_{I+1,J}, \quad (6.129c)$$

and

$$\phi_{I,J}^{(w)} = f^{(w)} \phi_{I-1,J} + (1 - f^{(w)}) \phi_{I,J} \quad (6.129d)$$

where f are (not necessarily constant) weighting factors in the range between 0 and 1. With the expressions (6.129), equation (6.128) can be rewritten in the fully discretized form

$$\mathcal{A}_\phi^{(P)} \phi_{I,J} = \mathcal{A}_\phi^{(N)} \phi_{I,J+1} + \mathcal{A}_\phi^{(S)} \phi_{I,J-1} + \mathcal{A}_\phi^{(E)} \phi_{I+1,J} + \mathcal{A}_\phi^{(W)} \phi_{I-1,J} + \mathcal{S}_\phi \quad (6.130)$$

where the coefficients \mathcal{A}_ϕ are given by

$$\mathcal{A}_\phi^{(N)} = \mathcal{D}_\phi^{(n)} - \mathcal{C}_\phi^{(n)} (1 - f^{(n)}), \quad (6.131a)$$

$$\mathcal{A}_\phi^{(S)} = \mathcal{D}_\phi^{(s)} + \mathcal{C}_\phi^{(s)} f^{(s)}, \quad (6.131b)$$

$$\mathcal{A}_\phi^{(E)} = \mathcal{D}_\phi^{(e)} - \mathcal{C}_\phi^{(e)} (1 - f^{(e)}), \quad (6.131c)$$

$$\mathcal{A}_\phi^{(W)} = \mathcal{D}_\phi^{(w)} + \mathcal{C}_\phi^{(w)} f^{(w)} \quad (6.131d)$$

and

$$\mathcal{A}_\phi^{(P)} = \mathcal{A}_\phi^{(N)} + \mathcal{A}_\phi^{(S)} + \mathcal{A}_\phi^{(E)} + \mathcal{A}_\phi^{(W)} + \mathcal{C}_\phi^{(n)} - \mathcal{C}_\phi^{(s)} + \mathcal{C}_\phi^{(e)} - \mathcal{C}_\phi^{(w)}. \quad (6.131e)$$

Equation (6.130) can be written in a shorter form as

$$\mathcal{A}_\phi^{(P)} \phi_{I,J} = \sum \mathcal{A}_\phi^{(nb)} \phi_{nb} + \mathcal{S}_\phi \quad (6.132)$$

where

$$\sum \mathcal{A}_\phi^{(nb)} \phi_{nb} = \mathcal{A}_\phi^{(N)} \phi_{I,J+1} + \mathcal{A}_\phi^{(S)} \phi_{I,J-1} + \mathcal{A}_\phi^{(E)} \phi_{I+1,J} + \mathcal{A}_\phi^{(W)} \phi_{I-1,J} \quad (6.133)$$

is the “sum over neighbouring grid points”.

It only remains to specify the weighting factors f . Here several choices are possible, for example $f = \frac{1}{2}$, which corresponds to the so called *central differencing scheme*, or $f = 1$, which corresponds to the so called *upwind differencing scheme* (cf. [108], ch. 5).

In this work the central differencing scheme has been chosen for the radial direction, hence

$$f^{(n)} = f^{(s)} = \frac{1}{2}. \quad (6.134)$$

Due to the choice of $f = \frac{1}{2}$, the central differencing scheme has a Taylor series truncation error of second order (like the central difference approximation (6.98)), all other choices for f yield only a Taylor series truncation error of first order.

Unfortunately, the central differencing scheme provides stable numerical solutions only if the convective flux is relatively small compared to the diffusive flux. A measure for the relative strength of the convective flux is given by the so called *Peclet number*

$$Pe = \frac{\mathcal{C}}{\mathcal{D}}. \quad (6.135)$$

For $Pe > 2$, some of the coefficients \mathcal{A} become negative and this may lead to physically impossible numerical solutions of equation (6.130). However, since radial velocity components are expected to be very small, hence convective fluxes are small compared to diffusive fluxes, the choice of the central differencing scheme is justified for the radial direction.

On the contrary, we can expect high Peclet numbers in the axial direction, hence the central differencing scheme is not applicable. A possible scheme that is stable for high Peclet numbers would be the upwind differencing scheme, but it lacks of accuracy, hence a relatively high number of grid points would be required. The scheme which has been chosen in this work is the so called *power-law scheme* which is stable for high Peclet numbers and provides reasonable accuracy (cf. [108], p. 125). The weighting factors $f^{(w)}$ and $f^{(e)}$

are given for the power-law scheme as

$$f^{(w)} = \begin{cases} -\frac{1}{Pe^{(w)}} & \text{for } Pe^{(w)} < -10 \\ \frac{(1+0.1 Pe^{(w)})^5 - 1}{Pe^{(w)}} & \text{for } -10 < Pe^{(w)} < 0 \\ 1 - \frac{1 - (1-0.1 Pe^{(w)})^5}{Pe^{(w)}} & \text{for } 0 < Pe^{(w)} < 10 \\ 1 - \frac{1}{Pe^{(w)}} & \text{for } Pe^{(w)} > 10 \end{cases} \quad (6.136a)$$

and

$$f^{(e)} = \begin{cases} 1 + \frac{1}{Pe^{(e)}} & \text{for } Pe^{(e)} < -10 \\ 1 + \frac{1 - (1+0.1 Pe^{(e)})^5}{Pe^{(e)}} & \text{for } -10 < Pe^{(e)} < 0 \\ \frac{1 - (1-0.1 Pe^{(e)})^5}{Pe^{(e)}} & \text{for } 0 < Pe^{(e)} < 10 \\ \frac{1}{Pe^{(e)}} & \text{for } Pe^{(e)} > 10 \end{cases} \quad (6.136b)$$

A graph of equations (6.136) is shown in figure 6.8.

Navier-Stokes equations

In order to have the pressure – velocity coupling introduced by the Navier-Stokes equations (cf. equations (6.117) and (6.123)) handled properly by a numerical solution algorithm, it is advantageous to use a so called *staggered grid* arrangement ([108], ch. 6) as illustrated in figure 6.9.

With this arrangement, the finite volume cells are shifted to the west by $\delta z/2$ and to the north by $\delta r/2$ for the axial and the radial component of the Navier-Stokes equations, respectively. Axial velocity cells are identified by a lowercase index i and an uppercase index J , with their centre points having the co-ordinates

$$(r_P, z_P)_{i,J} = ((J - 1/2) \delta r, (i + 1/2) \delta z) \quad (6.137)$$

and the axial velocity component being defined at these grid points by

$$u((J - 1/2) \delta r, (i + 1/2) \delta z) := u_{i,J}. \quad (6.138)$$

Likewise, radial velocity cells are denoted by an uppercase index I and a lowercase index j , with their centre points having the co-ordinates

$$(r_P, z_P)_{I,j} = (j \delta r, I \delta z) \quad (6.139)$$

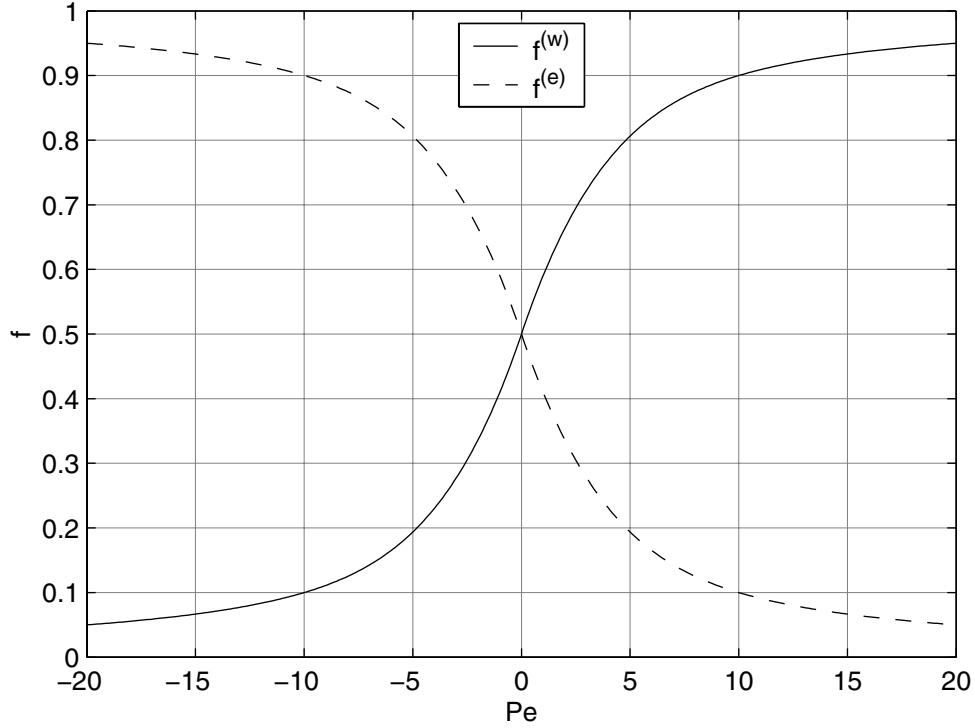


Figure 6.8: The weighting factors $f^{(w)}$ and $f^{(e)}$ as a function of the Peclet number Pe according to the power-law scheme

and the radial velocity component being defined at these grid points by

$$v(j \delta r, I \delta z) := v_{I,j}. \quad (6.140)$$

Due to this shift by a half cell the cell centre points of the axial velocity cells coincide with the centre points of the east and west faces of the scalar cells and vice versa. Likewise the cell centre points of the radial velocity cells coincide with the centre points of the north and south faces of the scalar cells and vice versa. This yields two advantages of the staggered grid as compared to a non-staggered grid arrangement:

- The appropriate velocity components are defined on the cell faces of a scalar cell, and hence can be used directly to compute the convective coefficients of the scalar transport equations.
- Since the pressure is a scalar quantity and thus defined on a scalar grid point, the pressure gradient in equations (6.117) and (6.123) can be directly computed, i.e. without the necessity of interpolation.

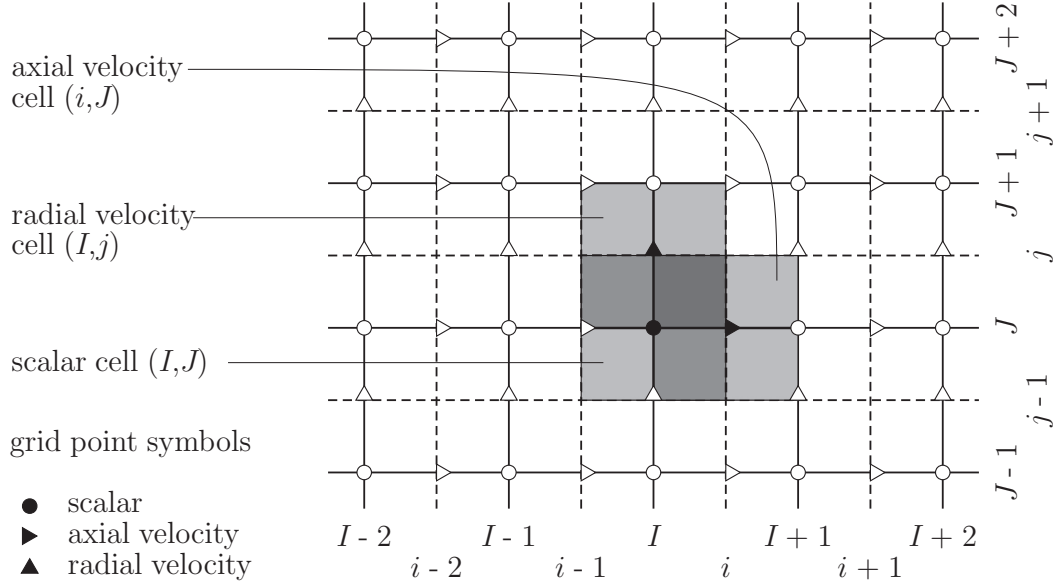


Figure 6.9: Staggered grid arrangement for the solution of the Navier-Stokes equations

In analogy to equation (6.130), the fully discretized Navier-Stokes equations can be written as

$$\mathcal{A}_u^{(P)} u_{i,J} = \sum \mathcal{A}_u^{(nb)} u_{nb} - \frac{\delta V}{\delta z} (p_{I+1,J} - p_{I,J}) + \mathcal{S}_u \quad (6.141)$$

and

$$\mathcal{A}_v^{(P)} v_{I,j} = \sum \mathcal{A}_v^{(nb)} v_{nb} - \frac{\delta V}{\delta r} (p_{I,J+1} - p_{I,J}) + \mathcal{S}_v \quad (6.142)$$

where the coefficients \mathcal{A}_u and \mathcal{A}_v are defined according to equations (6.131).

Continuity equation

The fully discretized cell-integrated continuity equation (6.94) is given for the (I, J) -cell by

$$\begin{aligned} & \frac{\rho_{I,J+1} + \rho_{I,J}}{2} v_{I,j} \delta A_{I,J}^{(n)} - \frac{\rho_{I,J} + \rho_{I,J-1}}{2} v_{I,j-1} \delta A_{I,J}^{(s)} + \\ & + \frac{\rho_{I+1,J} + \rho_{I,J}}{2} u_{i,J} \delta A_{I,J}^{(e)} - \frac{\rho_{I,J} + \rho_{I-1,J}}{2} u_{i-1,J} \delta A_{I,J}^{(w)} = 0. \end{aligned} \quad (6.143)$$

6.3.3 Solution algorithm

As it has been shown in the previous sections, the transport equations are coupled to each other in a quite complex way. For example, the velocity components v and u appear in the convective coefficients of all equations and diffusive coefficients and source terms contain parameters which are themselves functions of the flow variables. Furthermore, the continuity equation has to be fulfilled.

These facts imply that an iterative solution algorithm has to be used. The algorithm chosen in this work is a slightly modified version of the so called *SIMPLER*-algorithm ([108], ch. 6). SIMPLER is an acronym for Semi-Implicit Method for Pressure-Linked Equations — Revised. It represents essentially a predictor – corrector method for pressure and velocity.

The complete algorithm is shown in figure 6.10 and its essential steps are explained in the following paragraphs.

For iteration step ν , the results obtained from the previous step $\nu - 1$ are used as input to calculate the coefficients for the discretized transport equation.

If, during one phase of iteration step ν , a new value for a flow variable becomes available, it replaces the old value for calculations in subsequent phases of the same iteration step.

Iteration is continued until some convergence criteria are fulfilled. The convergence criteria chosen for this work are

$$\max |T_{I,J}^{(\nu)} - T_{I,J}^{(\nu-1)}| < \varepsilon_T \quad (6.144)$$

for the temperature and corresponding expressions for the other flow variables.

In *phase one*, new, improved values for the pressure are obtained using the following procedure

- Using the coefficients and source terms from equations (6.141) and (6.142), the so called *pseudo velocities* are calculated as

$$\hat{u}_{i,J} = \frac{\sum \mathcal{A}_{u;i,J}^{(nb)} u_{nb} + \mathcal{S}_{u;i,J}}{\mathcal{A}_{u;i,J}^{(P)}} \quad (6.145a)$$

$$\hat{v}_{I,j} = \frac{\sum \mathcal{A}_{v;I,j}^{(nb)} v_{nb} + \mathcal{S}_{v;I,j}}{\mathcal{A}_{v;I,j}^{(P)}} \quad (6.145b)$$

- In the discretized continuity equation (6.143), substitute

$$u_{i,J} \leftarrow \hat{u}_{i,J} - \frac{p_{I+1,J} - p_{I,J}}{\delta z} \frac{\delta V}{\mathcal{A}_{u;i,J}^{(P)}} \quad (6.146a)$$

$$v_{I,j} \leftarrow \hat{v}_{I,j} - \frac{p_{I,J+1} - p_{I,J}}{\delta r} \frac{\delta V}{\mathcal{A}_{v;I,j}^{(P)}} \quad (6.146b)$$

The result is a discretized equation for the pressure, henceforth called the *pressure equation*

$$\mathcal{A}_{p;I,J}^{(P)} p_{I,J} = \sum \mathcal{A}_{p;I,J}^{(nb)} p_{nb} + \mathcal{S}_{p;I,J} \quad (6.147)$$

where the coefficients $\mathcal{A}_{p;I,J}^{(N,S,E,W,P)}$ and the source term $\mathcal{S}_{p;I,J}$ follow from equation (6.143) and the substitutions (6.146).

- Solve the pressure equation.

In *phase two*, new, improved values for the velocity components are obtained using the following procedure

- Solve the discretized Navier-Stokes equations (6.141) and (6.142). This is the *predictor step* of the SIMPLER algorithm.
- In the discretized continuity equation (6.143), substitute

$$u_{i,J} \leftarrow u_{i,J} - \frac{p'_{I+1,J} - p'_{I,J}}{\delta z} \frac{\delta V}{\mathcal{A}_{u;i,J}^{(P)}} \quad (6.148a)$$

$$v_{I,j} \leftarrow v_{I,j} - \frac{p'_{I,J+1} - p'_{I,J}}{\delta r} \frac{\delta V}{\mathcal{A}_{v;I,j}^{(P)}} \quad (6.148b)$$

The result is a discretized equation for the pressure correction p' , henceforth called the *pressure correction equation*

$$\mathcal{A}_{p';I,J}^{(P)} p'_{I,J} = \sum \mathcal{A}_{p';I,J}^{(nb)} p'_{nb} + \mathcal{S}_{p';I,J} \quad (6.149)$$

where the coefficients $\mathcal{A}_{p';I,J}^{(N,S,E,W,P)}$ and the source term $\mathcal{S}_{p';I,J}$ follow from equation (6.143) and the substitutions (6.148).

- With the solution of the pressure correction equation, further improve the values for the velocity components. This is the *corrector step* of the SIMPLER algorithm.

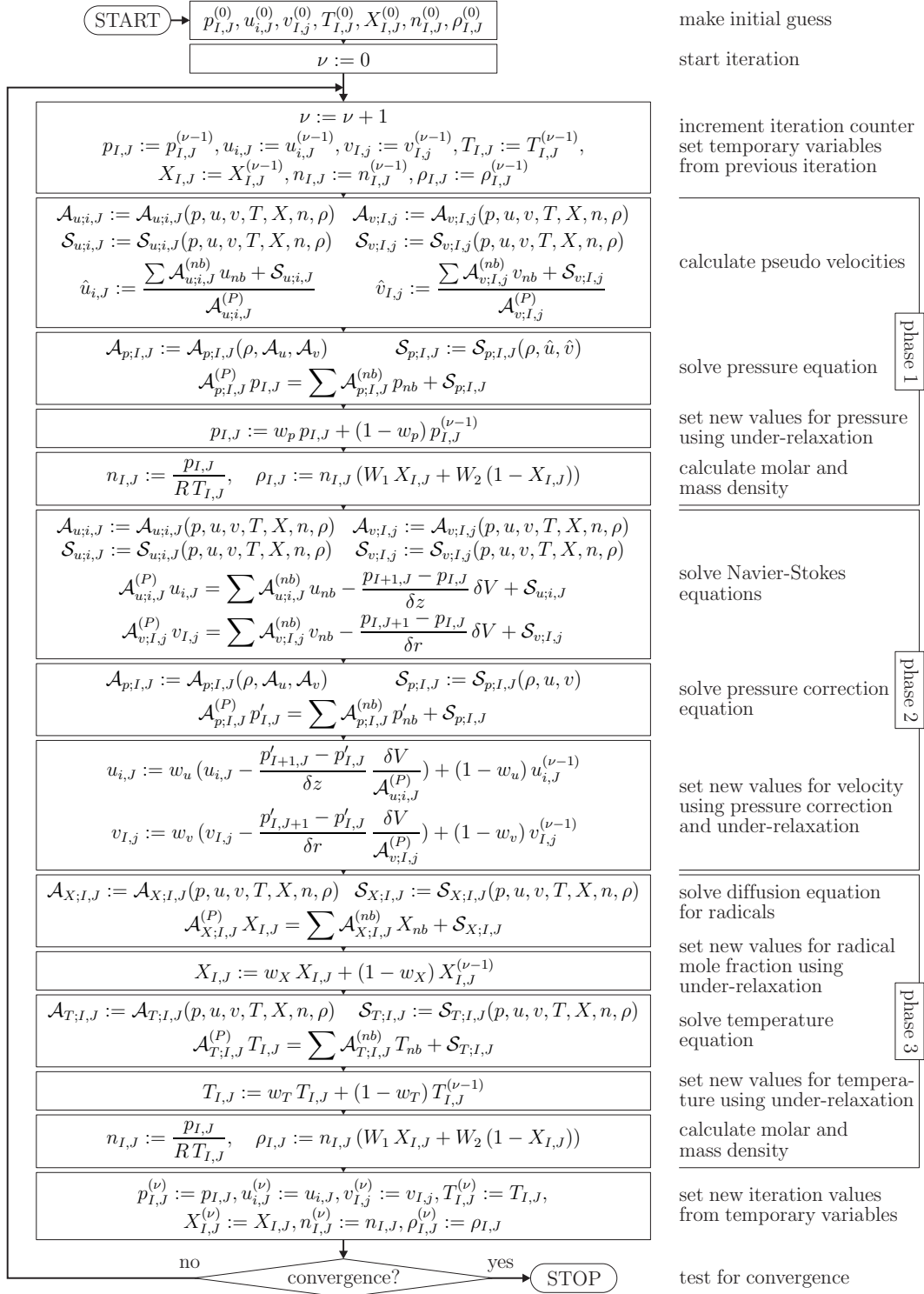


Figure 6.10: Outline of the simulation algorithm

In *phase three*, solve the discretized transport equations for the remaining flow variables (radical mole fraction and temperature).

The calculation of the coefficients of the transport equations is based on guessed values for the flow variables and the newly obtained flow variables tend to overcorrect the deviations of these guesses from the correct values, hence the solution tends to diverge.

To overcome this problem, *under-relaxation* is used to damp this overcorrection in all three phases of the algorithm, e.g. for the pressure

$$p_{I,J}^{(\nu)} = w_p p_{I,J} + (1 - w_p) p_{I,J}^{(\nu-1)} \quad (6.150)$$

where $p_{I,J}^{(\nu-1)}$ is the value from the previous iteration step, $p_{I,J}$ the solution of the pressure equation, and w_p a *relaxation factor* between 0 and 1.

Depending on the strength of the coupling between the flow variables and on the quality of the initial guesses, these relaxation factors have to be chosen quite small for the first iteration steps. In order to speed up convergence, an algorithm has been developed which decides to increase (or decrease) the relaxation factors depending on the development of the solutions, i.e. if the deviations $\max |\phi^{(\nu)} - \phi^{(\nu-1)}|$ tend to decrease (or increase). Since this algorithm is not essential for the overall solution algorithm it has not been included in figure 6.10.

6.3.4 Implementation

The simulation has been implemented using the MATLAB software package, version 6.0 [120]. MATLAB provides very powerful mechanisms to handle arrays of data (i.e. vectors, matrices, and higher dimensional arrays), so that the program code is highly vectorisable. In fact the program code for this simulation contains no loops at all except the main iteration loop. Furthermore, important routines for matrix manipulation, above all the reliable inversion of large matrices, are provided by the software package.

The performance of the simulation code is reasonable for the purpose of this work. On a PC equipped with an Intel Pentium II processor running at 300 MHz and 192 MB of random access memory and running the WindowsNT 4 operating system (and of course MATLAB), the execution time for a grid consisting of 50 axial times 20 radial grid points is typically below 5 minutes. The execution time depends very much on the strength of the coupling between the flow variables but also on the choice of the initial guesses.

6.4 Results

6.4.1 Verification of the simulation

As a first test, the flow of pure nitrogen gas through a tube with an inner diameter of 3.5 cm and a length of 2 m has been simulated for a range of values for the inlet and the outlet pressure. The total flow rate, calculated from the simulation results can be compared with a well established formula for the laminar flow rate of a fluid through a cylindrical pipe, which is given by Poiseuille's law [121]

$$\dot{Q} = \frac{\pi d^4}{128 \mu} \frac{\partial p}{\partial z} \bar{p}. \quad (6.151)$$

Here \dot{Q} is the flow rate, d the diameter of the pipe, μ the dynamic viscosity, and \bar{p} the mean pressure. $\frac{\partial p}{\partial z}$ is the pressure gradient along the pipe.

The results of this test are summarised in figure 6.11 on page 122. As it can be seen, the agreement between the simulation results and theory is very good except for high pressure gradients. The discrepancy at high pressure gradients can be explained by the fact that Poiseuille's law is applicable only if the fluid can be considered as *incompressible*. This assumption is not valid for gases if the flow velocities and pressure gradients are too high. However, the model does not rely on the assumption of incompressibility. It treats *compressible* fluids correctly.

6.4.2 Simulation results for a typical set of parameters

The simulation program has been executed for different sets of values of boundary conditions and parameters for a tube with an inner diameter of 3.5 cm and a length of 2 m.¹² A typical set of these values, summarised in the following table, has been chosen here to visualise the results produced by the simulation.

symbol	p_{in}	p_{out}	T_{wall}	X_{in}	γ
value	200 Pa	175 Pa	300 K	0.4	0.01

¹²These are the dimensions of the experimental vacuum chamber described in detail in chapter 7.

p_{in} and p_{out} are the pressure at the tube inlet and outlet, T_{wall} is the tube wall temperature, X_{in} the radical mole fraction at the tube inlet, and γ is the probability of wall recombination. The results, shown in the figures 6.12 – 6.14 (page 123 ff.) have been calculated on a grid of 41 axial \times 20 radial points.

A remark has to be made on the calculated cross section integrated mass flow shown in the lower graph of figure 6.14. It is given by

$$\dot{M}(z) = 2 \pi \int_0^R r \rho(r, z) u(r, z) dr \quad (6.152)$$

and according to the mass conservation law it should be independent of the choice of the cross section. The deviation from this constant value which is in the order of 0.1 % can be explained by the facts that the continuity equation is not solved directly in the simulation algorithm, but is used instead to calculate pressure and pressure correction. Furthermore we have introduced approximations during the discretization process, hence the value of the integral can also only be an approximation to the “real” value, and finally the numerical precision of the computer is limited.

6.4.3 Characteristic decay length of radicals

One of the main reasons to develop the simulation has been to calculate the distance over which radicals can travel. The results of this calculation shall be given in this section.

In figures 6.15 and 6.16 (pages 126 and 127), the cross section averaged radical mole fraction, given by

$$\langle X \rangle_A(z) = \frac{2 \pi \int_0^R r X(r, z) dr}{R^2 \pi} \quad (6.153)$$

is plotted against the axial coordinate z for a wide range of operating conditions. It can be seen that for $z > 1$ $\langle X \rangle_A$ follows an “almost perfect” exponential decay law as it can be expected when first order wall recombination is the dominant loss mechanism. Hence, we can approximate the longitudinal radical distribution by an exponential function of the form

$$\langle X \rangle_A(z > 1) \propto 10^{-z/\zeta} \quad (6.154)$$

with ζ being the *characteristic decay length*, i.e. the distance where the radical mole fraction is reduced by one order of magnitude.

The characteristic decay length has been calculated for a variety of operating conditions for a tube of an inner diameter of 3.5 cm and a length of 2 m and the results are summarised in figures 6.17 and 6.18 on pages 128 and 129.

6.4.4 Application of the simulation to an LHC dipole cold bore tube

In order to investigate if radical treatment is feasible in a “real world” application, the simulation has been carried out for a beam pipe as it will be used in the dipoles of the Large Hadron Collider at CERN. This beam pipe has an inner diameter of about 50 mm and a length of about 16 m. Before we jump to the results of this simulation a few words should be said on the choice of the operationg conditions.

From the previous section it can be concluded that the characteristic decay length of radicals increases with increasing pressure and increasing pressure gradient. Hence it would be advantegous to choose high values for both parameters. Unfortunately there is an upper limit for each of these parameters. The upper limit for the pressure is given by the radical source, specified by the manufacturer as 5 mbar [79]. We have seen during our experiments that the radical source works very well at pressures up to 6 mbar.

The first upper limit for the pressure gradient is given by the fact that the outlet pressure must be greater than zero. For a inlet pressure of $p_{in} = 600$ Pa and a tube length of $L = 16$ m it follows

$$\frac{\partial p}{\partial z} = \frac{p_{in} - p_{out}}{L} < \frac{600 \text{ Pa}}{16 \text{ m}} = 37.5 \text{ Pa} \cdot \text{m}^{-1}. \quad (6.155)$$

The second upper limit for the pressure gradient is given by the requirement that the flow should stay in the laminar regime. The flow regime can be classified by the *Reynolds number*

$$Re = \frac{\bar{\rho} \bar{u} d}{\mu} \quad (6.156)$$

where $\bar{\rho}$ is the mean mass density, \bar{u} the mean velocity, and μ the dynamic viscosity of the gas and d is the tube diameter. Transition to turbulence occurs

at a critical value of the Reynolds number $Re_{crit} \simeq 2000$.

Equation (6.156) can be rewritten in a more convenient way

$$Re = \frac{\dot{M} d}{A \mu} = \frac{\bar{W}}{RT} \frac{d}{A \mu} \dot{Q} \quad (6.157)$$

with \dot{M} and \dot{Q} being the mass flow and the volumetric flow rate, A the tube cross sectional area and \bar{W} the mean molar mass of the gas. For nitrogen (and many other gases) we can assume the viscosity to be about $2 \times 10^{-5} \text{ Pa} \cdot \text{s}$ at room temperature and with the molar mass of nitrogen of $0.028 \text{ kg} \cdot \text{mol}^{-1}$ we can calculate an upper limit for the volumetric flow rate of

$$\dot{Q} < Re_{crit} \frac{RT}{\bar{W}} \frac{A \mu}{d} \approx 140 \text{ Pa} \cdot \text{m}^3 \cdot \text{s}^{-1}. \quad (6.158)$$

With Poiseuille's law (6.151) and a mean pressure of $\bar{p} = 300 \text{ Pa}$, it follows immediately for the pressure gradient

$$\frac{\partial p}{\partial z} \lesssim 60 \text{ Pa} \cdot \text{m}^{-1}. \quad (6.159)$$

Finally, we have to consider that the pumping speed S at the tube outlet is limited. This limit is given by [121]

$$S \leq A a \left(\frac{2}{\kappa + 1} \right)^{\frac{\kappa+1}{2(\kappa-1)}} \quad (6.160)$$

where $a = \sqrt{\kappa RT / \bar{W}}$ is the *speed of sound* and κ is the *index of isentropic expansion*. For nitrogen gas it is $\kappa \approx 1.4$ ¹³ and $a \approx 350 \text{ m} \cdot \text{s}^{-1}$ at room temperature, hence we can have a maximum pumping speed of $S_{max} \approx 0.4 \text{ m}^3 \cdot \text{s}^{-1}$ for a tube with an inner diameter of 50 mm. From the equation

$$p_{out} S_{max} = \dot{Q} = \frac{\pi d^4}{128 \mu} \frac{p_{in} + p_{out}}{2} \frac{p_{in} - p_{out}}{L} \quad (6.161)$$

the smallest possible outlet pressure can be calculated. For an inlet pressure of $p_{in} = 600 \text{ Pa}$ it is $p_{out} \approx 200 \text{ Pa}$, hence in the case of this application the upper limit for the pressure gradient is given by

¹³For diatomic molecules assuming a perfect gas κ is equal to 1.4

$$\frac{\partial p}{\partial z} \lesssim \frac{600 \text{ Pa} - 200 \text{ Pa}}{16 \text{ m}} = 25 \text{ Pa} \cdot \text{m}^{-1}. \quad (6.162)$$

With respect to the limitations mentioned in the preceding paragraphs, the following choice has been made for the operating parameters:

symbol	p_{in}	p_{out}	T_{wall}	X_{in}	γ
value	600 Pa	200 Pa	300 K	0.1	0.005

The results of this simulation, summarised in figures 6.19 – 6.21 (page 130 ff.), have been obtained on a grid with 320 axial \times 25 radial grid points.

6.4.5 Application of the simulation to a 4 mm inner diameter copper tube

Another “real world” application could be the radical treatment of the accelerating structures of CLIC – a compact linear collider for electrons and positrons currently under investigation at CERN [122]. In the current design, these structures are made of copper and have a length of about 30 cm and an iris opening diameter varying from 3.5 mm to 4.5 mm [122, 123].

For the simulation, we assume a straight cylindircal tube with an inner diameter of 4 mm. The simulation was performed for three different lengths, assuming an inlet mole fraction of nitrogen radicals of $X_{in} = 0.1$ and a recombination probability of nitrogen radicals on copper of $\gamma = 0.01$. The inlet pressure is set to 600 Pa and flow rate and outlet pressure follow from equations (6.160) and (6.161).

The simulation parameters are summarised in the following table

R	L	X_{in}	γ	p_{in}	p_{out}	\dot{Q}
m	m			Pa	Pa	$\text{Pa} \cdot \text{m}^3 \cdot \text{s}^{-1}$
0.002	0.1	0.1	0.01	600	190	0.413
0.002	0.2	0.1	0.01	600	100	0.243
0.002	0.3	0.1	0.01	600	70	0.169

Axial distributions for partial and total pressure resulting from this simulation are shown in figure 6.22 on page 133.

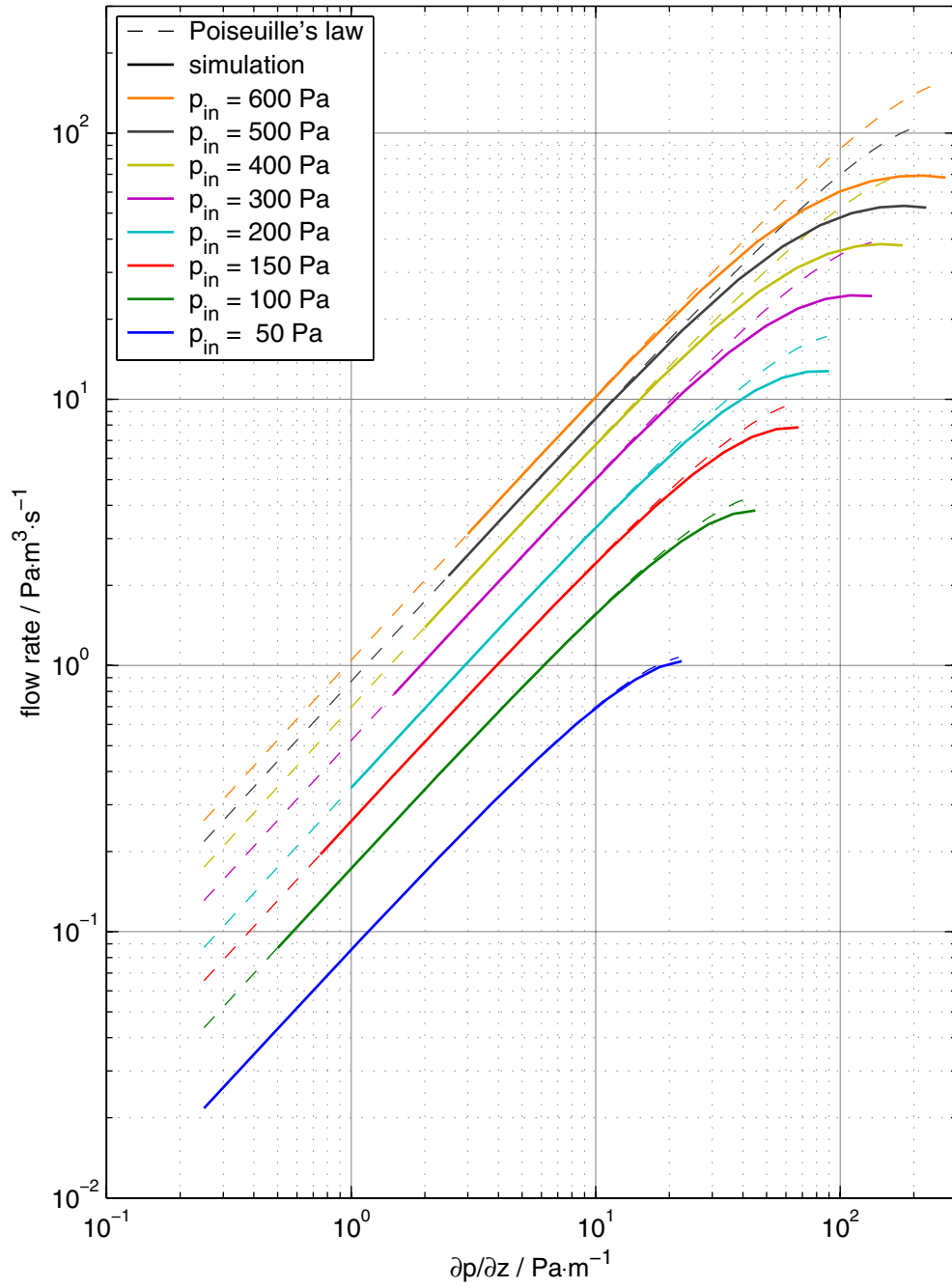


Figure 6.11: Comparison of Poiseuille's law with simulation results for a tube with an inner diameter of 3.5 cm and a length of 2 m.

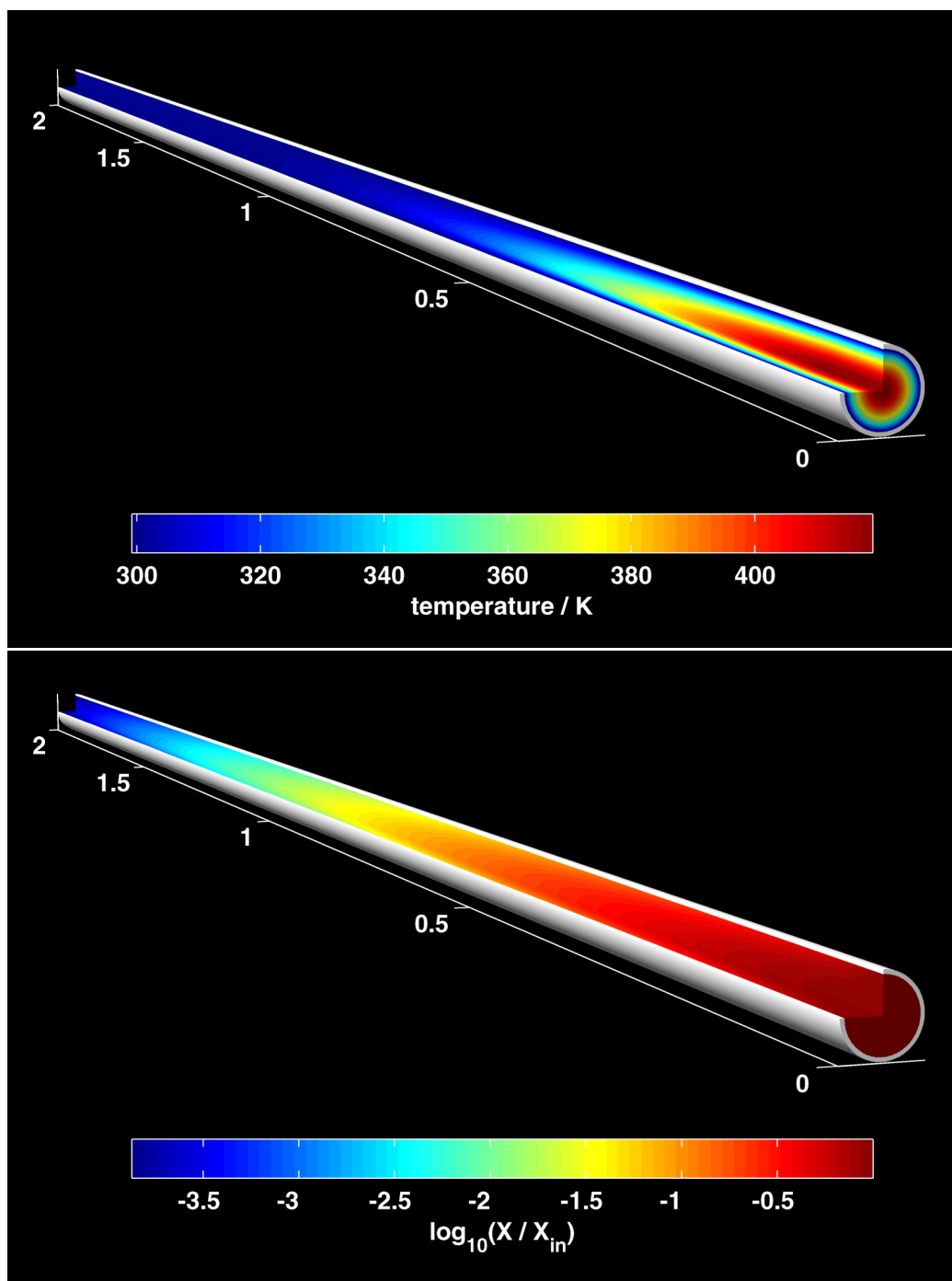


Figure 6.12: Simulation results: temperature and radical mole fraction

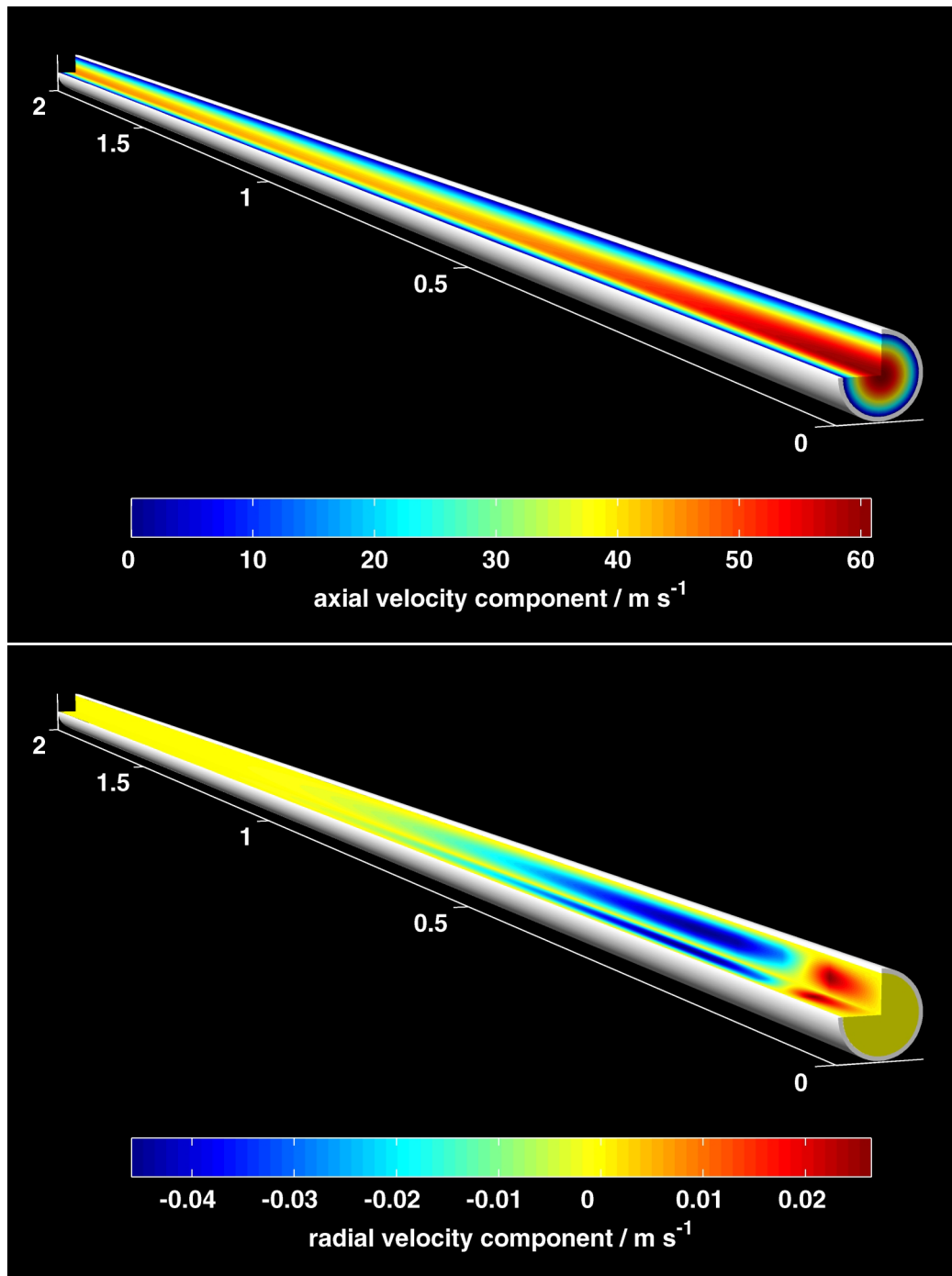


Figure 6.13: Simulation results: axial and radial velocity components

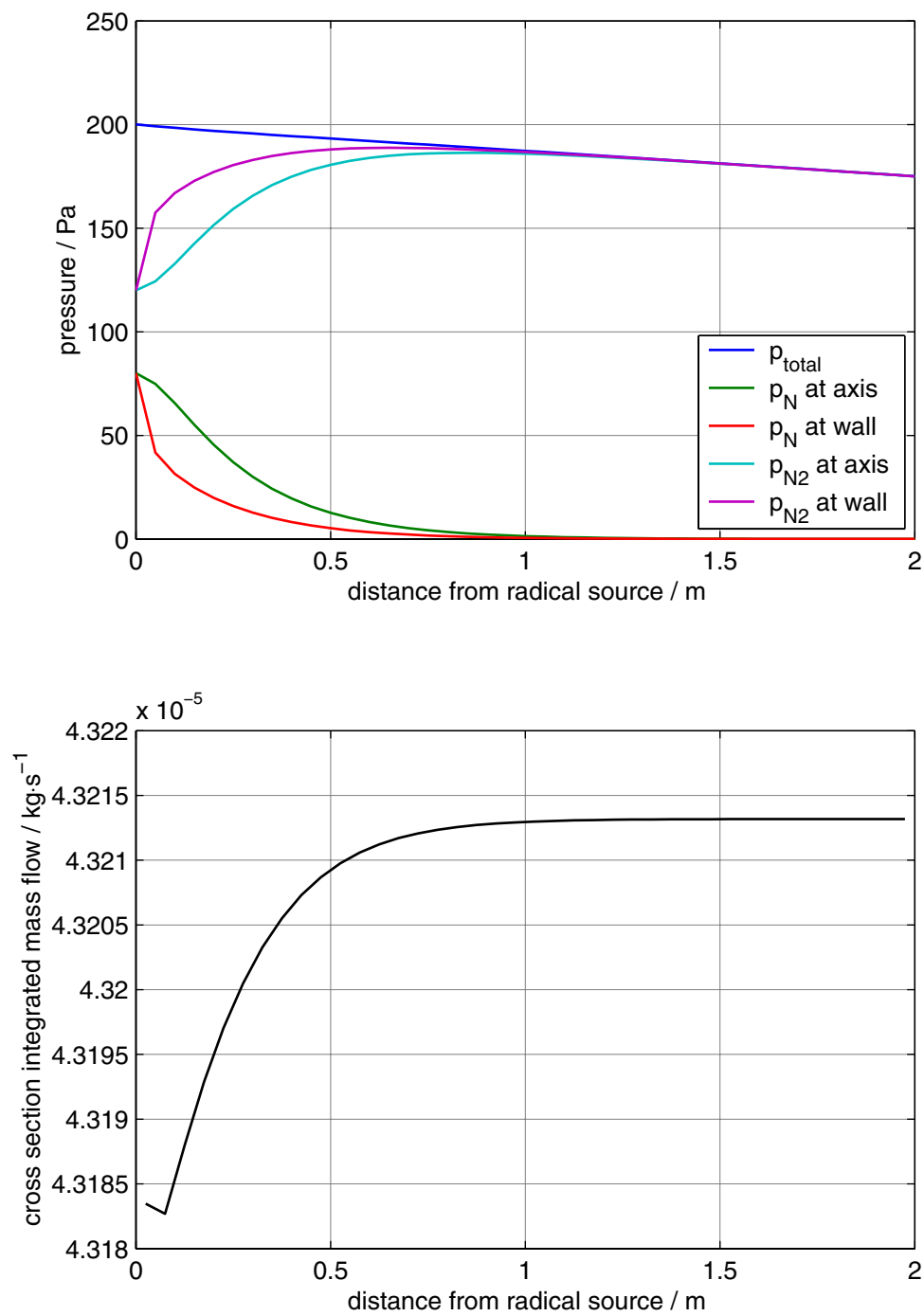


Figure 6.14: Simulation results: partial and total pressure (upper graph), mass flow through cross section of the tube (lower graph)

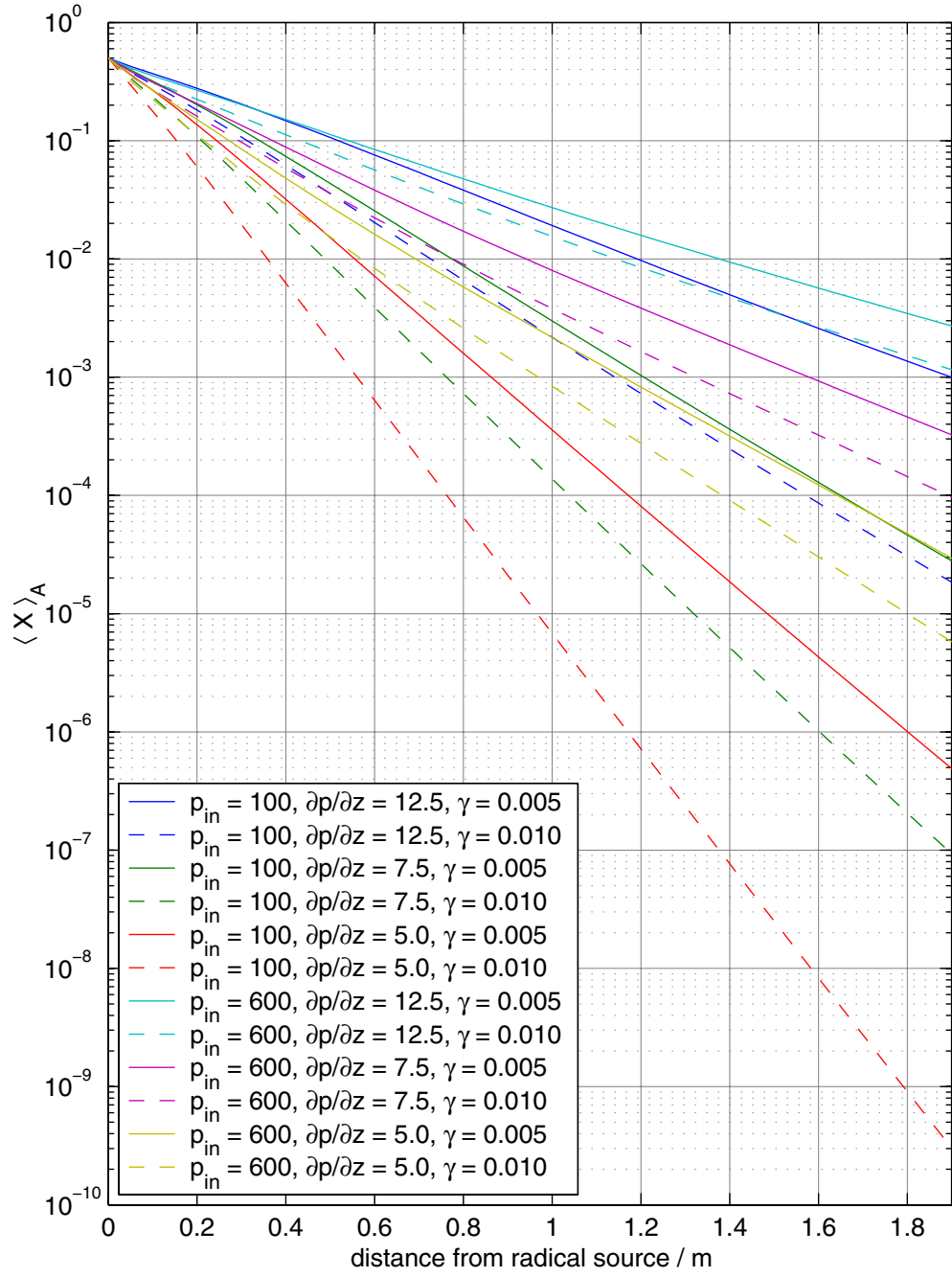


Figure 6.15: Simulation results: cross section averaged radical mole fraction as a function of the axial co-ordinate for a fixed value of $X_{in} = 0.5$

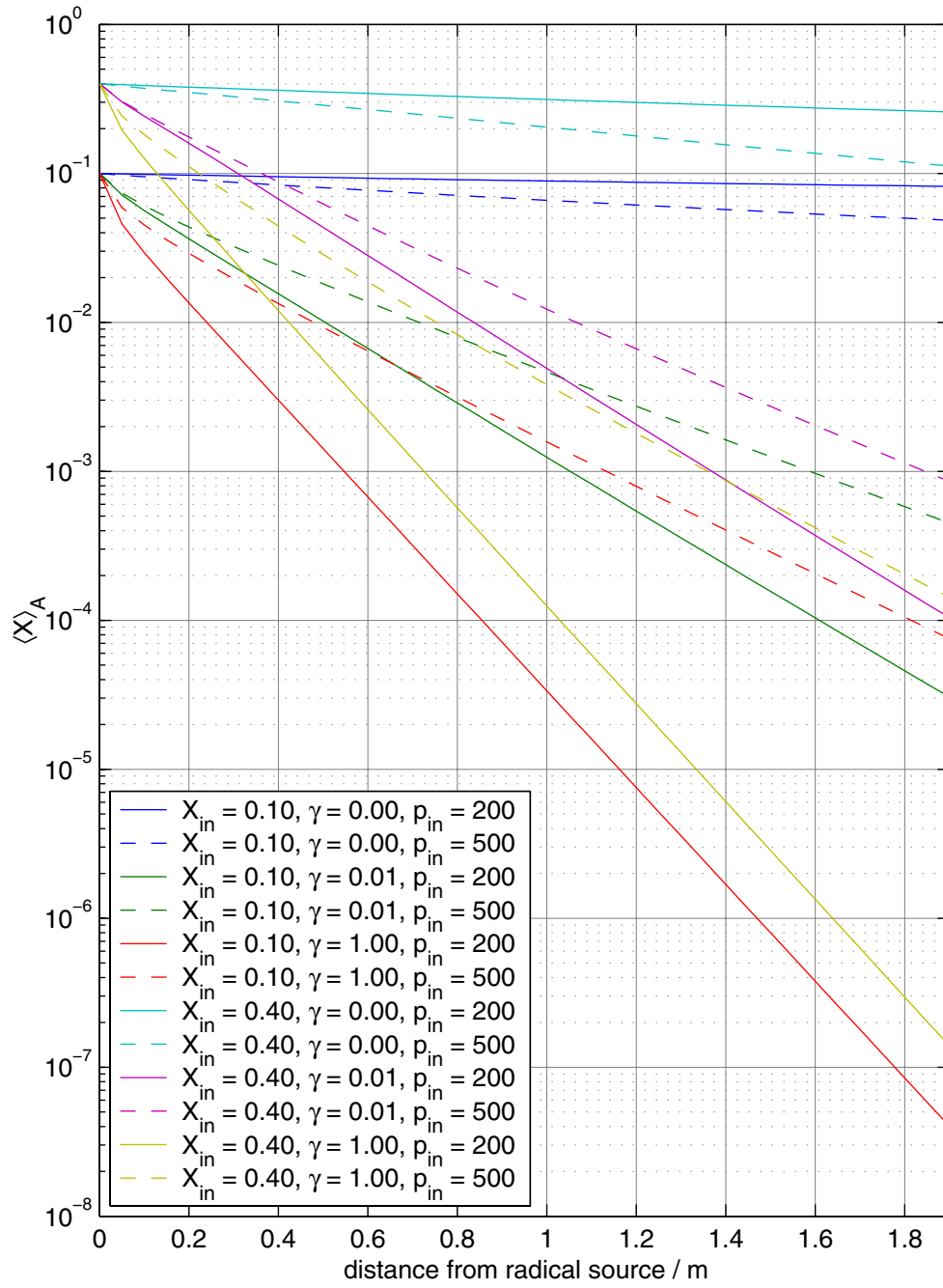


Figure 6.16: Simulation results: cross section averaged radical mole fraction as a function of the axial co-ordinate for a fixed value of $\frac{\partial p}{\partial z} = 12.5 \text{ Pa} \cdot \text{m}^{-1}$

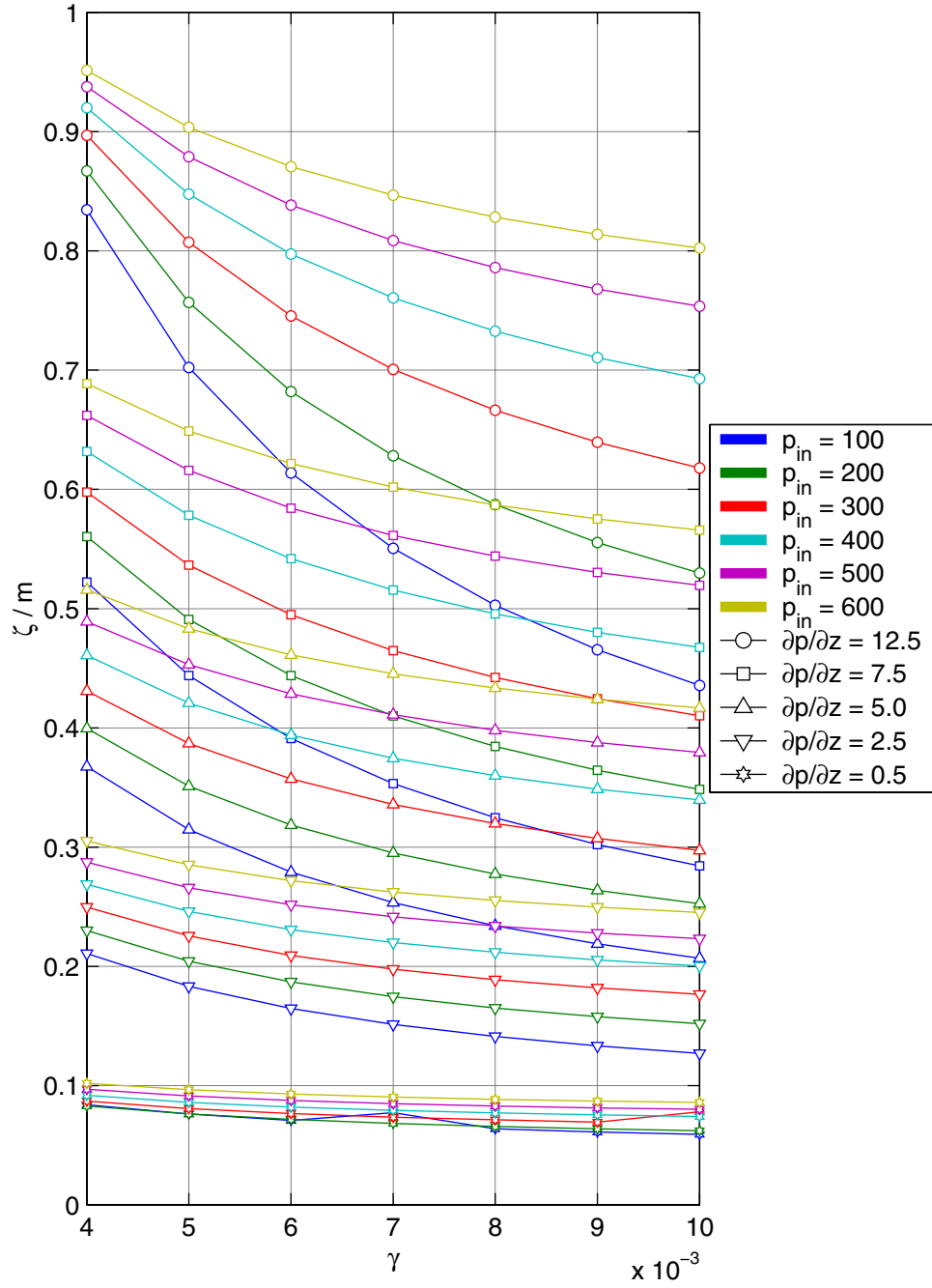


Figure 6.17: Simulation results: characteristic decay length ζ for a fixed value of $X_{in} = 0.5$

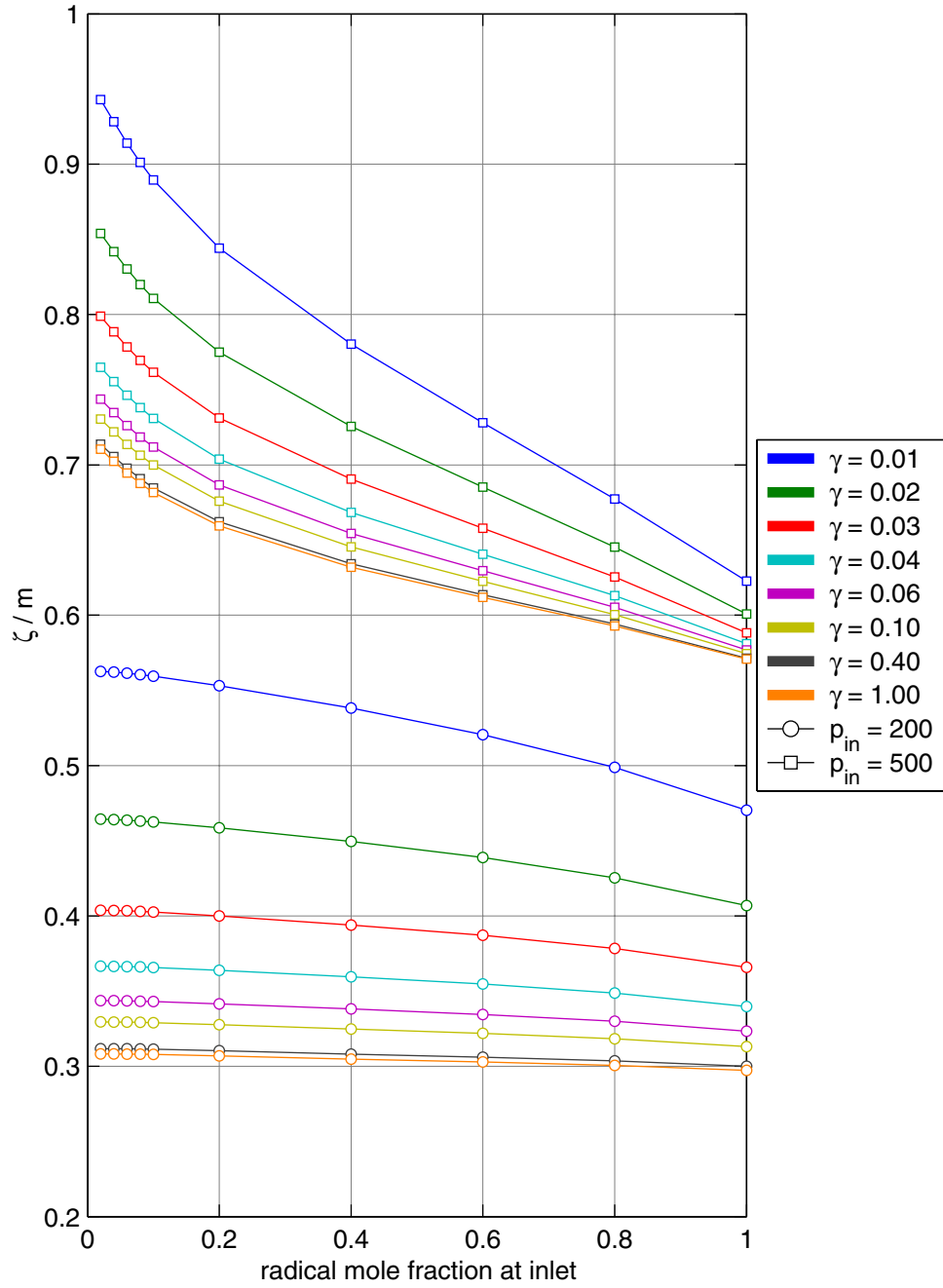


Figure 6.18: Simulation results: characteristic decay length ζ for a fixed value of $\frac{\partial p}{\partial z} = 12.5 \text{ Pa} \cdot \text{m}^{-1}$

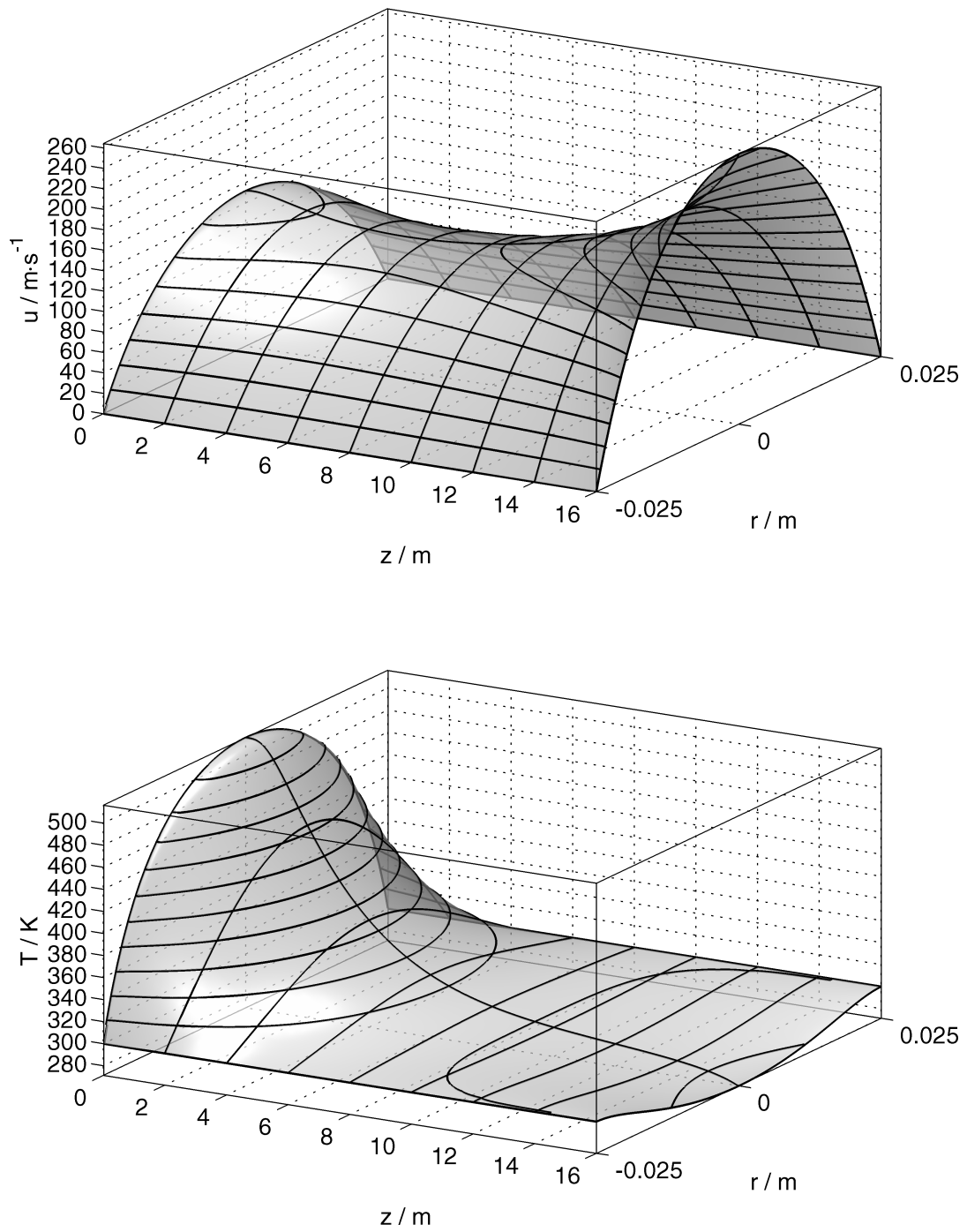


Figure 6.19: Simulation results for a cold bore tube: velocity and temperature

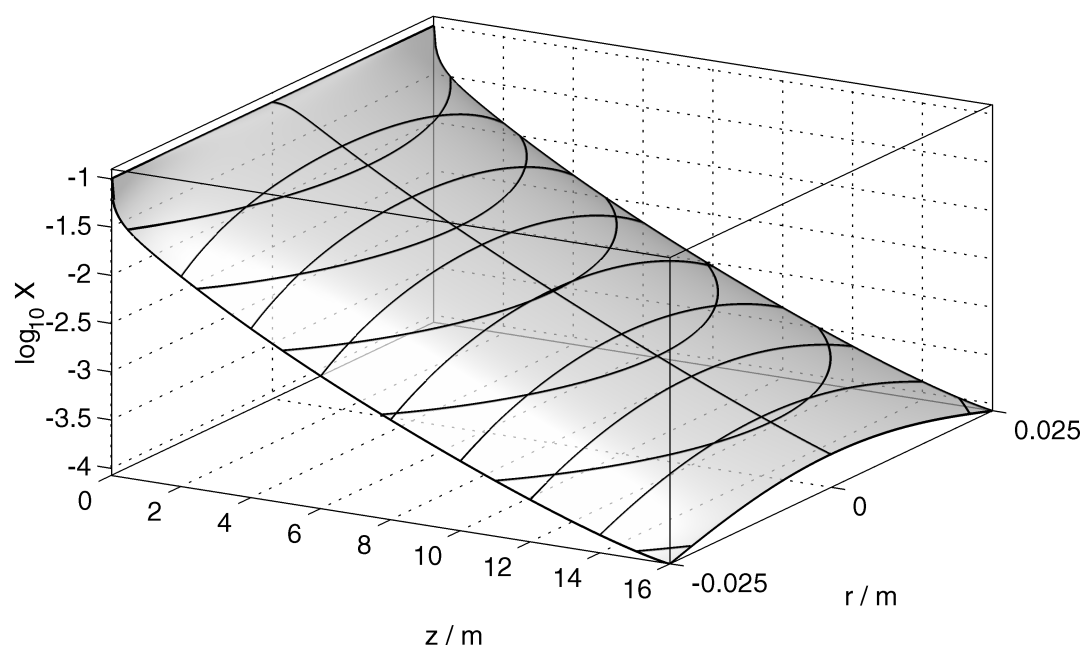
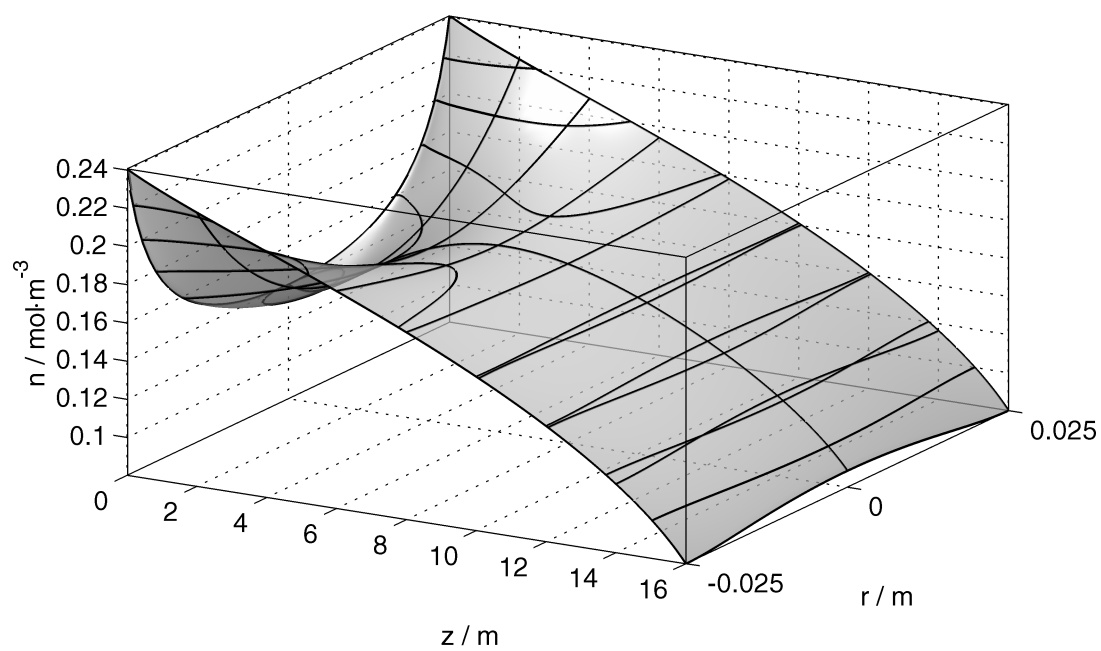


Figure 6.20: Simulation results for a cold bore tube: molar density and radical mole fraction

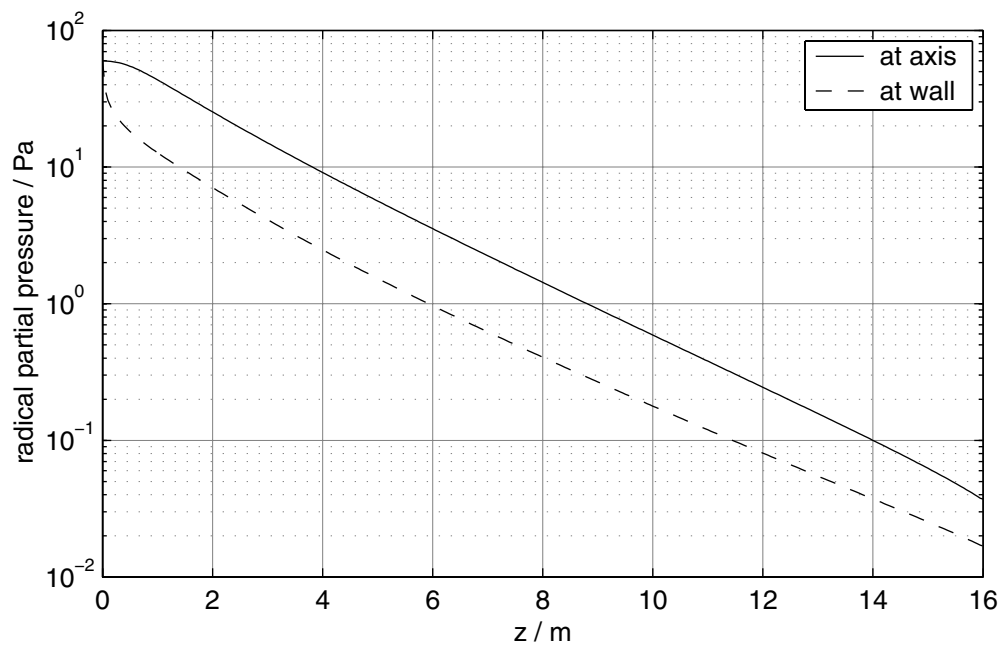
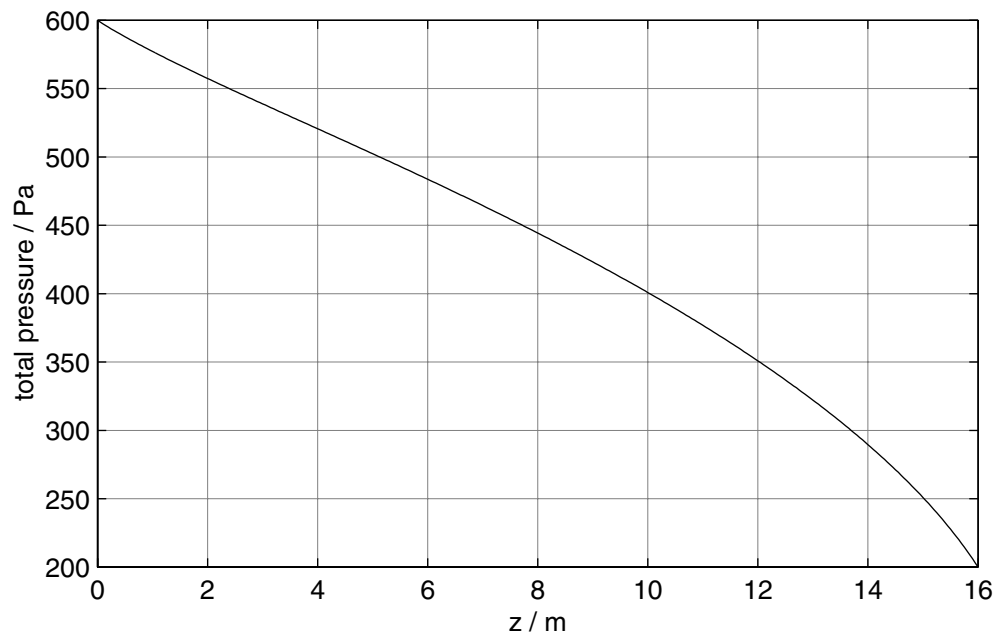


Figure 6.21: Simulation results for a cold bore tube: total and partial pressure

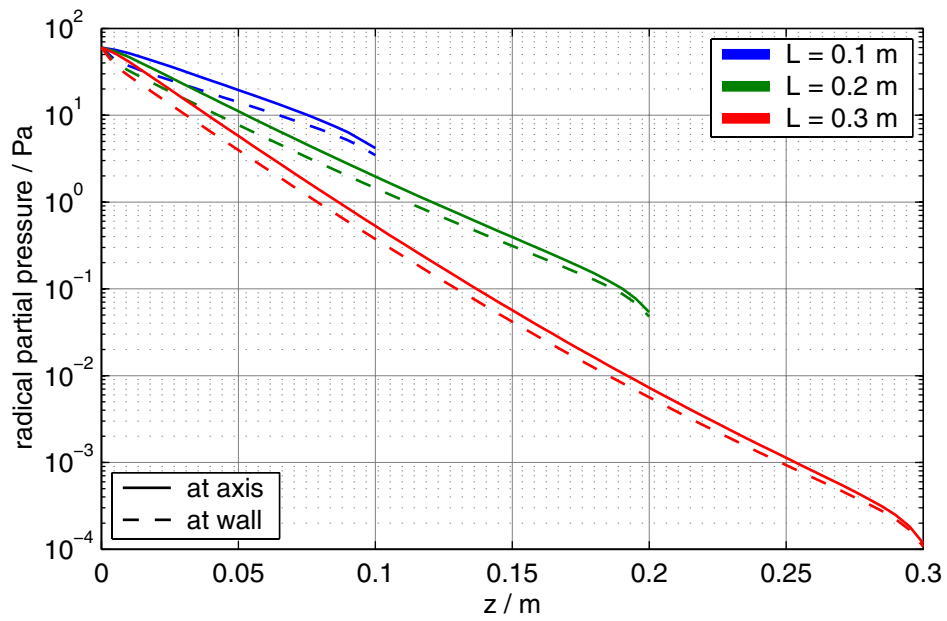
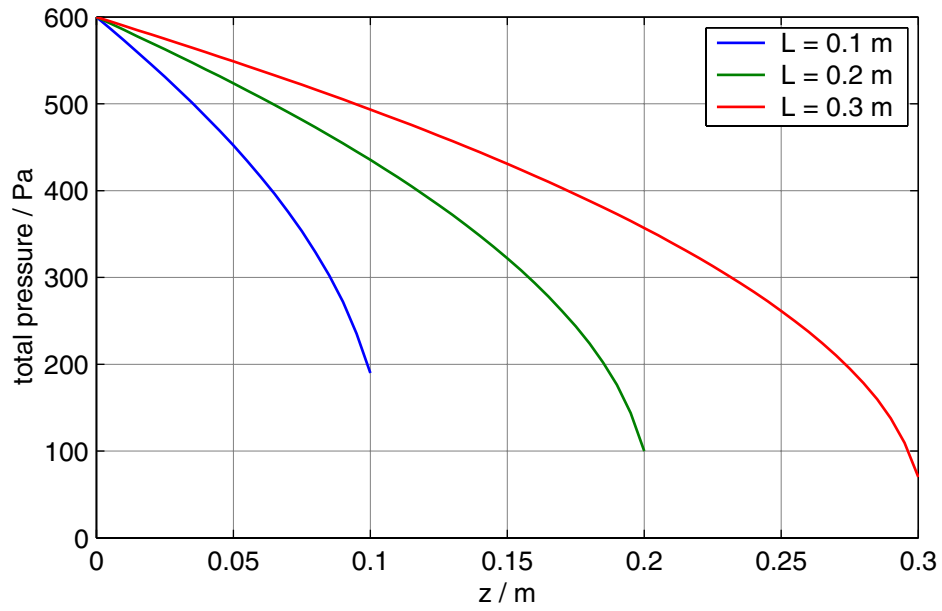


Figure 6.22: Simulation results for a 4 mm inner diameter copper tube

7 Temperature probes

7.1 Description of the experiment

The purpose of this experiment is to determine radical densities in the radical containing gas flow (the *flowing afterglow*) at various distances downstream of the radical source. The measurement method is based on the fact that radicals recombine predominantly on any solid surface rather than in the gas volume itself. Due to these recombination reactions, a considerable amount of heat is released onto that surface. This amount of heat is proportional to the rate of recombination (destruction) of radicals.

If the kinetic mechanism of the recombination reaction is known, it is possible to determine the radical density near an arbitrary solid surface by measuring the amount of heat deposited on this surface. Furthermore, if the vacuum chamber through which the radical containing gas flows is a cylindrical tube of constant radius, then it is possible to predict the distribution of radicals along this tube, which in this case follows basically an exponential decay law (see chapter 6) by determining the radical density at just a few points along the tube.

Experiments which are based on this principle have already been conducted successfully in the past (cf. [124]).

In order to measure the heat of recombination, an experimental vacuum chamber has been equipped with so called *temperature probes*. As it can be seen in figure 7.1, each of these probes consists of a thin stainless steel disk attached to the tip of a thermocouple. This thermocouple is fed radially through a double-sided UHV flange.

The stainless steel disk provides the surface on which the radicals can recombine. It has a diameter of 30 mm and a thickness of 0.5 mm, resulting in a surface area of about 14.1 cm².

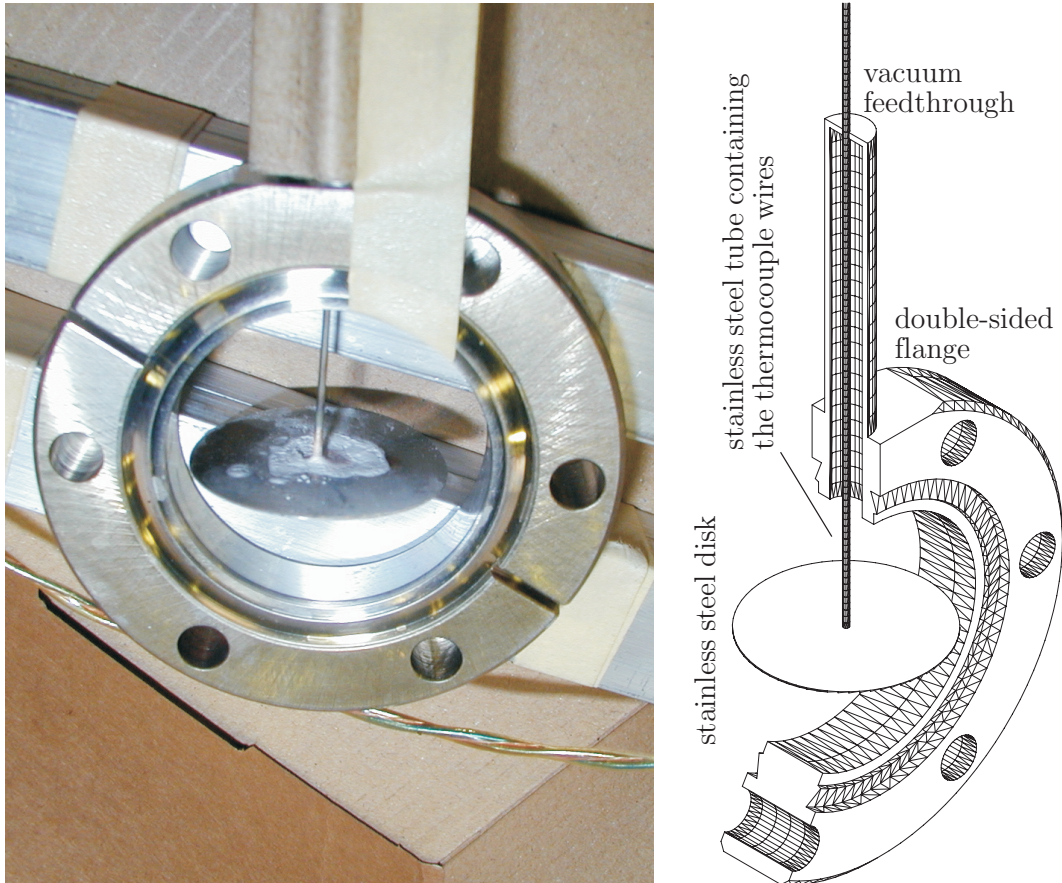


Figure 7.1: Picture and cutaway drawing of a temperature probe (for a description see the text).

The thermocouple consists of a chromel and a constantan conductor, a combination which is usually denoted as *E-type* thermocouple. The two conductors are surrounded by a stainless steel tube with an outer diameter of 1 mm and their *hot junction* (i.e. the point, where the temperature is measured) is located at the tip of this stainless steel tube¹. This construction has the advantage to be rigid enough to hold the temperature probe in place, hence no additional supports are required.

In order to minimise conductive heat losses through the thermocouple itself, the point where the thermocouple is fed through and welded to the flange is moved away from the flange axis by means of a 6 mm inner diameter stainless steel tube. The distance between the feedthrough point and the flange axis is 80 mm.

The flange itself conforms to the ConFlat standard DN40. It has an inner opening with a diameter of 38 mm and is equipped with knife edges on either side, hence it can easily be mounted between two flanges of the same kind.

¹This type of thermocouple is commonly used at CERN to control the bake-out of vacuum chambers

7.2 Experimental setup

As it can be seen in figure 7.2, three temperature probes are mounted into the experimental vacuum chamber which is basically a cylindrical stainless steel tube with an inner diameter of 35 mm. The temperature probes are placed at a distance of 23 cm, 77 cm, and 131 cm respectively downstream of the plasma zone of the radical source. The absolute temperature at the cold junction of the thermocouples is measured by a PT 100 temperature sensitive resistor. Since the thermoelectric voltages produced by the thermocouple are very low – usually in the order of some mV – the signals are amplified by a factor of 100 before being fed into the data acquisition system by means of voltage amplifiers which are placed close to the cold junction of the thermocouples.

The radical source – an XRG-801 microwave radical generator by Secon Semiconductor Equipment [79], already described in detail in chapter 3 – is attached to the inlet of the vacuum chamber by means of a ISO-KF NW40 flange using a Helicoflex metal seal [125].

Attached to the outlet of the vacuum chamber is a manually regulated all metal valve to which the pump – an ADP 81 multistage roots-type dry pump by Alcatel with a nominal pumping speed of $120 \text{ m}^3 \cdot \text{h}^{-1}$ [80] – is connected via a flexible bellow. The valve allows for regulation of the effective pumping speed up to a maximum of about $30 \text{ l} \cdot \text{s}^{-1}$.

The amount of gas flowing into the vacuum system is regulated by a type 1179A mass flow controller by MKS instruments [81] with a full range of 10000 standard cubic centimetre per minute which corresponds to a volumetric flow of about $169 \text{ mbar} \cdot \text{l} \cdot \text{s}^{-1}$. The total pressure in the vacuum chamber is monitored by a Balzers CMR263 compact capacitance gauge [82] with a pressure range of $(10^{-3} \dots 11) \text{ mbar}$. The gauge is mounted midway between inlet and outlet of the vacuum chamber.

Figure 7.3 shows some pictures of the experimental setup.

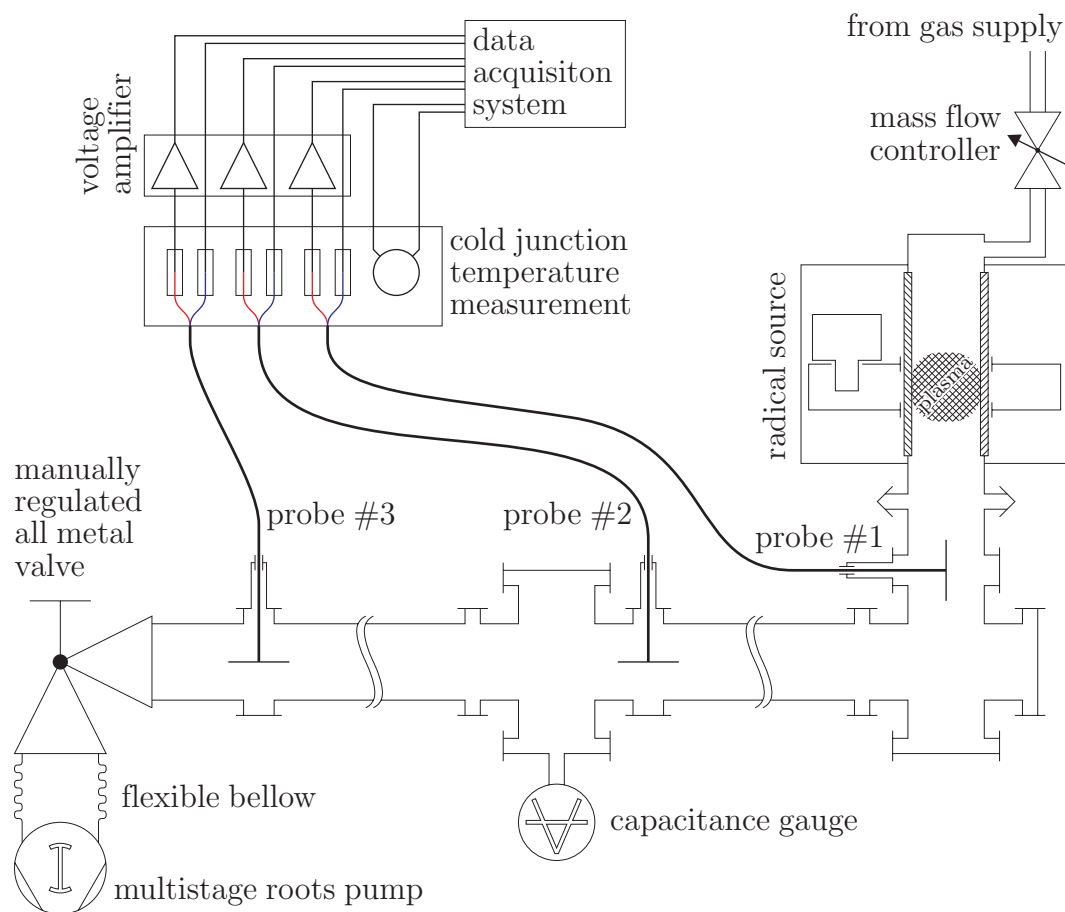


Figure 7.2: Experimental setup to measure the radical distribution along a test vacuum chamber (a description is given in the text)

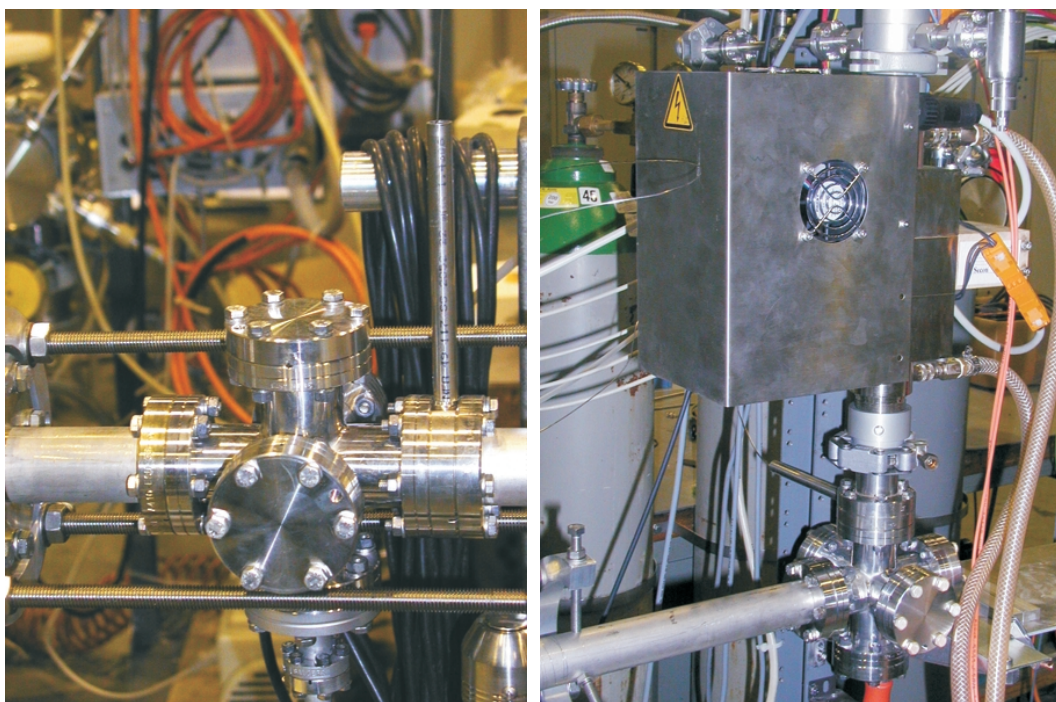


Figure 7.3: Pictures of the temperature probe experiment: the picture on the left side shows temperature probe #2 mounted between two CF40 flanges and the picture on the right side shows the radical generator equipped with electrical and cooling water connections and the installed temperature probe #1 just below.

7.3 Data evaluation

The evaluation of the recorded raw data involves three steps:

1. conversion of the thermoelectric voltage to temperature and compensation for the cold junction temperature,
2. calculation of the heat of recombination, and
3. calculation of the radical concentration.

7.3.1 Voltage to temperature conversion

The first, voltage to temperature conversion step is a straight forward calculation. It involves just one formula for the conversion of the thermoelectric voltage to temperature which is given by [126]

$$T = T(U_{tc} + U(T_{cj})) \quad (7.1)$$

where U_{tc} is the thermoelectric voltage and T_{cj} is the absolute temperature of the cold junction. The functions $T(U)$ and $U(T)$ describe the characteristic voltage-to-temperature and temperature-to-voltage curves of the thermocouple. They are highly non-linear and are usually given as polynomial fits

$$\frac{T}{\text{K}} = \sum_{k=1}^K a_k \left(\frac{U}{\mu\text{V}} \right)^k + 273.15 \quad (7.2)$$

and

$$\frac{U}{\mu\text{V}} = \sum_{k=1}^K c_k \left(\frac{T}{\text{K}} - 273.15 \right)^k. \quad (7.3)$$

The polynomial coefficients a_k and c_k are listed in [126] and summarised for an E-type in table 7.1.

$T = T(U)$		$U = U(T)$	
a_0	0	c_0	0
a_1	1.7057035×10^{-2}	c_1	58.66550871
a_2	$-2.3301759 \times 10^{-7}$	c_2	$4.503227558 \times 10^{-2}$
a_3	$6.5435585 \times 10^{-12}$	c_3	$2.890840721 \times 10^{-5}$
a_4	$-7.3562749 \times 10^{-17}$	c_4	$-3.30568967 \times 10^{-7}$
a_5	$-1.7896001 \times 10^{-21}$	c_5	$6.50244033 \times 10^{-10}$
a_6	$8.4036165 \times 10^{-26}$	c_6	$-1.9197496 \times 10^{-13}$
a_7	$-1.3735879 \times 10^{-30}$	c_7	-1.25366×10^{-15}
a_8	$1.0629823 \times 10^{-35}$	c_8	$2.14892176 \times 10^{-18}$
a_9	$-3.24470870 \times 10^{-41}$	c_9	$-1.4388042 \times 10^{-21}$
		c_{10}	$3.59608995 \times 10^{-25}$

Table 7.1: Polynomial coefficients for the characteristic curves of an E-type thermocouple for a temperature range of $0^\circ\text{C} < T < 1000^\circ\text{C}$ (T in $^\circ\text{C}$, U in μV)

7.3.2 Calculation of the heat of recombination

In the second step, we have to deduce the heat deposited on the temperature probe due to recombination of radicals from the temperature data calculated in step one. During the time when the radical source is switched on, the temperature of the probe will increase due to this heat load. The heat balance of the temperature probe is then given by

$$m C_p \frac{dT}{dt} = \dot{Q}_{recomb} - \dot{Q}_{cooling} \quad (7.4)$$

where m and C_p are the mass and the specific heat capacity (at constant pressure), respectively, of the temperature probe, \dot{Q}_{recomb} is the heating power due to chemical reactions and $\dot{Q}_{cooling}$ the heat loss due to cooling processes, namely heat conduction through the thermocouple itself, convective cooling by the surrounding gas flow, and radiative heat transfer between the temperature probe and the walls of the vacuum vessel. $\dot{Q}_{cooling}$ is a function of the probe temperature but this dependence will not be specified in detail here.

With the radical source being switched off, the heat balance is given by

property	value
material	stainless steel
diameter	0.03 m
thickness	5×10^{-4} m
surface area	1.414×10^{-3} m ²
mass density	7.9×10^3 kg · m ⁻³ [127]
mass	2.79×10^{-3} kg
specific heat capacity	510 J · kg ⁻¹ · K ⁻¹ [127]

Table 7.2: Some temperature probe properties

$$m C_p \frac{dT}{dt} = -\dot{Q}_{cooling}. \quad (7.5)$$

Immediately after switching off the radical source the heating power \dot{Q}_{recomb} sharply drops to zero whereas the cooling power $\dot{Q}_{cooling}$ stays the same². Hence, by subtracting equation (7.5) from (7.4), and evaluating them at time t_0 when the plasma is switched off, we get

$$m C_p \left(\lim_{t \rightarrow t_0} \frac{dT}{dt} - \lim_{t_0 \leftarrow t} \frac{dT}{dt} \right) = \dot{Q}_{recomb}. \quad (7.6)$$

In other words, by computing the (first) time derivative of the probe temperature just before and after the radical source has been switched off, the heating power due to recombination reactions can be determined. The corresponding heat flux density is then simply given by

$$\dot{q}_{recomb} = \dot{Q}_{recomb}/A \quad (7.7)$$

where A is the surface area of the temperature probe. Numerical values for some properties of the temperature probes are given in table 7.2.

Figure 7.4 shows typical plots of the temperature development of the three probes during a plasma on/off process. These plots have been recorded during an experimental run with nitrogen gas operating at a pressure of 500 Pa

²The temperature just before and just after switching off the radical source is the same

and a volumetric flow rate of $10 \text{ Pa} \cdot \text{m}^3 \cdot \text{s}^{-1}$. Shown below the temperature curves are the corresponding time derivatives. Also shown are curves fitted to the temperature data, whose purpose will be explained in the following paragraphs. Another measurement, taken at 200 Pa and $4 \text{ Pa} \cdot \text{m}^3 \cdot \text{s}^{-1}$ is shown in figure 7.5.

As it can be seen from figure 7.5, the difficulty at this point is how to accurately determine the time derivative of the temperature. To explain this difficulty, a short explanation of the structure of the data should be given.

For the purpose of this experiment, a value for the thermoelectric voltage has been recorded by the data acquisition system every 2 seconds. Each recorded voltage is the average of 100 samples and has a standard deviation of about $15 \text{ } \mu\text{V}$, resulting in a standard deviation of the temperature of about 0.2 K . Hence, the resulting random noise in the temperature data has a standard deviation of about $0.2/\sqrt{100}$ i.e. 0.02 K , a value which has actually been obtained from measurements with the probes being at ambient temperature.

If we would calculate the time derivative just by taking the difference between two consecutive temperature points as it is shown by the curves denoted as “data” in the lower half of figure 7.4, i.e.

$$\frac{dT}{dt} \approx \frac{T_{i+1} - T_i}{t_{i+1} - t_i}, \quad (7.8)$$

then we can expect a noise level of

$$\sigma\left(\frac{dT}{dt}\right) \approx \frac{\sqrt{2} 0.02 \text{ K}}{2 \text{ s}} \approx 0.015 \text{ K} \cdot \text{s}^{-1}. \quad (7.9)$$

It is not trivial to apply low-pass filters or other averaging techniques to the data since such procedures can easily remove the characteristic feature of the data, namely the “kink” in the temperature and the jump in the time derivative when the radical source is switched off.

The solution is to find a model which fits the data well – at least in the region around the switching point. This model can then be fitted to the data using many data points resulting in uncertainties in the model’s parameters which are small. The curves denoted as “fit 1” and “fit 2” in figure 7.4 have been obtained by fitting over 300 data points in the case of temperature probe 1 and 250 data points in the case of temperature probes 2 and 3 using only a few fit parameters.

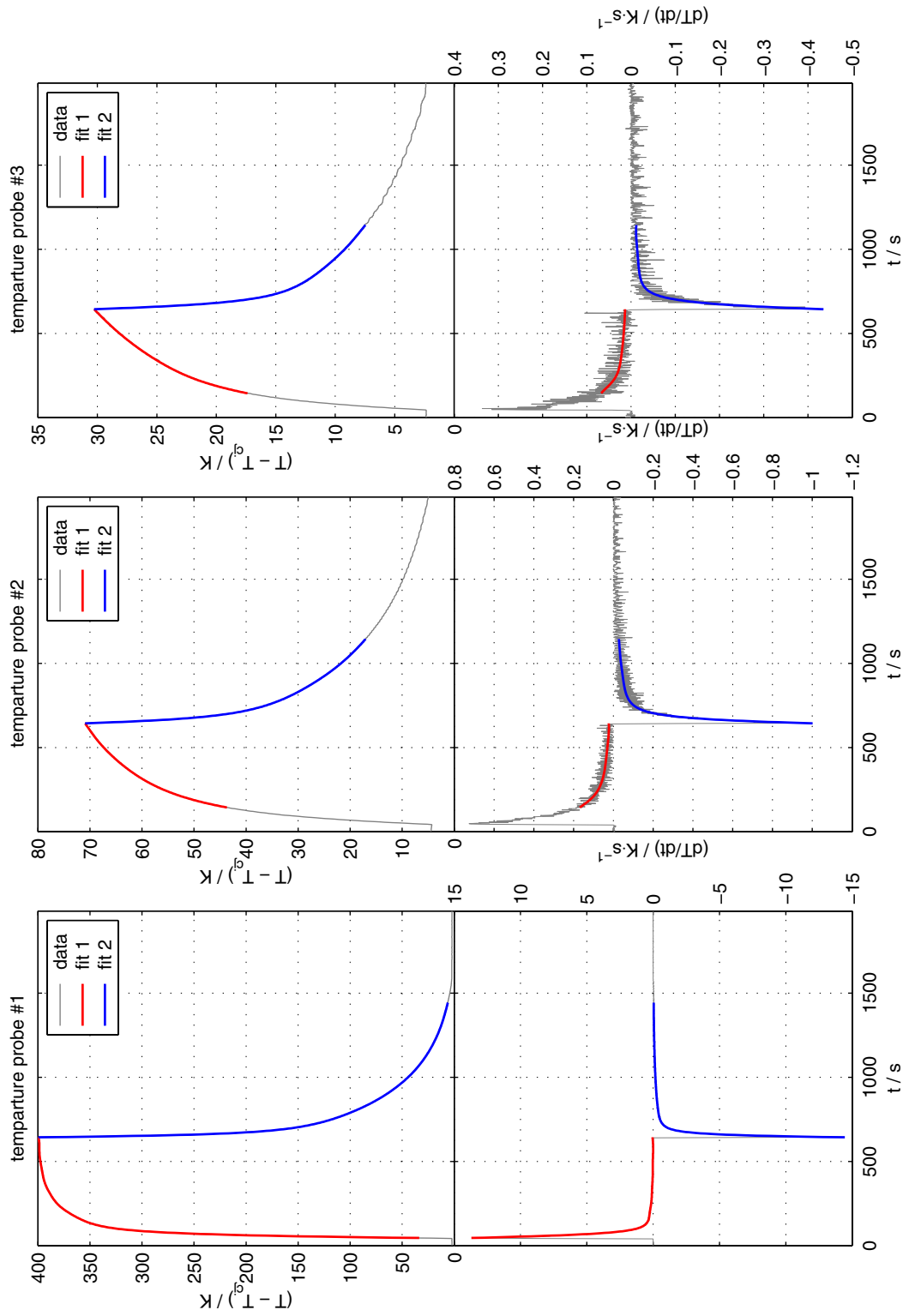


Figure 7.4: Measurement data of an experimental run with nitrogen at 500 Pa and $10 \text{ Pa} \cdot \text{m}^3 \cdot \text{s}^{-1}$

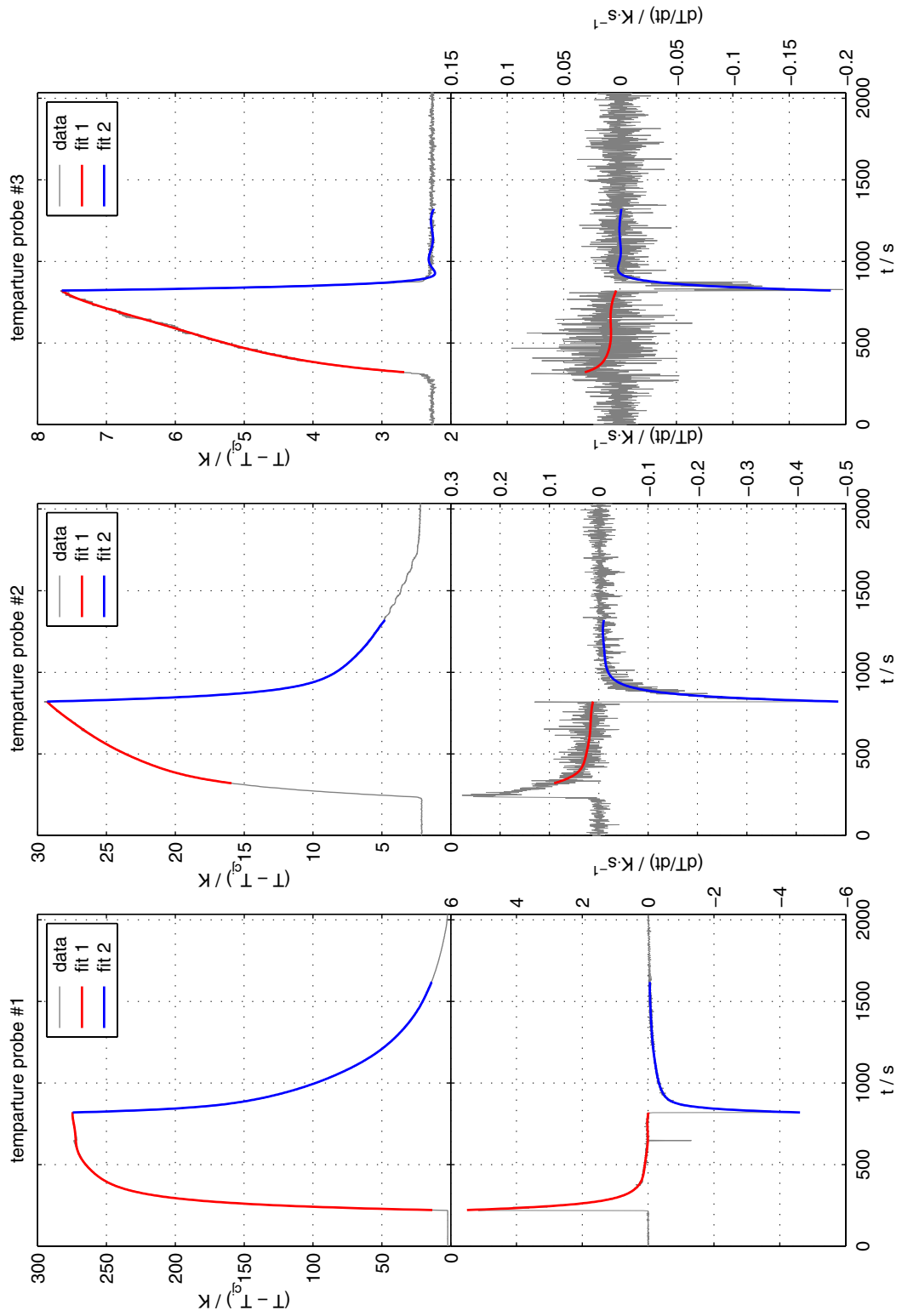


Figure 7.5: Measurement data of an experimental run with nitrogen at 200 Pa and $4 \text{ Pa} \cdot \text{m}^3 \cdot \text{s}^{-1}$

A model which has turned out to fit the data quite well is given by

$$\hat{T}(t; \mathbf{a}) = \hat{T}(t; a_0, \dots, a_K) = a_0 + \sum_{k=1}^K a_k \left[1 - \exp\left(-k \frac{t - t_0}{\tau}\right) \right]. \quad (7.10)$$

with τ being set to 500 s. This model does not reflect the actual physical behaviour of the data, hence it cannot be used to make predictions of the development of the data outside the fit region but it resembles the data well inside the fit region. The best fit parameters $\mathbf{a} = (a_0, \dots, a_K)$ are obtained by means of a χ^2 minimisation

$$\chi^2 = \sum_{i=1}^N \frac{(T_i - \hat{T}(t_i; \mathbf{a}))^2}{\sigma^2(T_i)} \implies \min \quad (7.11)$$

where the (t_i, T_i) are the data points and $\sigma(T_i) = 0.2$ K the standard deviation. To solve equation (7.11) a numerical algorithm is used as described in [128], chapter 15.

The fit is performed independently for the left side and the right side of the switching point t_0 , resulting in two different fit models $\hat{T}(t; \mathbf{a}^{(l)})$ and $\hat{T}(t; \mathbf{a}^{(r)})$. The derivatives, evaluated at t_0 , of these two fit models can now be used to calculate the heat of recombination on the temperature probes according to equation (7.6).

$$\dot{q}_{recomb} = \frac{m C_p}{A} \left(\left. \frac{d\hat{T}(t; \mathbf{a}^{(l)})}{dt} \right|_{t=t_0} - \left. \frac{d\hat{T}(t; \mathbf{a}^{(r)})}{dt} \right|_{t=t_0} \right). \quad (7.12)$$

Since not only the best fit parameters are obtained from the χ^2 minimisation, but also an estimation for the variances $\sigma^2(a_k)$ and the covariances $Cov(a_k, a_l)$ of the parameters \mathbf{a} , an estimation of the variance (or standard deviation) of the heat of recombination can be given. From equations (7.10) and (7.12), it follows for the estimated variance of \dot{q}_{recomb} , $\sigma^2(\dot{q}_{recomb})$

$$\begin{aligned} \sigma^2(\dot{q}_{recomb}) = \frac{m C_p}{A} & \left[\sum_{k=1}^K \frac{k^2}{\tau^2} \sigma^2(a_k^{(l)}) + 2 \sum_{k=1}^{K-1} \sum_{j=k+1}^K \frac{k j}{\tau^2} Cov(a_j^{(l)}, a_k^{(l)}) + \right. \\ & \left. + \sum_{k=1}^K \frac{k^2}{\tau^2} \sigma^2(a_k^{(r)}) + 2 \sum_{k=1}^{K-1} \sum_{j=k+1}^K \frac{k j}{\tau^2} Cov(a_j^{(r)}, a_k^{(r)}) \right]. \quad (7.13) \end{aligned}$$

7.3.3 Determination of the radical density

The last step in the data evaluation is to determine radical densities from the values for the heat of recombination obtained in the previous section. For this purpose, the mechanism of the recombination reaction must be known.

Surface recombination reactions have already been used in chapter 6 to derive a wall boundary condition for the radical concentration and the symbol γ , the recombination probability has been introduced. A very good explanation about the relationship between radical concentration in the gas surrounding a surface, surface recombination, and recombination probability is given by Hays et al. [76] and shall be summarised here.

Let $n \vec{V}$ be the net flux density of radicals (measured in $\text{mol} \cdot \text{m}^{-2} \cdot \text{s}^{-1}$) in the immediate vicinity of a surface. The flux density of radicals disappearing on the surface is then given by

$$\Gamma_s = n \vec{V} \cdot \vec{s} \quad (7.14)$$

where \vec{s} is the unit length outward directed surface normal. The directed velocity \vec{V} is a result of diffusion processes. The total flux density of radicals incident on the surface is given by

$$\Gamma_+ = n \int_{\vec{v} \cdot \vec{s} > 0} f(\vec{v} - \vec{V}) \vec{v} \cdot \vec{s} d^3v \quad (7.15)$$

where $f(\vec{v} - \vec{V})$ is the probability density function of the Maxwell-Boltzmann distribution. If the magnitude of \vec{V} is much smaller than the random thermal velocity \bar{v} , then Γ_+ can be calculated from equation (7.15) by means of a Taylor series development with truncation after the first order

$$\Gamma_+ = n \int_{\vec{v} \cdot \vec{s} > 0} (f(\vec{v}) - \vec{\nabla}_v f \cdot \vec{V}) \vec{v} \cdot \vec{s} d^3v = n \left(\frac{\bar{v}}{4} + \frac{\vec{V} \cdot \vec{s}}{2} \right). \quad (7.16)$$

The recombination probability is simply defined by the ratio between the number of particles disappearing on the surface and the number of particles hitting the surface, i.e.

$$\gamma = \frac{\Gamma_s}{\Gamma_+}. \quad (7.17)$$

Combining equations (7.14), (7.16), and (7.17), we get for Γ_s

$$\Gamma_s = n \frac{\bar{v}}{4} \frac{\gamma}{1 - \frac{\gamma}{2}}. \quad (7.18)$$

The net production rates for radicals and molecules due to surface reactions follows for example in the case of nitrogen atoms and molecules as

$$\dot{\sigma}_N = -\Gamma_s \quad \text{and} \quad \dot{\sigma}_{N_2} = \frac{1}{2} \Gamma_s \quad (7.19)$$

It has to be stated at this point that the dimension of $\dot{\sigma}$ is $\text{mol} \cdot \text{m}^{-2} \cdot \text{s}^{-1}$, whereas the dimension of “normal” production rates (due to reactions occurring in the gas volume) is $\text{mol} \cdot \text{m}^{-3} \cdot \text{s}^{-1}$. It is clear from the preceding paragraphs that the concept of surface reactions makes no sense without the concept of a net velocity directed onto the surface due to diffusion processes. On the other hand, the concentration of radicals in the vicinity of surfaces is constantly lowered due to surface recombination, resulting in a concentration gradient throughout the gas volume which in turn results in a net flux of radicals onto the surface. In many practical cases the diffusion processes are much faster than the consumption of particles at the surface, resulting in negligible concentration gradients. In these cases an equivalent volume production rate can be defined as

$$\dot{\omega}_s = \frac{A}{V} \dot{\sigma} \quad (7.20)$$

which has now the proper dimensions. A is then the total surface area and V the volume of the reaction chamber.

Two mechanisms are given in literature (cf. [76, 129, 114, 130]) for the surface recombination of radicals. In the first, so called *Langmuir-Hinshelwood* mechanism the reaction proceeds through the adsorption of two gas phase radicals on neighbouring sites on the surface, followed by recombination and desorption of the recombination product, whereas in the second, so called *Eley-Rideal* mechanism, a single gas phase radical reacts with a radical already adsorbed on the surface.

In the Langmuir-Hinshelwood mechanism, $\dot{\sigma}$ has a second order dependency on the radical concentration, hence the recombination probability depends linearly on the radical concentration. The reaction can be written for nitrogen as



where γ^{LH} indicates the recombination probability of the Langmuir-Hinshelwood recombination. On the other hand, $\dot{\sigma}$ has a first order dependency on the radical concentration in the Eley-Rideal mechanism and the recombination probability is independent of the radical concentration. This reaction is usually written as



As it has already been stated in chapter 6, the Eley-Rideal mechanism is dominant when dealing with metal surfaces and in the pressure range which is of interest in this work.

Having now described the mechanisms leading to surface recombination, the data evaluation process can be completed. The heat of recombination transferred onto the surface in the case of nitrogen is given by

$$\dot{q}_{recomb} = n \frac{\bar{v}}{4} \frac{\gamma}{1 - \frac{\gamma}{2}} (H_{\text{N}} - \frac{1}{2} H_{\text{N}_2}) \quad (7.23)$$

with H_{N} and H_{N_2} being the molar enthalpy of atomic and molecular nitrogen, respectively. Values of the molar enthalpies have been specified already in chapter 6 (see figure 6.6). For the purpose of the temperature probe measurements it is sufficient to take their difference at room temperature, which is about $4.72 \times 10^5 \text{ J} \cdot \text{mol}^{-1}$.

The computation of the radical concentration n follows directly from equation (7.23).

7.4 Results

7.4.1 Nitrogen radicals

A large set of data has been taken during experimental runs using pure nitrogen as process gas and covering a wide range of values for pressure and flow rate. The heat of recombination calculated from these data is summarised in figures 7.6 – 7.8 (page 154 ff.). In figure 7.6 some of the lines are drawn in a dashed style instead of a solid style. Dashed lines indicate that the downstream value (i.e. the point on the right side of this line) has an estimated relative uncertainty of 100% or more.

To calculate radical densities from these measurement data, a value for the recombination probability has to be specified. The usual value of the recombination probability for nitrogen on stainless steel in the pressure range of a few mbar is reported in literature [107, 106, 105, 130] as $\gamma \simeq 1\%$. It is also reported in literature that the value of γ depends on the total pressure, with γ increasing as the total pressure decreases [76, 107]. The values used in this work are taken from Adams et al. [107] and are summarised in table 7.3. Values of γ for pressures other than that given in table 7.3 are obtained by linear interpolation.

pressure	1 torr	3 torr	5 torr
γ	0.75%	0.63%	0.48%

Table 7.3: Recombination probability of nitrogen radicals on stainless steel

The results for the radical concentration, mole fraction, and partial pressure are summarised in figures 7.9 – 7.11 (pages 157 ff.).

7.4.2 Comparison of temperature probe measurements with simulation

As it has been stated already earlier in this work, the axial radical distribution should basically follow an exponential decay law, due to the fact that first order

wall recombination is the dominant loss process for radicals. Characteristic decay lengths have been calculated in chapter 6 and in this section these calculated values shall be compared to values obtained from the temperature probe measurement.

As it can be seen from figures 7.6, 7.9, 7.10, and 7.11, this exponential decay is fulfilled quite well except for the highest values for pressure and flow rate. There are different possible explanations for this deviation from the “ideal” curve.

A first explanation would be the temperature dependence of γ . For Pyrex and Silica this temperature dependence is well understood [76, 130, 105, 77], but not much data are available for metal surfaces [114]. To investigate this temperature dependence, temperature probe data have been recorded during an experimental run where the radical source has been repeatedly switched on and off, thus providing values for the heat of recombination at different probe temperatures. These measurement data are shown in figure 7.12 on page 160. The temperature of probe #1 is about 700 K when the radical source is being switched off and about 380 K when the radical source is being switched on. As it can be seen from figure 7.12, neither the heat of recombination nor the radical concentration show a significant temperature dependence.

A second possible explanation stems from the fact that we have considered the first order Eley-Rideal mechanism as the dominant recombination process, thereby neglecting second order effects. It could very well be that for high radical concentrations second order effects like the Langmuir-Hinshelwood mechanism are becoming significant. In order to investigate if second order effects could be responsible for this behaviour, the temperature probe data from the experimental runs with the highest flow rates have been evaluated using a simple second order model. Assuming constant flow velocity and ignoring diffusion, the radical concentration along the tube can be described by

$$\frac{dn}{dz} = -k_1 n - k_2 n^2 = -k_1 n (1 + \alpha n) \quad (7.24)$$

with $\alpha = k_2/k_1$. The solution of this equation is given by

$$n(z) = n(0) \frac{\exp[-k_1 z]}{1 + \alpha n(0) (1 - \exp[-k_1 z])} \quad (7.25)$$

and the heat of recombination is then given by

$$\dot{q}_{recomb}(z) \simeq (\alpha n(z) + 1) n(z) \gamma \frac{\bar{v}}{4} \Delta_f H \quad (7.26)$$

with $\Delta_f H \approx 472 \text{ kJ} \cdot \text{mol}^{-1}$ being the heat of formation of atomic nitrogen. This procedure is illustrated in figure 7.13 on page 161. As it can be seen, the model fits quite well for $\alpha \approx 300 \text{ m}^3 \cdot \text{mol}^{-1}$ in this particular case. Evaluating other high-flow data, we obtained a value for α between $100 \text{ m}^3 \cdot \text{mol}^{-1}$ and $500 \text{ m}^3 \cdot \text{mol}^{-1}$. A value of 0.005 has been used for γ .

It has to be stated that the preceding paragraphs should give only a possible explanation and we have no prove for the above statements. On the other hand the model compares favourably with the data, so the assumption of second order processes is at least not completely out of hand. Other possible reasons for the data deviating from an exponential decay law can stem from the experimental setup itself. As it can be seen from the figures 7.2 and 7.3 (pages 138 and 139), the temperature probe #1 is mounted very close to the radical source and in direct “line of sight” from the plasma. It could very well be, that radiation and/or charged particles from the plasma produce additional heat on this temperature probe.

In order to compare the temperature probe data with the computer simulation described in chapter 6, characteristic decay lengths ζ have been calculated both from the temperature data and from simulation results. In case of the measurement data we get

$$\zeta = -\frac{z_2 - z_1}{\log_{10} X_2 - \log_{10} X_1} \quad (7.27)$$

from the low-flow data (flow rate below $7 \text{ Pa} \cdot \text{m}^3 \cdot \text{s}^{-1}$), and

$$\zeta = -\frac{z_3 - z_2}{\log_{10} X_3 - \log_{10} X_2} \quad (7.28)$$

from the high-flow data (flow rate greater or equal to $7 \text{ Pa} \cdot \text{m}^3 \cdot \text{s}^{-1}$), with (z_i, X_i) being the position of and the radical mole fraction calculated from the i th temperature probe, respectively. In the case of the simulation the characteristic decay length has been calculated from simulation runs assuming an inlet radical mole fraction of $X_{in} = 0.1$ and a recombination probability ranging from $\gamma = 0.002$ to $\gamma = 0.01$. The results are summarised in figure 7.14 on page 162. As it can be seen, results from simulation and measurement fit

together quite well. The trend for the recombination probability decreasing with increasing pressure is also clearly visible from the graph.

7.4.3 Oxygen radicals

Temperature probe data have also been recorded during experimental runs using a mixture of argon and oxygen with mole fractions of 90% and 10% respectively and for a range of operating conditions.

Unfortunately, data for the recombination probability of oxygen radicals on stainless steel for the pressure range relevant for this work are not as detailed as in the case of nitrogen radicals. The value used in this work, $\gamma = 0.07$, is given by Mozetič et al. [124] who conducted a similar experiment in the pressure range of 10 Pa ... 100 Pa using pure oxygen gas. During our experiments the pressure was in the range of a few hundred pascal.

The results are summarised in figures 7.15 and 7.16 on pages 163 and 164.

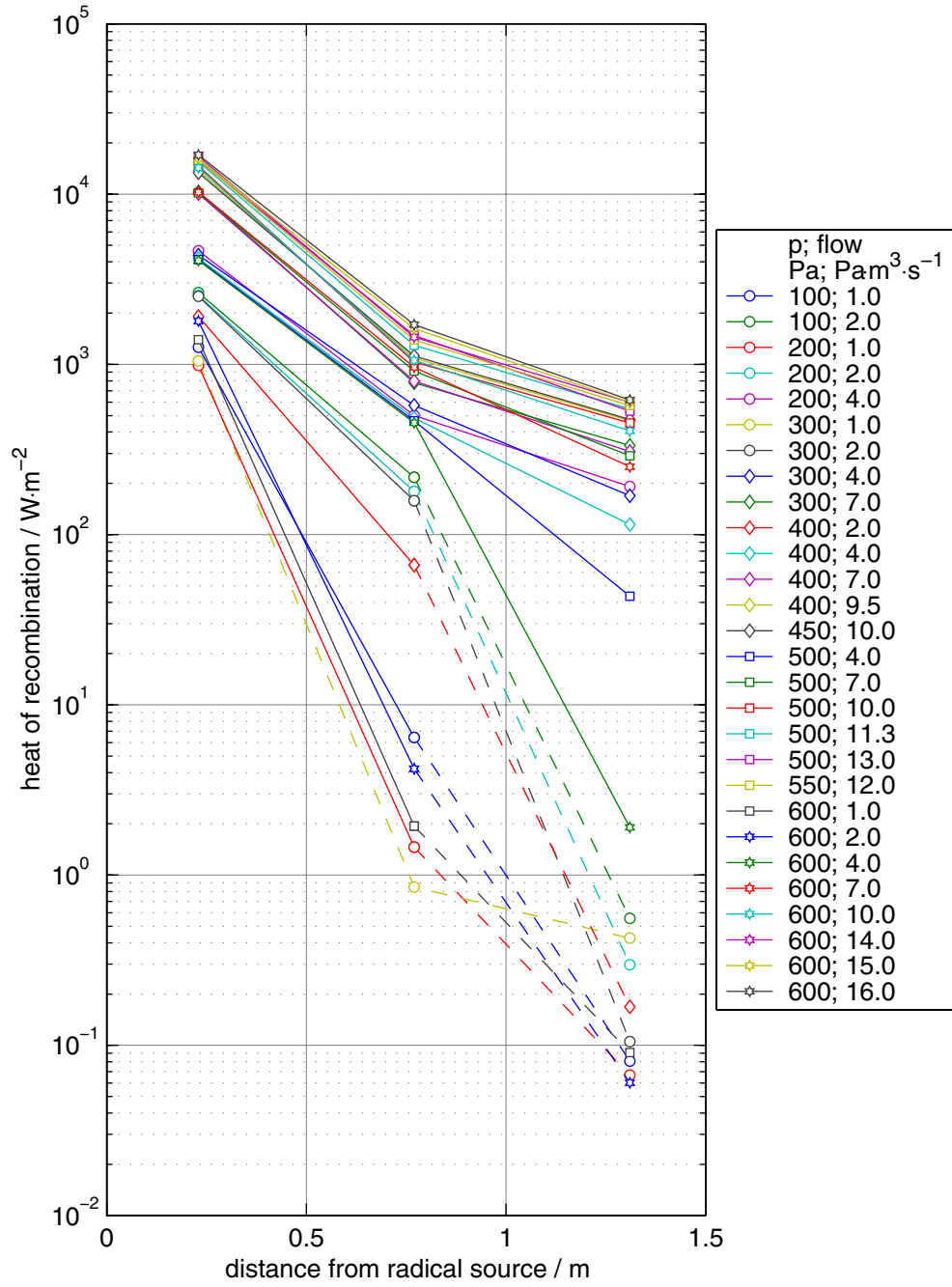


Figure 7.6: Temperature probe results for N_2 : heat of recombination as a function of the temperature probe position

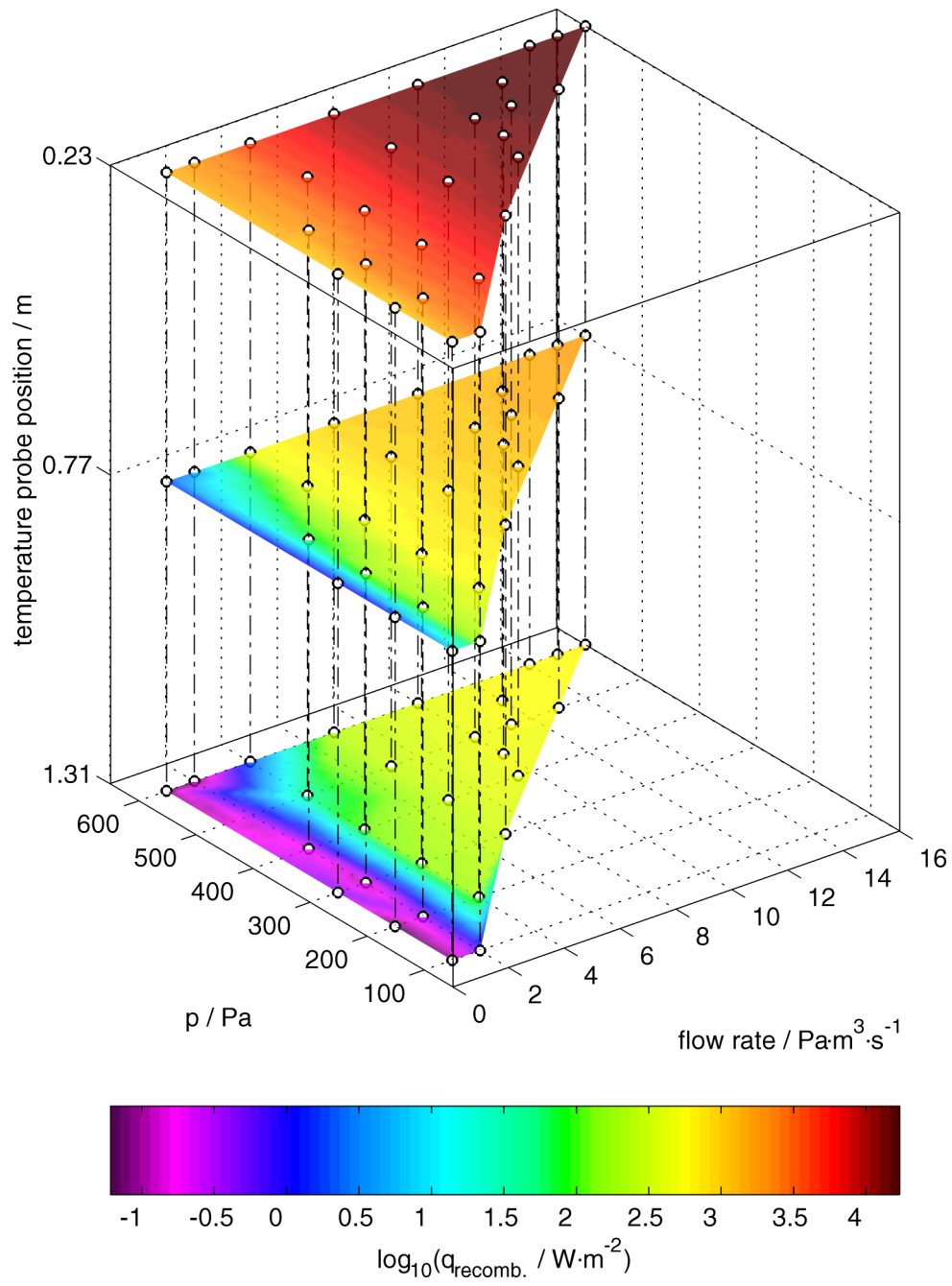


Figure 7.7: Temperature probe results for N_2 : heat of recombination as a function of pressure and flow rate

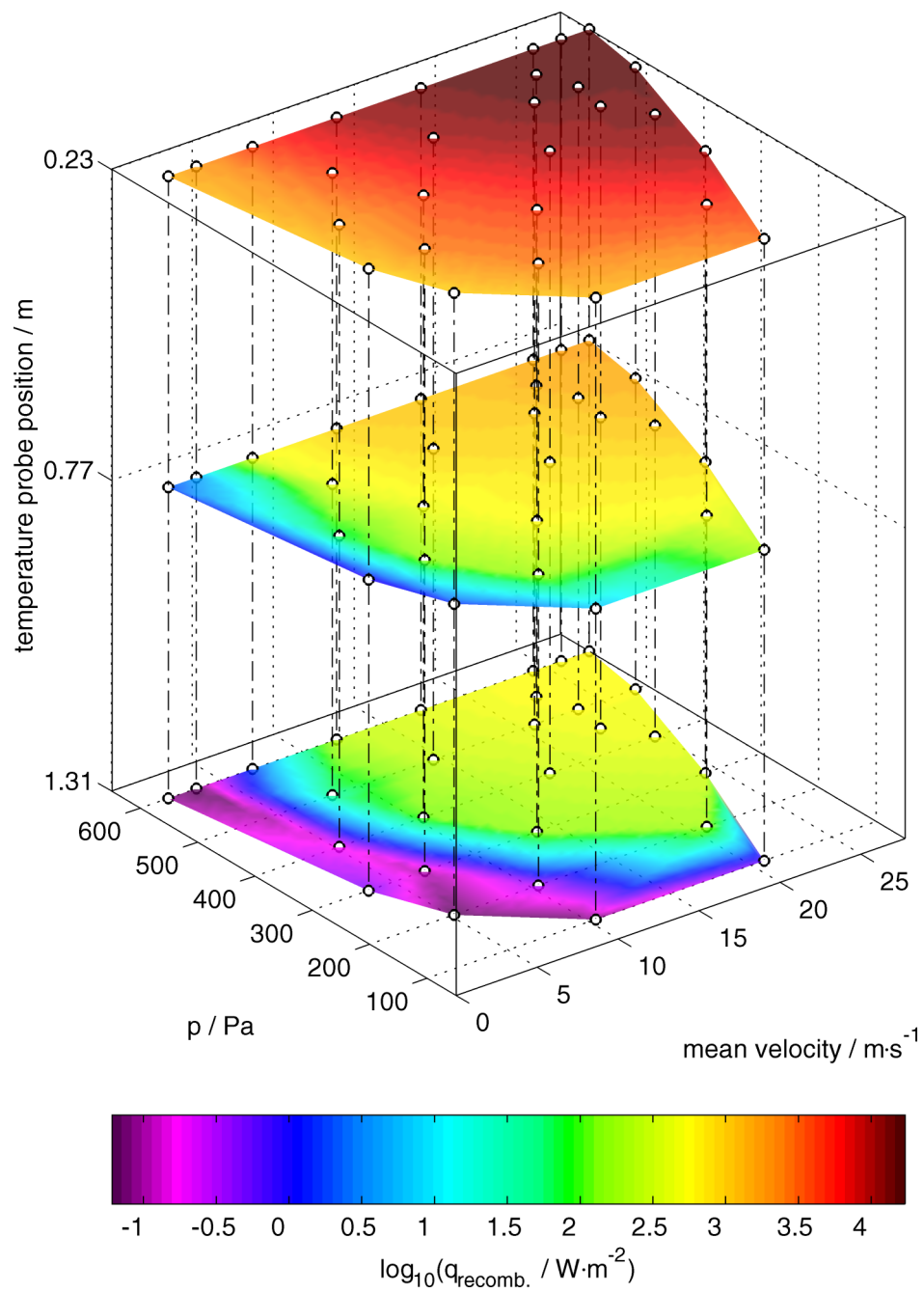


Figure 7.8: Temperature probe results for N_2 : heat of recombination of as a function of pressure and mean velocity

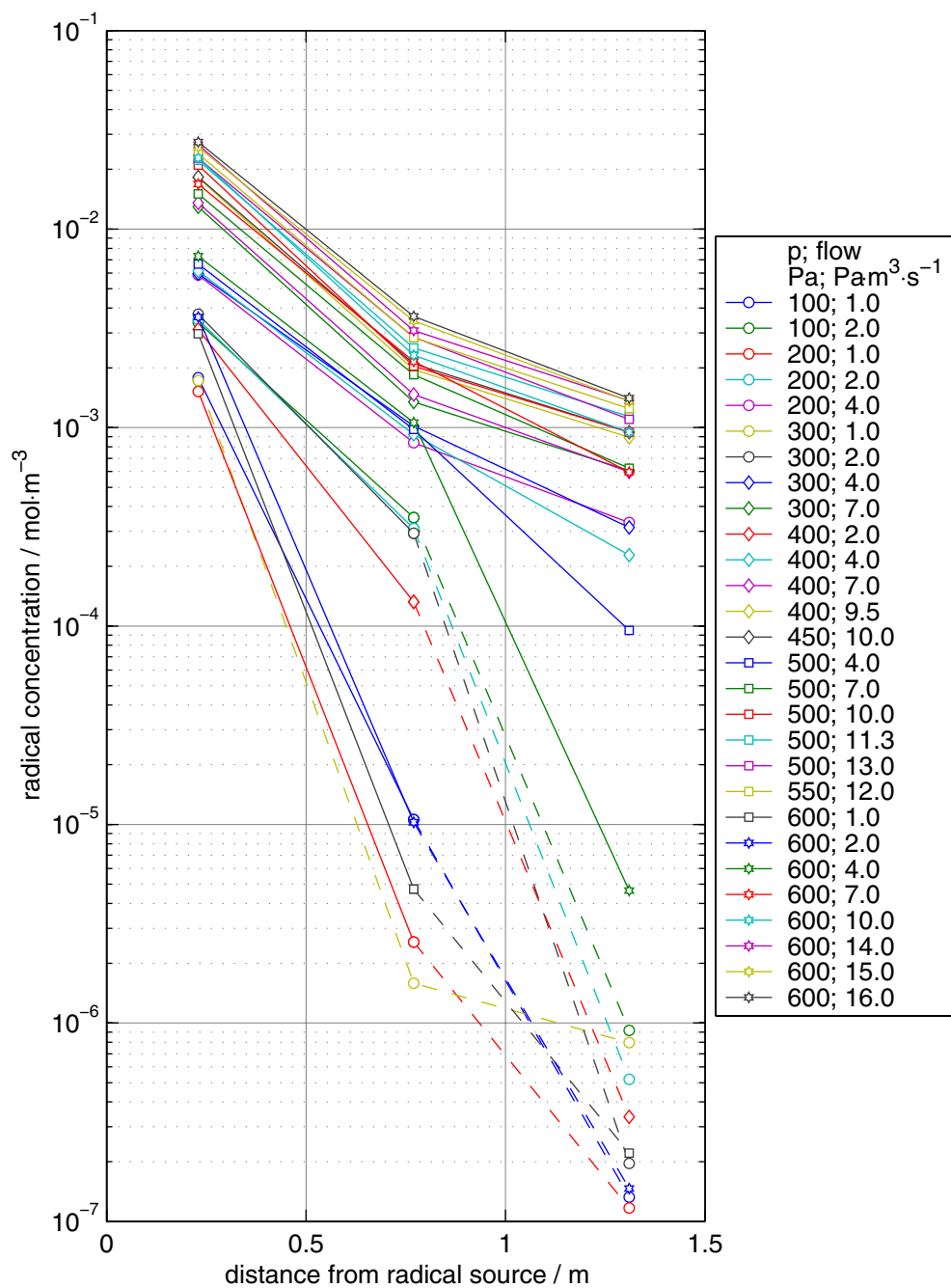


Figure 7.9: Temperature probe results for N₂: radical concentration as a function of the temperature probe position

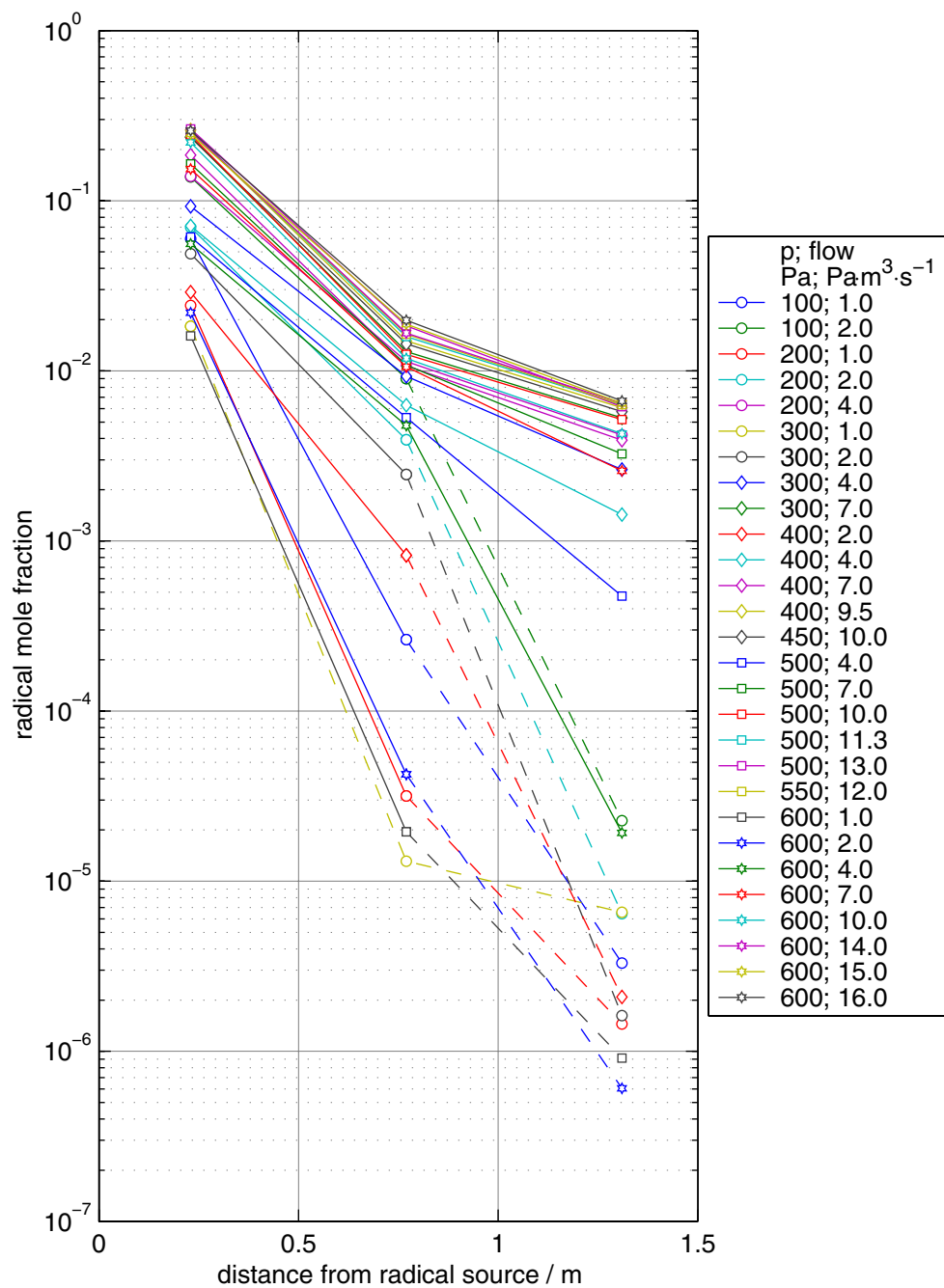


Figure 7.10: Temperature probe results for N₂: radical mole fraction as a function of the temperature probe position

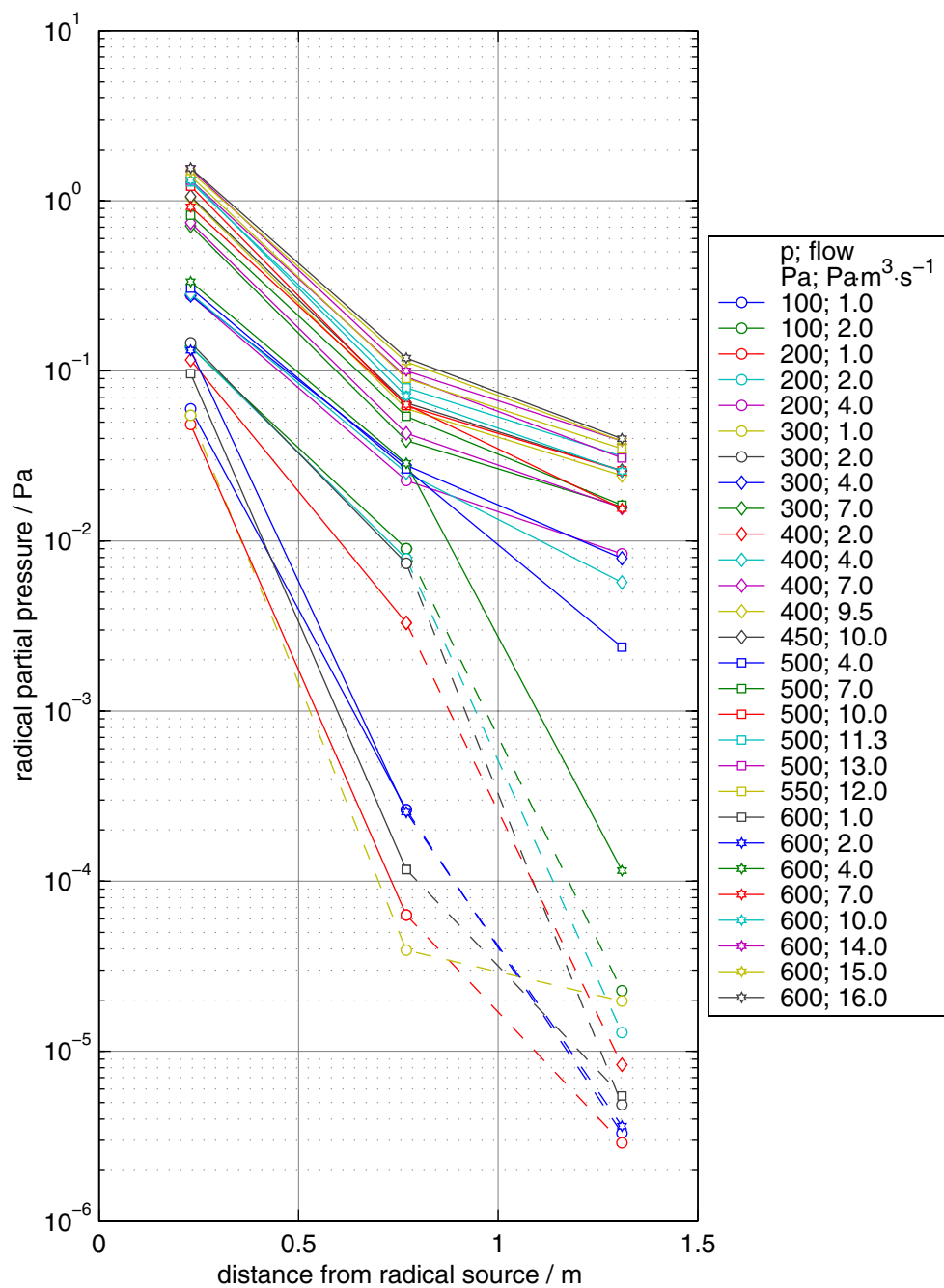


Figure 7.11: Temperature probe results for N_2 : radical partial pressure as a function of the temperature probe position

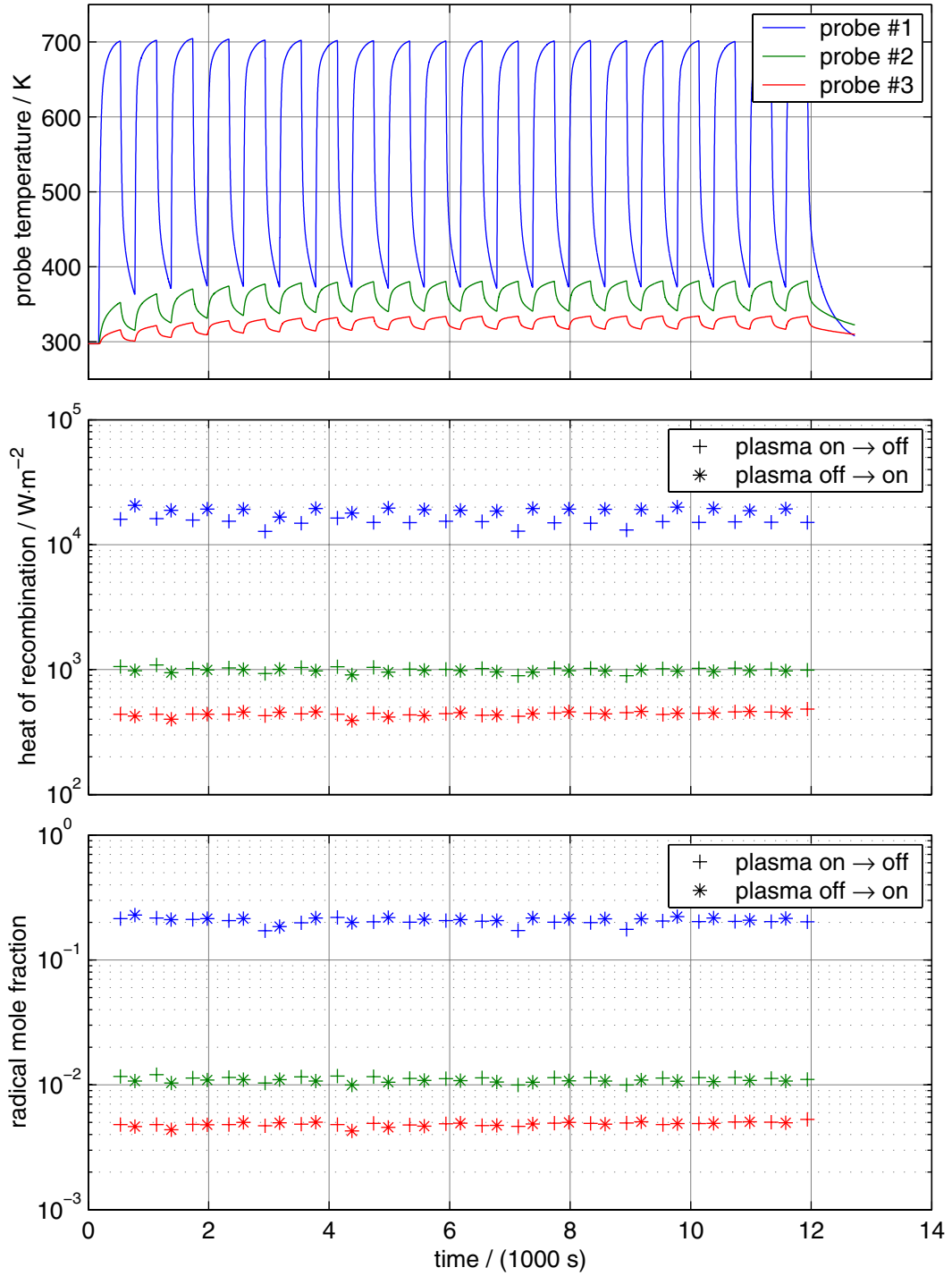


Figure 7.12: Measurement data from an experimental run with nitrogen at 500 Pa and $10 \text{ Pa} \cdot \text{m}^3 \cdot \text{s}^{-1}$ with the radical source being repeatedly switched on and off

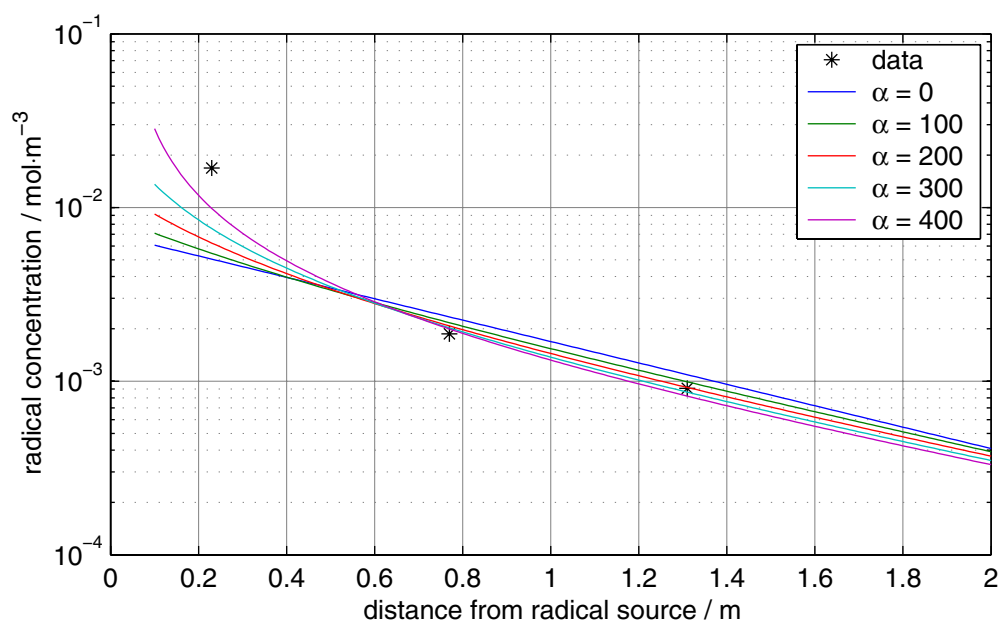
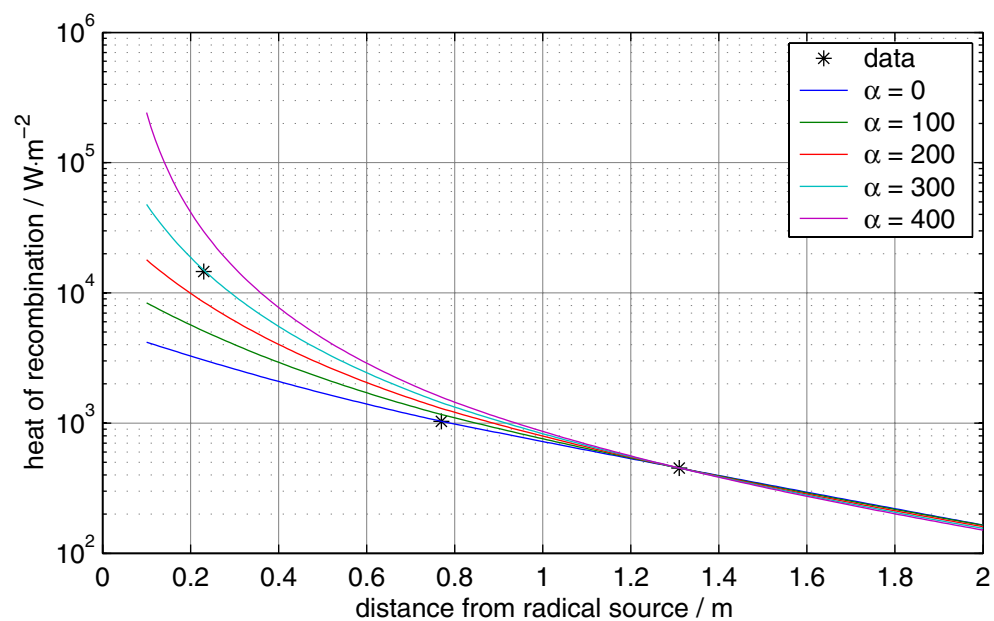


Figure 7.13: Evaluation of temperature probe data (500 Pa, $10 \text{ Pa}\cdot\text{m}^3\cdot\text{s}^{-1}$) using a second order model. The points marked as “data” are calculated from the measurement data using a constant value for γ .

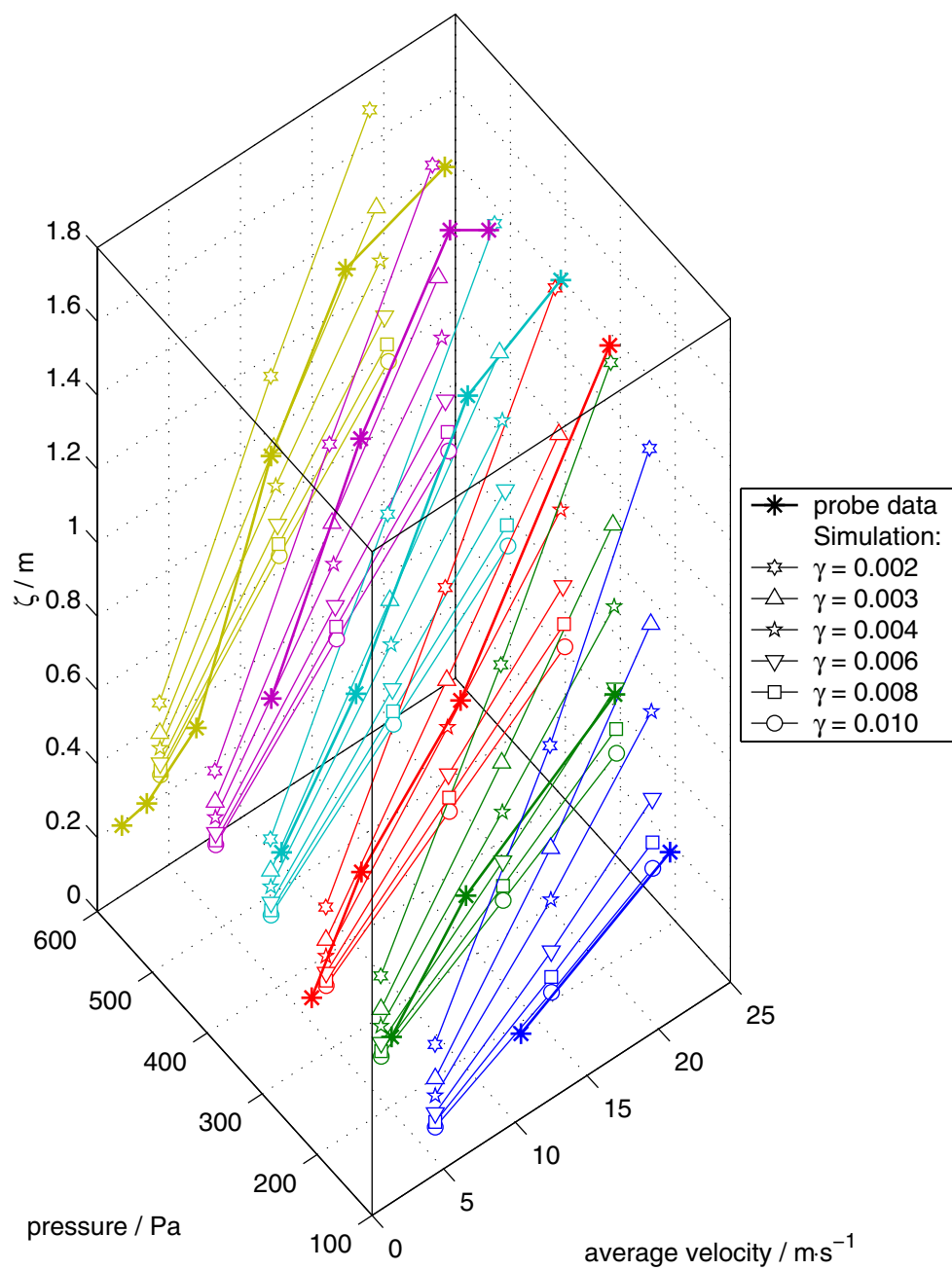


Figure 7.14: Comparison of characteristic decay lengths ζ of nitrogen radicals obtained from temperature probe data and simulation

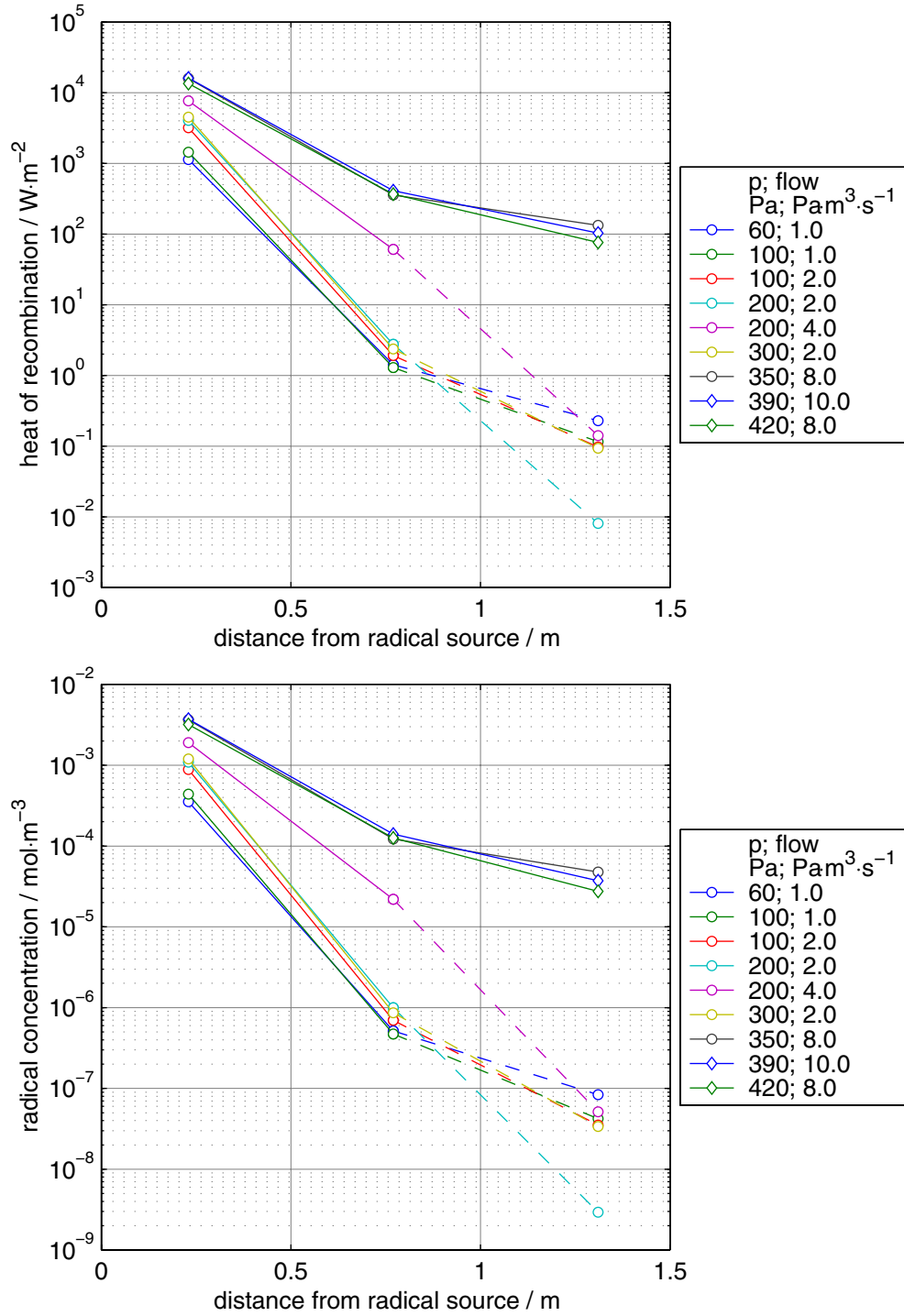


Figure 7.15: Temperature probe results for Ar – O₂: heat of recombination and concentration of oxygen radicals as a function of the temperature probe position

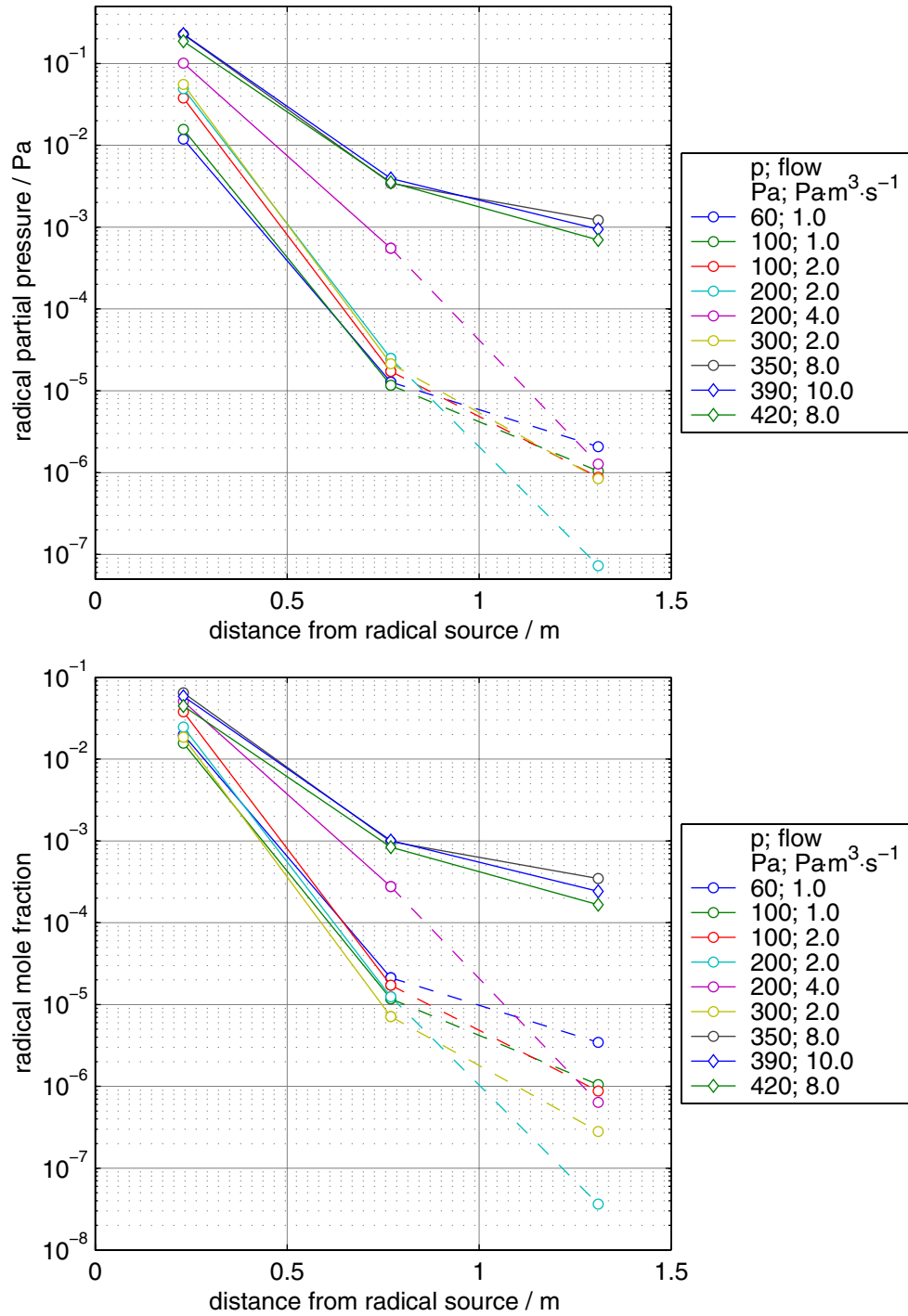


Figure 7.16: Temperature probe results for Ar – O₂: partial pressure and mole fraction of oxygen radicals as a function of the temperature probe position

Part IV

Summary

8 Discussion

In the preceding chapters a variety of experiments have been described, each with the intention to investigate a particular aspect of the radical treatment method. In this chapter the results shall be reviewed and discussed.

The ESD experiment was carried out to determine the cleaning efficiency of the radical treatment method. This choice is justified because the molecular desorption yield is an important parameter for the operation of LHC and it has been used as a measure of cleanliness many times in the past. The results of this experiment show, that a reduction of η by a factor 10 and more can be achieved after a reasonable treatment time (30 min in the case of oxygen radicals, 4 h in the case of nitrogen radicals). This reduction is comparable with values reported in literature for 24 h bake-out and glow-discharge cleaning, where reduction factors lie typically between 10 and 100. The results also show, that oxygen radicals reduce the molecular desorption yield much more efficiently than nitrogen radicals. Since the heat of recombination of these two species is comparable, this is a clear indication that in the case of oxygen radicals direct chemical reaction with surface adsorbates is more significant than in the case of nitrogen radicals.

The cleaning effect could also be confirmed with the Auger analyses of radical treated samples. Since these measurements were performed *ex situ* their results should be seen more in a qualitative than a quantitative way. Nevertheless, since we compared treated samples with non-treated samples, changes in surface composition are clearly visible, and a cleaning effect can be observed even on heavily contaminated samples.

The assumption that radicals also react with the surface material itself could be confirmed in the case of oxygen radicals. The results from XPS analysis reveal that the “natural” copper oxide Cu_2O is replaced with CuO . We assume that this is also the reason for the quite significant reduction of the secondary electron yield (as shown in figure 5.13 on page 70).

The simulation of the radical flow and measurement of the heat of recombination dealt with a completely different aspect of the radical treatment method. Their purpose was to investigate the mechanisms governing the radical transport through long and narrow vacuum chambers. It could be shown that the dominant loss mechanism is radial diffusion to the vacuum chamber wall with subsequent wall recombination. Longitudinal radical concentrations follow basically an exponential decay law, and the characteristic decay length depends mainly on the speed of the flow, the pressure, and the wall recombination probability. The results obtained from simulation and experiment are in quite good agreement, thus justifying the model used for the simulation. Comparison of the results even permits an estimation of the recombination probability (see figure 7.14 on page 162) which is in good agreement with literature.

Combining the results of all experiments allows us – at least for simple vacuum chamber geometries and for “simple” radicals like atomic nitrogen and oxygen – to specify reasonable operating conditions for practical applications and to estimate treatment time and cleaning efficiency. As an example, the treatment of a typical LHC beam pipe shall be given: from ESD measurements we know that a reduction of η by a factor of 10 is achieved after a treatment time of about 30 min, and simulation has shown a reduction of the radical concentration by a factor of 100 after 8 m (the half distance between the two extremities of an LHC dipole). Hence, we would need about two days of continuous treatment with oxygen radicals in order to achieve a reasonable reduction of the molecular desorption yield. Since the decay of radicals over the length of a long pipe is exponential, the radical concentration after a certain distance varies strongly with even a slight variation of the wall recombination probability. Hence, the necessary treatment time for long pipes depends strongly on the poorly known recombination probability.

9 Conclusion

This work was carried out in the vacuum group of the LHC division at CERN. Its aim was to investigate the radical treatment method in general and its application for the conditioning of surfaces in the LHC beam vacuum system in particular.

With the experiments described in this work we were able to demonstrate the capabilities and limitations of the radical treatment method. Of course, the picture is not (yet) complete, there are still open questions and a lot of ideas which could not be realised due to lack of time. The temperature probes are for example very “primitive” instruments to measure radical densities – more sophisticated techniques like titration, absorption spectroscopy, or laser induced fluorescence exist, but are much more expensive and time consuming to implement. Or, as another example, it would certainly be interesting and important to investigate in detail the reactions between radicals and surfaces that lead to the effects observed in our experiments.

In view of a practical application, the distance over which radicals have to travel is definitely a limiting factor. In the particular case of the LHC beam vacuum system, radical treatment is certainly feasible but for sure not very practicable. On the contrary, for shorter vacuum systems the radical treatment method is certainly an interesting alternative and/or supplement to existing treatment methods.

Appendix

A Fundamental physical constants

The numerical values of the fundamental physical constants are taken from [131], page 1808.

Quantity		Value
c	speed of light in vacuum	$299\,792\,458\,\text{m} \cdot \text{s}^{-1}$
μ_0	magnetic constant ($4\pi \cdot 10^{-7}$)	$12.566\,470\,614 \dots \times 10^{-7}\,\text{N} \cdot \text{A}^{-2}$
ϵ_0	electric constant ($\frac{1}{\mu_0 c^2}$)	$8.854\,187\,817 \dots \times 10^{-12}\,\text{F} \cdot \text{m}^{-1}$
h	Planck constant	$6.626\,068\,76(52) \times 10^{-34}\,\text{J} \cdot \text{s}$
\hbar	reduced Planck constant ($\frac{h}{2\pi}$)	$1.054\,571\,596(82) \times 10^{-34}\,\text{J} \cdot \text{s}$
e	elementary charge	$1.602\,176\,462(63) \times 10^{-19}\,\text{C}$
α	fine-structure constant ($\frac{e^2}{4\pi\epsilon_0\hbar c}$)	$7.297\,352\,533(27) \times 10^{-3}$
k	Boltzmann constant	$1.380\,6503(24) \times 10^{-23}\,\text{J} \cdot \text{K}^{-1}$
N_A	Avogadro constant	$6.022\,141\,99(47) \times 10^{23}\,\text{mol}^{-1}$
R	molar gas constant	$8.314\,472(15)\,\text{J} \cdot \text{mol}^{-1} \cdot \text{K}^{-1}$
m_e	electron mass	$9.109\,381\,88(72) \times 10^{-31}\,\text{kg}$
m_p	proton mass	$1.672\,621\,58(13) \times 10^{-27}\,\text{kg}$
u	atomic mass unit ($\frac{1}{12} m(^{12}\text{C})$)	$1.660\,538\,73(13) \times 10^{-27}\,\text{kg}$

B Some LHC design parameters

The values in this table, taken from [5], apply if LHC is operated with protons at nominal, or collision energy.

Parameter	Value	Unit
Proton energy at collision (nominal energy)	7	TeV
Relativistic factor	7461	
Ring circumference	26658.883	m
Revolution frequency	11.2455	kHz
Bunch spacing	7.48	m
Bunch separation	24.95	ns
Number of available bunch places	3564	
Number of bunches	2835	
Number of protons per bunch	1.05×10^{11}	
R.m.s. x,y beam size in arc	0.303	mm
R.m.s. x,y beam size at interaction points	15.9	μm
R.m.s. bunch length	7.7	cm
R.m.s. bunch length	0.257	ns
Circulating beam current	0.536	A
Stored energy per beam	334	MJ
Expected luminosity	1.00×10^{34}	$\text{cm}^{-2} \cdot \text{s}^{-1}$
Main bending magnets (dipoles)		
Number of main dipoles	1232	
Magnetic length per dipole	14.2	m

continued on next page

continued from previous page

Parameter	Value	Unit
Bending radius	2784.32	m
Nominal field	8.386	T
Synchrotron radiation in main dipoles		
Instantaneous power loss per proton	1.84×10^{-11}	W
Energy loss of a proton per turn	6.71	keV
Critical photon energy	44.1	eV
Number of emitted photons per unit time per proton	8.46×10^6	s ⁻¹
Synchrotron radiation power per unit length	0.206	W · m ⁻¹

C ESD experiment: settings and calibration data

This appendix summarises the numerical values of the parameters required to calculate the molecular desorption yield in chapter 4.

	$S/\text{l} \cdot \text{s}^{-1}$	$S/\text{m}^3 \cdot \text{s}^{-1}$
H ₂	44.72	4.472×10^{-2}
N ₂	26.48	2.648×10^{-2}
CO	26.48	2.648×10^{-2}
CO ₂	23.77	2.377×10^{-2}
CH ₄	29.73	2.973×10^{-2}
C ₂ H ₆	26.07	2.607×10^{-2}
Ar	24.34	2.434×10^{-2}
H ₂ O	29.06	2.906×10^{-2}

Table C.1: Effective pumping speed

SVT gauge	CSF gauge	mass spectrometer
$I_e^* = 4 \text{ mA}$	$I_e^* = 7.7 \text{ mA}$	$I_e = 1 \text{ mA}$

Table C.2: Emission current of the Bayard Alpert gauges and the quadrupole mass spectrometer

	SVT gauge		CSF gauge	
	s^*/torr^{-1}	s^*/Pa^{-1}	s^*/torr^{-1}	s^*/Pa^{-1}
H ₂	18.06	1.36×10^{-1}	4.70	3.53×10^{-2}
N ₂	46.57	3.50×10^{-1}	15.62	1.17×10^{-1}
CO	45.79	3.44×10^{-1}	17.02	1.28×10^{-1}
CO ₂	60.62	4.56×10^{-1}	19.88	1.49×10^{-1}
CH ₄	62.50	4.70×10^{-1}	23.79	1.79×10^{-1}
C ₂ H ₆	113.91	8.56×10^{-1}	35.15	2.64×10^{-1}
Ar	53.30	4.01×10^{-1}	17.99	1.35×10^{-1}
H ₂ O	64.73	4.87×10^{-1}	10.21	7.68×10^{-2}

Table C.3: Absolute sensibilities of the Bayard Alpert gauges

	H ₂	N ₂	CO	CO ₂	CH ₄	C ₂ H ₆	Ar	H ₂ O
s'	1.0000	0.7527	0.7881	0.4523	1.0711	0.8928	0.4819	0.5044

Table C.4: Sensibilities relative to H₂⁺ of the quadrupole mass spectrometer

M/Z	H ₂	N ₂	CO	CO ₂	CH ₄	C ₂ H ₆	Ar	H ₂ O
1	0.0333				0.1122	0.1311		0.2908
2	1.0000				0.0426	0.0913		
12			0.1022	0.2213	0.0367	0.0140		
13					0.0987	0.0246		
14		0.1876	0.0107	0.0018	0.1862	0.0591		
15					0.8572	0.0795		
16			0.0459	0.3022	1.0000			0.1048
17					0.0126			0.3144
18								1.0000
20							0.2246	
22				0.0282				
25						0.0540		
26						0.2626		
27						0.3528		
28		1.0000	1.0000	0.2263		1.0000		
29		0.0074	0.0111	0.0033		0.1935		
30						0.2293		
36							0.0044	
38							0.0015	
40							1.0000	
44				1.0000				

Table C.5: Cracking pattern of the quadrupole mass spectrometer (the numbers in the first column are approximate values for the mass-to-charge-ratio of the ions, measured in atomic mass unit per elementary charge)

D Calculation of partial pressures from gauge and mass spectrometer data

The procedure which is described in this chapter has been used in this work to calculate partial pressures and their variances from gauge and mass spectrometer data. It is based on a procedure frequently used in data analysis, the so-called *chi-square minimisation*, as described in [128], chapter 15.

If we consider a gas mixture consisting of J species, we have $J + 1$ unknowns, which are the partial pressures p_j ($j = 1 \dots J$) and the reference sensibility of the mass spectrometer s_{ref} . Hence, we need at least $J + 1$ equations to determine partial pressures of J species. These equations have to be provided by means of measurement. Since one equation results from the signal of the total pressure gauge, at least J different measurements are needed for different settings M/Z of the mass spectrometer. The system of equations is then given by

$$\begin{aligned}
 I_{m_1}^+ &= I_e s_{ref} \sum_{j=1}^J s'_j x_{m_1,j} p_j \\
 I_{m_2}^+ &= I_e s_{ref} \sum_{j=1}^J s'_j x_{m_2,j} p_j \\
 &\vdots \\
 I_{m_N}^+ &= I_e s_{ref} \sum_{j=1}^J s'_j x_{m_N,j} p_j \\
 I^* &= I_e^* \sum_{j=1}^J s_j^* p_j
 \end{aligned} \tag{D.1}$$

where N is the number of measurements from the mass spectrometer ($N \geq J$). $I_{m_i}^+$ are the signals from the mass spectrometer at $M/Z = m_i$, I_e the emission current, s'_j the relative sensibilities for species j , and $x_{m_i,j}$ the cracking pattern for species j at $M/Z = m_i$. I^* is the signal from the total pressure gauge, I_e^*

the emission current of the gauge, and s_j^* are the absolute sensibilities of the gauge for species j . With the definitions

$$y_i = \frac{I_{m_i}^+}{I_e}, \quad (\text{D.2})$$

$$a_j = s_{ref} p_j, \quad (\text{D.3})$$

and

$$X_{i,j} = s'_j x_{m_i,j}, \quad (\text{D.4})$$

equations (D.1) can be rewritten as

$$y_i = \sum_{j=1}^J X_{i,j} a_j; \quad i = 1 \dots N \quad (\text{D.5})$$

and

$$s_{ref} = \frac{I_e^*}{I^*} \sum_{j=1}^J s_j^* a_j. \quad (\text{D.6})$$

If $N > J$ the system of equations (D.5) is overdetermined and in general does not have a solution in a mathematical sense. Hence, we have to find the most likely values for a_j by some estimation. The mathematical means to do this is given by the chi-square minimisation. The χ^2 for (D.5) is given by

$$\chi^2 = \sum_{i=1}^N \frac{\left(y_i - \sum_{j=1}^J X_{i,j} a_j \right)^2}{\sigma^2(y_i)}. \quad (\text{D.7})$$

$\sigma^2(y_i)$ is the variance of y_i which has to be determined from measurement. From equation (D.2), it follows from the law of propagation of uncertainties that

$$\frac{\sigma^2(y_i)}{y_i^2} = \frac{\sigma^2(I_{m_i}^+)}{(I_{m_i}^+)^2} + \frac{\sigma^2(I_e)}{(I_e)^2} \quad (\text{D.8})$$

with $\sigma^2(I_{m_i}^+)$ and $\sigma^2(I_e)$ being the (measured) variances of $I_{m_i}^+$ and I_e , respectively.

Finding the minimum of χ^2 with respect to the parameters a_j is mathematically equivalent to solving the vector – matrix equation

$$\tilde{\alpha} \cdot \vec{a} = \vec{\beta} \quad (\text{D.9})$$

if the square matrix $\tilde{\alpha}$ and the vectors \vec{a} and $\vec{\beta}$ are given by

$$\tilde{\alpha} = \begin{pmatrix} \alpha_{1,1} & \cdots & \alpha_{1,J} \\ \vdots & \ddots & \vdots \\ \alpha_{J,1} & \cdots & \alpha_{J,J} \end{pmatrix}, \vec{\beta} = \begin{pmatrix} \beta_1 \\ \vdots \\ \beta_J \end{pmatrix}, \vec{a} = \begin{pmatrix} a_1 \\ \vdots \\ a_J \end{pmatrix} \quad (\text{D.10})$$

with the definitions

$$\alpha_{k,j} = \sum_{i=1}^N \frac{X_{i,j} X_{i,k}}{\sigma^2(y_i)} \quad (\text{D.11})$$

and

$$\beta_k = \sum_{i=1}^N \frac{y_i X_{i,k}}{\sigma^2(y_i)}. \quad (\text{D.12})$$

Hence, values of a_j that minimise χ^2 in equation (D.7) are given by the solution of equation (D.9)

$$\vec{a} = \tilde{\alpha}^{-1} \cdot \vec{\beta}. \quad (\text{D.13})$$

Besides of getting a mathematically well justified estimation of the parameters a_j (i.e. the so-called *maximum likelihood estimation*), the method of chi-square minimisation has also the huge advantage to give estimations for the variances (and covariances) of the parameters a_j , from which we can estimate the variances of the partial pressures p_j . The estimated variances of a_j are given by the main diagonal elements of inverse matrix $\tilde{\alpha}^{-1}$ and the covariances by the off-diagonal elements of $\tilde{\alpha}^{-1}$, hence

$$Cov(a_j, a_k) = (\alpha^{-1})_{j,k}. \quad (D.14)$$

and

$$\sigma^2(a_j) = Cov(a_j, a_j) = (\alpha^{-1})_{j,j}. \quad (D.15)$$

With the results from equation (D.13), the reference sensibility s_{ref} can be directly calculated using equation (D.6). The estimated variance of s_{ref} follows from the law of propagation of uncertainties (cf. [132], appendix A).

$$\frac{\sigma^2(s_{ref})}{s_{ref}^2} = \frac{\sigma^2(I^*)}{(I^*)^2} + \frac{\sigma^2(I_e^*)}{(I_e^*)^2} + \frac{\sum_{j=1}^J \sum_{k=1}^J s_j^* s_k^* Cov(a_j, a_k)}{\left(\sum_{j=1}^J s_j^* a_j \right)^2} \quad (D.16)$$

Finally the partial pressures can be calculated according to equation (D.3), hence

$$p_j = \frac{a_j}{s_{ref}} \quad (D.17)$$

and the estimated variance for p_j follows again from the law of propagation of uncertainties as

$$\frac{\sigma^2(p_j)}{p_j^2} = \frac{\sigma^2(a_j)}{a_j^2} + \frac{\sigma^2(s_{ref})}{s_{ref}^2} - 2 \frac{Cov(a_j, s_{ref})}{a_j s_{ref}} \quad (D.18)$$

where the covariance of a_j and s_{ref} follows from equation (D.6) as

$$Cov(a_j, s_{ref}) = \sum_{k=1}^J \frac{\partial s_{ref}}{\partial a_k} Cov(a_j, a_k) = \frac{I_e^*}{I^*} \sum_{k=1}^J s_k^* Cov(a_j, a_k). \quad (D.19)$$

E The covariant formalism

In this chapter, a short overview of the covariant formalism shall be given. Complete formulations of this powerful mathematical tool can be found for example in [110] and [111].

Throughout this chapter I will make use of the *summation convention* ([110], page 6):

Whenever the same latin letter (say n) appears in a product once as a subscript and once as a superscript, it is understood that this means a sum of all terms of this kind (i.e. for $n = 1, 2, 3$).

Covariant notation

In the Cartesian co-ordinate system, the three dimensional space is parameterised by the Cartesian co-ordinates x , y , and z :

$$\vec{r} = \vec{r}(x, y, z) = x \vec{e}_x + y \vec{e}_y + z \vec{e}_z \quad (\text{E.1})$$

where \vec{e}_x , \vec{e}_y , and \vec{e}_z are the unit vectors in x-, y-, and z-direction respectively. With the definitions $x^1 := x$, $x^2 := y$, $x^3 := z$ and $\vec{e}_1 := \vec{e}_x$, $\vec{e}_2 := \vec{e}_y$, $\vec{e}_3 := \vec{e}_z$ and with the summation convention, equation (E.1) can be written in a more compact way:

$$\vec{r} = x^i \vec{e}_i. \quad (\text{E.2})$$

We can now introduce a new set of co-ordinates (ξ^1, ξ^2, ξ^3) to parameterise space (e.g. (r, φ, z) for cylindrical co-ordinates or (r, ϑ, φ) for spherical co-ordinates), such that

$$\vec{r} = \vec{r}(\xi^1, \xi^2, \xi^3) = x^i(\xi^1, \xi^2, \xi^3) \vec{e}_i. \quad (\text{E.3})$$

The infinitesimal displacement vector is given by

$$d\vec{r} = \vec{r}(\xi^1 + d\xi^1, \xi^2 + d\xi^2, \xi^3 + d\xi^3) - \vec{r}(\xi^1, \xi^2, \xi^3) = \vec{g}_i d\xi^i. \quad (\text{E.4})$$

Here, the vectors \vec{g}_i are called the *covariant base vectors*. It follows from equation (E.4) that

$$\vec{g}_i = \frac{\partial \vec{r}}{\partial \xi^i}. \quad (\text{E.5})$$

A second set of base vectors, the *contravariant base vectors*, denoted by superscript indices can be defined through the relation

$$\vec{g}_i \cdot \vec{g}^j = \delta_i^j \quad (\text{E.6})$$

where δ_i^j is the *Kronecker delta* ($\delta_i^j = 1$ for $i = j$, otherwise $\delta_i^j = 0$).

Any vector entity \vec{a} can be described either in terms of the covariant base vectors or in terms of the contravariant base vectors:

$$\vec{a} = a^i \vec{g}_i = a_i \vec{g}^i. \quad (\text{E.7})$$

The a^i are called the *contravariant components* of vector \vec{a} , whereas the a_i are called the *covariant components* of vector \vec{a} .

As with vectors, any second rank tensor entity \tilde{c} can be described by its covariant components c_{ij} or contravariant components c^{ij} , but also by mixed components c_i^j or c^i_j .

Another important entity is the *metric tensor* \tilde{g} . Its covariant components are given by

$$g_{ij} = g_{ji} = \vec{g}_i \cdot \vec{g}_j \quad (\text{E.8})$$

and its contravariant components by

$$g^{ij} = g^{ji} = \vec{g}^i \cdot \vec{g}^j. \quad (\text{E.9})$$

By means of the metric tensor, contravariant components can be calculated from covariant components and vice versa (also called the *raising* or *lowering* of an index), for example:

$$a^i = g^{ij} a_j \quad \text{or} \quad a_i = g_{ij} a^j \quad (\text{E.10})$$

or

$$c^{ij} = g^{ik} g^{jl} c_{kl} \quad \text{or} \quad c_{ij} = g_{ik} g_{jl} c^{kl} \quad (\text{E.11})$$

Because of equations (E.6), (E.8), and (E.9), the dot product of two vectors \vec{a} and \vec{b} is given by any of the following expressions:

$$\vec{a} \cdot \vec{b} = a^i b_i = a_i b^i = a^i b^j g_{ij} = a_i b_j g^{ij}. \quad (\text{E.12})$$

It should be stated at this point that the value of the dot product of two vectors is independent of the choice of the co-ordinate system (i.e. an *invariant* with respect to co-ordinate transformations).

To write down the cross product of two vectors $\vec{a} \times \vec{b}$, we need to introduce two more entities: g , the determinant of the covariant coefficient matrix of the metric tensor \tilde{g}

$$g = \begin{vmatrix} g_{11} & g_{12} & g_{13} \\ g_{21} & g_{22} & g_{23} \\ g_{31} & g_{32} & g_{33} \end{vmatrix} \quad (\text{E.13})$$

and the *epsilon tensor* $\tilde{\varepsilon}$ (also called *Levi-Civita tensor*, [133], page 75)

$$\varepsilon_{ijk} = \begin{cases} +\sqrt{g} & \text{if } (i, j, k) \text{ is an even permutation of } (1, 2, 3) \\ -\sqrt{g} & \text{if } (i, j, k) \text{ is an odd permutation of } (1, 2, 3) \\ 0 & \text{otherwise} \end{cases} \quad (\text{E.14})$$

The cross product is now given by

$$\vec{a} \times \vec{b} = \varepsilon_{ijk} a^j b^k \vec{g}^i \quad (\text{E.15})$$

Covariant derivative

If we want to calculate how a vector \vec{v} changes (its length and direction) when one co-ordinate changes from ξ^j to $\xi^j + d\xi^j$, we have to proceed like follows:

$$\frac{\partial \vec{v}}{\partial \xi^j} = \frac{\partial}{\partial \xi^j} (v^i \vec{g}_i) = \frac{\partial v^i}{\partial \xi^j} \vec{g}_i + v^i \frac{\partial \vec{g}_i}{\partial \xi^j} = \frac{\partial v^i}{\partial \xi^j} \vec{g}_i + v^i \frac{\partial^2 \vec{r}}{\partial \xi^i \partial \xi^j}. \quad (\text{E.16})$$

The last term in equation (E.16) has been obtained using equation (E.5). The second derivative of \vec{r} is again a vector, hence it can be written in terms of its covariant or contravariant components:

$$\frac{\partial^2 \vec{r}}{\partial \xi^i \partial \xi^j} = \Gamma_{ijk} \vec{g}^k = \Gamma_{ij}^k \vec{g}_k. \quad (\text{E.17})$$

The Γ_{ijk} and Γ_{ij}^k are called the *Christoffel symbols*. Since they are the covariant and contravariant components of the same vector, it holds

$$\Gamma_{ij}^k = \Gamma_{ijl} g^{lk}. \quad (\text{E.18})$$

One way to calculate the Christoffel symbols is given by [110]

$$2 \Gamma_{ijk} = \frac{\partial g_{jk}}{\partial \xi^i} + \frac{\partial g_{ki}}{\partial \xi^j} - \frac{\partial g_{ij}}{\partial \xi^k}. \quad (\text{E.19})$$

Using equation (E.17), equation (E.16) can be written after some rearrangement of indices:

$$\frac{\partial \vec{v}}{\partial \xi^j} = \left(\frac{\partial v^i}{\partial \xi^j} + v^k \Gamma_{jk}^i \right) \vec{g}_i = v^i|_j \vec{g}_i. \quad (\text{E.20})$$

$v^i|_j$ are mixed variance components of a second rank tensor called the *covariant derivative* of \vec{v} .

Consequently we can define the covariant derivative of a tensor of any rank r , which is a tensor of rank $r + 1$, for example

$$\begin{aligned} \phi|_i &= \frac{\partial \phi}{\partial \xi^i} \\ v^i|_j &= \frac{\partial v^i}{\partial \xi^j} + v^k \Gamma_{jk}^i \\ A^{ij}|_k &= \frac{\partial A^{ij}}{\partial \xi^k} + A^{lj} \Gamma_{kl}^i + A^{il} \Gamma_{kl}^j \end{aligned} \quad (\text{E.21})$$

The commonly used operators in vector analysis, gradient, divergence, and curl can easily be written in terms of the covariant derivative:

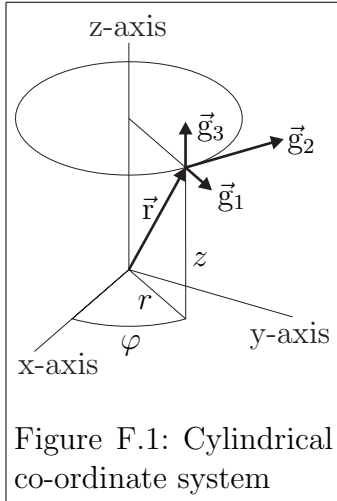
$$\text{grad } \phi = \vec{\nabla} \phi = \phi|_i \vec{g}^i = g^{ij} \phi|_j \vec{g}_i \quad (\text{E.22})$$

$$\text{div } \vec{v} = \vec{\nabla} \cdot \vec{v} = v^i|_i \quad (\text{E.23})$$

$$\text{curl } \vec{v} = \vec{\nabla} \times \vec{v} = \varepsilon^{ijk} v_j|_k \vec{g}_i \quad (\text{E.24})$$

F Cylindrical co-ordinate system

As it is shown in figure F.1, the cylindrical co-ordinates of a position vector \vec{r} are (r, φ, z) , where r is the distance from the z -axis, φ the angle of rotation around the z -axis, measured from the xz -plane, and z the distance from the xy -plane.



$$\vec{r} = \begin{pmatrix} r \cos \varphi \\ r \sin \varphi \\ z \end{pmatrix}. \quad (\text{F.1})$$

The Cartesian components of the covariant base vectors are given by

$$(\vec{g}_1, \vec{g}_2, \vec{g}_3) = \begin{pmatrix} \cos \varphi & -r \sin \varphi & 0 \\ \sin \varphi & r \cos \varphi & 0 \\ 0 & 0 & 1 \end{pmatrix} \quad (\text{F.2})$$

and the Cartesian components of the contravariant base vectors by

$$(\vec{g}^1, \vec{g}^2, \vec{g}^3) = \begin{pmatrix} \cos \varphi & -\frac{1}{r} \sin \varphi & 0 \\ \sin \varphi & \frac{1}{r} \cos \varphi & 0 \\ 0 & 0 & 1 \end{pmatrix} \quad (\text{F.3})$$

The metric tensor is given by

$$g_{ij} = \begin{pmatrix} 1 & 0 & 0 \\ 0 & r^2 & 0 \\ 0 & 0 & 1 \end{pmatrix} \quad \text{or} \quad g^{ij} = \begin{pmatrix} 1 & 0 & 0 \\ 0 & \frac{1}{r^2} & 0 \\ 0 & 0 & 1 \end{pmatrix} \quad (\text{F.4})$$

and the Christoffel symbols by

$$\{\Gamma_{ij}^1, \Gamma_{ij}^2, \Gamma_{ij}^3\} = \left\{ \begin{pmatrix} 0 & 0 & 0 \\ 0 & -r & 0 \\ 0 & 0 & 0 \end{pmatrix}, \begin{pmatrix} 0 & \frac{1}{r} & 0 \\ \frac{1}{r} & 0 & 0 \\ 0 & 0 & 0 \end{pmatrix}, \begin{pmatrix} 0 & 0 & 0 \\ 0 & 0 & 0 \\ 0 & 0 & 0 \end{pmatrix} \right\}. \quad (\text{F.5})$$

The gradient of a scalar field ϕ is given by

$$\text{grad } \phi = \frac{\partial \phi}{\partial r} \vec{g}_1 + \frac{1}{r^2} \frac{\partial \phi}{\partial \varphi} \vec{g}_2 + \frac{\partial \phi}{\partial z} \vec{g}_3, \quad (\text{F.6})$$

the divergence of a vector field \vec{v} by

$$\text{div } \vec{v} = \frac{1}{r} \frac{\partial(r v^1)}{\partial r} + \frac{\partial v^2}{\partial \varphi} + \frac{\partial v^3}{\partial z}, \quad (\text{F.7})$$

the curl of a vector field \vec{v} by

$$\begin{aligned} \text{curl } \vec{v} = & \frac{1}{r} \left(\frac{\partial v_3}{\partial \varphi} - \frac{\partial v_2}{\partial z} \right) \vec{g}_1 + \frac{1}{r} \left(\frac{\partial v_1}{\partial z} - \frac{\partial v_3}{\partial r} \right) \vec{g}_2 \\ & + \frac{1}{r} \left(\frac{\partial v_2}{\partial r} - \frac{\partial v_1}{\partial \varphi} \right) \vec{g}_3, \end{aligned} \quad (\text{F.8})$$

and the covariant derivative of a vector field \vec{v} by

$$v_i|_j = \begin{pmatrix} \frac{\partial v_1}{\partial r} & \frac{\partial v_1}{\partial \varphi} & \frac{\partial v_1}{\partial z} \\ \frac{\partial v_2}{\partial r} & \frac{\partial v_2}{\partial \varphi} & \frac{\partial v_2}{\partial z} \\ \frac{\partial v_3}{\partial r} & \frac{\partial v_3}{\partial \varphi} & \frac{\partial v_3}{\partial z} \end{pmatrix} + \begin{pmatrix} 0 & -\frac{v_2}{r} & 0 \\ -\frac{v_2}{r} & r v_1 & 0 \\ 0 & 0 & 0 \end{pmatrix} \quad (\text{F.9})$$

Bibliography

- [1] CERN – Centre Européenne pour la Recherche Nucléaire, Route de Meyrin, CH-1211 Genève 23, Switzerland; <http://www.cern.ch>.
- [2] G. M. Fraser, editor. *The particle century*. Institute of Physics Publishing, Bristol, 1998.
- [3] W. Noel Cottingham and Derek A. Greenwood. *An introduction to the standard model of particle physics*. Cambridge University Press, 1998.
- [4] F. Gianotti. Collider physics: LHC. In A. Olchovski, editor, *7th European School of High-Energy Physics*, Casta-Papiernicka, Slovak Republic, 22 August – 4 September 1999. Also published as CERN Yellow Report CERN-2000-007.
- [5] LHC Study Group. The Large Hadron Collider : conceptual design. Technical Report CERN-AC-95-05, CERN, 1995.
- [6] L. R. Evans. The Large Hadron Collider project. LHC Project Report 53, CERN, 1996.
- [7] ATLAS Collaboration. ATLAS : technical proposal for a general-purpose pp experiment at the Large Hadron Collider at CERN. Technical Report CERN-LHCC-94-43, CERN, 1994.
- [8] CMS Collaboration. CMS, the Compact Muon Solenoid : technical proposal. Technical Report CERN-LHCC-94-38, CERN, 1994.
- [9] LHCb Collaboration. LHCb : Technical Proposal. Technical Report CERN-LHCC-98-004, CERN, 1998.
- [10] ALICE Collaboration. ALICE : technical proposal for a large ion collider experiment at the CERN LHC. Technical Report CERN-LHCC-95-71, CERN, 1995.

- [11] Ph. Lebrun. Advanced Superconducting Technology for Global Science: The Large Hadron Collider At Cern. LHC Project Report 499, CERN, 2001.
- [12] A. P. Verweij and L. Buchsbaum. Experimental results of current distribution in Rutherford-type LHC cables. *Cryogenics*, 40:663–670, 2000.
- [13] Ph. Lebrun. Cryogenics for the Large Hadron Collider. LHC Project Report 338, CERN, 1999.
- [14] O. Gröbner. Overview of the LHC vacuum system. *Vacuum*, 60(1–2):25–34, 2001.
- [15] C. Wyss. LHC arc dipole status report. In *1999 Particle Accelerator Conference*, New York City, NY, USA, 29 March – 2 April 1999.
- [16] P. Fessia, D. Perini, S. Russenschuck, Ch. Voellinger, R. Vuillermet, and C. Wyss. Selection of the cross-section design for the LHC main dipole. LHC Project Report 347, CERN, 1999.
- [17] C. Wyss. The LHC magnet programme: From accelerator physics requirements to production in industry. In *7th European Particle Accelerator Conference* [134], pages 207–211.
- [18] M. Modena, M. Bajko, L. Bottura, M. Buzio, P. Fessia, O. Pagano, D. Perini, P. Pagnat, S. Sanfilippo, F. Savary, W. Scandale, A. Siemko, G. Spigo, E. Todesco, I. Vanenkov, J. Vlogaert, and C. Wyss. Final prototypes, first pre-series units and steps towards series production of the LHC main dipoles. LHC Project Report 487, CERN, 2001.
- [19] B. Angerth, F. Bertinelli, J.-C. Brunet, R. Calder, F. Caspers, P. Cruikshank, J.-M. Dalin, O. Gröbner, N. Kos, A. Mathewson, A. Poncet, C. Reymermier, F. Ruggiero, T. Scholz, S. Sgobba, and E. Wallén. The Large Hadron Collider Vacuum System. In *1995 Particle Accelerator Conference*, Dallas, Texas, USA, 1 – 5 May 1995.
- [20] O. Gröbner. Vacuum system for LHC. *Vacuum*, 46(8–10):797–801, 1995.
- [21] O. Gröbner. The LHC vacuum system. LHC Project Report 181, CERN, 1998.
- [22] O. Gröbner. LHC vacuum system. In Turner [135], pages 291–305. Also published as CERN Yellow Report CERN-99-05.

- [23] Edmund Wilson. *An Introduction to Particle Accelerators*. Oxford University Press, 2001.
- [24] C. Rathjen, F. Caspers, P. Pugnât, S. Russenschuck, and A. Siemko. Currents in, forces on and deformations/displacements of the LHC beam screen expected during a magnet quench. LHC Project Report 489, CERN, 2001.
- [25] P. Cruikshank, K. Artoos, F. Bertinelli, J.-C. Brunet, R. Calder, C. Campedel, I. Collins, J.-M. Dalin, B. Feral, O. Gröbner, N. Kos, A. Mathewson, L. Nikitina, I. Nikitine, A. Poncet, C. Reymermier, G. Schneider, I. Sexton, S. Sgobba, R. Valbuena, and R. Veness. Mechanical design aspects of the LHC beam screen. LHC Project Report 128, CERN, 1997.
- [26] K. Artoos, P. Cruikshank, and N. Kos. Mechanical and thermal measurements on a 11 m long beam screen in the LHC magnet test string during RUN 3 A. LHC Project Note 178, CERN, 1999.
- [27] F. Caspers, M. Morvillo, F. Ruggiero, and J. Tan. Surface resistance measurements and estimate of the beam-induced resistive wall heating of the LHC dipole beam screen. LHC Project Report 307, CERN, 1999.
- [28] F. Caspers, A. Mostacci, F. Ruggiero, and L. Palumbo. Image currents in azimuthally inhomogeneous metallic beam pipes. LHC Project Report 493, CERN, 2001.
- [29] O. Groebner, A. G. Mathewson, H. Stoeri, P. Strubin, and R. Souchet. Studies of photon induced gas desorption using synchrotron radiation. *Vacuum*, 33(7):397–406, 1983.
- [30] E. M. Williams, F. Le Normand, N. Hilleret, and G. Dominichini. Studies of photon induced desorption of surface gas within an aluminium vacuum chamber using an X-ray source. *Vacuum*, 35(3):141–148, 1985.
- [31] O. Gröbner, A. G. Mathewson, and P. C. Marin. Gas desorption from an oxygen free high conductivity copper vacuum chamber by synchrotron radiation photons. *Journal of Vacuum Science and Technology A*, 12(3):846–853, 1994.
- [32] V. V. Anashin, O. B. Malyshev, V. N. Osipov, I. L. Maslennikov, and W. C. Turner. Investigation of synchrotron radiation-induced

- photodesorption in cryosorbing quasiclosed geometry. *Journal of Vacuum Science and Technology A*, 12(5):2917–2921, 1994.
- [33] V. V. Anashin, G. Derevyankin, V. G. Dudnikov, O. B. Malyshev, V. N. Osipov, C. L. Foerster, F. M. Jacobsen, M. W. Ruckman, M. Strongin, R. Kersevan, I. L. Maslennikov, W. C. Turner, and W. A. Lanford. Cold beam tube photodesorption and related experiments for the Superconducting Super Collider Laboratory 20 TeV proton collider. *Journal of Vacuum Science and Technology A*, 12(4):1663–1672, 1994.
 - [34] V. Baglin, I. R. Collins, O. Gröbner, C. Grünhagel, and B. Jenninger. Molecular desorption by synchrotron radiation and sticking coefficient at cryogenic temperatures for H₂, CH₄, CO and CO₂. LHC Project Report 518, CERN, 2001.
 - [35] R. Calder, O. Gröbner, A. G. Mathewson, V. V. Anashin, A. Dranichnikov, and O. B. Malyshev. Synchrotron radiation induced gas desorption from a prototype Large Hadron Collider beam screen at cryogenic temperatures. *Journal of Vacuum Science and Technology A*, 14(4):2618–2623, 1996.
 - [36] V. V. Anashin, O. B. Malyshev, R. Calder, and O. Gröbner. A study of the photodesorption process for cryosorbed layers of H₂, CH₄, co or CO₂ at various temperatures between 3 and 68 k. *Vacuum*, 53:269–272, 1999.
 - [37] V. V. Anashin, O. B. Malyshev, I. R. Collins, and O. Gröbner. Photon-stimulated desorption and the effect of cracking of condensed molecules in a cryogenic vacuum system. *Vacuum*, 60(1–2):15–24, 2001.
 - [38] I. R. Collins, O. Gröbner, O. B. Malyshev, A. Rossi, P. Strubin, and R. Veness. Vacuum stability for ion induced gas desorption. LHC Project Report 312, CERN, 1999.
 - [39] O. B. Malyshev. The ion impact energy on the LHC vacuum chamber walls. In *7th European Particle Accelerator Conference* [134], pages 951–953.
 - [40] Marie-Hélène Achard. Desorption des gaz induite par des electrons et des ions de l’acier inoxydable, du cuivre OFHC, du titane et de l’aluminium purs. Technical Report CERN-ISR-VA/76-34, CERN, 1976.
 - [41] Marie-Hélène Achard, R. Calder, and A. Mathewson. The temperature dependence of the electron and ion induced gas desorption coefficients

- of some technological materials. Technical Report CERN-ISR-VA/78-2, CERN, 1978.
- [42] Marie-Hélène Achard, R. Calder, and A. Mathewson. The effect of bakeout temperature on the electron and ion induced gas desorption coefficients of some technological materials. *Vacuum*, 29(2):53–65, 1979.
 - [43] William C. Turner. Ion desorption stability in superconducting high energy physics proton colliders. *Journal of Vacuum Science and Technology A*, 14(4):2026–2038, 1996.
 - [44] J. C. Barnard, I. Bojko, and N. Hilleret. Desorption of H_2 and CO_2 from Cu by 5 keV Ar^+ and H_2^+ ion bombardment. *Vacuum*, 47(4):347–350, 1996.
 - [45] C. M. Lyneis, P. Kneisel, O. Stoltz, and J. Halbritter. On the role of electrons in RF breakdown. *IEEE Transactions on Magnetics*, MAG-11(2):417–419, 1975.
 - [46] W. Peter. Vacuum breakdown and surface coating of RF cavities. *Journal of Applied Physics*, 56(5):1546–1547, 1984.
 - [47] R. Calder, G. Dominichini, and N. Hilleret. Influence of various vacuum surface treatments on the secondary electron yield of niobium. Technical Report CERN-LEP-VA-87-61, CERN, 1987.
 - [48] Mauro Pivi. *Beam Induced Electron Multipacting in the CERN Large Hadron Collider Accelerator LHC*. PhD thesis, Università degli studi di Torino, 2000.
 - [49] I. R. Collins, O. Gröbner, N. Hilleret, J. M. Jimenez, and M. Pivi. Electron cloud potential remedies for the vacuum system of the SPS. In Le Roux et al. [136], pages 150–154.
 - [50] G. Arduini, K. Cornelis, O. Gröbner, N. Hilleret, W. Hofle, J. M. Jimenez, J.-M. Laurent, G. Moulard, M. Pivi, and K. Weiss. Electron cloud: Observations with LHC-type beams in the SPS. In *7th European Particle Accelerator Conference* [134], pages 939–941.
 - [51] G. Arduini, V. Baglin, O. Brünig, R. Cappi, F. Caspers, P. Collier, I. R. Collins, K. Cornelis, R. Garoby, O. Gröbner, B. Henrist, N. Hilleret, W. Höfle, J. M. Jimenez, J.-M. Laurent, T. Linnecar, E. Mercier, M. Pivi, F. Ruggiero, G. Rumolo, C. Scheuerlein, J. Tuckmantel, L. Vos, and

- F. Zimmermann. Electron cloud effects in the CERN SPS and LHC. In *7th European Particle Accelerator Conference* [134], pages 259–261.
- [52] Oliver S. Brüning. Simulations for the beam-induced electron cloud in the LHC beam screen with magnetic field and image charges. LHC Project Report 158, CERN, 1997.
 - [53] Miguel A. Furman. The electron-cloud effect in the arcs of the LHC. LHC Project Report 180, CERN, 1998. Also published as LBNL-41482/CBP Note 247.
 - [54] G. V. Stupakov. Photoelectrons and multipacting in the LHC: Electron cloud build-up. LHC Project Report 141, CERN, 1997.
 - [55] V. Baglin, I. Collins, B. Henrist, N. Hilleret, and G. Vorlaufer. A summary of main experimental results concerning the secondary electron emission of copper. LHC Project Report 472, CERN, 2001.
 - [56] V. Baglin, J. Bojko, O. Gröbner, B. Henrist, N. Hilleret, C. Scheuerlein, and M. Taborelli. The secondary electron yield of technical materials and its variation with surface treatments. In *7th European Particle Accelerator Conference* [134], pages 217–221.
 - [57] I. Bojko, J.-L. Dorier, N. Hilleret, and Ch. Scheuerlein. Lowering the secondary electron yield of technical copper surfaces by strong oxidation. Vacuum Technical Note 97-19, CERN, 1997.
 - [58] Iouri Bojko, Noël Hilleret, and Christian Scheuerlein. Influence of air exposures and thermal treatments on the secondary electron yield of copper. *Journal of Vacuum Science and Technology A*, 18(3):972–979, 2000.
 - [59] N. Hilleret, V. Baglin, I. Collins, O. Gröbner, B. Henrist, and G. Vorlaufer. The secondary electron yield of copper: New experimental results and their implications. In *International Workshop on Two-Stream Instabilities in Particle Accelerators and Storage Rings*, KEK, Tsukuba, Japan, 11 – 14 September 2001.
 - [60] M. Q. Ding and E. M. Williams. Electron stimulated desorption of gases at technological surfaces of aluminium. *Vacuum*, 39(5):463–469, 1989.
 - [61] J. Gómez-Góñi and A. G. Mathewson. Temperature dependence of the electron induced gas desorption yields on stainless steel, copper,

- and aluminum. *Journal of Vacuum Science and Technology A*, 15(6):3093–3103, 1997.
- [62] F. Billard, N. Hilleret, and G. Vorlaufer. Some results on the electron induced desorption yield of OFHC copper. Vacuum Technical Note 00-32, CERN, 2000.
 - [63] R. J. Reid. Cleaning for vacuum service. In Turner [135], pages 139–153. Also published as CERN Yellow Report CERN-99-05.
 - [64] A. G. Mathewson, J. P. Bacher, K. Booth, R. S. Calder, G. Dominichini, A. Grillot, N. Hilleret, D. Latorre, F. Le Normand, and W. Unterlerchner. Comparison of chemical cleaning methods of aluminum alloy vacuum chambers for electron storage rings. *Journal of Vacuum Science and Technology A*, 7(1):77–82, 1989.
 - [65] C. Benvenuti, G. Canil, P. Chiggiato, P. Collin, R. Cosso, J. Guérin, S. Ilie, D. Lattore, and K. S. Neil. Surface cleaning efficiency measurements for UHV applications. *Vacuum*, 53:317–320, 1999.
 - [66] R. Calder, A. Grillot, F. Le Normand, and A. Mathewson. Cleaning and surface analysis of stainless steel ultrahigh vacuum chambers by argon gas discharge. Technical Report CERN-ISR-VA-77-59, CERN, 1977.
 - [67] H. Stoeri. In situ glow discharge cleaning method for the LEP vacuum system. *Vacuum*, 33(3):171–178, 1983.
 - [68] K. Akaishi, K. Ezaki, Y. Kubota, and O. Motojima. Reduction of water outgassing and UHV production in an unbaked vacuum chamber by neon gas discharge. *Vacuum*, 53:285–289, 1999.
 - [69] A. Grillot and A. G. Mathewson. Ozone cleaning of metal surfaces. Vacuum technical note, CERN, 1990.
 - [70] K. Tatenuma, T. Momose, and H. Ishimaru. Quick acquisition of clean ultrahigh vacuum by chemical process technology. *Journal of Vacuum Science and Technology A*, 11(4):1719–1724, 1993.
 - [71] K. Tatenuma, K. Uchida, T. Itoh, T. Momose, and H. Ishimaru. Acquisition of clean ultrahigh vacuum using chemical treatment. *Journal of Vacuum Science and Technology A*, 16(4):2693–2697, 1998.
 - [72] Gerd Janzen. *Plasmatechnik*. Hüthig Buch Verlag GmbH, Heidelberg, 1992.

- [73] Johann Laimer. Skriptum zur Vorlesung “Plasmatechnologie”, Wintersemester 1996/97, TU Wien, Institut für allgemeine Physik.
- [74] Herbert Störi. Skriptum zur Vorlesung “Plasmachemie”, Sommersemester 1997, TU Wien, Institut für allgemeine Physik.
- [75] J. W. Metselaar, V. I. Kuznetsov, and A. G. Zhidkov. Photoresist stripping in afterglow of Ar – O₂ microwave plasma. *Journal of Applied Physics*, 75(10):4910–4916, 1994.
- [76] G. N. Hays, C. J. Tracy, and H. J. Oskam. Surface catalytic efficiency of a sputtered molybdenum layer on quartz and pyrex for the recombination of nitrogen atoms. *Journal of Chemical Physics*, 60(5):2027–2034, 1974.
- [77] L. Lefèvre, T. Belmonte, and H. Michel. Modeling of nitrogen atom recombination on Pyrex: Influence of the vibrationally excited N₂ molecules on the loss probability of N. *Journal of Applied Physics*, 87(10):7497–7507, 2000.
- [78] H. Störi. An in-situ glow discharge cleaning method for the LEP vacuum system. Technical Report CERN-ISR-VA-81-28, CERN, 1981.
- [79] Secon Semiconductor Equipment, Laxenburgerstraße 17, A-2353 Guntramsdorf, Austria. *XRG-801 Microwave radical generator – Operator’s manual*, 1998.
- [80] Alcatel CIT – Technologie du Vide, 98, avenue de Brogny, B.P. 2069, 74009 Annecy Cedex, France. *ADP & ADS Séries One, pompes sèches pour l’industrie du semiconducteur – Manuel de l’utilisateur*, 1997.
- [81] MKS Instruments, Six Shattuck Road, Andover, MA 01810-2449, USA; <http://www.mksinst.com>. *MKS Type 1179A and 2179A Mass-Flo[®] Controller and Type 179A Mass-Flo[®] Meter – Instruction manual*, 1997.
- [82] Balzers Instruments, Postfach 1000, FL-9496 Balzers, Liechtenstein; <http://www.bi.balzers.com>. *Compact Capacitance Gauge – Betriebsanleitung*.
- [83] Michel Gautier. Private communications, 2001.
- [84] National Instruments Corporation, 11500 North MoPac Expressway, Austin, TX 78759-3504, USA; <http://www.ni.com>.

- [85] Karl Jousten. Pressure measurement with ionization gauges. In Turner [135], pages 75–87. Also published as CERN Yellow Report CERN-99-05.
- [86] J. H. Leck. Partial pressure measurement. In Turner [135], pages 89–97. Also published as CERN Yellow Report CERN-99-05.
- [87] Gernot Eder. *Atomphysik*. Wissenschaftsverlag, Mannheim – Wien – Zürich, 1989. 2., überarbeitete Auflage.
- [88] V. Baglin, B. Henrist, N. Hilleret, E. Mercier, and C. Scheuerlein. Ingredients for the understanding and the simulation of multipacting. In Le Roux et al. [136], pages 130–135.
- [89] Mauro Taborelli and Daniel Latorre. Private communications in the form of internal notes about the Auger analysis of radical treated copper samples, 2000.
- [90] Robert J. Kee, Fran M. Rupley, Ellen Meeks, and James A. Miller. CHEMKIN-III: A FORTRAN chemical kinetics package for the analysis of gas-phase chemical and plasma kinetics. Technical Report SAND96-8216, Sandia National Laboratories, 1996.
- [91] Reaction Design, Inc., 6440 Lusk Boulevard, San Diego, CA 92121, USA; <http://www.reactiondesign.com>.
- [92] Robert J. Kee, Graham Dixon-Lewis, Jürgen Warnatz, Michael E. Coltrin, and James A. Miller. A FORTRAN computer code package for the evaluation of gas-phase, multicomponent transport properties. Technical Report SAND86-8246, Sandia National Laboratories, 1986.
- [93] Andrew E. Lutz, Robert J. Kee, and James A. Miller. SENKIN: A FORTRAN program for predicting homogeneous gas phase chemical kinetics with sensitivity analysis. Technical Report SAND87-8248, Sandia National Laboratories, 1997.
- [94] Richard S. Larson. PLUG: A FORTRAN program for the analysis of plug flow reactors with gas-phase and surface chemistry. Technical Report SAND96-8211, Sandia National Laboratories, 1996.
- [95] R. J. Kee, F. M. Rupley, J. A. Miller, M. E. Coltrin, J. F. Grcar, E. Meeks, H. K. Moffat, A. E. Lutz, G. Dixon-Lewis, M. D. Smooke, J. Warnatz, G. H. Evans, R. S. Larson, R. E. Mitchell, L. R. Patzold, W. C. Reynolds, M. Caracotsios, W. E. Stewart, P. Glarborg, C. Wang,

- and O. Adigun. *PREMIX – Manual from the CHEMKIN Collection, Release 3.6*. Reaction Design, Inc., San Diego, CA, 2000.
- [96] Concentration, Heat & Momentum Ltd., Bakery House, 40 High Street, Wimbledon Village, London SW19 5AU, UK; <http://www.cham.co.uk>.
 - [97] Computational Dynamics, 200 Shepherds Bush Road, London W6 7NY, UK; <http://www.cd.co.uk>.
 - [98] ANSYS, Inc., Southpointe, 275 Technology Drive, Canonsburg, PA 15317, USA; <http://www.ansys.com>.
 - [99] E. J. McInerney. Study of station flow dynamics in a sequential multiwafer chemical vapor deposition batch reactor using reactor chemistry. *Journal of Vacuum Science and Technology A*, 14(3):1152–1155, 1996.
 - [100] Christoph Werner, Matthias Ilg, and Kevin Uram. Three-dimensional equipment modeling for chemical vapor deposition. *Journal of Vacuum Science and Technology A*, 14(3):1147–1151, 1996.
 - [101] Christoph Gebhard Schwärzler. *Analytik und Modellierung der Gasphase bei der plasmaunterstützten Diamantsynthese*. PhD thesis, Technische Universität, Wien, 1997.
 - [102] Da Zhang and Mark J. Kushner. Mechanisms for CF_2 radical generation and loss on surfaces in fluorocarbon plasmas. *Journal of Vacuum Science and Technology A*, 18(6):2661–2668, 2000.
 - [103] G. Misslinger, J. Laimer, and H. Störi. Investigation of the plasma chemistry relevant for diamond deposition with chlorinated hydrocarbons. *Vacuum*, 61:413–417, 2001.
 - [104] Chin-Hao Chou, Ta-Chin Wei, and Jonathan Phillips. Detailed model of the afterglow region of a microwave generated oxygen plasma. *Journal of Applied Physics*, 72(3):870–878, 1992.
 - [105] S. Bockel, T. Belmonte, H. Michel, and D. Ablitzer. 3D modeling of a microwave post-discharge nitriding reactor. *Surface and Coatings Technology*, 97(1–3):618–625, 1997.
 - [106] T. Belmonte, S. Bockel, H. Michel, and D. Ablitzer. Study of transport phenomena by 3D modeling of a microwave post-discharge nitriding reactor. *Surface and Coatings Technology*, 112(1–3):5–9, 1999.

- [107] Steven F. Adams and Terry A. Miller. Surface and volume loss of atomic nitrogen in a parallel plate RF discharge reactor. *Plasma Sources Science and Technology*, 9(3):248–255, 2000.
- [108] H. K. Versteeg and W. Malalasekera. *An introduction to Computational Fluid Dynamics*. Addison Wesley Longman Limited, 1995.
- [109] H. Xu and C. Zhang. Numerical calculations of laminar flows using contravariant velocity fluxes. *Computers and Fluids*, 29:149–177, 2000.
- [110] Wilhelm Flügge. *Tensor Analysis and Continuum Mechanics*. Springer-Verlag, Berlin – Heidelberg – New York, 1972.
- [111] A. J. McConnell. *Applications of Tensor Analysis*. Dover publications, Inc., New York, 1957. formerly titled: Applications of the Absolute Differential Calculus.
- [112] M. S. Day and J. B. Bell. Numerical simulation of laminar reacting flows with complex chemistry. *Combustion Theory and Modelling*, 4:535–556, 2000.
- [113] National Institute of Standards and Technology: NIST Chemical Kinetics Database <http://kinetics.nist.gov>.
- [114] T. Belmonte, S. Bockel, C. Bordot, D. Ablitzer, and H. Michel. Measurement of the loss probability of nitrogen atoms at 823 K on iron nitride $\epsilon - \text{Fe}_2\text{N}_{1-x}$. *Applied Surface Science*, 135(1–4):259–268, 1998.
- [115] Harmeet Singh, J. W. Coburn, and David B. Graves. Recombination coefficients of O and N radicals on stainless steel. *Journal of Applied Physics*, 88(6):3748–3755, 2000.
- [116] S. Suzuki, H. Itoh, N. Ikuta, and H. Sekizawa. Reflection of diffusing metastable gas molecules at the boundary. *Journal of Physics D*, 25:1568–1573, 1992.
- [117] I. M. Rusinov, G. W. Paeva, and A. B. Blagoev. A method for simultaneous determination of the diffusion coefficient of particles in gas media and their reflection coefficient at the wall. *Journal of Physics D*, 30:1878–1884, 1997.
- [118] Ilko Rusinov, Susumu Suzuki, Alexander Blagoev, and Haruo Itoh. Studies of diffusion losses in gaseous media using a boundary condition

- of the third kind. *Japanese Journal of Applied Physics Part 1*, 39(5A):2799–2803, 2000.
- [119] National Institute of Standards and Technology: NIST Chemistry Webbook: <http://webbook.nist.gov>.
 - [120] The Mathworks, 3 Apple Hill Drive, Natick, MA 01760-2098, USA; <http://www.mathworks.com>.
 - [121] Carl Recker et al. *Hoch- und Ultrahochvakuum: Erzeugung und Anwendung*. expert verlag, Sindelfingen, 1984.
 - [122] R. W. Assmann, F. Becker, R. Bossart, H. Burkhardt, H. Braun, G. Carron, W. Coosemans, R. Corsini, E. T. D’Amico, J.-P. Delahaye, S. Doebert, S. Fartoukh, A. Ferrari, G. Geschonke, J.-C. Godot, L. Groening, G. Guignard, S. Hutchins, J.B. Jeanneret, E. Jensen, J. Jowett, T. Kamitani, A. Millich, O. Napoly, P. Pearce, F. Perriollat, R. Pittin, J.-P. Potier, A. Tiche, L. Rinolfi, T. Risselada, P. Royer, T. Raubenheimer, F. Ruggiero, R. Ruth, D. Schulte, G. Suberlucq, I. Syratchev, L. Thorndahl, H. Trautner, A. Verdier, I. Wilson, W. Wuensch, F. Zhou, and F. Zimmermann. A 3 TeV $e^+ e^-$ Linear Collider Based on CLIC Technology. Yellow Report CERN 2000-008, CERN, 2000.
 - [123] I. Wilson and W. Wuensch. The CLIC main linac accelerating structure. CLIC Note 456, CERN, 2000. CERN/PS 2000-057 (RF).
 - [124] Miran Mozetič and Anton Zalar. Recombination of neutral oxygen atoms on stainless steel surface. *Applied Surface Science*, 158(3–4):263–267, 2000.
 - [125] HELICOFLEX Company, P.O. Box 9889, Columbia, SC 29290, USA; <http://www.helicoflex.com>.
 - [126] Travis Ferguson. Measuring temperature with thermocouples – a tutorial. Application Note 043, National Instruments Corporation, 11500 North MoPac Expressway, Austin, TX 78759-3504, USA, 2001.
 - [127] K. Gieck. *Technische Formelsammlung*. Gieck Verlag, D-7100 Heilbronn/N, 1984. 28. deutsche Auflage.
 - [128] William H. Press, Brian P. Flannery, Saul A. Teukolsky, and William T. Vetterling. *Numerical Recipes*. Cambridge University Press, 1986. see also <http://www.nr.com/> for an online version.

- [129] V. Lj. Marković, Z. Lj. Petrović, and M. M. Pejović. Surface recombination of atoms in a nitrogen afterglow. *Journal of Chemical Physics*, 100(11):8514–8521, 1994.
- [130] B. Gordiets, C. M. Ferreira, J. Nahorny, D. Pagnon, M. Touzeau, and M. Vialle. Surface kinetics of N and O atoms in $N_2 - O_2$ discharges. *Journal of Physics D*, 29(4):1021–1031, 1996.
- [131] Peter J. Mohr and Barry N. Taylor. CODATA recommended values of the fundamental physical constants: 1998. *Journal of Physical and Chemical Reference Data*, 28(6):1713–1852, 1999.
- [132] Barry N. Taylor and Chris E. Kuyatt. Guidelines for evaluating and expressing the uncertainty of nist measurement results. NIST Technical Note 1297, NIST, 1994.
- [133] I. N. Bronstein and K. A. Semendjajew. *Ergänzende Kapitel zu [137]*. Verlag Harri Deutsch, Thun und Frankfurt (Main), 4. Auflage, 1986.
- [134] *7th European Particle Accelerator Conference*, Vienna, Austria, 26–30 June 2000.
- [135] S. Turner, editor. *CERN Accelerator School on Vacuum Technology*, Scanticon Conference Centre, Snekersten, Denmark, 28 May – 3 June 1999. CERN. Also published as CERN Yellow Report CERN-99-05.
- [136] P. Le Roux, J. Poole, and M. Truchet, editors. *10th Workshop on LEP-SPS Performance*, Chamonix, France, 17 – 21 Jan 2000.
- [137] I. N. Bronstein and K. A. Semendjajew. *Taschenbuch der Mathematik*. Verlag Harri Deutsch, Thun und Frankfurt (Main), 22. Auflage, 1985.

Acknowledgements

First of all I would like to thank my supervisors, Noël Hilleret at CERN and Herbert Störi at the Vienna University of Technology. Herbert, who has been guiding my studies since several years and who encouraged me to apply at CERN in the first place, has been a “Doktorvater” in the sense of the word. Noël has been the best “boss” one could imagine. I most appreciated his support, professional and personal, and his scientific and practical experience. He gave me a lot of freedom in doing my work and was always open for discussions. At the same time, he did not spare me with criticism and helped me to keep in mind the final goal of my work.

I am indebted to Miguel Jimenez, Bernard Henrist, and all the other colleagues in the vacuum group. Without their help, this work would not exist. I am also indebted to Mauro Taborelli and Daniel Latorre of the EST-SM group who realised the surface analyses and gave me most valuable input for my work. Special thanks also go to Jean-Luc Dorier, now at EPFL Lausanne, to Johann Laimer and Gerhard Misslinger from the Vienna University of Technology and to Christian Scheuerlein of the EST-SM group for their valuable suggestions and comments.

I would like to thank my friend and colleague Christian Rathjen, for all the fun, nightlong discussions, and countless weekends in the French alps. I also wish to thank Lukas Tlustos, Mauro Pivi, Gerhard Schneider, Richard Madden, Vassili Maroussov, Zebulon Vilakazi, Reiner Geyer and Madjid Boutemour who turned out to be real friends. I will always remember the evenings in the CERN cafeteria with endless discussions and all the fun we had together.

Last but not least I would like to thank my mother and my father, who made it possible for me to study physics in the first place and who always encouraged me to carry on.

This work has been carried out in the framework of the Austrian Doctoral Student Program at CERN.

Curriculum Vitae

Georg Vorlauffer

born on 3rd of September, 1968 in Vienna, Austria

Education

Sep 1974 – June 1978	Primary School
Sep 1978 – June 1986	gymnasium with emphasis on natural science, “Matura” degree obtained June 1986
Oct 1986 – Sep 1998	Vienna University of Technology, department of technical physics, masters degree in physics obtained September 1998
Oct 1998 – Sep 2001	Doctoral student at CERN, defence of the thesis March 2002

Professional experience

Aug 1985	work on construction sites in Moscow with my father’s company
Aug 1986	IBM Austria
Aug 1988 – June 1991	Austrian Research Center Seibersdorf, research contract
July 1991 – Sep 1995	Philips Communications & Processing, software engineer
July 1996 – Sep 1998	Origin Information Technology, project management and software development for the Print & Publishing department

Other biographic data

Oct 1985 – June 1986	participation in the “Mathematical Olympic Games”, first place in the national contest in 1986
Sep 1976 – June 1992	education in classical piano in the public music school of the city of Vienna
Oct 1995 – May 1996	military service